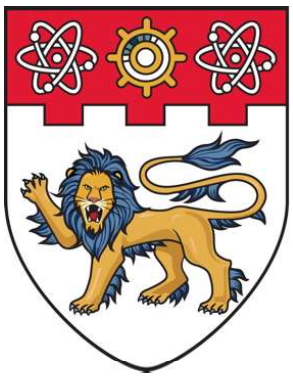

NANYANG TECHNOLOGICAL UNIVERSITY
SINGAPORE

# ANTI-CORROSION CARBON-BASED COMPOSITE EPOXY COATING FOR MARINE INDUSTRY

**ARTEMOVA ANASTASIIA**

**SCHOOL OF MATERIALS SCIENCE AND ENGINEERING**

**2019**

# ANTICORROSION CARBON-BASED EPOXY COMPOSITE COATING FOR MARINE INDUSTRY

**ARTEMOVA ANASTASIIA**

SCHOOL OF MATERIALS SCIENCE AND ENGINEERING

A thesis submitted to the Nanyang Technological University
in partial fulfilment of the requirement for the degree of
Doctor of Philosophy

**2020**

## Statement of Originality

I hereby certify that the work embodied in this thesis is the result of original research, is free of plagiarised materials, and has not been submitted for a higher degree to any other University or Institution.

20.08.2019

. . . . . .
Date

. . . . . .
Artemova Anastasiia

## Supervisor Declaration Statement

I have reviewed the content and presentation style of this thesis and declare it is free of plagiarism and of sufficient grammatical clarity to be examined. To the best of my knowledge, the research and writing are those of the candidate except as acknowledged in the Author Attribution Statement. I confirm that the investigations were conducted in accord with the ethics policies and integrity standards of Nanyang Technological University and that the research data are presented honestly and without prejudice.

20.08.2019

..... .....

Date Prof. Shen Zexiang

# Authorship Attribution Statement

Chapter 6. is published as A. Artemova, Y. Huang, Z.X. Shen, and S. Savilov, Influence of the UV Radiation on the Corrosion Resistance of the Carbon-Based Coatings for the Marine Industry. In *CORROSION 2019. NACE International,* (2019).

The contributions of the co-authors are as follows:

- Prof Shen provided the initial project direction and edited the manuscript drafts.
- I prepared the manuscript drafts. The manuscript was revised by Prof. Huang and Prof. Savilov.
- I performed all the simulation experiment and coating characterization at the School of Materials Science and Engineering and School of Physical and Mathematical Science Singapore. I also analyzed the data.
- All microscopy, including sample preparation, was conducted by me in the Facility for Analysis, Characterization, Testing, and Simulation.
- Prof. Savilov provided the facilities for the synthesis of the carbon nanotubes pigments.
- Prof. Huang provided guidance in the interpretation of the electrochemical measurement data.

This thesis does not contain any materials from papers published in peer-reviewed journals in which I am listed as an author. Y. Dai, H. Zhang, W. Wei, J. Zhang, A.O. Artemova, M. Chen, Effect of Si-based compound nanoparticles on the anticorrosive properties of epoxy resin. *Journal of Nanoscience and Nanotechnology*, V. 20, pp. 1-20, 2020. DOI:10.1166/jnn.2020.18481

The contributions of the co-authors are as follows:

- Prof. Chen suggested the project area and edited the manuscript drafts.

- Y. Dai wrote the drafts of the manuscript. The manuscript was revised together with W. Wei and H. Zhang.
- I provided the scientific advice for the data explanations and performed the final revision of the manuscript.
- H. Zhang conducted the electrochemical experiments together with Y. Dai.
- J. Zhang prepared the samples for the FTIR and XRD studies and carried the analysis.

Carbon nanomaterials which was synthesized as alternative materials for anti-corrosion protection was used as electrode materials for potassium ion batteries and published as Huanhuan Wang; Anastasiia Artemova; Guang Yang; Lili Zhang; Ekaterina Arkhipova; Jilei Liu; Yizhong Huang; Jianyi Lin; Ze Xiang Shen, Lotus Root-like Porous Carbon for Potassium Ion Battery with High Stability and Rate Performance. *Journal of Power Sources (reviewed*), (2020)

The contributions of the co-authors are as follows:

- Prof Shen and Jianyi Lin provided the initial project direction and edited the manuscript drafts.
- I synthesize the carbon materials which were used in current research
- Huanhuan Wang was conducting the fabrication and testing of the carbon nanomaterials
- Huanhuan Wang prepared the manuscript drafts. The manuscript was revised by Jilei Liu and Yizhong Huang
- Ekaterina Arkhipova prepared the template for the synthesis of the carbon materials
- Guang Yang and Lili Zhang helped to conduct the physico-chemical analysis and also analyze the data.

20.08.2019

. . . . . .  . . . . . .

Date  Artemova Anastasiia

## Abstract

Corrosion and biofouling are severe global problems that cost hundreds of billion dollars annually. The protective coating is the most widespread technology among various methods used in anti-corrosion and anti-fouling. Traditional coating materials (e.g., Cr-based, Zn-based, or biocide-containing anti-corrosive/fouling coatings) suffer from poor performance, environmental hazards, and high cost. This project aims to develop coating materials with carbon nanomaterials additives that provide triple protection (anti-corrosion, anti-fouling, and anti-decay) and are also environmentally friendly, non-cytotoxic, low cost, and long-lasting.

In this manuscript, the performance in the corrosion protection of the graphene oxide-based and carbon nanotubes-based composite coatings were investigated. Based on the literature review, the corrosion mechanism is complex, and a number of factors affected on it, such as coating composition, environmental conditions, and design. Several mechanisms of the corrosion protection are described, cathodic and anodic protection, inhibitors and coatings, which were chosen as an object of the investigation due to the most comprehensive anti-corrosion technology. Composite coatings consist of binder, pigments, solvent, and additives. The first two components are the most important in the anti-corrosion protection. For the marine industry, the most common binder is epoxy resin and polyurethane. Bisphenol A epoxy resin was used to control the cost-effectiveness of the development coating. Different pigments can provide anti-corrosion protection, but the carbon-based pigments are the most perspective one, therefore was used as an object for this research work.

Carbon-based materials are excellent materials for applications in the coating due to its exceptional chemical inertness, outstanding mechanical strength, non-cytotoxicity, and unique antibacterial/anticorrosive properties. Besides graphene oxide (GO), other carbon nanomaterials such as nitrogen-doped graphene oxide (N-GO), cylindrical and conical carbon nanotubes (cyl-, con-CNT), nitrogen-doped carbon nanotubes (N-CNT) are chosen and synthesized for anti-corrosion pigment purpose, and physicochemical properties of

materials are explored to have better understanding of the nature of the pigment. It was hypothesized that nitrogen doping of the carbon nanomaterials would improve the protection properties. This thesis focused on the investigation of the influence of the carbon-based materials on the coating and coating performance under different aggressive conditions, which are described in four chapters.

The first chapter described the performance of the carbon-based coatings system in the 3.5% NaCl solution. The effect of the different carbon-based materials on the coating performance is introduced, and the electrochemical parameters were investigated. It was found that nitrogen contain decreases the corrosion rate in four times, however, carbon-based pigments - in only two times in comparison with pure epoxy coating. Secondary, the impact of the ultraviolet radiation on the coating degradation was explored, and the degree of the coating degradation was calculated. It was shown that carbon-based pigments absorb the UV radiation and prevent the coating from deterioration. The carbon nanotubes due to the structure provide better prevention form the UV radiation and pitting corrosion. In the third part, the effect of the immersion to the sodium chloride solution was studied. The importance of the structure of the pigment materials and its composition was established. The nitrogen-doped carbon nanotube composite coating showed the lowest absorption volume, and corrosion rate, and however the nitrogen-doped graphene oxide composite coating absorbs much water it still decreases the corrosion rate, prevent the pitting corrosion and hydrolytic degradation. Finally, the coating behavior under weathering degradation was explained, and the mechanism of the protection by the nitrogen-doped pigments was formulated.

The novelty of this research is that the impact of the structure and composition of the carbon-based nanomaterials were studied, as well as using nitrogen-doped graphene oxide and nitrogen-doped carbon nanotubes as anti-corrosion pigment was reported for the first time. The recommendation for future research, such as investigation of the concentration and nitrogen percentage influence on the protection properties are suggested to reach the highest effectiveness of the coating. This fundamental study is the first step in solving the global problem of corrosion.

## Lay Summary

Corrosion is a significant challenge for most industries, including infrastructure, manufacturing, and transportation. Each year, several thousands of billions of dollars are spent on different direct and indirect corrosion issues. The consequences of corrosion could be grave, such as the sinking of the tanker Erika in 1999, the EL AL Boeing 747 crash in 1992, or the oil spills in Santa Barbara, California, in 2015, which cost the lives of many people and caused damage to the environment. Fundamental research in corrosion engineering helps to create novel solutions in this field.

Protective coatings are the most widely used mechanisms of metal protection. This research focused on the development of novel coatings for the marine industry, which will provide sufficient protection in different environments. Coatings are complex systems consisting of a binder; a solvent; and pigments, which play different roles, such as providing color or corrosion protection; and additives that improve the wetting, leveling, biofouling, and stability of the coating. An industrial coating consists of more than thirty components.

In the current manuscript, novel carbon-based anticorrosion pigments, which are very promising due to their outstanding mechanical and physicochemical properties, are developed. The originality of this work lies in using coatings with doped with heteroatom carbon nanomaterials doped with heteroatom and in the investigation of protective properties in aggressive environments, such as ultraviolet radiation or corrosive solutions.

## Acknowledgements

Author would like to acknowledge the financial, academic and technical support from Nanyang Technological University, as well as Singapore International Graduate Award (SINGA) to support my Ph.D. research study.

Firstly, I should thank my supervisors Prof. Shen ZeXiang, Prof. Savilov Serguei，and Prof. Huang Yizhong，for the opportunity to do Ph.D. in NTU and to be the member of a warm, vibrant and creative group. Their rigorous thinking, open mind and original views always let me sober up every time. Under their guidance, I begin to have the ability and quality as a researcher.

I would like to acknowledge Prof Chen Zhong and his group members Dr. Shunli Zheng and Mr. Daniel A. Bellido-Aruilar for their appreciative help with conducting weathering experiment and using UV Test chamber (Atlas Material Testing Technology Ltd.) of it.

Besides, I should give my sincere thanks to all the technical staff in Organic Materials Service and Facility for Analysis Characterization Testing & Simulation laboratories for their great patience and kind help make great difference in my experiments.

My sincere thanks also give to all members in group in Nanyang Technological University, Prof. Ni Shibing, Assoc. Prof. Chen Minghua, Dr. Jiang Liyong, Dr. Yuan Guanghui, Dr. Lai Linfei, Dr. Yan Jiaxu, Dr Jiang Yuanyuan, Dr. Liu Jilei, Mr. Chao Dongliang, Ms. Lekina Yulia, Mr. Wang Haisheng, Ms. Wang Jin, Miss Cai Xiaoyi, Miss Yin Tingting, Miss Xia Juan, Miss Chen Zhen, Mr. Eason Chan, Miss Wang Huanhuan and Mr. Qian Cheng for their kind helps, good suggestions and effective discussions.

And, I thank all members of Laboratory of Catalysis and Gas Electrochemistry of Chemistry Department Lomonosov Moscow State University, Accos. Prof. Ivanov Anthon, Dr. Suslova Evgenia, Dr. Shumiantsev Alexey, Dr. Egorov Alexandr, Dr. Novotortsev

Roman, Dr. Strokova Natalia, Miss Nesterova Ekaterina and for their scientific ideas and support in research work. Specially, I would like to thank Dr. Maslakov Konstantin for conducting X-ray photoelectron spectroscopy (XPS), Miss Arkhipova Ekaterina for help in synthesis cylindrical and conical carbon nanotubes, Dr. Chernyak Serguei for conducting the scanning electron microscopy (SEM) of the carbon-based materials.

I should give my sincere thanks to my husband Mr. Artemov Fedor, my family and friends who are my spiritual pillars. They always encourage and support me when I am down, and give advice in.

**Table of Contents**

## Table Captions

## Figure Captions

# Abbreviations

| | |
|---|---|
| ASTM | American Society for Testing and Materials |
| ATR | Attenuated Total Reflectance |
| BPA | Bisphenol A Epoxy Resin |
| CE | Counter Electrode |
| CNT | Carbon nanotubes |
| CNTcon | Conical Carbon Nanotubes |
| CNTcyl | Cylindrical Carbon Nanotubes |
| CPE | Constant Phase Element |
| CVD | Chemical Vapor Deposition |
| DIW | Deionized Water |
| DETA | Diethylenetriamine |
| EA | Elemental Analysis |
| $E_{corr}$ | Potential of Corrosion |
| EIS | Electrochemical Impedance Spectroscopy |
| Ep | Pitting Potential |
| FESEM | Field Emission Scanning Electron Microscopy |
| FTIR | Fourier Transform Infrared Spectroscopy |
| GO | Graphene Oxide |
| $H_{12}MDI$ | Hydrogenated Diphenyl Methane Diisocyanate |
| HDI | Hexamethylene Diisocyanate |
| HPDMS | Hydroxyl-terminated Poly(dimethyl)siloxane |

| | |
|---|---|
| $I_{corr}$ | Corrosion Current Density |
| IPDI | Isophorone Diisocyanate |
| MDI | Diphenyl Methane Diisocyanate |
| n | Indicator of constant phase element |
| N-CNT | Nitrogen-doped Carbon Nanotubes |
| N-GO | Nitrogen-doped Graphene Oxide |
| OCP | Open Circuit Potential |
| P2BA | Poly(2-butylaniline) |
| PANi | Polyaniline |
| PTFE | Polytetrafluoroethylene |
| PVC | Pigment Volume Concentration |
| PVD | Physical Vapor Deposition |
| RE | Reference Electrode |
| SCC | Stress-Corrosion Cracking |
| SCE | Saturated Calomel Electrode |
| SEM | Scanning Electron Microscopy |
| SHE | Standard Hydrogen Electrode |
| SS | Stainless Steel |
| TBTF | Tributyltin Fluoride |
| TBTO | Tributyltin Oxide |
| TDI | Toluene Diisocyanate |
| TGA | Thermal Gravimetric Analysis |
| TPTF | Triphenyl Tin Fluoride |

| | |
|---|---|
| UNESCO | United Nations Educational, Scientific and Cultural Organization |
| UV | Ultraviolet |
| WE | Working Electrode |
| XPS | X-ray photoelectron Spectroscopy |

# Chapter 1

# Introduction

*Corrosion is the degradation of materials by reaction with the environment. The corrosion process is an issue of worldwide significance. Just like other natural hazards (earthquakes or tornadoes), corrosion can cause severe and expensive damage to everything from automobiles to infrastructure. Besides, corrosion causes loss or contamination of the product, costly maintenance, reduction in efficiency, and expensive overdesign. The main complexity of the problem arises from the fact that corrosion is a multidisciplinary issue. Investigation of corrosion mechanisms, applying protective systems, and using corrosion-resistant materials are the main steps in corrosion prevention.*

## 1.1. Background and Problem Statement

Corrosion is a fundamental issue due to economic, safety, and conservation reasons. Economic losses are divided into direct losses and indirect losses. [1] Direct losses include replacing the cost of structures, machinery, or their components—for example, metal roofing and pipelines. The following five elements contribute to the indirect cost of corrosion:

- Social value, also called user cost, incurred due to the loss of time and money during the period of repair and rehabilitation
- Loss of products due to spillage or leakage
- Loss of efficiency due to the accumulation of corrosion products in the flow stream
- Production loss due to unexpected shutdowns
- Cost related to overdesign

Corrosion losses are found in different industry sectors, such as utilities, infrastructure, and transportation. The breakdown across industrial sectors is shown in Figure 1.1.

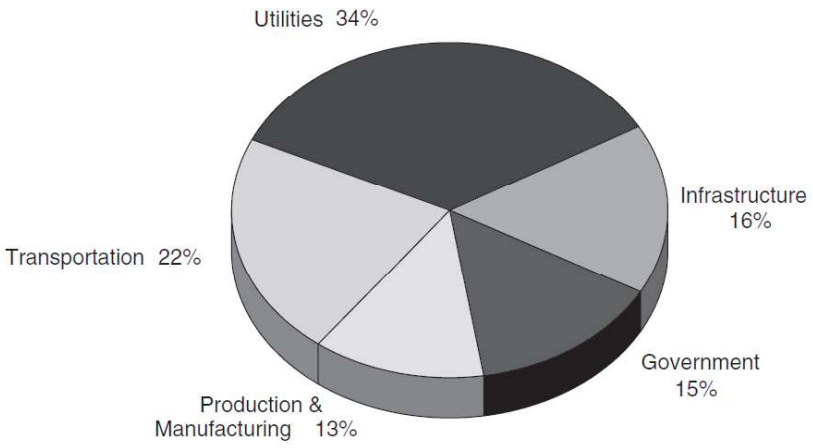


**Figure 1.1.** Corrosion costs breakdown across industrial sectors. [2]

Based on the gross world product (GWP), the global direct cost of corrosion is USD 990 billion, and the global indirect cost of corrosion is USD 940 billion; thus,

the total global value of corrosion is USD 1930 billion, or 3.8% of the GWP, and this amount increases significantly every year.[3]

Corrosion prevention starts with the determination of the proper design, followed by the appropriate selection of the materials and protection mechanism (cathodic protection, coatings). [4] Composite protective coating is the most widely spread technology among various methods used in corrosion protection for the marine industry. The main challenge in the preparation of protective coatings is to eliminate gaps and inhomogeneities in the coating film and provide an entirely impermeable film. Carbon-based materials are the most promising anticorrosion pigments due to their mechanical strength, chemical inertness, noncytotoxicity, and powerful absorption of UV and visible light.

Graphene consists of one atomic layer of sp2-hybridized carbon atoms in a hexagonal lattice, which can be oxidized to obtain graphene oxide. The graphene layer is impermeable to all atoms and molecules at room temperature, which is the most promising barrier material for protective coating. Carbon nanotubes are unique carbon-based materials that can demonstrate not only a barrier effect but also a passivation effect via the adsorption of molecular species of oxygen and hydroxyl, chloride, and sulfate anions. [5] Although the adsorption capacity is higher for graphene oxide [6] than carbon nanotubes [7], the energy of adsorption is several times lower. [8]

The successful integration of carbon-based materials with polymers provides a breakthrough in coating technology due to the following advantages:

- Carbon-based pigments are environmentally friendly and noncytotoxic.
- The graphene sheet is impermeable to water, and all ions/ionic groups and carbon nanotubes are able to absorb ions and molecules. [5]
- Carbon-based materials are a potent blocker of UV and visible light, which can prevent epoxy/polymer decay. [9] [10]

- Carbon-based pigment–polymer composites can be easily prepared via chemical oxidative polymerization and turned into a gel-like paint; they can easily be applied to the protected surface by a scalable coating process, such as spraying, rolling, or dip coating, which is essential for industrial tests.
- The incorporation of carbon-based pigments into the polymer can significantly improve its optical [11] mechanical, thermal, electrical [12] and protective properties. [13]
- The polymer can enhance the adhesion, toughness, and compatibility of the graphene coating; it can seal open pores/channels between graphene sheets (corrosion-promotion centers) and hence improve the anticorrosion/antifouling properties of the coating. [14]
- The graphene-based coating also inhibits bacterial growth and fouling. [15]

Carbon-based materials demonstrate the ability to agglomerate, which decreases coating performance by the formation of unprotected parts, and functionalization of the materials improves the uniform dispersion of the pigment in the binder. Functionalization by an organic compound such as 3-aminopropyl triethoxysilane [16] and p-phenylenediamine [17] improves the coating's protection properties. However, the application of nitrogen-doped carbon-based pigments as a way of enhancing anticorrosion properties and dispersion of the pigment has not been reported yet.

## 1.2. Objectives

This study was conducted as part of the development of solving the fundamental problem of corrosion, including the work on creating the new coating for the marine and shipping industry based on precious carbon materials. [18] The main aim of this study is to develop a high-efficiency anticorrosion coating using carbon-based pigments, with long-term reliability, easy maintenance, and low cost.

In the present study, graphene oxide (GO) and cylindrical and conical carbon nanotubes (CNT) were investigated as anticorrosion pigments due to their unique combination of properties, low cost, and nontoxicity. Graphene shows high thermal conductivity [19], mechanical properties [20], and barrier behavior due to its impermeability. [21]. The corrosion prevention of graphene oxide is very promising because it decreases the corrosion rate several times. [13, 22, 23] Carbon nanotubes are used in different industries due to their unique structure, mechanical properties, and high conductivity. [24] Using carbon nanotubes as anticorrosion pigment is very promising due to two ways of protection: barrier and adsorption. [5, 25, 26]

Nitrogen-doped graphene oxide and nitrogen-doped carbon nanotubes were, for the first time, tested for their ability to prevent corrosion. It was suggested that nitrogen doping improves the dispersion of the carbon nanomaterials in the binder, boosts the coating performance, and enhances the stability of the composite under ultraviolet radiation and in corrosive environments due to amine groups on the surface of the doped carbon nanomaterials, which are formed by chemical bonding with the epoxy group of the binder.

The composite coating was exposed to different types of environments to investigate the protection mechanism. The simulation experiment helps to understand the coating's performance in real-life situations. An investigation of coating performance under different conditions was conducted. The influence of ultraviolet radiation and sodium chloride solution, together with water condensation, on the stability of the composite coating was examined.

An investigation of the mechanism of corrosion protection and the influence of graphene oxide and carbon nanotube functionalization on it were reported.

## 1.3. Dissertation Overview

The thesis contributes to solving the global problem of corrosion protection by organic coatings and the development of environmentally friendly pigments with

efficient performance based on graphene oxide and carbon nanotube structures.

*Chapter 1* provides a rationale for the importance of corrosion and the necessity of research in this field. The advantages and limitations of the carbon-based pigments that were selected for investigation are described. Based on this background, the hypothesis of the importance of material functionalization and the objectives of the research are formulated. After that, an overview of the dissertation is described chapter by chapter, and finally, the main findings and outcomes are introduced.

*Chapter 2* reviews the literature concerning the corrosion process and the physicochemical aspects of corrosion electrochemistry. Different corrosion protection mechanisms are listed and described. The composition of protective organic coatings is introduced, and the contribution of each component, such as binder, pigment, solvent, and additives, is explained. The chapter also mentions the advantages and performance of different carbon materials to formulate the objectivities of the current study. Finally, an explanation of the marine environment and coating requirements are given.

*Chapter 3* discusses the principles of the synthesis of carbon-based materials and the preparation process of coatings. The procedure of the simulation experiments that were conducted to investigate the influence of different environments on coating performance is described. The physicochemical methods that were used to characterize the synthesized carbon-based materials and composite coatings are listed, together with the calculations of the main electrochemical parameters.

*Chapter 4* describes the physicochemical characterization of the carbon-based materials synthesized for anti-corrosion purposes. Thermogravimetric analysis, elemental x-ray photoelectron spectroscopy was carried out to demonstrate the purity and composition of the pigment respectfully. The surface structure controlled by scanning electron spectroscopy.

*Chapter 5* illustrates the composite coating's electrochemical characteristics, which were prepared using different pigments. The surface analysis demonstrates the coating profile before and after the corrosion experiment. The results of the mechanical properties, such as adhesion and hardness, were listed for all composite coatings.

*Chapter 6* demonstrates the evaluation of the composite coating under ultraviolet radiation. The Fourier-transform infrared spectroscopy was carried out to estimate the degree of coating degradation and understand the mechanism. The field emission scanning electron microscopy results illustrate the changes in the coating surface.

*Chapter 7* emphasized the composite coatings properties after immersion in sodium chloride solution. The water intake amount and its effect on the composite coating performance are discussed. The two mechanisms of the degradation are pointed out based on the results of the Fourier-transform infrared spectroscopy. The corrosion rate was calculated for all composite coating after immersion degradation.

*Chapter 8* expressed the effect of the weathering experiment on coating stability. The electrochemical experiments were carried out, and the effect of the carbon-based materials on the coating's behavior is explained. The influence of the ultraviolet radiation combined with water condensation has a strong effect on the coating, and the coating degrades very rapidly.

*Chapter 9* draws together all sections and summarizes the findings, according to the results obtained, the mechanism of the protection by nitrogen-doped carbon-nanomaterials is demonstrated. The general conclusions of the study are listed, and recommendations on future work to enhance the coating's performance are described.

## 1.4. Findings and Outcomes

This research led to several innovative outcomes:

1. Carbon nanotubes with a cylindrical and conical structure, graphene oxide, nitrogen-doped graphene oxide, and nitrogen-doped carbon nanotubes, with a high content of nitrogen of 5.4% and 3% on the surface, respectively, were synthesized for anticorrosion purposes using chemical vapor deposition and Hummer's method. The structure and composition of the anticorrosion pigments played an important role in their protection ability. Owing to their unique structure and two ways of providing protection, composite coatings with carbon nanotubes pigments show a lower corrosion rate than flat graphene oxide sheets. Cylindrical carbon nanotubes, which have a less defective structure than conical carbon nanotubes, demonstrate better performance. Nitrogen doping improves the protection properties of the pigment and provides better dispersion and corrosion resistance.

2. The effect of different environments was studied, such as ultraviolet radiation, immersion, weathering, and ultraviolet radiation switched with water condensation every 4 hours. The design of the simulation experiments was developed and performed for all the coating compositions. The mechanisms of the coating's degradation were described, as well as the way in which the pigment protects the coating. The following two main mechanisms could be in operation during the coating's degradation: (a) photo-oxidation of alkyd and phenyl groups and (b) hydrolysis of the aromatic ether linkage units. The combination of water condensation and ultraviolet radiation requires several anticorrosion pigments and additives in the coating's structure due to the aggressivity of the conditions.

3. Nitrogen doping of the carbon-based materials, as was suggested, improves the dispersion and coating resistance and prevents pitting corrosion from occurring. Nitrogen-containing groups form chemical bonds with the epoxy group of the binder. The mechanism of pigment–polymer interaction is introduced in this research. Nitrogen-doping also improves mechanical properties, such as adhesion and hardness. Nitrogen-doped carbon nanotubes are the materials with the best perspective for use in industrial coatings.

**References**

[1] R. Winston Revie, H. H. Uhlig, *Corrosion and Corrosion Control: An Introduction to Corrosion Science and Engineering* **2008**.

[2] P. R. Roberge, in *Corros. Insp. Monit.* **2007**.

[3] R. Bhaskaran, N. Palaniswamy, N. S. Rengaswamy, in *ASM Handbook, Vol. 13B Corros. Mater.*, Vol. 13B **2005**.

[4] P. Zarras, J. D. Stenger-Smith, in *Intell. Coatings Corros. Control*, Elsevier Inc. **2015**.

[5] E. V. Butyrskaya, L. S. Nechaeva, S. A. Zapryagaev, *Comput. Theor. Chem.* **2016**, *1090*, 1–5.

[6] Y. Zhang, Y. Tang, S. Li, S. Yu, *Chem. Eng. J.* **2013**, *222*, 94–100.

[7] I. I. Fasfous, E. S. Radwan, J. N. Dawoud, *Appl. Surf. Sci.* **2010**, *256*, 7246–7252.

[8] O. Leenaerts, B. Partoens, F. M. Peeters, *Phys. Rev. B*. **2008**, *77*, 125416.

[9] A. Ghasemi-Kahrizsangi, J. Neshati, H. Shariatpanahi, E. Akbarinezhad, *Prog. Org. Coatings*. **2015**, *85*, 199–207.

[10] E. J. Petersen, T. Lam, J. M. Gorham, K. C. Scott, C. J. Long, D. Stanley, R. Sharma, J. Alexander Liddle, B. Pellegrin, T. Nguyen, *Carbon N. Y.* **2014**, *69*, 194–205.

[11] F. Bonaccorso, Z. Sun, T. Hasan, A. C. Ferrari, *Nat. Photonics*. **2010**, *4*, 611–622.

[12] D. Liu, W. Zhao, S. Liu, Q. Cen, Q. Xue, *Surf. Coatings Technol.* **2016**, *286*, 354–364.

[13] D. Prasai, J. C. Tuberquia, R. R. Harl, G. K. Jennings, K. I. Bolotin, *ACS Nano*. **2012**, *6*, 1102–1108.

[14] W. Sun, L. Wang, T. Wu, Y. Pan, G. Liu, *J. Mater. Chem. A*. **2015**, *3*, 16843–16848.

[15] A. Najjar, S. Sabri, R. Al-Gaashani, V. Kochkodan, M. Atieh, *Appl. Sci.* **2019**, *9*, 513.

[16] B. Ramezanzadeh, A. Ahmadi, M. Mahdavian, *Corros. Sci.* **2016**, *109*, 182–

205.

[17] B. Ramezanzadeh, S. Niroumandrad, A. Ahmadi, M. Mahdavian, M. H. Mohamadzadeh Moghadam, *Corros. Sci.* **2016**, *103*, 283–304.

[18] A. M. Berendsen, *Marine Painting Manual*, Springer-Science+Business Media, B.V. **1989**.

[19] D. Balandin, Alexander A.Teweldebrhan, C. N. Lau, S. Ghosh, W. Bao, I. Calizo, F. Miao, *Nano Lett.* **2008**, *8*, 902–907.

[20] C. Lee, X. Wei, J. W. Kysar, J. Hone, *Science (80-. ).* **2008**, *321*, 385–388.

[21] Y. Su, V. G. Kravets, S. L. Wong, J. Waters, A. K. Geim, R. R. Nair, *Nat. Commun.* **2014**, *5*, 1–5.

[22] K. Krishnamoorthy, K. Jeyasubramanian, M. Premanathan, G. Subbiah, H. S. Shin, S. J. Kim, *Carbon N. Y.* **2014**, *72*, 328–337.

[23] M. Rajabi, G. R. Rashed, D. Zaarei, *Corros. Eng. Sci. Technol.* **2014**, *50*, 509–516.

[24] J. Han, in *Carbon Nanotub. Sci. Appl.* (Ed: M. Meyyappan) **2004**.

[25] H. Wei, D. Ding, S. Wei, Z. Guo, *J. Mater. Chem. A*. **2013**, *1*, 10805–10813.

[26] D. Song, Z. Yin, F. Liu, H. Wan, J. Gao, D. Zhang, X. Li, *Prog. Org. Coatings*. **2017**, *110*, 182–186.

# Chapter 2.

# Literature Review

*Corrosion is a fundamental issue, and in this chapter, the electrochemistry of the corrosion process and the methods of corrosion protection are described. The background reported in this chapter lays the foundation for this thesis. Different types of protective coatings, as well as anticorrosion pigments, which are used in recent studies, are reported. Carbon-based pigments, which showed high performance remain limitations in using protective coatings.*

## 2.1. Introduction to the Corrosion Process.

Corrosion process might be considered by thermodynamics and kinetics. Thermodynamics gives the answers about the Gibbs activation energy and answers the question "when?" the corrosion starts. On the other hand, kinetics gives us information about the corrosion rate and answers the question, "how fast?" the corrosion will occur.

In the corrosion of the metal in an aqueous environment, at least two reactions occurred, oxidation of the metal (M) and reduction of oxygen. Schematically both reactions can be written, as shown in the equation:

$$M + 2H_2O + O_2 - (n\text{-}4)\, e^- \leftrightarrow M^{n+} + 4OH^-$$

### 2.1.1. Corrosion Process

Corrosion is a physicochemical interaction between a metal and an environment that changes the properties of the metal. The mechanism of corrosion is illustrated in Figure 2.1.

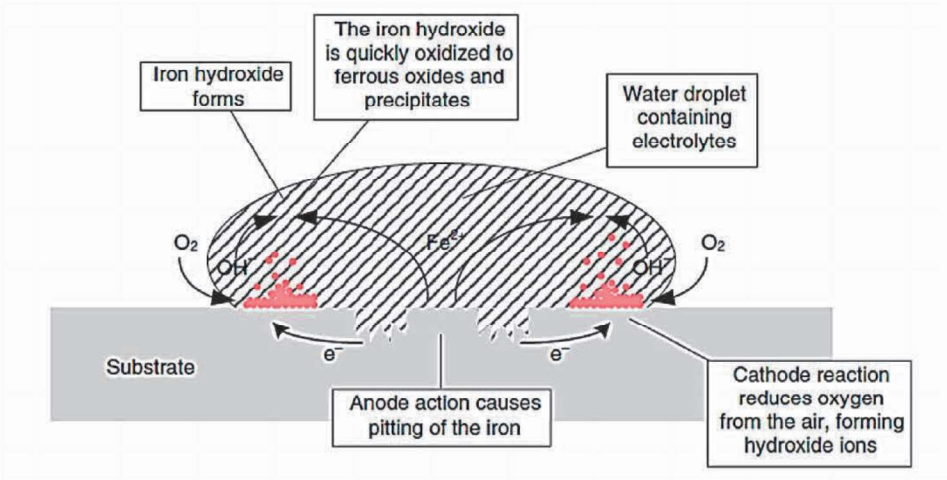


**Figure 2.1.** Corrosion process of steel in aqueous environment. [1]

Aqueous corrosion is a complex process that is affected by chemical, electrochemical, and metallurgical factors such as metal composition, environment properties, and protective film presence.

There are eight primary forms of corrosion presented by Fontana and Greene [2]: uniform attack, crevice corrosion, pitting, intergranular corrosion, selective leaching, erosion-corrosion, stress corrosion, and hydrogen damage. In another widely-used NACE document, Paul Dillon and coauthors describe another type of corrosion, and nowadays, there are more than twenty different forms of corrosion. [3] Only eight main forms will be emphasized in this report. (Figure 2.2.)

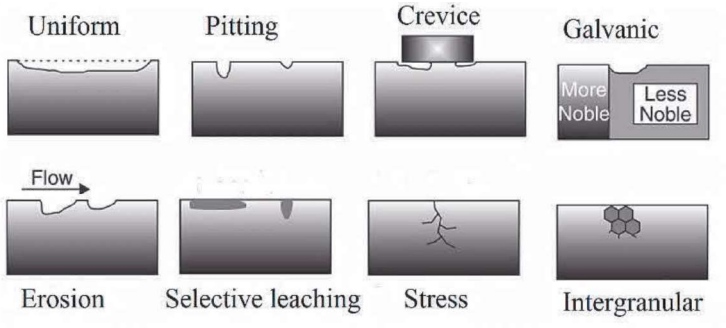


**Figure 2.2**. Main corrosion forms. [4]

Uniform corrosion, or general corrosion, represented the corrosion attack on the surface of the metal and followed by even rust formation and the most significant metal weight lost. This corrosion type is the most detectable and predictable for corrosion engineers. More about the way how to analyze and calculate the rate and the potential of uniform corrosion will be described in Chapter 2.1.3.

Pitting corrosion is one of the localized forms of corrosion where small holes or “pits” are formed in the metal. [5] This is the most common and dangerous type of localized corrosion. One of the terrible disasters happens due to a single pit that killed 215 people in Guadalajara, Mexico, in 1992. (Figure 2.3.a.) [6] At least 90% of metal damage and service failures due to pitting corrosion. The initiation process started with the breakdown of the passive layer and followed by electrolytic cell formation. Once the pit is initiated, it starts to grow by the autocatalytic process. [7] Passive metals such as aluminum, titanium, and stainless steel are mainly corroded by this form of corrosion initiated by chloride ions. [8] (Figure 2.3.b.)

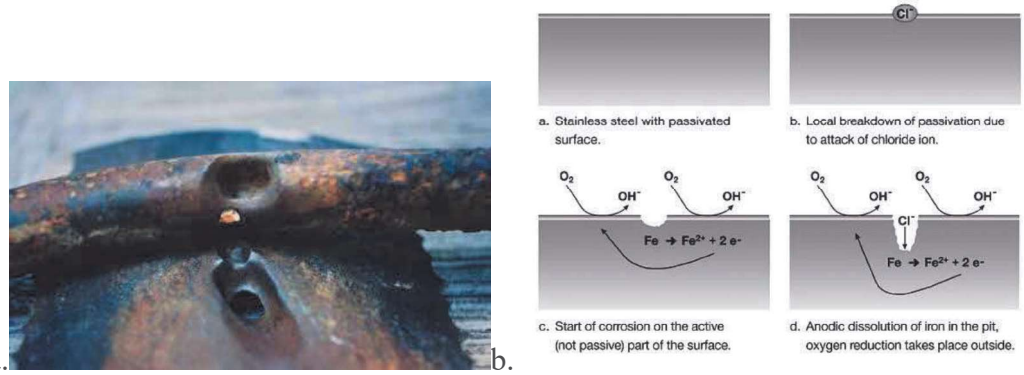


**Figure 2.3**. a. Corrosion damage pipeline in 1992 Guadalajara catastrophe [9]; b. Pitting corrosion of stainless steel.

Crevice corrosion initiated by diffusion of the oxygen and electrolyte into the in cracks or crevices between two surfaces. [10] (Figure 2.4.) Usually, the gap between the two surfaces is around 0.1 to 100µm. [11] There are different ways to classify the crevice corrosion: metal-to-metal or metal-to-nonmetal, human-made, or natural. Crevice corrosion is tough to determine by usual methods, and the mechanism may differ significantly from the environment [12]; therefore it is vital to eliminate it at the design stage.

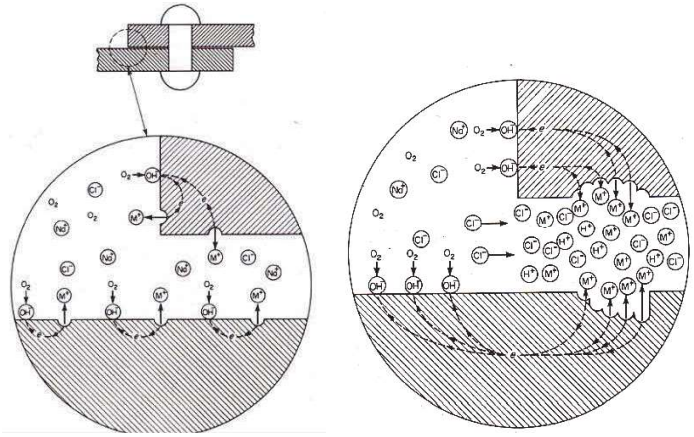

**Figure 2.4.** Mechanism of crevice corrosion.

Galvanic corrosion is corrosion damage where two different metals are in contact in the presence of a corrosive electrolyte. In galvanic corrosion, the less noble material becomes the anode and starts to corrode. [13] Thus, the galvanic series is sufficient to predict the galvanic relationships. Figure 2.5. shows the galvanic series for the most commonly used metals. Depends on the solution, the values of potential

might be different; temperature and velocity also can affect the potentials. The area is another strong factor which effects on the galvanic corrosion. If the area of the cathode (noble metal) is more substantial to the area of the anode, the oxygen reduction reaction occurs hence higher the galvanic current and faster corrosion reaction.

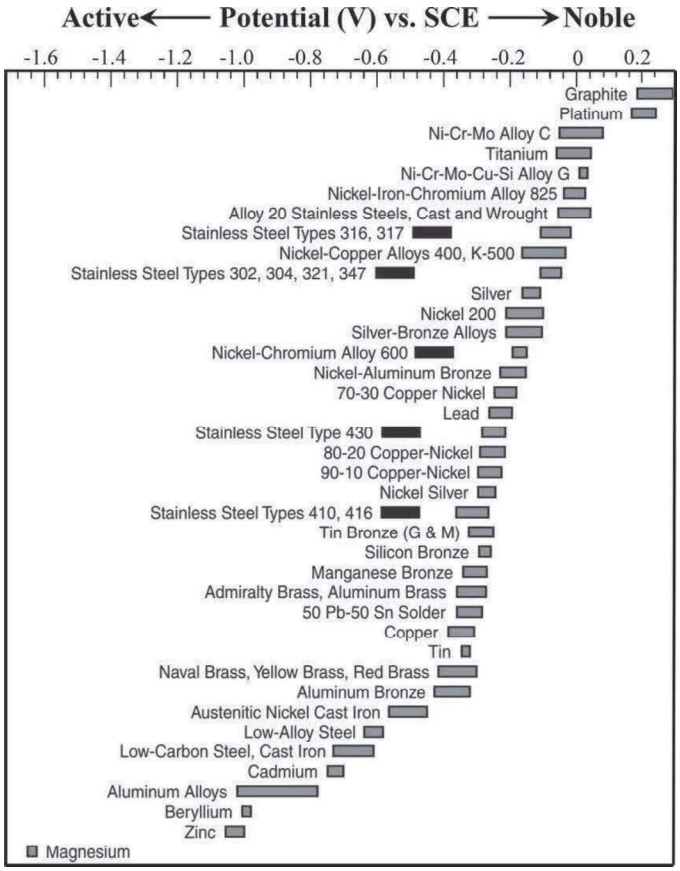


**Figure 2.5.** Galvanic series in seawater [14]

Erosion corrosion is a fast-flowing chemical attack on the metal surface by the environment affected by the rate of flow of the corrosive environment, turbulence, and the concentration of abrasive particles. [15] (Figure 2.6.) Content of some elements like molybdenum, copper, and chromium can decrease the mass loss of the metal and erosion-corrosion rate. [16]

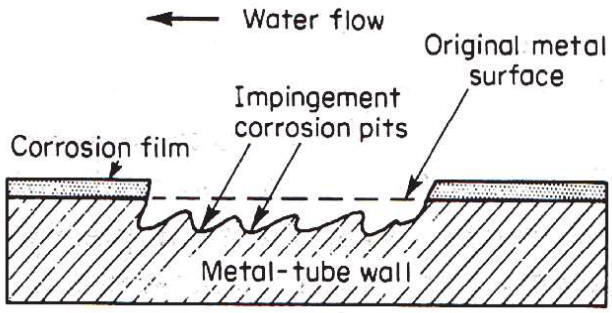


**Figure 2.6.** Mechanism of erosion corrosion. [17]

Selective leaching (dealloying or parting corrosion) involves the selective removal (leaching) one of the elements of an alloy by either preferential attack or by the dissolution of the matrix material. The typical examples of selective leaching corrosion are dezincification and graphitization. Dezincification identifies with the leaching of the zinc phase in alloys such as brasses that contain more than 15% of Zn. [18] Graphitic corrosion is leaching where only the graphite phase of the material leaves under the influence of dilute acids, or soils, especially those containing chlorides or seawater. [19]

Stress-corrosion cracking (SCC) happened when stress and corrosive environment (seawater) effect on susceptible alloy such as austenitic stainless steel. [20] Almost all metals subject to SCC under the particular environment (example: SS in chlorides, caustic, polythionic acids, or pure water + $O_2$ environment). [21] Stress-corrosion cracking is a very complicated process and can be initiated by pitting, intergranular cracking, or surface defects and propagate in several stages: slow, steady-state crack propagation and final, fast failure, see Figure 2.7.

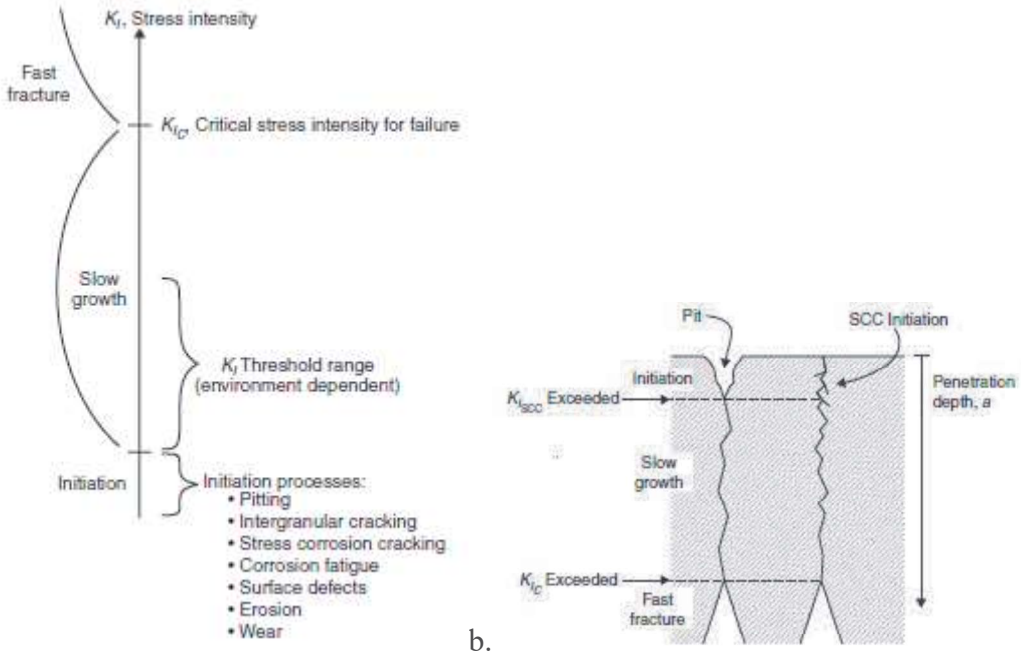


**Figure 2.7**. a. Schematic view of SCC process; b. Morphological regimes. [22]

Intergranular corrosion is one of the most dangerous types of corrosion which happens along the grain boundaries of the metal. By the intergranular corrosion, the material loses mechanical strength and breaks even at low loads. [18] The difference in corrosion potential between the grain boundaries initiate the intergranular corrosion, which might be happening due to migration of the impurities or alloying elements to the grain boundary. [23]

Usually, several forms of corrosion might have happened at the same time; therefore, it is necessary to elaborate methods of corrosion control, that will be described in Chapter 2.2.

### 2.1.2. Thermodynamics of the Corrosion.

The main task of the chemical thermodynamics is to evolve the mathematical explanation of the chemical equilibrium and driving force of chemical reaction.

The Nernst equation, named after the German chemist Walther Nernst, is established relations between the energy and the potential of a cell to the concentrations of participating species.

$$\Delta G = G^\circ + RT \ln Q_{reaction}$$

In the case of an electrochemical reaction, the substitution of the relationships $\Delta G = -nFE$ and $\Delta G^o = -nFE^o$ into the expression of a reaction free energy and division of both sides by $-nF$ gives the Nernst expression for an electrode reaction described in the equation:

$E = E^\circ - \frac{RT}{nF} \ln K_{reaction}$, where E is the electrode potential, E° is the standard electrode potential (emf), $R$ is the gas constant (8,314 J/K mol), $T$ is the absolute temperature (in degrees Kelvin), $n$ is the number of moles of electrons transferred in the half-cell reaction, $F$ is the Faraday constant ($F$ = 96,485 J/volt equivalent), and $K_{reaction} = \frac{a_{ox}}{a_{red}}$, where $a_{ox}$ and $a_{red}$ are the activities of the oxidized and reduced species, respectively. [24]

The electromotive force series describes the standard equilibrium potential of a metal in contact with its ions at a concentration equal to unit activity. The more negative potential corresponds to the more active metal. (Table 2.1.)

**Table 2.1.** Standard-state reduction half-cell potentials. [4]

| Half-Reaction | $E^0$ red |
|---|---|
| $O_3(g) + 2H^+ + 2e^- = O_2(g) + H_2O$ | 2.07 |
| $H_2O_2 + 2H^+ + 2e^- = 2H_2O$ | 1.776 |
| $Au^+ + e^- = Au$ | 1.68 |
| $PbO_2 + 4H^+ + 2e^- = Pb^{2+} + 2H_2O$ | 1.467 |
| $Cl_2(g) + 2e^- = 2Cl^-$ | 1.3583 |
| $O_2 + 4H^+ + 4e^- = 2H_2O$ | 1.229 |
| $Pt^{2+} + 2e^- = Pt$ | 1.2 |
| $H_2O_2 + 2e- = 2OH-$ | 0.88 |
| $Hg^{2+} + 2e^- = Hg$ | 0.851 |
| $Ag^+ + e^- = Ag$ | 0.7996 |
| $Hg_2^{2+} + 2e^- = Hg$ | 0.7961 |
| $Cu^{2+} + 2e^- = Cu$ | 0.522 |
| $O_2 + 4H^+ + 4e^- = 4OH^-$ | 0.401 |
| $Cu^+ + 2e^- = Cu$ | 0.3402 |
| $2H+ + 2e- = H_2$ | 0.0000 |
| $Fe^{3+} + 3e^- = Fe$ | -0.036 |
| $Pb^{2+} + 2e^- = Pb$ | -0.1263 |
| $Sn^{2+} + 2e^- = Sn$ | -0.1364 |
| $Ni^{2+} + 2e^- = Ni$ | -0.23 |
| Co2+ +2e- = Co | -0.28 |
| Fe2+ + 2e- = Fe | -0.409 |
| Cr3+ + 3e- = Cr | -0.74 |
| Zn2+ + 2e- = Zn | -0.7628 |
| Mn2+ + 2e- = Mn | -1.04 |
| Al3+ + 3e- = Al | -1.706 |
| Mg2+ + 2e- = Mg | -2.375 |
| Na+ + e- = Na | -2.7109 |
| K+ + e- = K | -2.924 |

In the measurement of emf, interest is usually focused on the reaction that occurs at one electrode only, and the reference electrode is used because it has a fixed potential in the environment where it is used. Any change in emf is due to changes in the potential of the electrode and not because of the reference electrode. It is necessary to notice that many different reference electrodes are available, and others can be designed for particular problems. [25] Each electrode has its potential value,

Table 2.2, which can be used to convert the results obtained into numbers expressed concerning other references, for example, standard hydrogen electrode (SHE). [26]

**Table 2.2.** Equilibrium potential at 25°C of commonly used reference electrodes [4]

| Name | Equilibrium reaction and Nernst equation | Conditions | Potential (V vs. SHE) | T coefficient (mV/C) |
|---|---|---|---|---|
| Standard hydrogen electrode (SHE) | $2H^+ + 2e^- = H2$ | pH=0 | 0.00 | |
| | $E^o$ - 0.059pH | | | |
| Silver chloride | $AgCl + e^- = Ag + Cl^-$ | $a_{Cl^-} = 1$ | 0.2224 | -0.60 |
| | $E^o$ - 0.059 $lga_{Cl^-}$ | 0.1M KCl | 0.2881 | .. |
| | | 1.0 M KCl | 0.235 | .. |
| | | Saturated (KCl) | 0.199 | .. |
| | | Seawater | 0.250 | .. |
| Calomel | $Hg_2Cl_2 + 2e^- = 2Hg + 2Cl^-$ | $a_{Cl^-} = 1$ | 0.268 | |
| | $E^o$ - 0.059$lga_{Cl^-}$ | 0.1 M KCl | 0.3337 | -0.06 |
| | | 1.0 M KCl | 0.280 | -0.24 |
| | | Saturated | 0.241 | -0.65 |
| Mercurous sulfate | $Hg_2SO_4 + 2e^- = 2Hg + SO_4^{2-}$ | $a_{SO_4^{2-}} = 1$ | 0.6151 | |
| | $E^o$ -0.0295$lga_{SO_4^{2-}}$ | | | |
| Mercuric oxide | $HgO + 2e^- + H^+ = Hg + H_2O$ | | 0.926 | |
| | $E^o$ -0.059pH | | | |
| Copper sulfate | $Cu^{2+} + 2e^- = Cu$ (sulfate solution) | $a_{Cu^{2+}} = 1$ | 0.340 | |
| | $E^o$ +0.0295$lga_{Cu^{2+}}$ | Saturated | 0.318 | |

The stability of the metal depends on many factors, which may vary pH and oxidation or power limitations of the medium. Pourbaix diagrams or potential-pH (E-pH) diagrams represent the impact of aqueous environments on metals.

Pourbaix diagram for water describes two processes: hydrogen ions and hydrogen gas equilibrium in an aqueous environment, water decomposition into oxygen. (Figure 2.8.) Equations bellow describes reactions of hydrogen evolution, oxygen evolution reactions and dependence electrochemical potential on pH [23]

$2H^+ + 2e^- \rightarrow H_2\,(g)$ (acid)

$2H_2O + 2e \rightarrow H_2\,(g) + 2OH^-$ (neutral and base)

$$E_{H^+/H_2} = E°_{H^+/H_2} - 0.059pH$$

$O_2 + 4H^+ + 4e^- \rightarrow 2\ H_2O$ (acid)

$O_2 + 2H_2O + 4e^- \rightarrow 4OH^-$ (neutral and base)

$$E_{O_2/H_2O} = E°_{O_2/H_2O} - 0.059pH$$

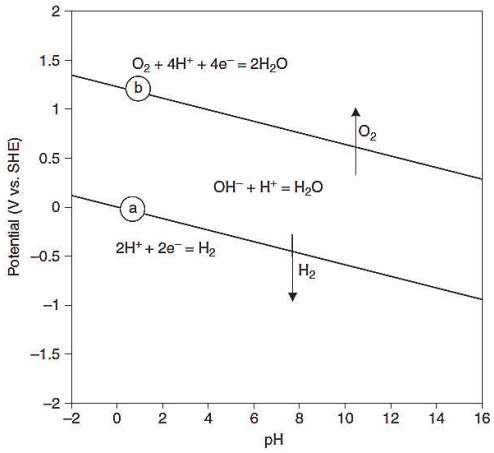


**Figure 2.8.** Pourbaix diagram of water at 25°C. [23]

The E-pH diagram for iron at 25°C (Figure 2.8.) was calculated considering possible reaction which has happened with iron in aqueous atmosphere listed in Table 2.3

**Table 2.3**. Possible reactions between the most stable species in wet conditions in the Fe-$H_2O$ system. [4]

| Equilibria |
|---|
| $2e^- + 2H^+ = H_2$ |
| $4e^- + O_2 + 4H^+ = 2H_2O$ |
| $2e^- + Fe(OH)_2 + 2H^+ = Fe + 2H_2O$ |
| $2e^- + Fe^{2+} = Fe$ |
| $2e^- + Fe(OH)_3^- + 3H^+ = Fe + 3H_2O$ |
| $1e^- + Fe(OH)_3 + H^+ = Fe(OH)_2 + H_2O$ |
| $1e^- + Fe(OH)_3 + 3H^+ = Fe^{2+} + 3H_2O$ |
| $Fe(OH)_3^- + H^+ = Fe(OH)_2 + H2O$ |
| $1e^- + Fe(OH)_3 = Fe(OH)_3^-$ |
| $Fe^{3+} + 3H_2O = Fe(OH)_3 + 3H^+$ |
| $Fe^{2+} + 2H_2O = Fe(OH)_2 + 2H^+$ |
| $1e^- + Fe^{3+} = Fe^{2+}$ |
| $Fe^{2+} + H_2O = FeOH^+ + H^+$ |

| |
|---|
| $FeOH^+ + H2O = Fe(OH)_{2(sin)} + H^+$ |
| $Fe(OH)_{2(sin)} + H_2O = Fe(OH)_3^- + H^+$ |
| $Fe^{3+} + H_2O = FeOH^{2+} + H^+$ |
| $FeOH^{2+} + H_2O = Fe(OH)_2^+ + H^+$ |
| $Fe(OH)_2^+ + H_2O = Fe(OH)_{3(sin)} + H^+$ |
| $FeOH^{2+} + H^+ = Fe^{2+} + H2O$ |
| $1e^- + Fe(OH)_2^+ + 2H^+ = Fe^{2+} + 2H_2O$ |
| $1e^- + Fe(OH)_{3(sin)} + H^+ = Fe(OH)_{2(sin)} + H_2O$ |
| $1e^- + Fe(OH)_{3(sin)} + 2H^+ = FeOH^+ + 2H_2O$ |
| $1e^- + Fe(OH)_{3(sin)} + 3H^+ = Fe^{2+} + 3H_2O$ |

A horizontal line represents a reaction that, neither $H^+$ nor $OH^-$ is involved, as in the reaction, $Fe^{2+} + 2e^- \rightarrow Fe$. A vertical line includes reaction with $H^+$ or $OH^-$, but not electrons; for example, $2Fe^{3+} + 3H_2O \rightarrow Fe_2O_3 + 6H^+$. A sloping line presupposes $H^+$, $OH^-$, and electrons. [26] (Figure 2.9.)

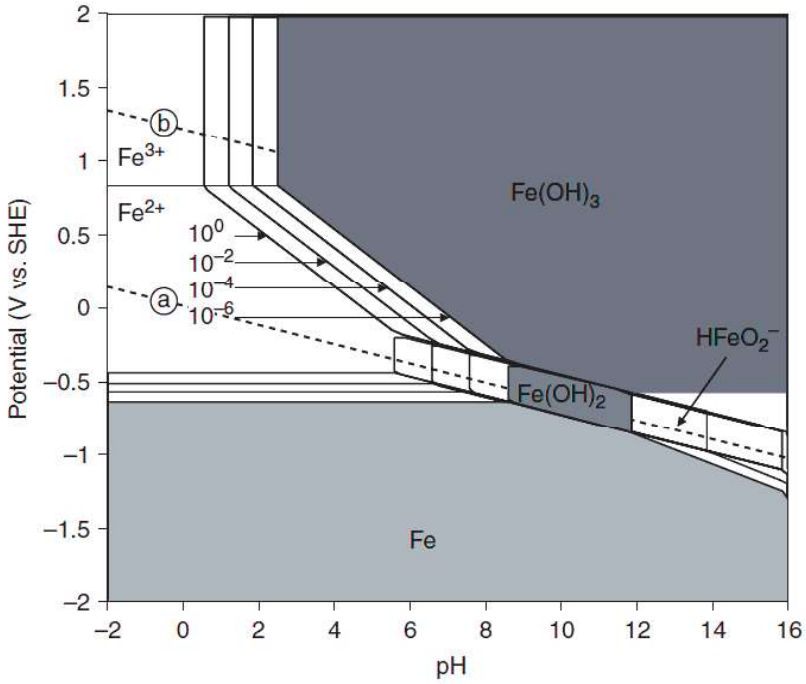


**Figure 2.9.** Pourbaix diagram for the iron – water system at 25 ° C [4]

Unfortunately, Pourbaix diagrams provide no information on rates of reaction because it only based on thermodynamic data.

### 2.1.3. Kinetics of the Corrosion.

Thermodynamic principles can help to explain corrosion in terms of the stability of chemical species and reactions which might occur but cannot be used to predict corrosion rates. Kinetics provides the current – potential dependence and helps to calculate the corrosion rate.

The polarization, which is quantified in terms of overpotential ($\eta$) is the difference between the resultant potential ($E$) and each reaction equilibrium potential ($E_{eq}$).

$$\eta = E - E_{eq}$$

There are three distinct types of polarization, and the total is the sum of activation overpotential, concentration polarization, and ohmic drop.

$\eta_{total} = \eta_{act} + \eta_{conc} + iR$, where $\eta_{act}$ is the activation overpotential, which describes the charge transfer of the electrochemical reaction; $\eta_{conc}$ is the concentration overpotential, characterizing the mass transport limitations; $iR$ is the ohmic drop, due to the electrolytic resistivity of an environment. When the environment is a good electrolytic conductor such as seawater, the ohmic drop is negligible. [4]

In the activation or charge-transfer control reactions, the corrosion reactions are controlled by the electron flow. (Figure 2.11.) The overall anodic reaction involves several intermediate reactions between the equilibrium of metal lattice and $Fe^{2+}$cations, i.e.:

$$Fe_{lattice} \rightarrow Fe^{+}_{surface}$$

$$Fe^{+}_{surface} \rightarrow Fe^{2+}_{surface}$$

$$Fe^{2+}_{surface} \rightarrow Fe^{2+}_{solution}$$

The same situation happens in the equilibrium between protons and hydrogen gas, i.e.,

$H^+ \rightarrow H_{ads}$

$H_{ads} + H_{ads} \rightarrow H_2$ (molecule)

$H_2$ (molecule) $\rightarrow H_2$ (gas) [23]

The Butler-Volmer equation represents the polarization of an electrode supporting one redox system:

$$i_{reaction} = i_0 \left\{ \exp(\beta_{reaction} \frac{nF}{RT} \eta_{reaction}) - (\exp(-(1-\beta_{reaction}) \frac{nF}{RT} \eta_{reaction}) \right\}$$

where $i_{reaction}$ – anodic or cathodic current; $\beta_{reaction}$ – charge transfer barrier or symmetry coefficient for the anodic or cathodic reaction, close to 0.5; $\eta_{reaction} = E_{applied} - E_{eq}$ , i.e., positive for anodic polarization and negative for cathodic polarization, $n$ _ number of participating electrons. [24]

When the reaction is anodic, the second term in the Butler- Volmer equation becomes negligible and $i_a$ can be expressed in the logarithmic form:

$\eta_a = b_a \log\left(\frac{i_a}{i_0}\right)$, where $b_a$ is the Tafel coefficient that can be obtained from the slope of the anodic plot, i.e., $\eta_a$ against log$i$, with the intercept yielding a value for $i_0$. (Figure 2.10.)

Similarly, in the cathodic reactions, the first term in the Butler-Volmer equation becomes negligible and $i_c$ can be more merely present by:

$\eta_c = b_c \log\left(\frac{i_c}{i_0}\right)$.

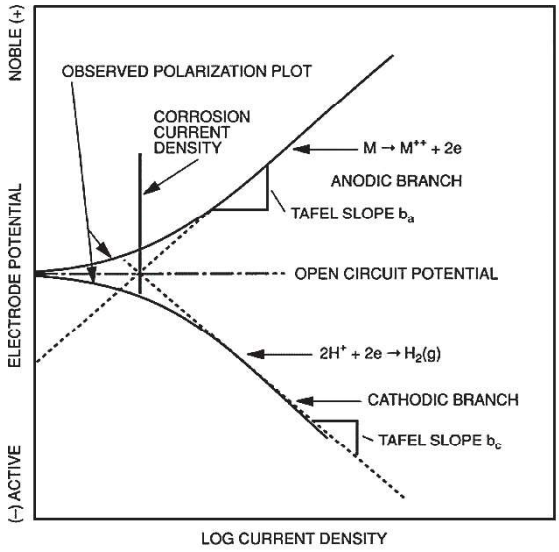


**Figure 2.10.** Plot of η against $\log_i$ or Tafel plot. [27]

Using the Tafel plot, the basic corrosion parameters can be investigated ($E_{corr}$ and $I_{corr}$). The point where cathodic and anodic slop cross together is described as the current and potential of the corrosion. From Faraday's law, the corrosion rate can be calculated using corrosion current density, in terms of penetration rate (CR) or mass loss rate (MR) [28], accordantly following equations:

$$CR = K_1 \times \frac{i_{corr}}{\rho} \times EW$$

$$MR = K_2 \times i_{corr} \times EW$$

Where: CR in mm/yr; $i_{corr}$ - μA/cm$^2$; $K_1$ = 3.27E-03 mm g/μA cm yr; ρ – density in g/cm$^3$; MR – g/m$^2$ d; $K_2$ = 8.954E-03 g cm$^2$/μA m$^2$ d. [29]

The situation changes when the mass transport of the species to the metal surface becomes rate controlling. Figure 2.11. shows a graphic representation of the processes that happen on the metal surface.

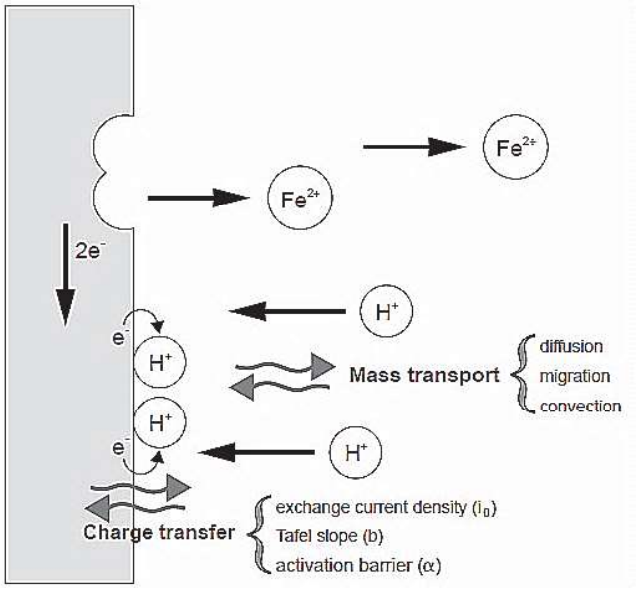


**Figure 2.11.** Schematic processes occurring at an electrochemical interface. [23]

For instance, assuming the concentration of a chemical species O (ex: $O_2$, $H_2O$, $H^+$) changes, as shown in Figure 2.12., the cathodic current is limited:

$$i_c = i_L = -nFD_o \frac{C_{o,bulk}}{\delta}$$

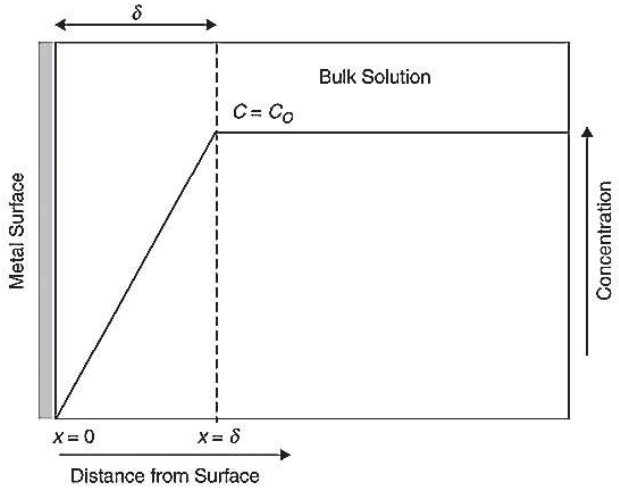


**Figure 2.12.** Nernst diffusion layer for a limiting current situation. [30]

For intermediate cases, that is, when the cathodic current is smaller than $i_L$, $\eta_{conc}$ can be described from Nernst equation [4]:

$$\eta_{conc} = \frac{2.303RT}{nF}\log(1-\frac{i}{i_L})$$

For the concentration control situation, the behavior of the Tafel plot is signifying changed (Figure 2.13 b), and the point of corrosion current and potential shifts to the more positive potential.

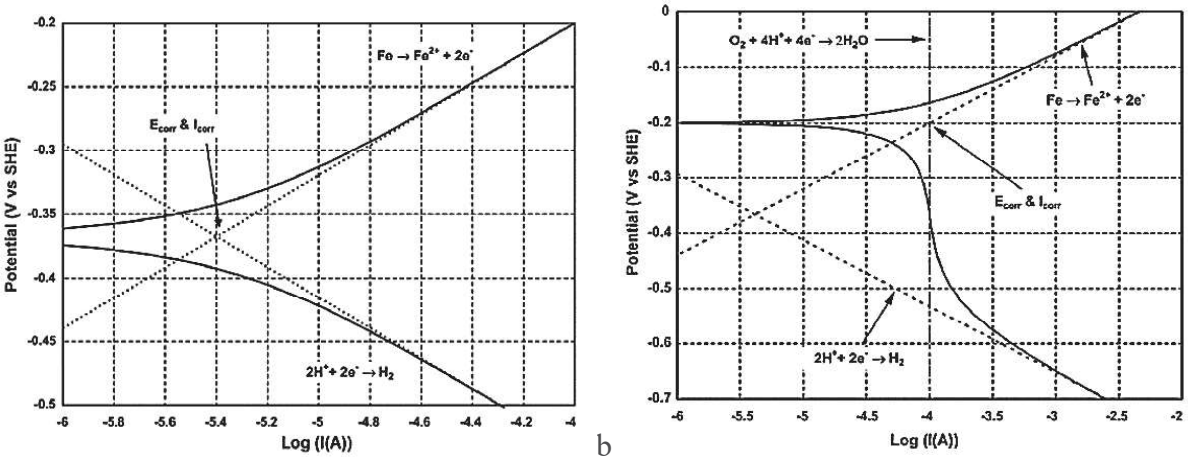


a b

**Figure 2.13.** a. Tafel plot of activation controlled process; b. Tafel plot of concentration controlled process at pH 5.[23]

The transport of metal dissolution product also affects the corrosion rate but in a different way. If the corrosion product is allowed to build up at the surface, supersaturation with regard to solid oxides and hydroxides can occur, leading to film formation reactions. For $E > E_{pass}$, the metal is in the passive region. In this region, the current is independent of potential, and metal dissolution occurs at a constant rate.

There are two types of passivity. The first type is when the metal in the curtain environment shows the behavior of the noble metal in the emf series, like nickel, chromium, iron in an oxidizing environment, stainless steel. The metal is passive even in case of thermodynamics has active potential in the given environment, as the lead in sulfuric acid. [31] (Figure 2.14.)

The reactions describing the passive layer can be very complicated, the following reactions might occur in the passive region [32]:

Active $M \rightarrow M^{n+}$

Passive $M \rightarrow M_xO_y \rightarrow M^{n+}$

Transpassive $M_xO_y \rightarrow M^{(n+1)+}$

Oxygen evolution $H_2O \rightarrow O_2$

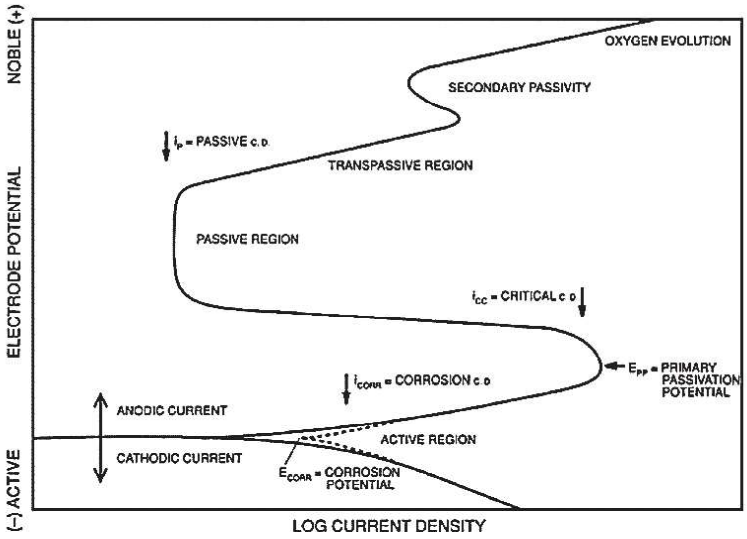


**Figure 2.14.** Polarization curve for a metal/metal ion system that undergoes an active to passive transition. [33]

The polarization curve has been changed if pitting or crevice corrosion occurs in the system. At the potential when current density increased rapidly, the stabled pit starts to grow that potential named pitting potential (Ep). On the reversal scan direction, the repassivation potential ($E_R$) can be determined. [34] (Figure 2.15.)

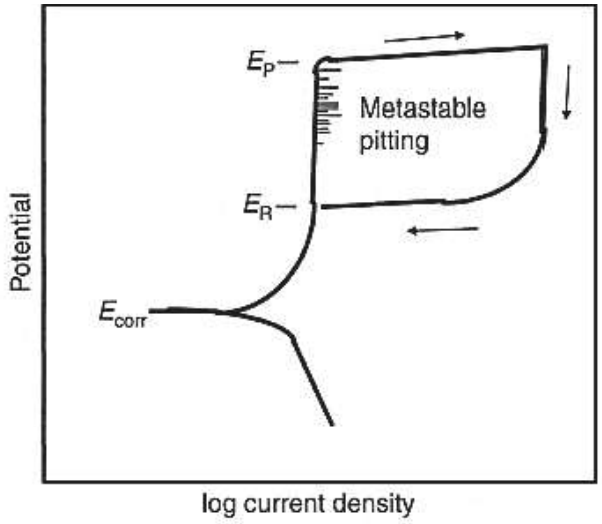


**Figure 2.15.** Polarization curve of pitting corrosion [5]

If the pitting potential is high and the gap between the corrosion and pitting potential is big enough, there are little possibilities for the pitting corrosion to start. If the repassivation potential is higher than corrosion potential, it is a very low likelihood that pitting will occur at all. [35]

## 2.2. Corrosion Protection Mechanism

There are many ways to protect metals from corrosion. The environment determines the choice of method, specific operating conditions, etc. Currently, to increase the service life of the protection and to ensure its reliability, the following methods of corrosion protection are most frequently used: application of protective coatings, the use of corrosion inhibitors, chemical, and electrical protection.

### 2.2.1. Cathodic Protection

Cathodic protection is an electrochemical protection mechanism which usually applied to non-passive metal. The nature of the cathodic protection is to apply to the product of the external current from the negative pole, which polarizes the cathodic elements increasing the potential. The positive pole of the power source is attached to the anode. Thus, the corrosion protected structure is almost reduced to zero. The anode is gradually destroyed and should be replaced periodically. Figure 2.16. shows a simple cathodic protection system. [36]

There are two types of cathodic protection: sacrificial anode, or passive, systems and impressed current, or active systems. Both types are widely used.

Sacrificial anode systems are based on more electroactive metal with played role anode, for example, magnesium, zinc, or aluminum alloys, which selected for the specific environment. [37] A simple sacrificial anode cathodic protection system used to control corrosion on a buried pipeline is shown in Figure 2.16. b. [38]

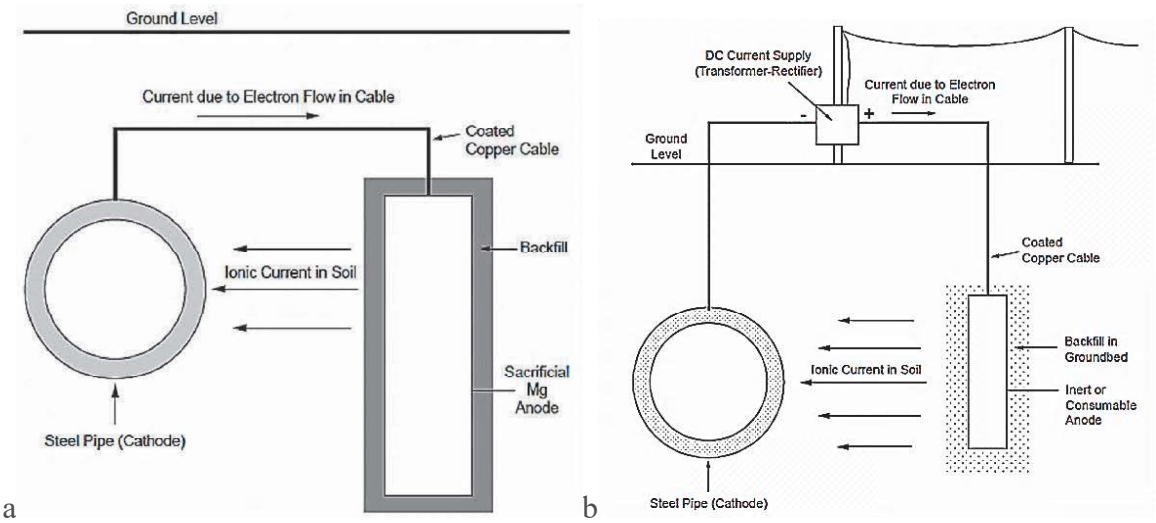


**Figure 2.16.** Schematic principle of cathodic protection with a- sacrificial anode; b - impressed current. [23]

Impressed current systems are more complex, and based on applying external power, The anode for this system should have high corrosion resistance such as graphite, platinum, silicon iron, lead alloys. [38] The advantages and limitations of both systems are shown in Table 2.4.

**Table 2.4.** Advantages and limitation of sacrificial anode and impressed current system. [39]

| Sacrificial anode system | Impressed current system |
|---|---|
| **Advantages** | |
| No external power sources | High current and power output |
| Easy installation | Large area of protection |
| Low maintenance | May protect poorly coated structure |
| Self-regulated | Ability to change protection level |
| Uniform current distribution | May be designed for long lives |
| Can be used in the low resistivity soil | Possibility of variation |
| Lesser interference with the other metallic structures | |
| Economical | |

| Limitation | |
|---|---|
| Limited current and power output | Risk of the interference effect |
| High-resistivity environment require increasing number of electrodes | Low reliability and high maintenance |
| Anode should be replaced under high current | Use the external power |
| Anode increase weight if it is attached to the structure | More complex and less robust |
| The cost of protection is high for bare systems | Risk of incorrect polarity connection |
| No above-ground equipment is used | Less economical for smaller jobs. |

There can be complicated in cathodic corrosion protection, such as stray current corrosion. This type of corrosion is associated with the undesired current such as welding machines, elevators, electroplating machines, etc. the uncontrolled current from these sources cause corrosion at the point of leakage from the system. [40]

### 2.2.2. Anodic Protection

In contrast to cathodic protection, anodic protection is relatively new. It is used in the operation of the equipment in a well-conductive medium and made of easily passivating materials – carbon steel, low-alloy stainless steels, titanium, high-doped iron-based alloys. [23] Anodic protection is promising in the case of equipment made of dissimilar materials are passivated, for example, of stainless steels of different composition. [41]

In the case of the anodic protection, potential of the active dissolving metal is shifted in a positive direction to achieve the sustainable passive state. (Figure 2.17.) The result is not only a significant (thousands of times) reduction of corrosion rate of metal, but it is prevented contamination of the produced product. [42] Translation of the potential in the positive direction can be achieved by an external current

source, adding oxidant into the solution or by adding elements in the alloy, contributing to improving the efficiency of the cathode process. [43]

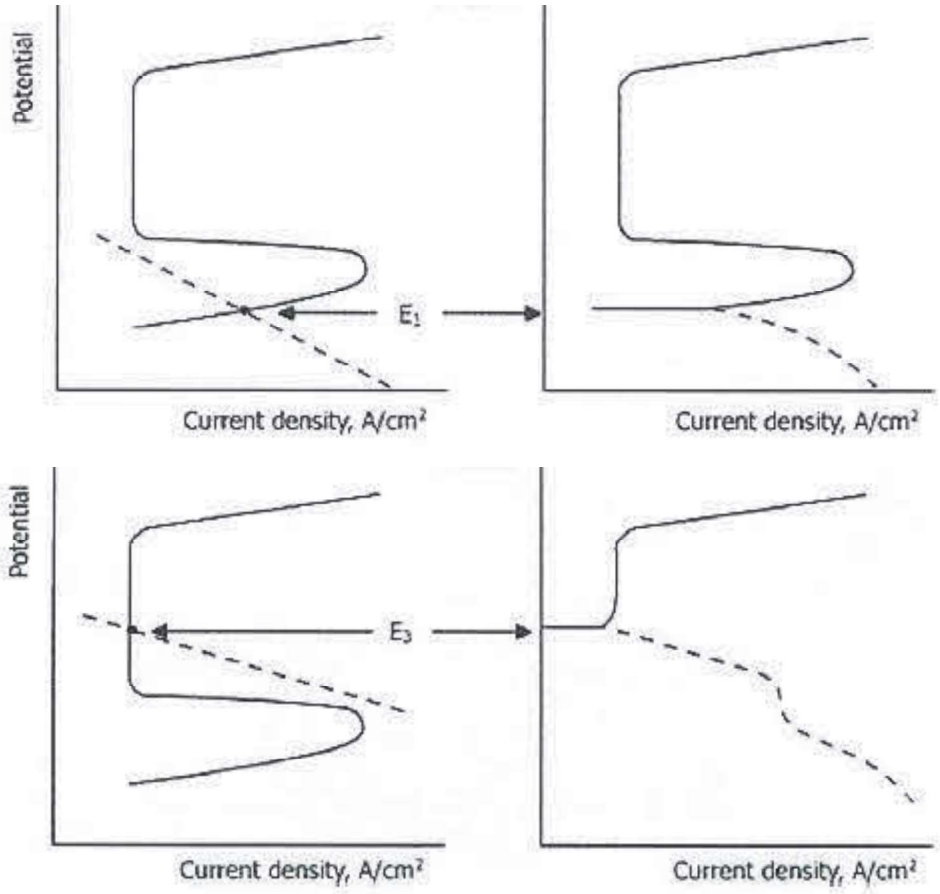


**Figure 2.17.** Polarization curve of the passive metal. [44]

Anodic protection by passivating inhibitors-oxidants is based on the fact that the current is in the process of recovery; it is sufficient for the metal transfer to the passive state. As inhibitors nitrate salts, dichromates and others can be used. [45] The main disadvantage of this method of protection is the contamination of process fluid.

Anodic protection is used in the construction of storage vessels, process reactors, heat exchangers [46], etc. Anodic protection successfully reduces the mass loss of low-carbon steel during the storage of sulfuric acid. [47]

### 2.2.3. Inhibitors

The chemicals which react with a metal surface and provide a certain level of protection are called inhibitors, they adsorb on the metal surface and form the protecting film. [23] Inhibitors can be spread from the dispersion or solution, or included in the coating formulation

The behavior of the corrosion potential can be used to determine which of the half reactions is most affected by the inhibitor. Figure 2.18. illustrates three cases: the corrosion inhibitor affects the anodic and cathodic curves equally. The corrosion rate is reduced to the value $I_{inhib}$, but the corrosion potential is unaffected. In Figure 2.18. b, the cathodic reaction is affected, and the corrosion potential moves to a more negative value. In Figure 2.18 c, the opposite situation, the anodic reaction is affected, and the potential moves to a more positive value. The change in corrosion potential in the presence of an inhibitor can thus be used to estimate the kinetics of the inhibition.

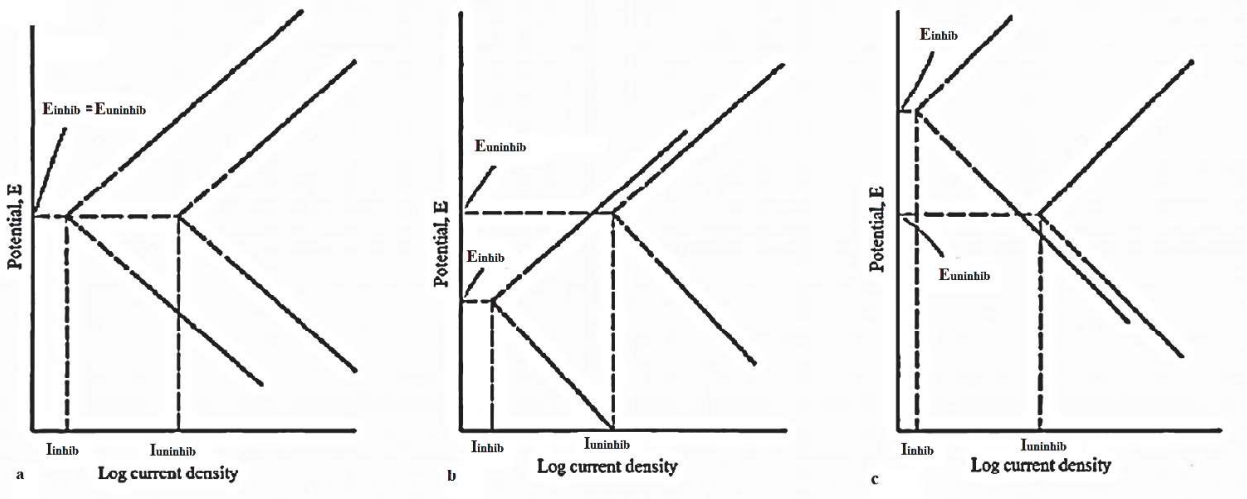


**Figure 2.18.** Effect of inhibitors on corrosion process [48]

The inhibitors can work as passivators, barriers, poisons, scavengers, or neutralizers. The passivation inhibitor performs by several mechanisms: stabilize the passive film, repassivate the damaged films, or prevent the adsorption of the aggressive ions, such as $Cl^-$. [49] Inhibitors which act as barrier layer should cover the whole surface of metal to protect from environment interaction by forming a

physical barrier and decreasing the diffusion of reactant; reducing metal reactivity and adsorbing on active sites; affecting on electrode reaction by shifting the surface potential; or by forming stable complex on the surface. [50] Group VA: P, As. Sb, and Bi elements, and brass work as poisons and inhibit hydrogen or oxygen reduction reaction, respectively. Sulfites and hydrazine are the scavengers and eliminate the dissolving of oxygen from the system in neutral or alkaline water. [51] Neutralizer inhibits the corrosion by reducing the concentration of proton ion. Morpholine and cyclohexylamine are the most common neutralizing inhibitor. [52]

By the functionality, the inhibitors can be classified differently, as shown in Figure 2.19.

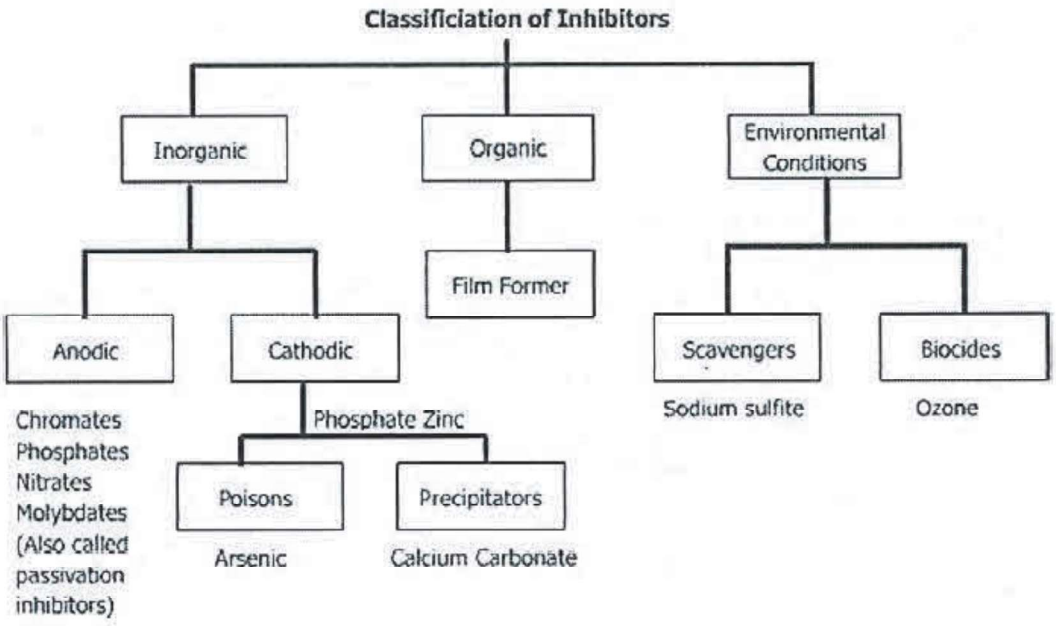


**Figure 2.19.** Classification of inhibitors [53]

### 2.2.4. Protection by the Design

Design is an essential part of engineering the object. Bad design can increase the corrosion rate in several times. The main aims of good design are to decrease the attack time of the corrosive environment and protect the surfaces from the subsequent corrosion degradation. (Figure 2.20.) [54] During the design, the engineer should

avoid the forms that can collect water or other corrosive liquids, as shown in Figure 2.20. 1.a, 1.b, 2.a-d.

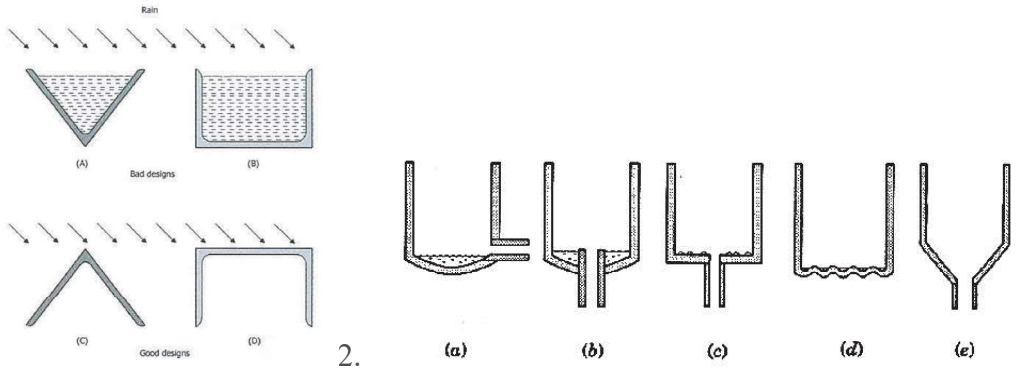


1. 2.

**Figure 2.20.** 1.a,b – bad design; 1.c,d – good design; 2.a,b,c,d – bad design of the tank; 2.e – good design of the tank [55]

The four steps are required to follow in the design process: [55]

- To clarify design objectives
- To identify the functional requirements
- To specify the performance
- To improve the cost-effective

The good design of the system can prevent not only from uniform attack but also from the galvanic, crevice, pitting, and stress corrosion. [56] (Figure 2.21.)

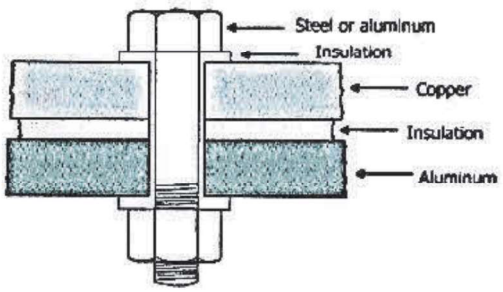


**Figure 2.21.** Design of good bolted joint to avoid galvanic and crevice corrosion [56]

The protection by design should be used with other protection methods to achieve better corrosion protection and long-lasting of the object. [57]

### 2.2.5. Coating

Protective coatings are widely used in corrosion prevention. The main advantage of it is that they are easy to apply and maintain compared with other method, and they provide long-term protection in different corrosion environments. The coatings have a list of advantages such as easy to prepare and apply, proper corrosion protection, and wild industries of usage. There different types of coating that can follow the requirement for any industry. [58] The following table describes the main groups of coatings.

**Table 2.5.** Classes of coatings [59]

| Metallic | Inorganic | Conversion | Organic |
|---|---|---|---|
| Galvanizing | Silicates | Anodizing | Phenolic |
| Vapor deposition | Ceramics | Phosphating | Vinyl |
| Electroplating | Glass | Chromate | Acrylic |
| | | Molybdate | Epoxy |
| | | | Alkyd |
| | | | Urethanes |

Metallic coatings are the layer coating which changes the surface properties of the metal. By applying the metallic coating, the material becomes a composite that is durable and corrosion-resistant. It can be applied by hot dipping, electroplating, spraying, deposition from the vapor phase of ions, and chemical vapor deposition. The cadmium, chromium, nickel, aluminum, and zinc coatings are wildly used. [60] The vapor deposition process can be divided on physical (PVD) and chemical (CVD) The main principle of PVD is to bombard the substrate by gas ions produced at high voltage. CVD required a very high temperature of about 1000ºC, but the thick, dense, and high-quality film can be produced at a relatively low cost. [61] By electroplating tin, chromium, as well as zinc (galvanizing), can be electrodeposited on the metal surface to improve properties like corrosion and chemical resistance, electrical, and magnetic properties. There are many advantages of electroplating: the variety of coating composition, improving galvanic protection of the surface, control the thickness; but still have some limitations such as size, design, and color variety. [62]

The inorganic coating is impermeable and forms a strong chemical bond with the metal surface. The inert nature of these coatings makes them particularly useful in resisting mineral acids such as sulfuric acid and hydrochloric acid, salt spray, and also that they have good electrical insulation properties and weathering. [63] Porcelain enamel is a glass coating consisting of the ground coat, which provides good adhesion to the metal usually from borosilicate glasses and cover coat with titania-opacified frits to provide acid resistance or zirconium oxide for alkali resistance. [64] Ceramic coating is a high-temperature coating formed from oxides, borides, silicides, cermets, etc. The material of the coating has to be chosen according to the environment of use. [65]

Conversion coating is a coating composed of insoluble salts and oxides, resulting from the interaction between metal and solutions. The phosphate, chromate, and anodizing coatings are widely used in conversion coating.

Phosphate coatings are mainly used in the preparation before painting. There are three ways of applying phosphate coatings: slow phosphate, phosphate, and accelerated at room temperature. [66] Insoluble tertiary metal (Me) phosphates the main component of the phosphate conversion coating. There are four main steps in phosphate coating application: cleaning from the oil and grease by using alkaline or organic solvents; activation or conditioning by exposing to a titanium colloid solution at neutral pH [67]; phosphating in the bath which usually consist of phosphoric acid and divalent metal cations; and posttreatment to decrease the pore amount such sealing bi chromium or other polyvalent metal cations to form oxides, hydroxides, phosphates, and so forth on the metal surface. [68]

Chromate coatings are applied to the surface of the zinc, galvanized steel, or cadmium components. They are also used to protect objects made of magnesium, copper, aluminum, and other metals. The main component of the chromate coating is trivalent and hexavalent chromium. [69] Chromate conversion coating increases

the inhibiting effect on the cathodic and anodic reaction, improves the localized corrosion resistance and long-term interfacial adhesion. [70]

During the anodizing, the metal such as aluminum, magnesium or titanium, convert to the metal oxide by electrochemical method. The anodizing process consists of several steps, such as pretreatment, rinsing, etching, desmutting, anodizing, coloring (optional), and sealing. [71] Pretreatment is critical to clean the metal surface and remove oil and dust. After cleaning the metal rises in the deionized water and following by etching or chemical milling in the sodium hydroxide solution and desmutting the metal placed in the acidic solution to remove metal thin film and alloy particles. During the anodizing, the metal placed in the tank with acidic electrolytes in which the direct current is passed. The most typical electrolyte is sulfuric acid, which can produce the coating with good corrosion resistance and relatively low cost. Chromic, oxalic, and phosphoric acids are also used in the anodizing process. [72] Anodizing process is finished by optional coloring and sealing (Figure 2.22.), which usually perform in boiling water to produce a metal hydroxide layer and minimize the pore of the oxide layer.

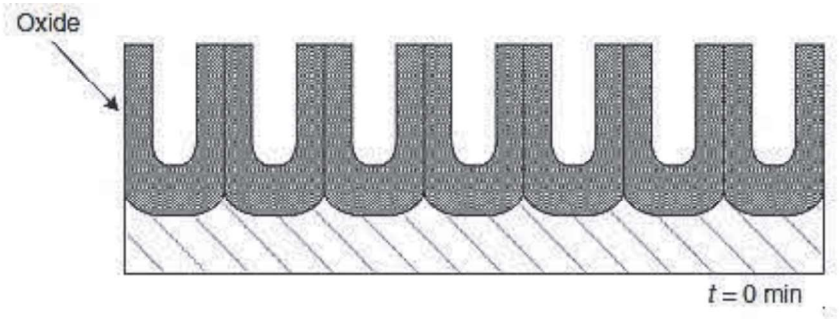

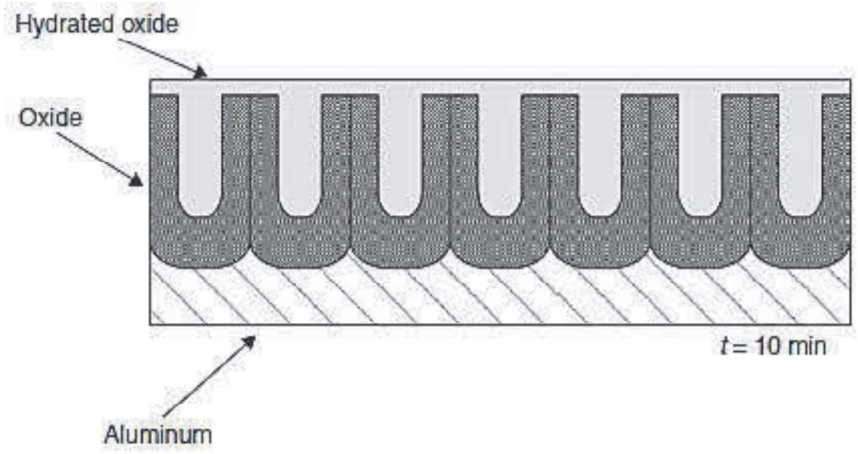


**Figure 2.22.** Sealing in anodizing process [4]

The organic coatings will be fully described in Chapter 2.3.

## 2.3. Protective Organic Coatings

Organic coatings provide protection either as a barrier layer, which is limited due to permeability of water and oxygen or as active corrosion inhibition and cathodic protection due to the pigments in the coating. Usually, coating system consists of several layers of protection, such as primer, the intermediate layer, and top coating. The primer executes the following functions [73]:

- Adhesion
- Cohesion
- Inertness
- Bonding with the intermediate layer
- Flexibility
- Corrosion protection

Intermediate or body coatings are usually used to increase thickness and mechanical properties, and it provides [23]:

- Thickness
- Chemical resistance

- Moisture resistance
- Cohesion
- Adhesion to the primer and top coating

In the coating system, the topcoat should provide many functions due to its direct contact with the environment, such as [74]:

- Mechanical and wear resistance
- Barrier to the environment
- Water, chemicals, and weather resistance
- Corrosion and biofouling protection
- Pleasant appearance

Organic coatings consist of binder, pigments, solvents to reduce the viscosity of binder and pigment, and additives to provide the specific function such as thickness, UV protection, surface wetting, etc., as shown in Figure 2.23. [75]

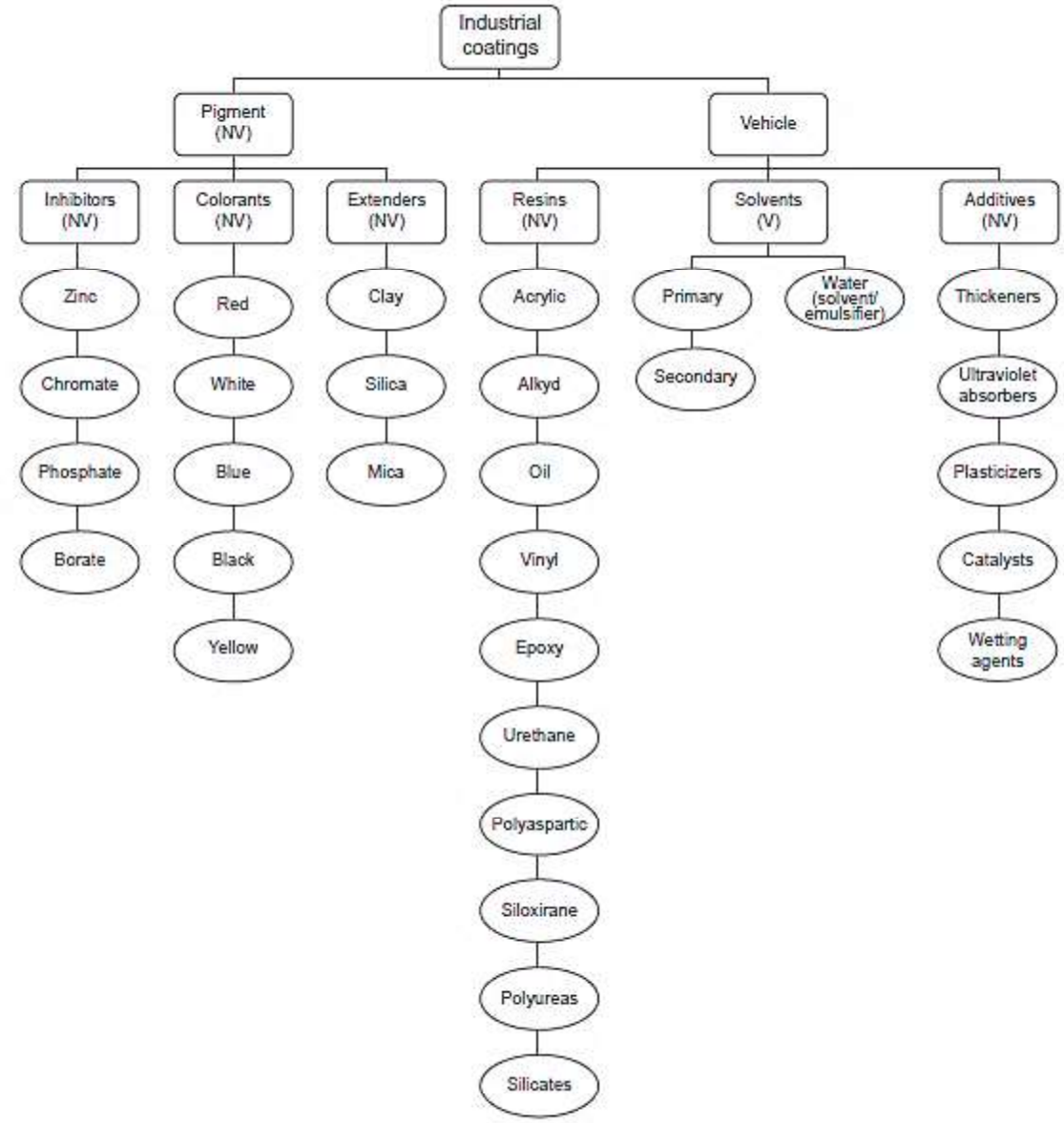


**Figure 2.23.** Components of industrial coating. [75]

### 2.3.1. Coating Application

The method of coating application usually depends on several factors, such as the purpose of use, the shape of the object, environment, type of paint, and cost. [59]

There are four main methods of paint application [76]:

- Spreading (brush, roller, doctor blade, paint pad)

- Spraying (hot spray, air-fed spray, electrostatic spray)
- Flow coating (dipping, curtain coating, roller coating)
- Electrodeposition.

In the marine industry, paints are mainly applied by roller, brush, or spraying (pneumatic or airless). [73]

The simplest way to apply the coating is by using the brush. This method provides a sufficient coating of the pores, cracks, and surface irregularities, but it is complex to reach the uniform film, and the application time is very long. [77]

Applying coating by the roller is much faster than brush painting but it is complicated to paint such objects as pipes, profiles, and frames. [59] The losses of paint using this method the same as by brush are negligible. During the rolling, the air is mixed with paint, and coating film has points of moisture, therefore, roller used to apply top coat rather than the primer. [78]

Spray painting helps to achieve a more uniform and smoother surface. There are two most common spraying methods: conventional and airless. In the conventional spraying (pneumatic), the paint is applied using the pump or pressurized air. The pressure which is necessary to apply paint is about 0.2-0.4 MPa. [73] In this type of application, the process goes very fast and allows to get the uniform film, but on the other hand, the paint losses are high.

The paint in airless spraying is carried at high pressure around 7.5-30 MPa and sprayed through the narrow orifice (nozzle, tip). Airless spraying provides a better finish than conventional spraying, especially in the corners. The principle of the airless sprayer is shown in Figure 2.24. There are four main components of airless strayer: airless pump, compressed air intake, filter, and spray gun. [78]

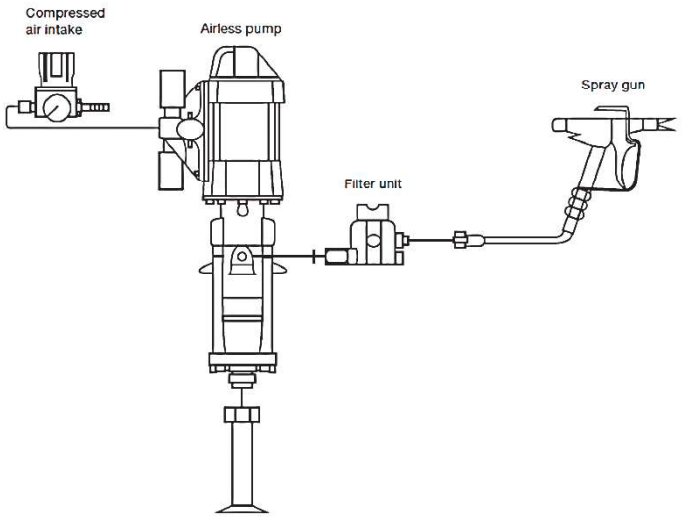


**Figure 2.24.** Schematic principle of the airless spray [79]

This type of applying methods has a list of the advantages and disadvantages as compared to conventional spray, which described in Table 2.6. [77]

**Table 2.6.** Advantages and limitations of the conventional spray.

| Advantages | Disadvantages |
|---|---|
| Thicker film application | High pressure |
| High production rate | Fan pattern is not adjustable |
| Easier to use by the operator, because there is only one hose | Difficulties in process |
| Higher viscosity of paints | High cost |
| Easier clean up | Requires special care |

### 2.3.2. Binder

The binder is one of the main components of the paint, and it might be classified according to the drying mechanism.

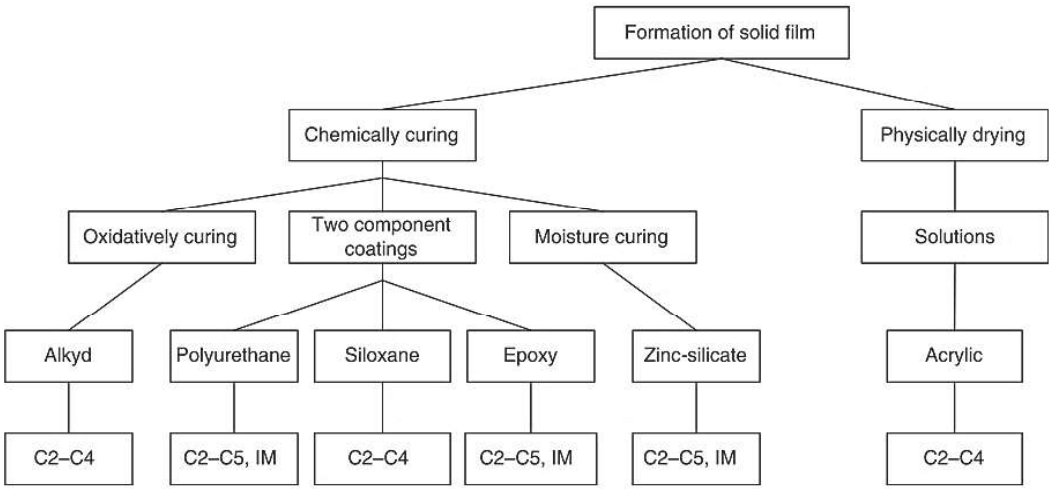


**Figure 2.25.** Classification of binders and suggested areas of application from low to very heavy (C2-C5) and immersion in soil, freshwater, or seawater (IM). [80]

Not all types of resins can be used in the marine industry. Polyurethane, epoxy, and zinc-silicate coating has very high corrosion, moisture [27], and weather-resistant [59] and usually used in the marine industry. [80] (Figure 2.25)

**Epoxy Resin**

The number of epoxy resins that can be used for corrosion protection such as bisphenol A and F epoxy, epoxy phenol novolac [81], waterborne epoxy [82], etc. Epoxy resins based on bisphenol A (BPA) are commercially the most important epoxy resins. Coatings based on BPA epoxy resin offer a unique combination of performance characteristics, including exceptional adhesion and corrosion resistance, excellent chemical resistance, low shrinkage, high strength, good heat resistance, toughness, and excellent electrical properties. [83] Figure 2.26. shows the structural components which correspond to the properties of the polymer. The main disadvantage of BPA epoxy resin is weak resistance to the ultraviolet light; it starts to yellow and chalk.

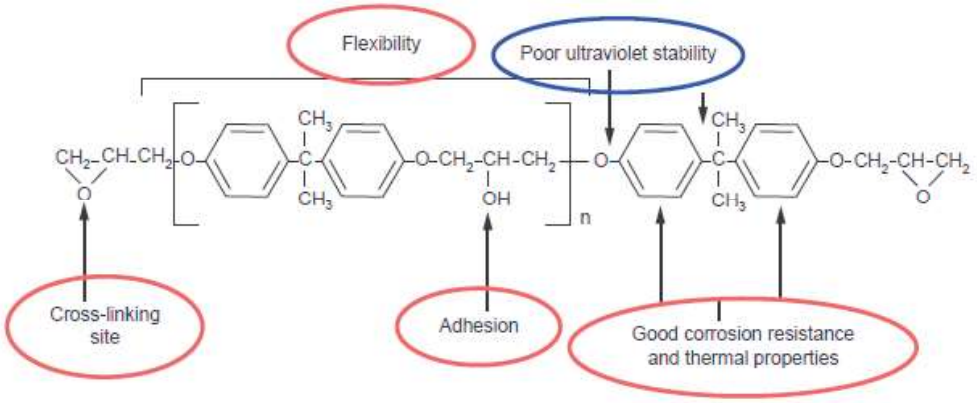


**Figure 2.26.** Structure/property relationship of bisphenol A epoxy resin [81]

Bisphenol F epoxy resin has the structure very similar to BPA, but the absence of methyl groups provides higher cross-linked density, as shown in Figure 2.27., and as a result, better thermal and chemical resistance. Epoxy phenol novolac resin contains epoxy-group at each repeatable unit. This resin provides higher chemical resistance than all other types of epoxy resins, but the coating is less flexible and has a higher cost. [84]

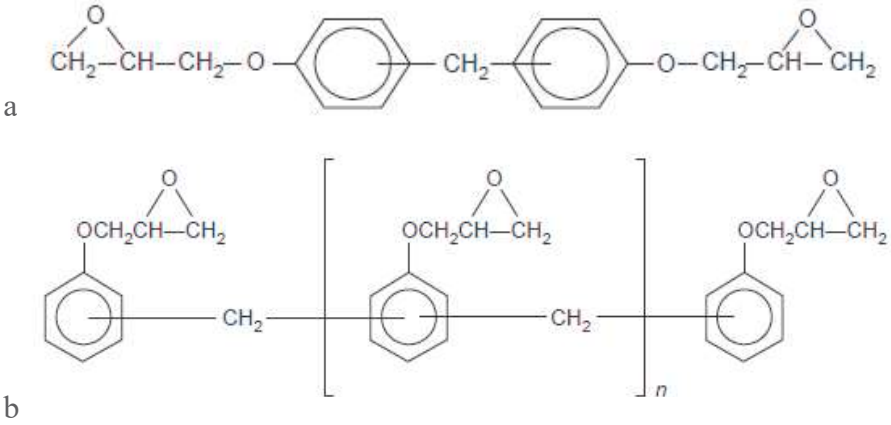


**Figure 2.27**. a. Bisphenol F epoxy resin; b. epoxy phenol novolac resin [81]

Epoxy resin usually is two-component coating, and different current agents can be used. The selection of the curing precursor depends on the porpoise of use. Figure 2.28. shows different types of the functional groups that can form the chemical bond with epoxy resin.

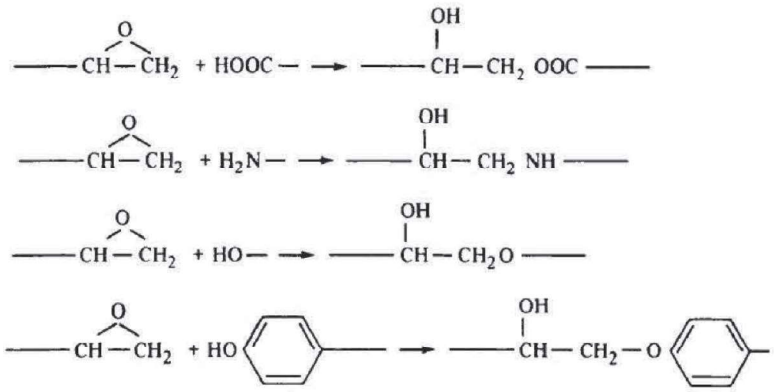

**Figure 2.28.** Common reactions with epoxy group. [85]

Phenol-formaldehyde, isocyanate, amines, amides, polysulfides, melamine, or urea-formaldehyde can be used as a curing agent. Aliphatic, polyamines, and polyamides are the most common one for epoxy resin. [86] In the marine industry, usually polyamides and aliphatic amines (polyethylene polyamine, diethylenetriamine, etc.) are used due to exceptional performance and easy way to use. Polyamides, in comparison with aliphatic amines, have high viscosity and high cost. [87]

Due to the high reactivity epoxy group, epoxy resin can be modified by silicones, acrylics, phthalates, and other thermoplastic materials which have been blended into epoxy coating formulations to provide better flexibility, water resistance, elongation, or chalking resistance. [88] These materials interlace with the cross-linked structure of the epoxy resin/curing agent binder and fill the voids

The epoxy resin can be modified by different siloxanes, but the most popular represent in Figure 2.29., due to the higher bond strength of the Si–O bond compared to C–C bonds. [89]

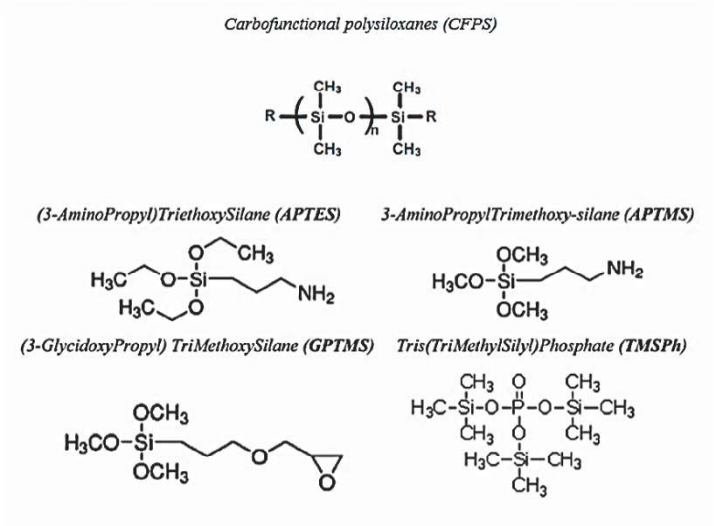


**Figure 2.29**. Silane and siloxane compound for modification epoxy resin. [90] [91]

Siloxane compounds are highly resistant to UV degradation, high temperature, and corrosion, and have good mechanical properties. The epoxy-siloxane coating reduces the corrosion rate of nineteen times in comparison with pure epoxy coating. [92] As shown in Table 2.7. the composite coating has good stability in aggressive environments such as 10% NaOH, 5% HCl, 3,5% NaCl, ethyl methyl ketone, and methanol in compare with pure epoxy. [93] (Table 2.7.)

**Table 2.7.** Resistance data of epoxy siloxane coating. [93]

| Chemical | Epoxy | Epoxy-siloxane |
|---|---|---|
| $H_2O$ (45 days) | b | e |
| NaOH (10wt%, 7days) | a | e |
| HCl (5wt%, 7days) | a | d |
| NaCl (3.5 wt%, 15 days) | a | e |
| Ethyl methyl ketone (2 days) | - | d |
| Methyl alcohol (2 days) | - | e |

a: film partially removed, b: film slightly affected but remain intact, c: loss in gloss, d: loss in gloss and weight, e: unaffected.

Conductive polymers also can be used to modify the epoxy resin and change the electroactivity of the film, such as polyaniline (PANi), polypyrrole, and thiophenes can also be added to modify the conductivity. However, their use is

limited by way of synthesis [94] and poor mechanical properties [95]. Among these, PANi has been successfully put into practice.

PANi can provide protection not only as a physical barrier, which prevents penetration of corrosive ions across the coating but also passivates the metal surface by formation of a thin oxide layer, as shown in Figure 2.30. [96]

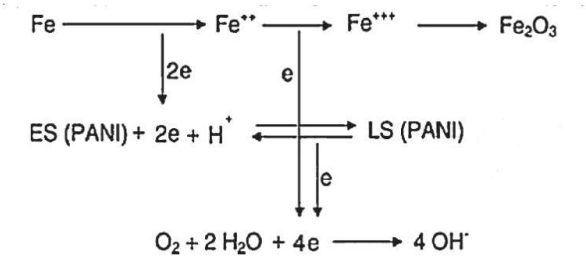


**Figure 2.30.** Mechanism of PANI protection of the steel. [97]

In case using polyaniline – epoxy coating the corrosion current density substantially decreases from 8.73 μA/cm$^2$ (for aluminum) to 0,00076 μA/cm$^2$ in 0,6M NaCl. [98] And also coating shows good stability in salt and acid solution. (Figure 2.31.)

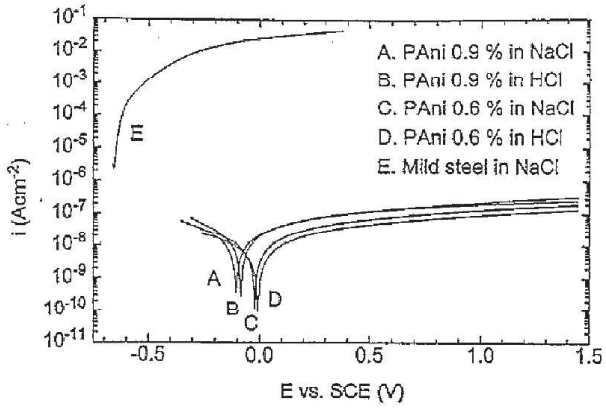


**Figure 2.31.** Tafel plot of polyaniline-epoxy coatings on mild steel in 0.6 M NaCl and 0.1 M HCI after one week of immersion. [99]

**Polyurethane**

The main advantages of isocyanate coatings are its weathering, corrosion, and ultraviolet radiation resistance; therefore, it usually used as a top coating. [100] Polyurethane resin also shows high resistance to solvents, acid, and alkaline

solutions. [101] Figure 2.32. showed reactions to synthesize urethane and urea polymers.

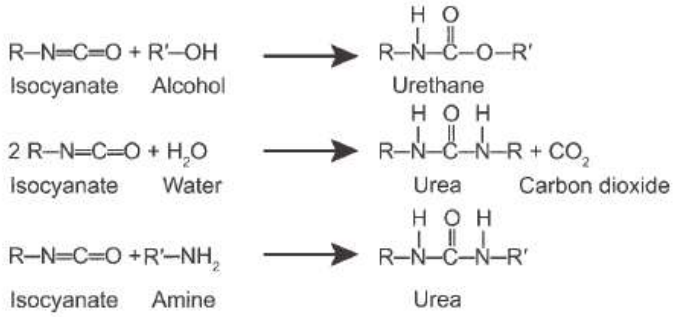


**Figure 2.32.** Reactions with isocyanates to form urethane or urea. [102]

Polyurethane resin could be one or two-component systems, and different cutting ways can be used, such as moisture curing or temperature curing. Blocked isocyanates are very popular, which polymerized under heat. [103] ASTM has classified polyurethane resin on six different groups. [104] According to Table 2.8. two-component polyurethane coatings show very high resistance to the environment and can be used in marine or aircraft industry. [85]

**Table 2.8.** Classification [105] and properties [59] of urethane coatings.

| ASTM description | Type I one-package (pre-react) | Type II one-package (moisture cured) | Type III one-package (heat cured) | Type IV two-package (catalyst) | Type V two-package (Polyol) | Type VI one-package (non-reactive lacquer) |
|---|---|---|---|---|---|---|
| Characteristics | Unsaturated drying oil modified; no fee isocyanate | Contains free isocyanate | Blocked isocyanate | Isocyanate prepolymer and catalyst | Part A: isocyanate rich, Part B: polyols or amines | Fully polymerized Pus Dissolved in solvents |
| Abrasion resistance | Fair-Good | Excellent | Good-Excellent | Excellent | | Fair |
| Hardness | Medium | Medium-Hard | Medium-Hard | Soft-Very Hard | | Soft-Medium |
| Flexibility | Fair-good | Good-Excellent | Good | Good-Excellent | | Excellent |
| Impact resistance | Good | Excellent | Good-Excellent | Excellent | | Excellent |
| Solvent resistance | Fair | Poor-Fair | Good | Excellent | | Poor |
| Chemical resistance | Fair | Fair | Good | Excellent | | Fair-Good |

| | | | | | |
|---|---|---|---|---|---|
| Corrosion resistance | Fair | Fair | Good | Excellent | Good-Excellent |
| Adhesion | Good | Fair-Good | Fair | Excellent | Fair-Good |
| Toughness | Good | Excellent | Good | Excellent | Good-Excellent |
| Elongation | Good | Poor | Poor | Excellent | Excellent |
| Tensile | Fair | Good | Fair-Good | Good-Excellent | Excellent |
| Cure rate | Slow | Slow | Fast | Fast | None |
| Cure temperature | Room | Room | 300-390°F (149-199°C) | 212°F (100°C) | 150-225°F (66-108°C) |

Polyurethane film is formed by the poly-additional reaction of the components: polyol diisocyanate and chain extender. [106] The chain extender can change thermal and hydrothermal properties and also solubility. [107] (Figure 2.33.)

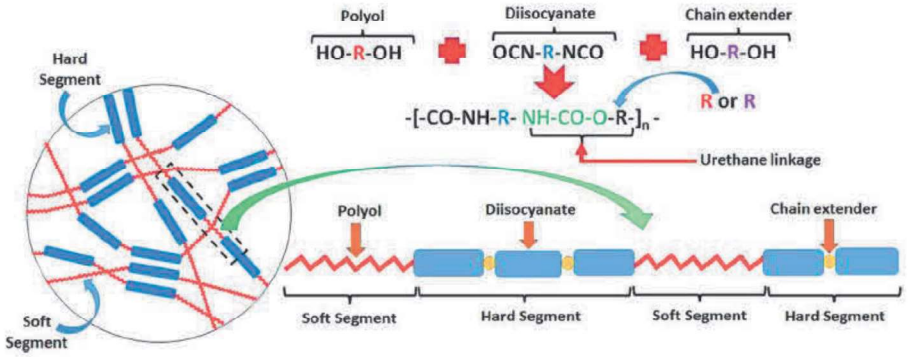


**Figure 2.33.** Schematic of the basic reaction of polyol, diisocyanate and chain extender for synthesis of polyurethane [108]

A variety of different polymeric backbones can be functionalized with the isocyanate group, for example, it can be attached to aromatic rings, cycloaliphatic rings, or linear aliphatic structures. (Figure 2.34.) Because of this wide variety, urethane coatings can be formulated to be elastomeric or rigid, ultraviolet light stable, highly chemical resistant, hard but tough, all within a wide range of formulated cost/performance specifications.

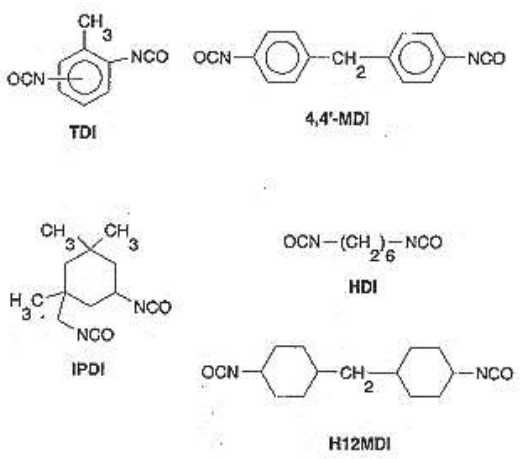


**Figure 2.34.** Typical isocyanates used in industrial maintenance coating. TDI - Toluene diisocyanate, MDI - diphenyl methane diisocyanate, IPDI - isophorone diisocyanate, HDI - hexamethylene diisocyanate, $H_{12}$MDI - hydrogenated diphenyl methane diisocyanate. [109]

Corrosion protection behavior of the polyurethane coating is significant, and it decreases the corrosion current density more than twenty times from 162μA/cm$^2$ to 7.63μA/cm$^2$. [110] And the stability of the film is more than 300 hours in the solution of 3% NaCl without noticeable changes, as shown in Figure 2.35.

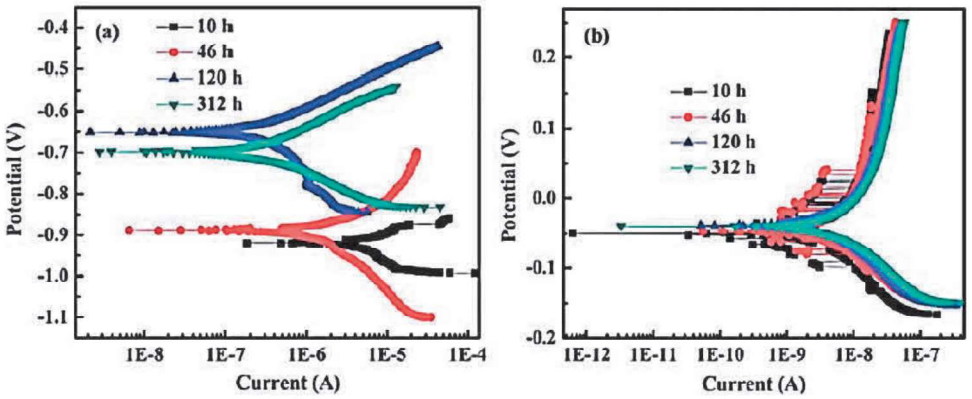


**Figure 2.35.** Stability of the electrodes: a – stainless steel, b – polyurethane carbon nanotubes composite coated stainless steel. [110]

### Zinc Silicate Coating

Zinc silicate coating is an inorganic film that forms by the reaction of the excess of zinc particles with polysilicic acid in the presence of moisture (humidity of

50–60% [111]) and possible to provide cathodic protection. [112] Figure 2.36 shows porous zinc silicate coating, where zinc joined by a silicate binder.

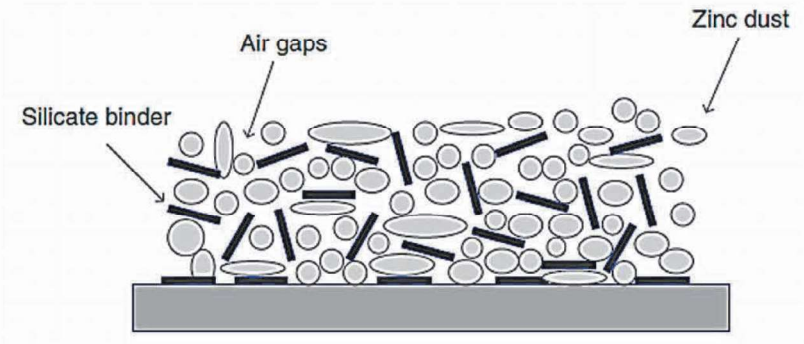


**Figure 2.36.** Schematic zinc-silicate coating. [80]

Zinc-rich silicate primer usually used for offshore structures, bridges, chemical-processing industries because it can also minimize pitting corrosion. [113] Organic and inorganic additives can be used to improve the corrosion resistance [114] and quality [115] of the coating film.

### 2.3.3. Pigments, Solvents and Additives

***Pigments***

In the coating formulation, several pigments are used to perform different functions such as color, corrosion protection, reinforcement, coverage, gloss, adhesion. Pigments are essential and improved strength, permeability, and impact resistance. The shape of the pigments also plays a significant role in properties, as shown in Table 2.9. [75]

**Table 2.9.** Particle shape and coating film properties of pigments [116]

| Particle shape | Benefit | Usage | Pigment type |
|---|---|---|---|
| Platey | Barrier properties | Barrier primers | Aluminum |
| | Corrosion resistance | Exterior house paints | Mica |
| | Bleed and stain killing<br>Enamel Holdout | Interior high PVC flats | Glass flake |
| | $TiO_2$ extension (spacers) in high-PVC flats (clays) | Latex paint | Stainless steel |
| | Stress relief via slippage of overlapping plates | Stain-killing paints | Talc |

| | | | |
|---|---|---|---|
| | Cracking and checking resistance | Smooth finishes | Clays |
| | Mudecracking resistance at high PVC/CPVC | Paper coating | Silver and nickel flake |
| | Soft in-can pigment sedimentation | Conductive coatings | Graphite |
| | High vehicle demand | Sealers and undercoaters | |
| | High viscosity | | |
| | Improved application properties | | |
| | Good stain removal and scrub resistance | | |
| Acicular | Film reinforcement | Exterior coatings | Wollastonite |
| | Cracking and checking resistance | Roof coatings | Zinc oxide |
| | Improved durability | Block fillers | Chopped-fiber glass |
| | Mudecracking resistance at high PVC/CPVC | Textured coatings | Talc |
| | Texture | | Many of the organic pigments are slightly acicular |
| Fibrous | Film reinforcement | Roof coatings | Asbestos |
| | Cracking and checking resistance | Block fillers | Cut textile fibers |
| | Mudecracking resistance at high PVC/CPVC | Textured coatings | Cellulosic |
| | Texture | Zinc-rich primers | Polyolefins |
| | Thixotropy | High-build mastics | Acrylics |
| | High buikl capabilities | Asphaltic and coal tar coatings | Polyaramids |
| | Nonsagging | Tennis court coatings | |
| | Nonsettling | | |
| | High viscosity | | |
| | Crack bridging | | |
| Nodular | Excellent filling properties | Gloss and semigloss coating | Calcium carbonate silica |
| | Low vehicle demand | Wood fillers | Titanium dioxide |
| | Low viscosity | High-solid coatings | Iron oxides |
| | Water resistance (nodular silica) | Floor and deck coatings | Barytes |
| | | Mar and burning resistance | Nepheline syenite |
| | | | Chromium green oxide |
| | | | Most inhibitive pigments |
| Spherical | Excellent filling properties | Zinc-rich primers | Zinc dust |
| | Low vehicle demand | High solids | Synthetic vesiculated spheres |
| | Low viscosity | Low-VOC systems | |
| | Opacity | | |
| | Hardness (vesiculated spheres) | | |

| | | | |
|---|---|---|---|
| Irregular | Excellent flatting properties<br>Moderate film reinforcement<br>High vehicle demand<br>High viscosity | Flat paints | Diatomaceous silica |

*Corrosion Pigments*

Corrosion inhibiting pigments are significant, and it could prevent corrosion by providing the physical barrier to the metal surface, cathodic protection, or inhibition. Traditionally anticorrosion pigments are chromium, lead, zinc, and iron-based compounds. [117] Most of these pigments are very toxic (lead and chromium) and nowadays limited to use in industry. [118]

Red lead ($Pb_3O_4$) and lead silicochromate (core $SiO_2$, coating $PbSiO_3$ 3PbO $PbCrO_4$) provide excellent protection be passivation iron or steel surface. Chromate-based compound demonstrates the powerful level of protection. Zinc, strontium, barium chromate was used in the early days. The mechanism of protection involves the reduction of $Cr^{6+}$ to $Cr^{3+}$and followed with irreversible adsorption to the surface of metal and formation protective layer, also $Cr^{6+}$ inhibits oxygen reduction reaction. [119] Chromium-based pigments also inhibit the crevice and pitting corrosion. [120]

Zinc-based pigments are very promising and widely used in different industries. Zinc dust protects the substrate by galvanic protection and physical barrier. Zinc phosphate, zinc-aluminum phosphate, etc. are the most frequently used in paint composition. These pigments have relatively low cost, environmentally friendly, and replace lead and chromium-based pigments. [121] Modification of zinc phosphate, even more, improves the corrosion resistance and weathering resistance and interlayer adhesion, for example, zinc molybdenum phosphate. [122]

Iron oxides and hydroxide-oxides can be used as the anticorrosion pigments, like α-FeO(OH), α-$Fe_2O_3$, or iron mica, it also enhances the weather, ultraviolet resistance, and mechanical properties. [123] Titanium dioxide another example of multifunctional color pigment, which shows good heat resistance and low electrical

conductivity and increases the corrosion resistance. Titanium dioxide is worked as an ultraviolet radiation blocker because of its high reflective index. [121]

Graphite is a unique pigment that can provide a combination of properties, not only corrosion protection but also color, conductivity, ultraviolet, chemical, and thermal resistance. More about carbon-based pigment is described in Chapter 2.4.

*Color Pigments*

Color pigments are vital in the appearance of the total object. Pigments could be multifunctional, for example, phthalocyanine blue pigment provides excellent resistance from alkali, acid, and heat. [74] Usually, the pigments for primary colors are used: white, black, yellow, red, orange, blue, green; all others are obtained using coloring technique. Also, there are metallic pigments which give the metallic shine to the film, such as stainless steel powder, copper, zinc, aluminum, or lead flake. [124]

Lithopone (30% ZnS, 70% $CaSO_4$), zinc sulfide, zinc oxide, white lead, etc. can be used as a white pigment, but the most wildly used is titanium dioxide because it is less costly and high efficiency. [125] There are seven different types of modified or non-modified titanium dioxide-based on rutile or anatase structure accordantly ASTM D476 standard, for different applications. [126]

Carbon black, lamp black (carbon and 3% moisture [127]), and black iron oxide (ferroso-ferric oxide $FeOFe_2O_3$) are the most common black pigments. [128]

Colored pigments can be divided into organic and inorganic pigments. Usually, organic pigments are not very stable under ultraviolet. Inorganic colored pigments could be classified into four groups: lead chromates (chrome yellow $PbCrO_4$ $xPbSO_4$, chrome orange $PbO{\cdot}xPbCrO_4$, chrome green $PbCrO_4{\cdot}xPbSO_4{\cdot}yFeNH_4Fe(CN)_6$), metal oxides (yellow iron oxide $Fe_2O_3{\cdot}xH_2O$, red iron oxide $Fe_2O_3$, green chromium oxide $Cr_2O_3$), sulfides (cadmium yellow CdS,

cadmium red CdS·xCdSe) and miscellaneous (iron blue $Fe(NH_4)_2Fe(CN)_6 \cdot xH_2O$, cobalt blue $CoAl_2O_4$). [129] Organic pigments are very complicated and have different classes of the materials. Red color can produce azo reds which contain —N=N— group, quinacridone red with high durability due to hydrogen bonding, benzimidazolone reds. (Figure 2.37.a.-c.) Copper phthalocyanine blue is the most common and wildly used organic blue pigment. (Figure 2.37.d.) To obtain the yellow color monoarylates are used, which are derivatives from azo pigments. (Figure 2.37.e.) [130]

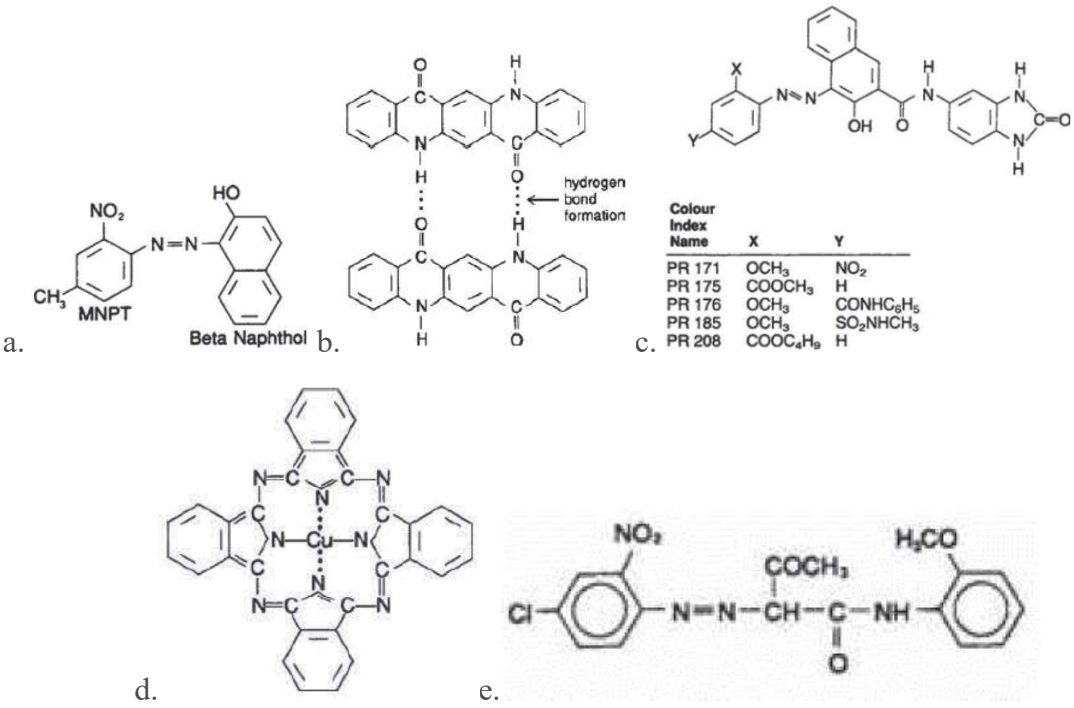


**Figure 2.37.** a. Azo red - Toluidine Red (2-nitro-4-toluidine (MNPT)-2-naphthol (beta naphthol)); b. quinacridone reds; c. benzimidazolone reds; d. copper phthalocyanine blue; e. monoarylide yellow. [130]

*Extender Pigments*

Extenders are pigments whose primary function is to decrease the cost of the paint. It is also can improve the mechanical properties and adjust the pigment volume concentration (PVC), which is the ratio of the volume of pigment to the volume of the dried coating. But it can affect rheological, anti-settling, and strength properties. [131]

Calcium carbonate $CaCO_3$, kaolin $Al_2O_3$ $2SiO_2$ $2H_20$, talc $3MgO{\cdot}4SiO_2{\cdot}H_2O$, silica $SiO_2$, mica $K_2O{\cdot}3Al_2O_3{\cdot}6SiO_2{\cdot}2H_2O$ [132], wollastonite $CaO{\cdot}SiO_2$, barium sulfate $BaSO_4$ are usually used as extenders for different types of coating.

***Solvent***

The viscosity of the paint is significant, and several parameters dependent on it, such as coating film appearance, adhesion, durability, and physical properties, therefore choosing the correct solvent is a key task. [133] Solvency and evaporation rate are the main parameters of the solvents to control. The evaporation rate effects on the coating flow at the application stage and the leveling and uniform at the curing stage. [134]

Solvents are individual for each type of binder and should be chosen according to the application purpose. There are three leading families of the solvents: hydrocarbons, oxygenated solvents, and water. For the epoxy and urethanes coating, oxygenated solvents are usually used, for example, ketones (methyl ethyl ketone, methyl isobutyl ketone, etc.), esters (ethyl acetate, isobutyl acetate, etc.), nitroparaffins (2-nitropropane), furans (tetrahydrofuran, tetrahydrofurfuryl alcohol), and N-methyl-2-pyrrolidone. [75]

***Additives***

Additives improve different properties such as surface wetting, biofouling, the stability of the color and gloss, etc. [135] The surfactants are surface-active agents with the capability to modify interfacial interactions through adsorption at interfaces. They could provide different functionals, as described below. [136]

Defoamers are used to illuminate bubbles in the paint by lowering the surface tension. Silicone-based defoamers, such as BYK-A 530 [137] and Afcona 2722 [138], are silicone-based common defoamers with high surface activity and mobility. Antisettling additives improve the homogeneity of the paint and hold the pigments

in suspension during the storage. The nature of it could be different, for example, BYK ANTI-TERRA-203 based on alkylammonium salt of a polycarboxylic acid [139] or AEROSIL® 200 with fumed silica. [140] Dispersing agents eliminate the aggregation and improve the incorporation of pigments and extenders in the paint, for example, BYK-9076 alkylammonium salt of a high molecular-weight copolymer. [141] Wetting agents displace the air from a solid surface by the liquid and reduce the interfacial surface tension between solid and liquid, for example, BYK – 333 polyether-modified polydimethylsiloxanes. [142]

Microbicides are the additives that prevent the coating from the biodegradation. It could be classified accordantly the biological species they are preventing from algae, bacteria, and fungi. [143] Plasticizer one more type of additives which improve the mechanical properties of the coating film. The mechanism of changing the flexibility of the resin is to form strong polar interaction between polymer and plasticizer and reduce van der Waals forces between polymer molecules. [144]

## 2.4. Carbon-based Pigment

As mentioned in Chapter 2.3.3. some of the anti-corrosion pigments are very toxic and nowadays do not use in industry. That's why it's imperative to find new anticorrosive pigments, which provide effective protection, environmentally friendly, and low cost. Carbon-based materials are very promising in corrosion prevention of coatings. There are several forms of novel nanostructured carbons which might be used: graphene, carbon nanotubes, and fullerenes.

### 2.4.1. Carbon Black

Carbon black is colorant pigment and is widely used in the painting industry, which could provide other functions, like ultraviolet radiation [145] and corrosion protection. Carbon black prevents the coating from the degradation by several mechanisms: ultraviolet stabilizer, which absorbs the radiation; free radical

scavenger; and blocked micropores, which have not been observed in the composite, as Figure 2.38.a. described. [146]

Carbon black prevents the corrosion by barrier mechanism, but an agglomeration of the particles should be controlled to regulate the adsorption properties. [147]

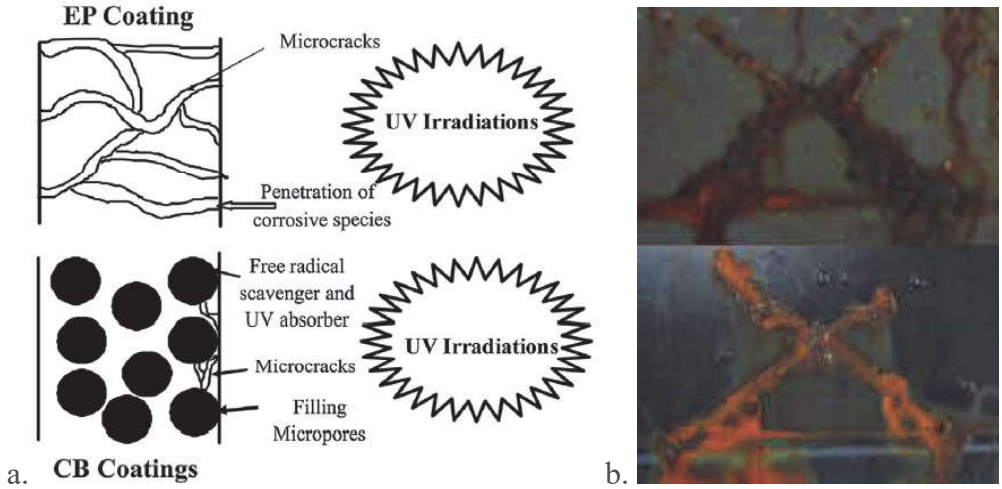


**Figure 2.38.** a. Scematic illustration of the mechanism prevention from the ultraviolet radiation by the carbon black [146]; b. Surface apperance of epoxy coating (upper) and 2.5% carbon black composite coating after 720h in salt spray chamber. [147]

Carbon black is a conductive material and in critical concentration, which called percolation concentration, could initiate changing insulating polymer matrix to the semiconductor or conductor. [148] The composite coating with carbon black weight percent above the percolation value provide better corrosion protection than with lower concentration. [149]

### 2.4.2. Graphene

Graphene is an atomic-scale hexagonal lattice made from carbon atoms that can be modified to the graphene oxide and reduced graphene oxide. Graphene shows high thermal conductivity [150], mechanical properties, such as elasticity and

intrinsic strength [151], and impermeability to oxygen and water molecules. [152] Agglomeration process as proper to graphene and graphene oxide, can be minimized by mechanical (ultrasound) [153] or modification way. The functionalization of the graphene and graphene oxide improve the dispersion and eliminate the agglomeration process. Interfacial bonding between graphene and matrix enhances the dispersion and also physical and chemical properties. [154]

It was reported a lot of different ways to improve the dispersity of the graphene oxide. Silane precursors improve the corrosion properties and lower coating delamination and blistering. Silanes form the chemical bonding with hydroxy-group of graphene oxide and can cross-link with epoxy [155] or polyurethane resin. [156] (Figure 2.39.a.)

Electroactive polymers can be used as functional material or as the dispersant. Graphene oxide modified by polyaniline [157] or polyvinylpyrrolidone [158] could decrease the corrosion rate in more than 5 times. Poly(2-butylaniline) works as a great dispersant due to strong π-π interaction between conjugated polymer and graphene sheets. Well stabilized single-layer graphene could decrease the corrosion rate in more than three order compare with the neat binder. [159] (Figure 2.39.b.)

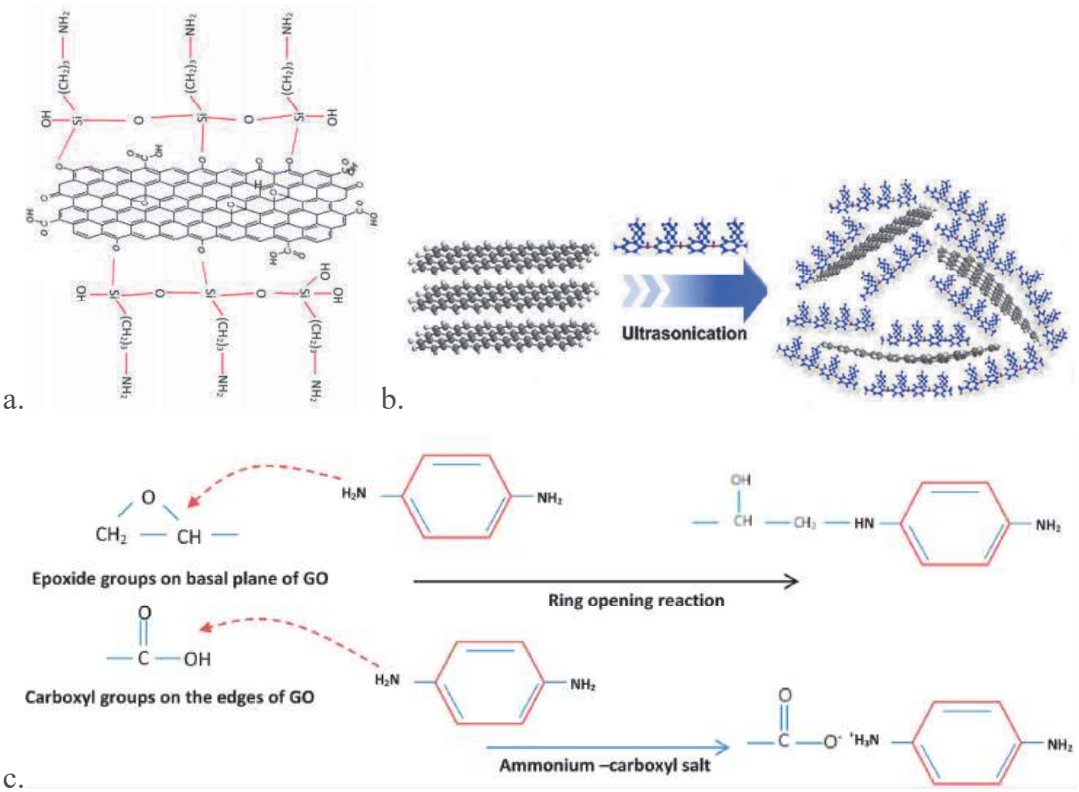


**Figure 2.39.** a. Graphene oxide functionalized by 3-aminopropyl triethoxysilane [155]; b. Dispersed graphene by poly(2-butylaniline) [159]; c. *p*-Phenylenediamine reactions with graphene oxide. [160]

The formation of the cross-linked system between pigment and binder enhances barrier and corrosion properties. *p*-Phenylenediamine could form a chemical bond with epoxide and carboxyl groups of the graphene oxide, as shown in Figure2.39.c., and on the other side, react with epoxy resin. [160]

Fabrication of novel hydride pigments with modified nanoparticles of commonly used pigments and graphene oxide magnify the barrier and corrosion properties and reduce the delamination rate. Nanoparticles of titanium dioxide (TiO2) [161] or silica (SiO2) [162] could be stabilized by 3-aminopropyltriethoxysilane of its mixture with tetraethylorthosilicate, respectively. The amine groups of the silane react with graphene oxide and form hybrid corrosion pigment.

The reduction of the graphene oxide could also improve the orientation of the sheets in the binder. [163] Ideally single layer parallel to a metal surface-oriented graphene or graphene oxide provide maximal barrier protection, as shown in Figure 2.40. [164]

In Table 2.10., some examples of graphene-based coating are summarized.

**Table 2.10.** Performance of graphene-based coatings.

| Graphene material | Binder | Thickness, μm | Potential, V polymer/ composite | Current density, μA/cm$^2$ | Ref |
|---|---|---|---|---|---|
| Graphene | Water-borne epoxy | 50 (wet) | -0.637/-0.566 | 0.121/0.055 | [165] |
| Modif. graphene | Polyaniline | 30 (dry) | -0.647/ 0.537 | 3.7/0.38 | [166] |
| Graphene oxide | Epoxy | 40 (dry) | - | 0.501/0.202 | [153] |
| Modif. graphene oxide | Polystyrene | 15 (dry) | -0.662/-0.344 | 4.9/0.037 | [167] |
| Modif. reduced graphene oxide | Epoxy | 10 (dry) | -0.9/-0.408 | 0.75/0.48 | [158] |
| Graphene oxide | Alkyd resin | 150 (wet) | -1.047 (Me)/-0.995 | Efficiency 76,6% | [168] |
| Carboxyl graphene | Electroactive polyimide | 30 (dry) | -0.573/ -0.432 | 2.75/0.15 | [169] |

The mechanism of protection by graphene or graphene oxide is based on the barrier formation, which reduces the permeability of water and oxygen atoms. (Figure 2.40.)

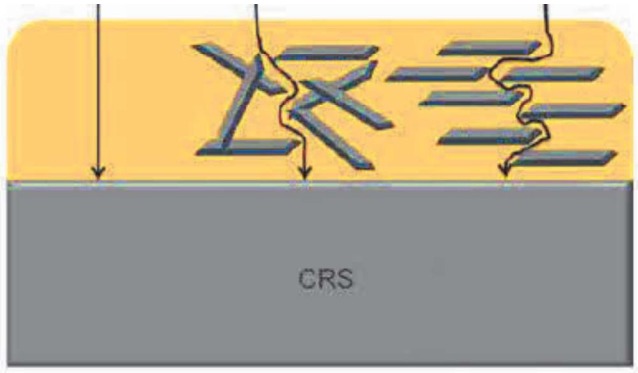


**Figure 2.40.** Schematic representation of $O_2$ and $H_2O$ following a tortuous path through the graphene-based coating. [164]

### 2.4.3. Carbon Nanotubes

Carbon nanotubes due to their unique structure used in different industries, like aerospace and construction. Carbon nanotubes could provide high thermal and electrical conductivity, mechanical strength, and lightweight. [170] Due to these properties, they are promising materials for the anticorrosion application.

Carbon nanotubes, compared with graphene, has different mechanisms of protection. Carbon nanotubes can play not only barrier effect but also have a passivation effect via adsorbing molecular species of oxygen [171], hydroxyl [172], chloride, and sulfate anions [173]. The carbon nanotubes might absorb atoms and ions in three ways: on the end of the nanotube, on the side of the wall, and inside carbon nanotube, as shown in Figure 2.41. The values of adsorption energy increase from the end of the nanotube to the side of the wall: $E_{end} > E_{inside} > E_{side}$.

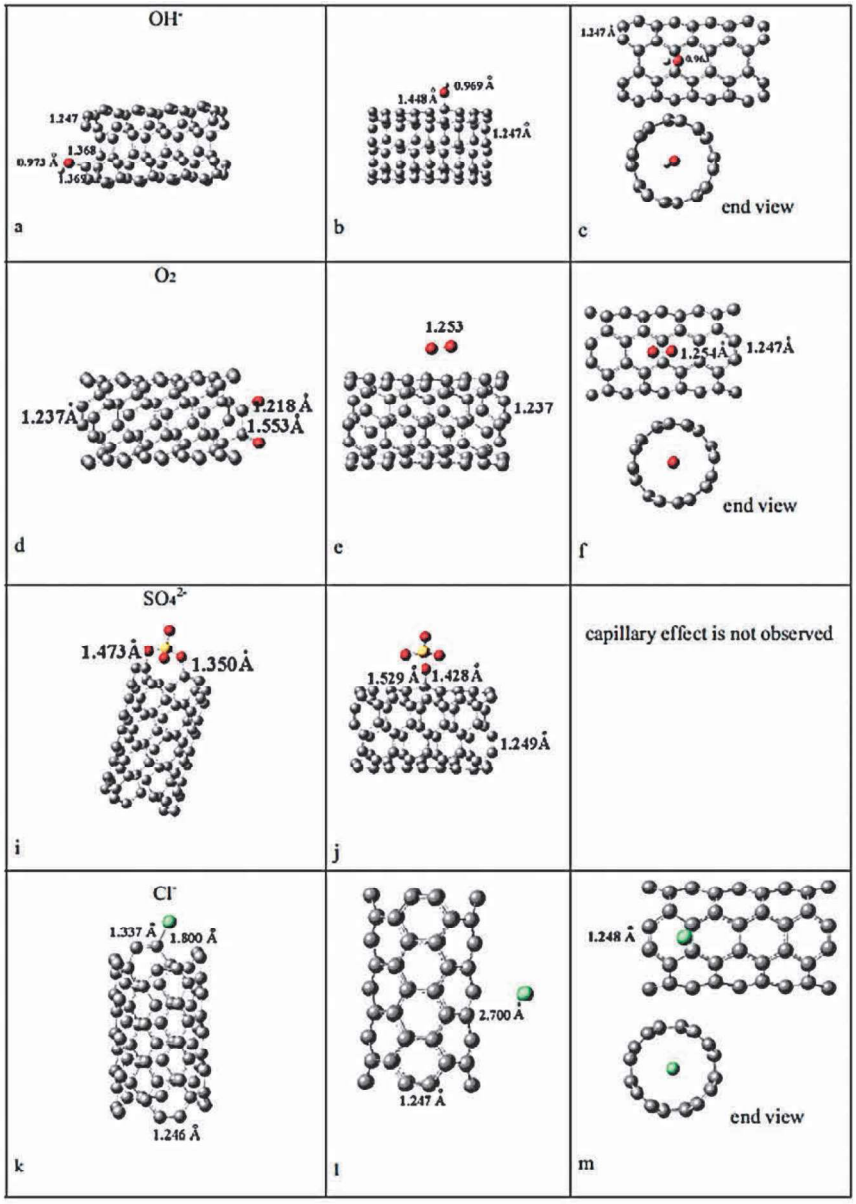


**Figure 2.41.** Schematic mechanism of sorption a-c hydroxyl ions; d-f oxygen molecules; i-j sulphate ions; k-m chloride anions. [173]

Carbon nanotube pigment enhances the adhesion, stiffness, and wear of the composite coating. The pore resistance of the composite increase due to the 3D dispersion of the carbon nanotubes in the binder. [174] The diffusion coefficient decreases with increasing the carbon nanotube presence, and absorption of water minimized, therefore, the delamination and blister formation improved. [175] Carbon nanotubes can also impact on the ultraviolet radiation resistance of the epoxy resin, which quickly degrades under radiation. [176]

The carbon nanotubes improve the corrosion resistance of the different types of coatings, such as polyurethane [110], water-borne acrylic [177], and epoxy. The influence on corrosion protection of carbon nanotubes in the zinc-rich epoxy coating is shown in Figure 2.42. after 30 cycles of hydrothermal testing. [178]

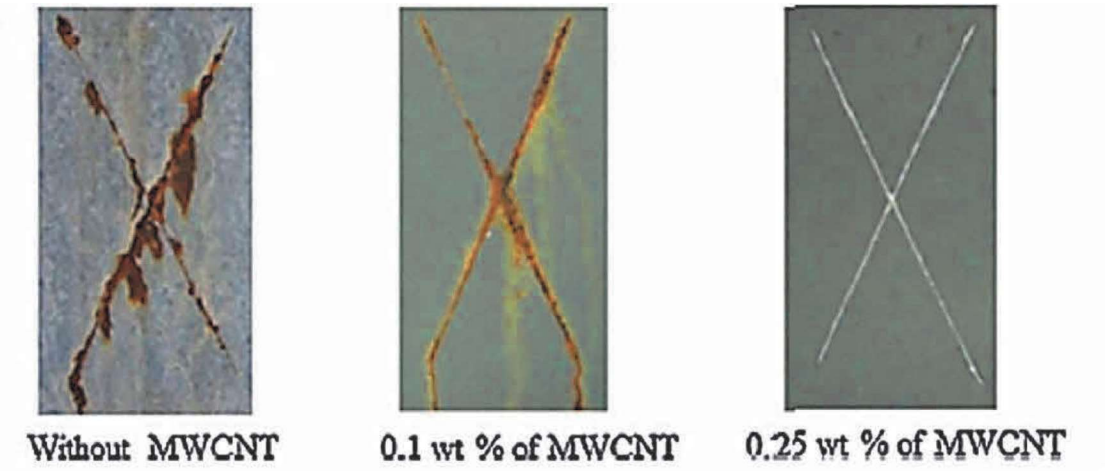


**Figure 2.42.** Surface of epoxy zinc coated carbon steel with various contents of carbon nanotubes after corrosion treatment. [178]

The higher weight percentage reduces the composite performance due to the agglomeration of carbon nanotubes. Corrosion behavior and adhesion dropped significantly, as shown in Figure 2.43. [179] The poly(2-butylaniline) could be used as dispersant carbon nanotubes (Figure 2.43.b.), the same as for graphene oxide [159], which minimize the agglomeration via π-π interaction. [180]

a.

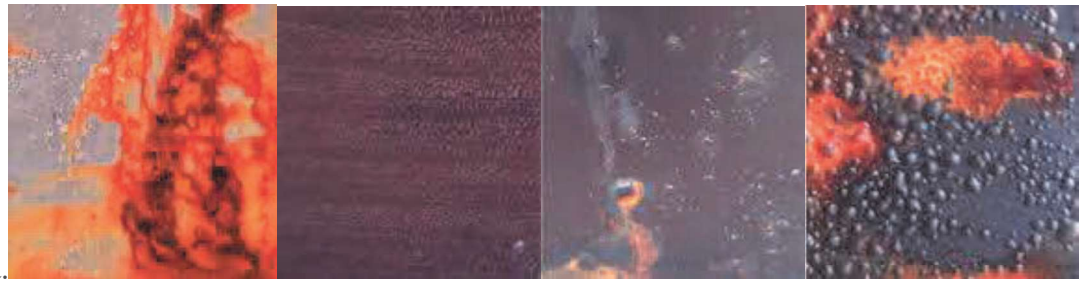

b.

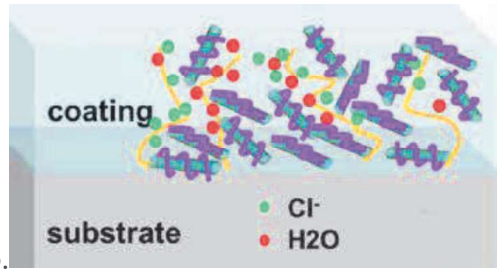


**Figure 2.43.** a. 0%, 0.4%, 0.7% and 1% carbon nanotubes polyurethane coating after 500H in salt spray chamber [179]; b. schematic illustration of the corrosion in well-dispersed coating. [180].

### 2.4.4. Fullerene

Fullerene is another carbon material and can be used in corrosion protection. But the structure difference causes the change in the barrier protection, and it is not as high as by graphene sheets. (Figure 2.44) [181]

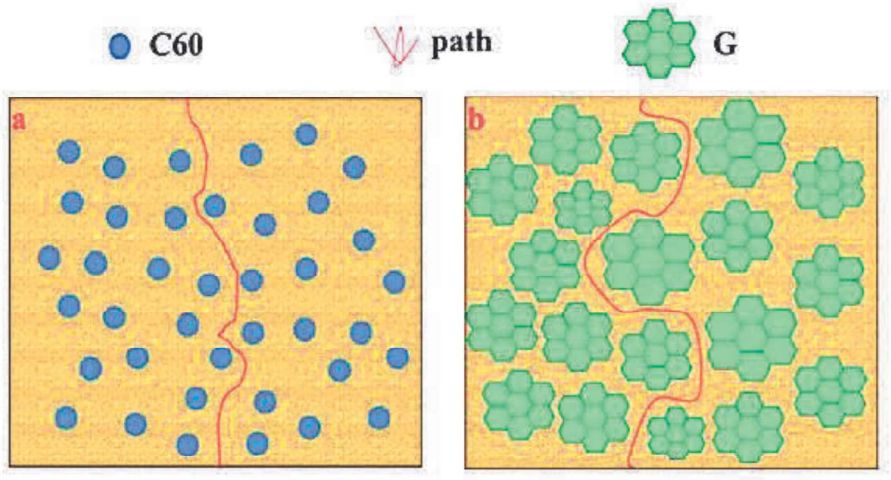


**Figure 2.44.** Schematic illustration of path way of a – fullerene; b – graphene based coating. [181]

The electrochemical measurements showed that adding fullerene decreased corrosion rate by fourfold but adding graphene eightfold. Therefore, the graphene-based materials more popular in corrosion protection studies.

**Table 2.11.** Comparison table of electrochemical data of fullerene and graphene based coating. [181]

| Sample | $I_{corr}$ ($\mu A/cm^2$) | $E_{corr}$, V |
|---|---|---|
| Epoxy coating | 8.09 | -0.575 |
| Fullerene based epoxy coating, 0.5% | 2.07 | -0.609 |
| Graphene based epoxy coating, 0.5% | 1.29 | -0.549 |

## 2.5. Marine Corrosion

The corrosivity of the atmospheric environment is dependent on the level of pollution, climate, and distance to the sea, and there are six categories from very low (C1) to very high corrosivity (C5-I and C5-M), which describes in Table 2.12. The marine environment is one of the most aggressive ones because many factors affect the corrosion rate. [182]

**Table 2.12**. Atmospheric corrosive environment and examples of typical environments. [182]

| Corrosivity category | Examples of typical environments in a temperate climate (informative only) | |
|---|---|---|
| | Exterior | Interior |
| C1 very low | - | Heated buildings with clean atmospheres, e.g. offices, shops, schools, hotels. |
| C2 low | Atmospheres with low level of pollution. Mostly rural areas. | Unheated buildings where condensation may occur, e.g. depots, sports halls. |
| C3 medium | Urban and industrial atmospheres, moderate sulfur dioxide. Coastal areas with low salinity. | Production rooms with high humidity and some air pollution, e.g. food-processing plants, laundries, breweries, dairies. |
| C4 high | Industrial areas and coastal areas with moderate salinity. | Chemical plants, swimming pools, coastal ship- and boatyards. |
| C5-I very high (industrial) | Industrial areas with high humidity and aggressive atmosphere. | Building or areas with almost permanent condensation and with high pollution. |
| C5-M very high (marine) | Coastal and offshore areas with salinity | Building or areas with almost permanent condensation and with high pollution. |

The corrosion rate in the marine atmosphere depends on the depth. As shown in Figure 2.45., there are five zones (the marine atmosphere, the splash zone, tidal, continuously submerged, and subsoil zones), and the most corrosive is the splash zone due to the combination of the seawater, ultraviolet radiation, and wind. [183] Marine atmosphere is a coastal area or offshore contractions above the water level.

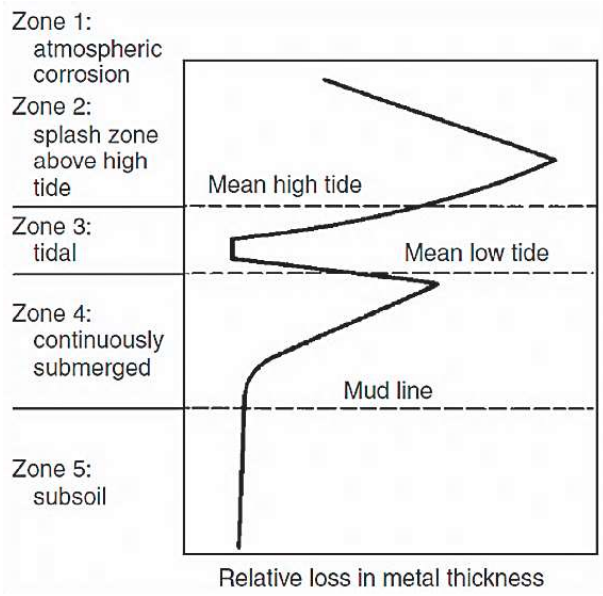


**Figure 2.45.** Zones of corrosion for steel in seawater. [184]

### 2.5.1. Marine Environment

Several factors, such as moisture, temperature, velocity, winds, airborne contaminants, chloride ion, electrical conductivity, oxygen concentration, pH, pollution, and biofouling, contribute to marine corrosion. [27]

The salinity, from one side, increases the conductivity of the water, so it means that the resistance of the electrolyte plays a minor role in corrosion rate determination and galvanic series for galvanic corrosion initiation are much more spread apart. On the other hand, the chloride ions destroy the passive layer of the metal and initiate crevice and pitting corrosion. The salinity determinate by UNESCO as S (‰) = 1.80655Cl (‰). [185] The total salt content of open ocean seawater varies from 32 to 36 ‰.

In case if all parameters stay constant, the corrosion rate increases with increasing temperature. For example, for low carbon steel, the corrosion rate doubled with every 30$^{o}$C with constant oxygen concentration.[186]

Many of the minor constituents that are important to corrosion processes are dissolved gasses such as carbon dioxide and oxygen. Their concentrations are influenced by the air-sea exchange as well as by biochemical processes. The corrosion rate decreases with the decline of the dissolved oxygen concentration linearly. The effect of concentration dissolved oxygen is dominated when oxygen and temperature vary together. [187]

The concentration of carbon dioxide and carbonate ions affected the pH value of the seawater by the formation of a buffer solution. The pH value is about 7.5 to 8.3 in the open sea. The pH changing in seawater does not seriously affect the corrosion rate for most metals except aluminum alloys. The decrease of pH value from the water surface to deep water increases the corrosion rate of aluminum and initiate the pitting and crevice corrosion. [188] The influence of the depth on the parameters mentioned above and their correlations are shown in Figure 2.46.

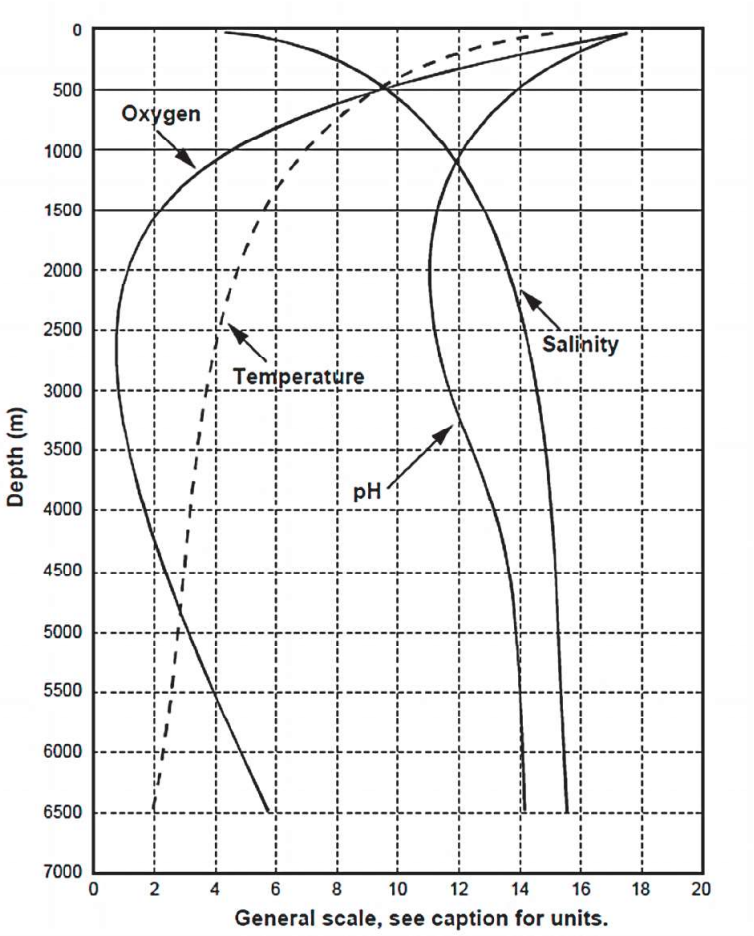


**Figure 2.46.** Variations of the parameters in Pacific Ocean with depth. The units conversion: oxygen, scale * 0.333 (ppm); temperature, scale * 1 (°C); salinity, 33.0 + scale * 0.1 (‰); pH, 6.4 + scale * 0.1 (pH unit). [23]

The main effect of polluted seawater arises from the presence of sulfur- or nitrogen-containing substances such as $S^{2-}$, $SO_2$, $NO_2$, $NH_4$, etc. [27] The presence of $SO_2$ in the atmosphere increases the aggressiveness of the environment. The influence of $SO_2$ on corrosion rate is linear, the corrosion rate increases in a higher concentration of oxide. [189]

Biofouling is one of the critical problems for the marine environment. The growth of bio-organisms is speedy. The extra fuel waste increases rapidly under certain fouling percent, for example, if the fouling is 12-50%, the fuel loss is over 30%. [190] Biofouling mechanism and coating for biological organism growing prevention is described in Chapter 2.5.3.

### 2.5.2. Marine Coating

Marine coating is a multifunctional coating which could provide effective protection under aggressive environments and meet with the requirements [191]:

- Corrosion protection
- Water impermeable
- Abrasion resistance
- Smooth
- Consistent with the cathodic protection system
- Anti-fouling
- Weather resistance
- Impact–resistant
- Scratch–resistant
- Easy to clean

Marine coating could be classified as bottom or underwater coating, boottopping, splash zone area, and topside. [192] The paint system consists of a primer, barrier anti-corrosion coating, and top anti-fouling coat with total thickness over 250μm. Only some of the binders can be used in the marine environment with category C5M. (Figure 2.25.) [80] These binders were described in detail in Chapter 2.3.2.

### 2.5.3. Biofouling

Seawater is a very aggressive medium that consists not only of corrosive elements but also a lot of micro- and macroscopic organisms which initiate the bio-corrosion or biofouling. The macroscopic organisms can be separated into groups: grass fouling or soft, such as seaweeds and red algae, and shell fouling or hard, for example, mussels, polyzoans, tubeworms. [73] The mechanism of biofouling includes four steps: conditioning, when organic particles adhere to the surface; attachment, when bacteria or diatoms attached; colonization, increasing the

population or microfouling; growth or macrofouling, which shown in Figure 2.47. The adsorbed organisms started to grow and form a biofilm matrix. [193]

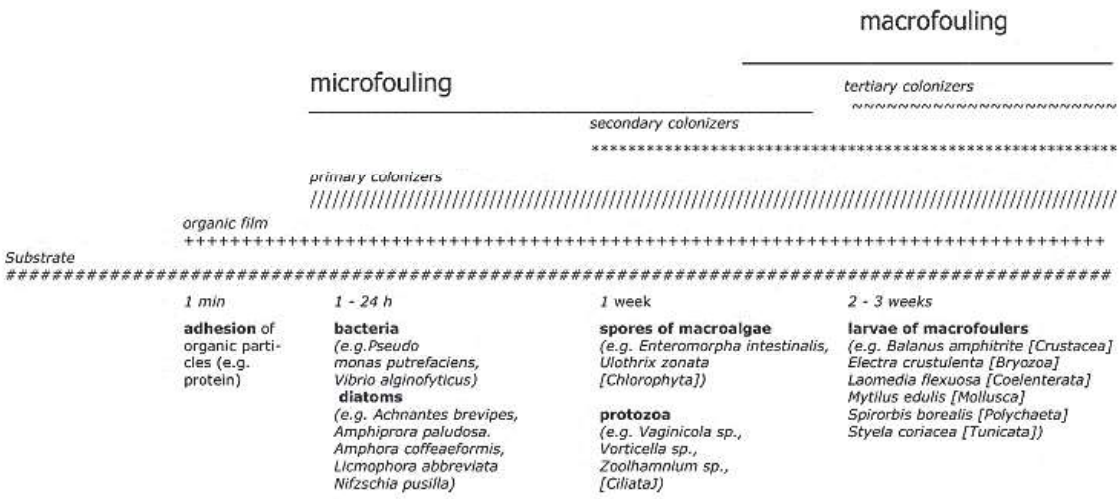


**Figure 2.47.** Schematic mechanism of biofilm growing. [194]

The growth of biofilm rate depends on the ocean biological spacemen variety. (Figure 2.48.) For example, the biofouling after 3 months around Tuticorin (India) is heavily fouled in comparison with the rod exposed near Florida (USA). [195]


**Figure 2.48.** Comparison of the fouling rate in USA and India. [195]

The classification of the additives preventing biofouling is described in Chapter 2.3.3. It is necessary to investigate the environment while designing the anti-biofouling coating and the substrate, which strongly affecting efficiency. (Figure 2.49.)

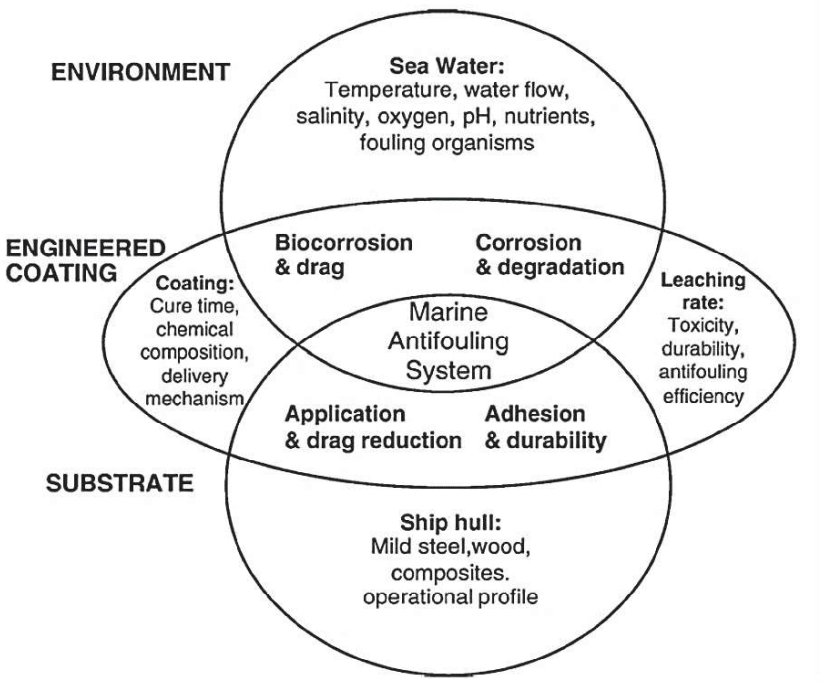


**Figure 2.49.** Key parameters affecting antifouling system. [196]

The efficiency of the optimal antifouling coating system is determined by the requirement listed in Table 2.13.

**Table 2.13.** Requirements for an optimal antifouling system. [193]

| Must be: | Must not be: |
|---|---|
| Anticorrosive | Toxic to the environment |
| Antifouling | Persistent in the environment |
| Environmentally acceptable | Expensive |
| Economically viable | Chemically unstable |
| Long life | A target for non-specific species |
| Compatible with underlying system | |
| Resistant to abrasion/biodegradation/erosion | |
| Capable of protecting regardless of operational profile | |
| Smooth | |

Two main methods are performed to control the fouling process: biocide release coating and fouling release coating. The mechanism of the biocide release

described in Figure 2.50. Released biocide kills or prevents the settling of the bio-organism. There are three main types of biocide release coating: contact paint or insoluble matrix paint, soluble matrix paint, and self-polishing copolymer coating. [197]

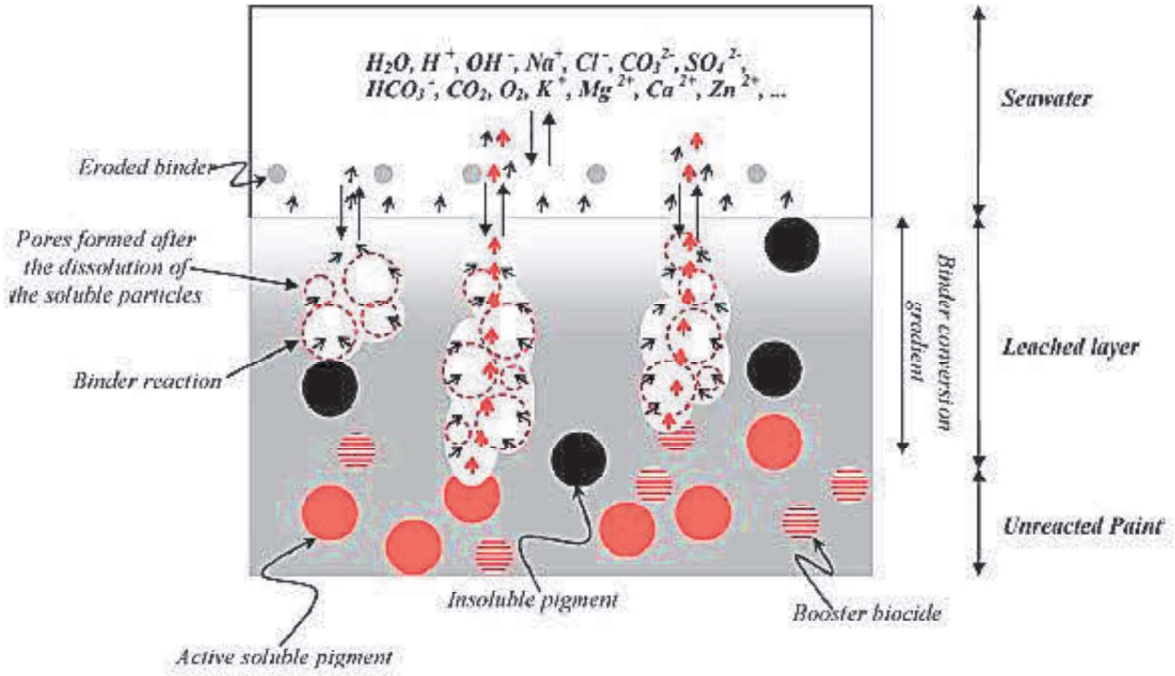


**Figure 2.50.** Schematic illustration of the biocide release mechanism. [198]

In early days, the main biocides for anti-biofouling coatings were cuprous oxide and/or organometallic compounds such as tributyltin fluoride (TBTF), tributyltin oxide (TBTO), or triphenyl tin fluoride (TPTF). [199] But tributyltin compounds are very toxic, and in 2003 International Maritime Organization ban on it, and the tin-free coating started to become popular. [200]

Foul release coating due to low surface energy minimizes the bio-organisms to fix to the surface. The surface of the coating is very smooth, and beyond the critical velocity of the ship (around 10-20 knot) allows for organisms to be dislodged. There are two main types of foul released coating based on fluoropolymer or silicone. [201] In 2010, Jotun paint company introduced silicone-based paint with foul release properties, and in 2012, International Marine Coating present fluoropolymer foul release coating with slime control. [202]

Currently, tin-free coatings are used such as controlled depletion paints, which same with soluble matrix paint but with tin-free biocides, and tin-free biocide-containing self-polished paint with zinc or silyl acrylate groups. [199] The modern approaches of anti-biofouling coatings are to create biocide-free antifouling paint with acceptable prices.

**References**

[1] D. Jones, *Principles and Prevention of Corrosion*, Macmillan Publ. Co. **1992**.

[2] M. G. Fontana, N. D. Greene, *Corrosion Engineering*, McGraw Hill Companies **1967**.

[3] C. P. Dillon, **1982**.

[4] P. R. Roberge, *Corrosion Engineering: Principles and Practice* **2008**.

[5] G. S. Frankel, in *Corros. Fundam. Testing, Prot. Vol 13A, ASM Handbook,* **2003**.

[6] U. J. Malo JM, Salinas V, *Mater. Perform.* **1994**, *33*, 63.

[7] F. MG, *Corrosion Engineering*, New York : McGraw-Hill **1986**.

[8] A. I. Asphahani, W. L. Silence, in *ASM Handb. Corros. Vol 13* **2003**.

[9] N. Singh, *Case Study on Some of the Major Corrosion Catastrophes in History* **2009**.

[10] R. M. Kain, in *ASM Handb. Corros. Vol 13* **1987**.

[11] R.G. Kelly, in *Corros. Fundam. Testing, Prot. Vol 13A, ASM Handbook,* **2003**.

[12] R. M. Kain, *Corros. 2000*. **2000**, *40*, paper no 00827.

[13] R. Baboian, S. L. Pohlman, in *ASM Handb. Corros. Vol 13* **1987**.

[14] ASTM International, *ASTM G82-98*. **2014**, 1–7.

[15] W. Glaeser, I. G. Wright, *ASM Handb. Corros. vol 13*. **1987**, 290–310.

[16] B. Chexal, J. Horowitz, B. Dooley, *Electr. Power Res. Inst.* **1998**.

[17] H. Pratikno, *Procedia Earth Planet. Sci.* **2015**, *14*, 41–46.

[18] R. Steigerwald, *ASM Handb. Corros. vol 13*. **1987**, 262–290.

[19] R. Parrington, in *ASM Handb. Fail. Anal. Prev. Vol 11*, Vol. 11 **2002**.

[20] R. H. Jones, in *ASM Handbook. Corros. Fundam. Testing, Prot. Vol 13A*

**2003**.

[21] S. A. Bradford, *Corrosion Control* **1993**.

[22] S. RW, in *Uhlig's Corros. Handb.*, Wiley-Interscience **2000**.

[23] P. R. Roberge, *Handbook of Corrosion Engineering*, The McGraw-Hill Companies, Inc. **2000**.

[24] A. J. Bard, L. R. Faulkner, *Electrochemical Methods : Fundamentals and Applications*, 2nd ed., JOHN WILEY & SONS, INC. **2001**.

[25] A. J. Bard, L. R. Faulkner, *Electrochemical Methods, Fundamentals and Applications*, 2nd ed. **2001**.

[26] R. Winston Revie, H. H. Uhlig, *Corrosion and Corrosion Control: An Introduction to Corrosion Science and Engineering* **2008**.

[27] R. BABOIAN, Ed. , *NACE CORROSION ENGINEER ' S REFERENCE Third Edition*, 3rd ed., NACE International **2002**.

[28] Dean, S. W., Jr., W. D. France, Jr., S. J. Ketcham, in *Handb. Corros. Test. Eval.* (Ed: W. H. Ailor), John Wiley **1971**.

[29] A. International, *ASTM G102-89*. **2015**, 1–7.

[30] D. W. Shoesmith, in *ASM Handbook, Corros. Fundam. Testing, Prot. Vol 13A,* ASM International **2003**.

[31] J. Kruger, in *Corros. Fundam. Testing, Prot. Vol 13A, ASM Handb.*, ASM International **2003**.

[32] ASM, *Corrosion: Fundamentals, Testing, and Protection*, Vol. 13A **2003**.

[33] A. International, *ASTM G3-14*. **2014**, 1–9.

[34] B. E. Wilde, E. Williams, *Electrochim. Acta*. **1971**, *16*, 1971–1985.

[35] B. E. Wilde, E. Williams, *J. Electrochem. Soc.* **2007**, *117*, 775.

[36] R. H. Heidersbach, in *ASM Handb. Corros. Vol 13* **2003**.

[37] H. BOHNES, G. FRANKE, in *CATHODIC Corros. Prot.*, Elsevier Science **1997**.

[38] W. von Baeckmann, W. Schwenk, W. Prinz, Editors, *Handbook of Cathodic Corrosion Protection*, Third ed., Gulf Professional Publishing **1997**.

[39] Z. Ahmad, in *Princ. Corros. Eng. Corros. Control*, Elsevier **2006**.

[40] D. W. Allen, M. D. Ames, in *Cathodic Prot.* (Eds: V. Ashworth, C. J. L.

Booker), Ellis Horwood **1986**.

[41] P. Natishan, in *ASM Handb. Corros. Vol 13*, ASM Handbook **1987**.

[42] H. Kaesche, *Corrosion of Metals. Physicochemical Principles and Current Problems* **2003**.

[43] C. E. Locke, in *Corros. Fundam. Testing, Prot. Vol 13A, ASM Handb.* **2003**.

[44] S. A. Bradford, in *Corros. Control* **1993**.

[45] J. OLEN L. RIGGS, C. E. LOCKE, *ANODIC PROTECTION: Theory and Practice in the Prevention of Corrosion*, Plenum Press **1981**.

[46] T. Xu, J. Li, *Chem. Eng. Mach*. **1996**, *23*, 80.

[47] V. Kuzub, V. Novitskiy, *Proc. Int. Congr. Met. Corros.* **1984**, *1*, 307–308.

[48] H. Leidheiser, *ASM Handb. Corros. vol 13*. **1987**, 857–862.

[49] P. R. Roberge, in *Handb. Corros. Eng.*, McGraw-Hill **1999**.

[50] G. Gece, *Corros. Sci.* **2011**, *53*, 3873–3898.

[51] V. S. Sastri, *Green Corros. Inhib.* **2011**, 139–166.

[52] S. A. Bradford, in *Corros. Control* **1993**.

[53] Z. Ahmad, in *Princ. Corros. Eng. Corros. Control* **2006**.

[54] P. Elliott, in *Corros. Fundam. Testing, Prot. Vol 13A, ASM Handb.*, ASM International **2003**.

[55] Z. Ahmad, in *Princ. Corros. Eng. Corros. Control* **2006**.

[56] S. A. Bradford, in *Corros. Control* **1993**.

[57] C. G. Munger, L. D. Vincent, in *Corros. Prev. by Prot. Coatings*, 3rd ed. **2014**.

[58] K. B. Tator, in *Corros. Fundam. Testing, Prot. Vol 13A, ASM Handb.* **2003**.

[59] P. a. Schweitzer, *Paint and Coatings - Applications and Corrosion Resistance* **2006**.

[60] J. Mazia, D. S. Lashmore, in *ASM Handb. Corros. Vol 13* **1987**.

[61] H. O. Pierson, *Corros. Vol 13, ASM Handb.* **1987**, 456–458.

[62] T. Mooney, in *Corros. Fundam. Testing, Prot. Vol 13A, ASM Handb.* **2003**.

[63] G. D. Maloney, in *Corros. Vol 13, ASM Handb.* **1987**.

[64] J. C. Oliver, D. D. Giese, J. F. Wright, in *Surf. Eng.*, Vol. 5 **1994**.

[65] W. W. Carpenter, *Surf. Eng.* **1994**, *5*, 469–481.

[66] Thomas W. Cape, in *ASM Handb. Corros. Vol 13* **1987**.

[67] G. Jernstedt, *Trans. Electrochem. Soc.* **1943**, *83*, 361–376.

[68] K. Ogle, M. Wolpers, in *Corros. Fundam. Testing, Prot. Vol 13A, ASM Handb.* **2003**.

[69] K. A. Korinek, in *ASM Handb. Corros. Vol 13* **1987**.

[70] R. G. Buchheit, A. E. Hughes, in *Corros. Fundam. Testing, Prot. Vol 13A, ASM Handb.* **2003**.

[71] H. Takahashi, in *Corros. Fundam. Testing, Prot. Vol 13A, ASM Handb.* **2003**.

[72] C. A. Grubbs, *Met. Finish.* **1999**, *97*, 476–493.

[73] A. M. Berendsen, *Marine Painting Manual*, Springer-Science+Business Media, B.V. **1989**.

[74] C. G. Munger, L. D. Vincent, in *Corros. Prev. by Prot. Coatings*, 3rd ed., NACE International **2014**.

[75] C. Stewart, in *ASM Handbook, Vol. 5B, Prot. Org. Coatings* **2015**.

[76] R. Lambourne, in *Paint Surf. Coatings - Theory Pract.* (Eds: R. LAMBOURNE, T. A. STRIVENS), Second edi ed., Woodhead Publishing Ltd **1999**.

[77] K. B. Tator, in *ASM Handb. Corros. Vol 13* **1987**.

[78] K. B. Tator, in *Corros. Fundam. Testing, Prot. Vol 13A, ASM Handb.*, ASM International **2003**.

[79] T. Oy, *Handb. Corros. Prot. Steel Surfaces by Paint.* **2012**, 1–76.

[80] P. A. Sørensen, S. Kiil, K. Dam-Johansen, C. E. Weinell, *J. Coatings Technol. Res.* **2009**, *6*, 135–176.

[81] K. B. Tator, in *Prot. Handbook, Vol. 5B, Prot. Org. Coatingsve Org. Coatings* **2015**.

[82] S. Liu, L. Gu, H. Zhao, J. Chen, H. Yu, *J. Mater. Sci. Technol.* **2016**, *32*, 425–431.

[83] M. J. Watkins, in *Paint Coat. Test. Manual, 15th Ed.* **2012**.

[84] K. B. Tator, in *Corros. Fundam. Testing, Prot. Vol 13A, ASM Handb.* **2003**.

[85] J. Bently, in *Paint Surf. Coatings - Theory Pract.* **1999**.

[86] HULL C G, S. J. H, in *Handb. Coatings Addit. Vol. 2* (Ed: C. LJ), M. Dekker **1987**.

[87] H. Q. Pham, M. J. Marks, *Ullmann's Encycl. Ind. Chem.* **2015**, 155–244.

[88] L. S. Salem, *J. Prot. Coatings Linings*. **1996**, *13*, 77–98.

[89] M. F. Montemor, *Surf. Coatings Technol.* **2014**, *258*, 17–37.

[90] F. Brusciotti, D. V. Snihirova, H. Xue, M. F. Montemor, S. V. Lamaka, M. G. S. Ferreira, *Corros. Sci.* **2013**, *67*, 82–90.

[91] J. J. Chrusciel, E. Lesniak, *Prog. Polym. Sci.* **2015**, *41*, 67–121.

[92] J. M. Yeh, H. Y. Huang, C. L. Chen, W. F. Su, Y. H. Yu, *Surf. Coatings Technol.* **2006**, *200*, 2753–2763.

[93] S. Ahmad, A. P. Gupta, E. Sharmin, M. Alam, S. K. Pandey, *Prog. Org. Coatings*. **2005**, *54*, 248–255.

[94] C. K. Tan, D. J. Blackwood, *Corros. Sci.* **2003**, *45*, 545–557.

[95] R. Arefinia, A. Shojaei, H. Shariatpanahi, J. Neshati, *Prog. Org. Coatings*. **2012**, *75*, 502–508.

[96] G. M. Spinks, A. J. Dominis, G. G. Wallace, D. E. Tallman, *J. Solid State Electrochem.* **2002**, *6*, 85–100.

[97] A. Mostafaei, F. Nasirpouri, *Prog. Org. Coatings*. **2014**, *77*, 146–159.

[98] G. Gupta, N. Birbilis, A. B. Cook, A. S. Khanna, *Corros. Sci.* **2013**, *67*, 256–267.

[99] A. Tale, P. Passiniemib, S. Yl, *Synth. Met.* **1997**, *85*, 1333–1334.

[100] G. Howarth, *Surf. coatings Int. part B coatings …*. **2003**, *86*, 111–118.

[101] Z. Ahmad, in *Princ. Corros. Eng. Corros. Control* **2006**.

[102] S. Reinstadtler, C. T. Williams, A. Olson, in *ASM Handbook, Vol. 5B, Prot. Org. Coatings* (Ed: K. B. Tator) **2015**.

[103] H. X. Xiao, J. V. Koleske, in *Paint Coat. Test. Man.*, 15th ed., ASTM International **2012**.

[104] A. International, *ASTM D16-00*. **2000**.

[105] D. K. Chattopadhyay, K. V. S. N. Raju, *Prog. Polym. Sci.* **2007**, *32*, 352–418.

[106] A. K. Sen, *COATED TEXTILES Principles and Applications* **2001**.

[107] P. Fibers, M. I. K. Ausch, B. Ag, *Ullmann's Encycl. Ind. Chem.* **2011**.

[108] M. Joshi, B. Adak, B. S. Butola, *Prog. Mater. Sci.* **2018**, *97*, 230–282.

[109] S. L. Bassner, C. R. Hegedus, *J. Prot. Coatings Linings*. **1996**, *13*, 52–65.

[110] H. Wei, D. Ding, S. Wei, Z. Guo, *J. Mater. Chem. A*. **2013**, *1*, 10805–10813.

[111] R. P. Socha, N. Pommier, J. Fransaer, *Surf. Coatings Technol.* **2007**, *201*, 5960–5966.

[112] C. Munger, *Corros. Prev. Contr.* **1994**, *41*, 140.

[113] K. B. Tator, in *ASM Handbook, Vol. 5B, Prot. Org. Coatings*, ASM International **2015**.

[114] K. Aramaki, *Corros. Sci.* **2002**, *44*, 1621–1632.

[115] M. Hara, R. Ichino, M. Okido, N. Wada, *Surf. Coatings Technol.* **2003**, *169–170*, 679–681.

[116] C. H. Hare, in *Prot. Coatings Fundam. Chem. Compos.* **1994**.

[117] A. G. Abel, in *Paint Surf. Coatings* **1999**.

[118] M. Kendig, *J. Electrochem. Soc.* **2006**, *144*, 3721.

[119] W. J. Clark, R. L. McCreery, *J. Electrochem. Soc.* **2002**, *149*, B379.

[120] E. McCafferty, *J. Electrochem. Soc.* **2006**, *137*, 3731.

[121] L. Veleva, in *Paint Coat. Test. Man.* (Ed: J. V. Koleske), Fifteenth ed. **2012**.

[122] B. Del Amo, A. R. Di Sarli, J. Lecot, J. J. Caprari, *Surf. Coatings Int. Part B Coatings Trans.* **2003**, *86*, 143–148.

[123] A. Kalendová, D. Veselý, J. Stejskal, M. Trchová, *Prog. Org. Coatings*. **2008**, *63*, 209–221.

[124] R. L. Ferguson, in *Paint Coat. Test. Man.* **2012**.

[125] J. H. Braun, in *Paint Coat. Test. Man.*, ASTM International **2012**.

[126] ASTM International, *ASTM D476-15*. **2015**, 1–3.

[127] ASTM International, *ASTM D209-12*. **2012**, 1–2.

[128] F. R. Spinelli, in *Paint Coat. Test. Man.* **2012**.

[129] P. A. Lewis, in *Paint Coat. Test. Man.* **2012**.

[130] P. Merchak, *Paint Coat. Test. Man.* **2012**, 215–233.

[131] R. A. Eppler, in *Paint Coat. Test. Man.* **2012**.

[132] W. S. Stoy, F. J. Washabaugh, in *Encycl. Polym. Sci. Eng.* (Ed: J. I. Kroschwitz), Wiley **1987**.

[133] R. Lambourne, in *Paint Surf. Coatings* **1999**.

[134] J. Stephen A. Yuhas, R. G. Montemayor, in *Paint Coat. Test. Man.*, ASTM

International **2012**.

[135] R. A. Jeffs, W. Jones, *Paint Surf. Coatings*. **1999**, 185–197.

[136] E. Stesikova, H. Plaumann, in *Paint Coat. Test. Man.* **2012**.

[137] TDS, *BYK-A 530 from BYK-Chemie GmbH*. **2016**.

[138] TDS, *Afcona - 2722 from AFCONA Addit.* **n.d.**

[139] TDS, *BYK ANTI-TERRA-203 from BYK-Chemie GmbH*. **2015**, 2.

[140] TDS, *AEROSIL ® 200 from Evonik Ind.* **2019**, 2.

[141] TDS, *BYK-9076 from BYK-Chemie GmbH*. **2019**, 1–4.

[142] TDS, *BYK-333 from BYK-Chemie GmbH*. **2012**, 1–4.

[143] J. H. Woodward, in *Paint Coat. Test. Man.*, ASTM International **2012**.

[144] P. Tan, L. G. Krauskopf, in *Paint Coat. Test. Man.*, ASTM International **2012**.

[145] A. Ghasemi-Kahrizsangi, J. Neshati, H. Shariatpanahi, E. Akbarinezhad, *Prog. Org. Coatings*. **2015**, *85*, 199–207.

[146] A. Ghasemi-Kahrizsangi, H. Shariatpanahi, J. Neshati, E. Akbarinezhad, *Appl. Surf. Sci.* **2015**, *353*, 530–539.

[147] A. Ghasemi-Kahrizsangi, H. Shariatpanahi, J. Neshati, E. Akbarinezhad, *Appl. Surf. Sci.* **2015**, *331*, 115–126.

[148] J. B. Donnet, *Carbon N. Y.* **1994**, *32*, 1305–1310.

[149] Y. H. Wei, L. X. Zhang, W. Ke, *Corros. Sci.* **2007**, *49*, 287–302.

[150] D. Balandin, Alexander A.Teweldebrhan, C. N. Lau, S. Ghosh, W. Bao, I. Calizo, F. Miao, *Nano Lett.* **2008**, *8*, 902–907.

[151] C. Lee, X. Wei, J. W. Kysar, J. Hone, *Science (80-. ).* **2008**, *321*, 385–388.

[152] Y. Su, V. G. Kravets, S. L. Wong, J. Waters, A. K. Geim, R. R. Nair, *Nat. Commun.* **2014**, *5*, 1–5.

[153] M. Rajabi, G. R. Rashed, D. Zaarei, *Corros. Eng. Sci. Technol.* **2014**, *50*, 509–516.

[154] M. Tong, Yao, Bohm, Siva, Song, *Austin J. Nanomedicine Nanotechnol.* **2013**, *1*, 1003.

[155] B. Ramezanzadeh, A. Ahmadi, M. Mahdavian, *Corros. Sci.* **2016**, *109*, 182–205.

[156] P. Haghdadeh, M. Ghaffari, B. Ramezanzadeh, G. Bahlakeh, M. R. Saeb, *J. Taiwan Inst. Chem. Eng.* **2018**, *86*, 199–212.

[157] B. Ramezanzadeh, P. Kardar, G. Bahlakeh, Y. Hayatgheib, M. Mahdavian, *J. Phys. Chem. C*. **2017**, *121*, 20433–20450.

[158] Z. Zhang, W. Zhang, D. Li, Y. Sun, Z. Wang, C. Hou, L. Chen, Y. Cao, Y. Liu, *Int. J. Mol. Sci.* **2015**, *16*, 2239–2251.

[159] C. Chen, S. Qiu, M. Cui, S. Qin, G. Yan, H. Zhao, L. Wang, Q. Xue, *Carbon N. Y.* **2017**, *114*, 356–366.

[160] B. Ramezanzadeh, S. Niroumandrad, A. Ahmadi, M. Mahdavian, M. H. Mohamadzadeh Moghadam, *Corros. Sci.* **2016**, *103*, 283–304.

[161] Z. Yu, H. Di, Y. Ma, Y. He, L. Liang, L. Lv, X. Ran, Y. Pan, Z. Luo, *Surf. Coatings Technol.* **2015**, *276*, 471–478.

[162] B. Ramezanzadeh, Z. Haeri, M. Ramezanzadeh, *Chem. Eng. J.* **2016**, *303*, 511–528.

[163] J. Li, J. Cui, J. Yang, Y. Li, H. Qiu, J. Yang, *Compos. Sci. Technol.* **2016**, *129*, 30–37.

[164] K. C. Chang, W. F. Ji, C. W. Li, C. H. Chang, Y. Y. Peng, J. M. Yeh, W. R. Liu, *Express Polym. Lett.* **2014**, *8*, 908–919.

[165] S. Liu, L. Gu, H. Zhao, J. Chen, H. Yu, *J. Mater. Sci. Technol.* **2016**, *32*, 425–431.

[166] C. H. Chang, T. C. Huang, C. W. Peng, T. C. Yeh, H. I. Lu, W. I. Hung, C. J. Weng, T. I. Yang, J. M. Yeh, *Carbon N. Y.* **2012**, *50*, 5044–5051.

[167] Y.-H. Yu, Y.-Y. Lin, C.-H. Lin, C.-C. Chan, Y.-C. Huang, *Polym. Chem.* **2014**, *5*, 535–550.

[168] K. Krishnamoorthy, K. Jeyasubramanian, M. Premanathan, G. Subbiah, H. S. Shin, S. J. Kim, *Carbon N. Y.* **2014**, *72*, 328–337.

[169] K. C. Chang, C. H. Hsu, H. I. Lu, W. F. Ji, C. H. Chang, W. Y. Li, T. L. Chuang, J. M. Yeh, W. R. Liu, M. H. Tsai, *Express Polym. Lett.* **2014**, *8*, 243–255.

[170] J. Han, in *Carbon Nanotub. Sci. Appl.* (Ed: M. Meyyappan) **2004**.

[171] R. Khorrampour, M. D. Esrafili, N. L. Hadipour, *Phys. E Low-Dimensional Syst. Nanostructures*. **2009**, *41*, 1373–1378.

[172] P. K. Shukla, P. C. Mishra, *Chem. Phys.* **2010**, *369*, 101–107.

[173] E. V. Butyrskaya, L. S. Nechaeva, S. A. Zapryagaev, *Comput. Theor. Chem.* **2016**, *1090*, 1–5.

[174] N. W. Khun, B. C. R. Troconis, G. S. Frankel, *Prog. Org. Coatings*. **2014**, *77*, 72–80.

[175] H. Jeon, J. Park, M. Shon, *J. Ind. Eng. Chem.* **2013**, *19*, 849–853.

[176] E. J. Petersen, T. Lam, J. M. Gorham, K. C. Scott, C. J. Long, D. Stanley, R. Sharma, J. Alexander Liddle, B. Pellegrin, T. Nguyen, *Carbon N. Y.* **2014**, *69*, 194–205.

[177] D. Song, Z. Yin, F. Liu, H. Wan, J. Gao, D. Zhang, X. Li, *Prog. Org. Coatings*. **2017**, *110*, 182–186.

[178] S. Park, M. Shon, *J. Ind. Eng. Chem.* **2015**, *21*, 1258–1264.

[179] B. E. Gu, C. Y. Huang, T. H. Shen, Y. L. Lee, *Prog. Org. Coatings*. **2018**, *121*, 226–235.

[180] M. Cui, S. Ren, S. Qiu, H. Zhao, L. Wang, Q. Xue, *Surf. Coatings Technol.* **2018**, *340*, 74–85.

[181] D. Liu, W. Zhao, S. Liu, Q. Cen, Q. Xue, *Surf. Coatings Technol.* **2016**, *286*, 354–364.

[182] International Organization for Standardization (ISO), **1998**.

[183] S. C. Dexter, in *ASM Handb. Vol. 13C Corros. Environ. Ind.*, Vol. 13C **2006**.

[184] L. La Que, *Protein Sci.* **1975**, *4*, 233.

[185] UNESCO, *UNESCO Tech. Pap. Mar. Sci.* **1966**, *4*.

[186] S. C. Dexter, in *Corros. Vol 13, ASM Handb.* **1987**.

[187] H. H. Revie, R.W, Uhlig, in *Corros. Corros. Control An Introd. to Corros. Sci. Eng.*, A JOHN WILEY & SONS, INC **2008**.

[188] H. H. Revie, R.W, Uhlig, *Corros. Corros. Control An Introd. to Corros. Sci. Eng.* **2008**, 383–398.

[189] R. Griffin, in *ASM Handb. Vol. 13C Corros. Environ. Ind.*, Vol. 13 **2006**.

[190] X. H. Wang, J. Li, J. Y. Zhang, Z. C. Sun, L. Yu, X. B. Jing, F. S. Wang, Z. X. Sun, Z. J. Ye, *Synth. Met.* **1999**, *102*, 1377–1380.

[191] A. M. Berendsen, in *Mar. Paint. Man.* **1989**.

[192] R. Lambourne, in *Paint Surf. Coatings* **1999**.

[193] L. D. Chambers, K. R. Stokes, F. C. Walsh, R. J. K. Wood, *Surf. Coatings Technol.* **2006**, *201*, 3642–3652.

[194] S. Abarzua, S. Jakubowski, *Mar. Ecol. Prog. Ser.* **1995**, *123*, 301–312.

[195] J. R. Matias, J. Rabenhorst, A. Mary, A. A. Lorilla, *Poseidon Sci. A Life Sci. Co. Discov. Nov.* **2003**, 1–7.

[196] L. D. Chambers, F. C. Walsh, R. J. K. Wood, K. R. Stokes, in *ICMES Proceedings, Inst. Mar. Eng. Sci. Technol.* **2006**.

[197] *Fish. Occas. Publ. No. 55*. **2009**, 1–24.

[198] D. M. Yebra, S. Kiil, K. Dam-Johansen, *Prog. Org. Coatings*. **2004**, *50*, 75–104.

[199] E. Almeida, T. C. Diamantino, O. de Sousa, *Prog. Org. Coatings*. **2007**, *59*, 2–20.

[200] M. Champ, *Proc. 24th UJNR Mar. Facil. Panel Meet.* **2001**, 1–7.

[201] R. F. Brady Jr, *Prog. Org. Coatings*. **2001**, *43*, 188–192.

[202] C. G. Munger, L. D. Vincent, in *Corros. Prev. by Prot. Coatings (3rd Ed.* **2014**.

# Chapter 3

# Experimental Methods

*In this chapter, the chemicals used in the synthesis of carbon nanomaterials and the preparation of the coating film were listed. The methodology of the synthesis of the catalyst for the carbon nanotubes obtained was described. The procedure of the synthesis of cylindrical and conical carbon nanotubes and graphene oxide, as well as nitrogen-doped carbon nanotubes and nitrogen-doped graphene oxide, was reported, and the steps in the application of the coating were specified. The coating film was degraded using different ways of degradation, such as degradation under ultraviolet radiation, immersion degradation, and weathering degradation. The methods used for the characterization of the carbon-based pigments and coating film before and after degradation were listed in the last part of the chapter.*

.

## 3.1. Materials and Chemicals

Materials for the carbon nanomaterials synthesis: cobalt nitrate hexahydrate (≥99.9%, Merck); magnesium nitrate hexahydrate (≥99.9%, Merck); ammonium molybdate tetrahydrate (≥99.9%, Merck); iron (III) nitrate nonahydrate (≥99.9%, Merck); nickel (II) acetylacetonate (≥99%, Merck); citric acid (≥98%, Merck); glycine (≥99%, Merck); benzene (>99.9%, Merck); hexane (>97%, Sigma Aldrich); acetonitrile (99%, Sigma Aldrich); hydrogen (A.C.S.); nitrogen (A.C.S.); hydrochloric acid (37%, Schedelco); natural graphite (Alfa Aesar); sulphuric acid (99.99% Sigma Aldrich); potassium permanganate (Sigma Aldrich); hydrogen peroxide (33%, technical, VWR).

Materials for the polymer synthesis and coating characterization: bisphenol A diglycidyl ether (Sigma Aldrich); diethylenetriamine (DETA) (99%, Sigma Aldrich); sodium chloride (BioXtra, ≥99.5% (AT) Sigma Aldrich); stainless steel 316L 2B (Hong Hock Hardware PTE. LTD) (Table 3.1.) Silicon carbide abrasive paper with 800, 1200, and 2000 grit (Sui Sun.Co.LTD) were used to polish the stainless steel sample before coating.

Ultra-pure deionized water (obtained at 18 MΩ cm) and ethanol (99.86%, Sigma Aldrich, with 5% methanol) were used throughout the experiment.

**Table 3.1.** Composition of stainless steel 316L 2B. (Error%) TDS from Hong Hock Hardware PTE. LTD

| C,10% | Si,10% | S,25% | P,10% | N,10% | Mn,15% | Cr,5% | Fe,15% | Ni,25% | Mo,25% |
|---|---|---|---|---|---|---|---|---|---|
| 0.019 | 0.39 | 0.003 | 0.028 | 0.029 | 1.75 | 17.4 | 68.251 | 10.1 | 2.02 |

Platinum sheet (Pt sheet,1 $cm^2$), saturated calomel electrode (SCE-6802) (Rex Electric Chemical, Shanghai), and the electrochemical workstation (CHI 760D) (Shanghai Chenhua instrument co., LTD) was used for electrochemical measurements. The PTFE magneton and magnetic stirring apparatus (Heidolph MR.Hei.Standard) were used for the realization of the homogeneous solution.

## 3.2. Synthesis

In this chapter, the methodology of the synthesis of carbon-based materials: cylindrical, conical, and nitrogen-doped carbon nanotubes, graphene oxide, and nitrogen-doped graphene oxide are described. The application of the coating film is detailed in Chapter 3.2.5.

### 3.2.1. Synthesis of Catalyst for Obtaining Cylindrical and Nitrogen-doped Carbon Nanotubes

Solution of 35.1g (0.468 mol) $NH_2CH_2COOH$ and 44.9g (0.234 mol) citric acid in 50ml DIW was poured to the mixture of 200g (0.78 mol) Mg(NO3)2*6H2O, 45.39g (0.156 mol) $Co(NO_3)_3*9H_2O$, 60.84 (0.156 mol) $Fe(NO_3)_3*9H_2O$ and 0,16g (0.00039 mol) $(NH_4)_2Mo_2O_7*4H_2O$ with constant mixing. After that homogeneous mixture was dried in the oven at 200 ºC for 4 hours and then was burned at 500 ºC for 5 hours. [1]

This catalyst was used for the synthesis of cylindrical and nitrogen-doped carbon nanotubes.

### 3.2.2. Synthesis of Carbon Nanotubes

Carbon nanotubes were synthesized using the quartz reactor placed in a TZF 12/100/900 three-zone pipe furnace (Carbolite, Great Britain). as shown in Figure 3.1. in different modes: ultrasonic spraying of the catalyst solution in the organic solvent in the reaction tube (for conical carbon nanotubes); gas permeation through the organic solvent and CVD synthesis using a catalyst (for cylindric and nitrogen-doped carbon nanotubes). [2]

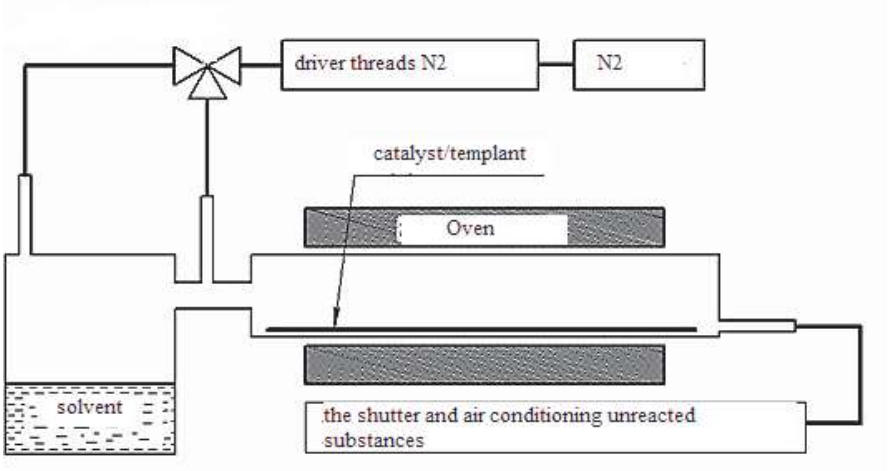


**Figure 3.1.** Reactor for synthesis of carbon nanotubes.

The main element of the equipment is the reactor – quartz tube with an inner diameter of 50mm and length of 1.2m. The catalyst was placed inside the tube. The heating was conduct at a nitrogen flow of 200ml/min which was regulated with a gas flow controller (Meta-Chrom, Russia), after reaching the temperature of synthesis, the required gas was turned on. Since the end of synthesis, heating was turned off, and nitrogen flow was turned on till the room temperature of the reactor. The synthesis conditions of carbon nanotubes are shown in Table 3.2.

The resulting carbon nanotubes were purified from impurities by boiling in 10% hydrochloric acid solution followed by washing with deionized water and drying at 120°C for 24 h in a vacuum dryer (Tula-Term, Russia). The unstructured carbon impurities were removed by annealing in air at 350°C for 3 h.

**Table 3.2.** Synthesis condition of carbon nanotubes.

| Name of the sample | Catalyst | Organic solvent | Temperature of the synthesis, ºC | Time of the synthesis | Gas, ml/min |
|---|---|---|---|---|---|
| CNT cylindric | $MgCo_{0.2}Mo_{0.01}O$ | hexane | 730 | 6 | $H_2$, 500 |
| CNT conical | $Ni(acac)_2$ | benzene | 620 | 5 | $H_2$, 500 |

| | | | | | |
|---|---|---|---|---|---|
| N-CNT | $MgCo_{0.2}Mo_{0.01}O$ | acetonitrile | 800 | 5 | $N_2$, 500 |

### 3.2.3. Synthesis of Graphene Oxide (GO)

Natural graphite (5g) was added into the glass flask with 200 mL of $H_2SO_4$ and stirred for an hour at room temperature. After cooling the mixture in the ice bath, 25g of $KMnO_4$ was slowly (over 1-2 hour) poured with continuous stirring at room temperature overnight. Using dropping funnel 200 mL of $H_2O$ was supplemented, and at the end, $H_2O_2$ was added until no gas was released. Then the solution was centrifuged twice and put into the dialysis bag and dialysis until pH = 4-5. Finally, the GO was taken out and ultrasonicated for 3 hours. [3]

The concentration of GO solution was 9.8mg/mL

### 3.2.4. Synthesis of Nitrogen-doped Graphene Oxide (N-GO)

A total of 300mg of melamine was dispersed in 20mL of DIW, and then the resulting solution was added into 30,6 mL of concentrated GO solution (the melamine to GO mass ratio is 1:1). (Figure 3.2.) The mixture was ultrasonicated until the melamine powder was evenly mixed in the dispersion. The mixture was freeze-dried to obtain a GO/melamine powder. Then it underwent thermal annealing at 430ºC in the air for 3 hours. [4]

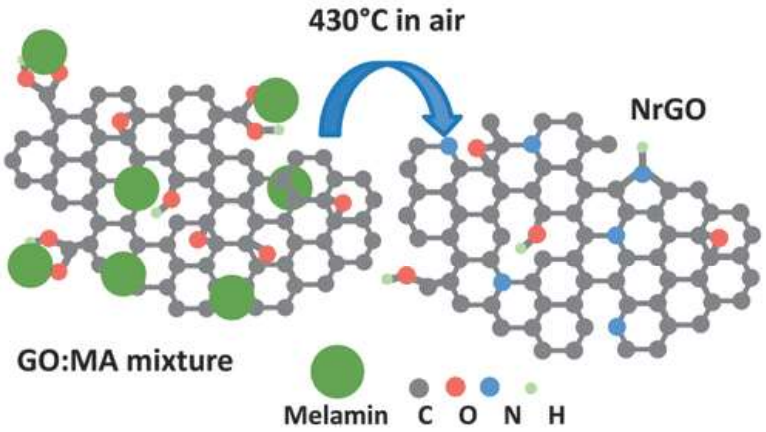


**Figure 3.2.** Schematic diagram of synthesis of nitrogen-doped graphene oxide [4]

### 3.2.5. Preparation of Carbon-based Nanomaterials – Epoxy Composite

In the beaker 5ml of bisphenol A diglycidyl ether and 0,05 wt% of the carbon nanomaterials were added, stirred using a glass rod and ultrasound for 4 hours, then placed overnight to the vacuum oven at 70 ºC 93,3kPa to eliminate the presence of water and air in the paint. DETA with 10% in excess was added to the paint and stirred for 15 min.

The stainless steel samples 10cm×10cm were washed with the soap to remove the oils and dust, washed with acetone and ethanol and dry in the oven at 40 ºC, then was gritted with abrasive paper 800, 1200, and 2000 grit and rinsed off with ethanol. The coating was applying by the wire-wound rod (BYK) 100 μm thickness. The samples were drying in the convection oven at 60 ºC for 12 hours. The thickness of the coating was measured using Mitutoyo IP65 (C/N 293-340-30) with an error 0.001mm.

## 3.3. Simulation of the Degradation

As described in the Chapter 2.5., different factors affect the coating, such as moisture, ultraviolet radiation, salinity, temperature, etc. The simulation experiments predict coating behavior under certain conditions.

### 3.3.1. Ultraviolet Radiation Degradation

One-part of the samples were exposed under ultraviolet (UV) radiation. The UV lamps (UVA-340) (Shenzhen Guanhongya Optoelectronic Technology Co, Ltd) with a length of 1200cm and a pick wavelength of 340 nm (Figure 3.3.a.), were used to simulate direct solar UV radiation. The UV lamps were placed under the tested samples 20 cm above. (Figure 3.3.b.) Degradation of the coating under UV was analyzed after 1000 hours of exposure. Temperature and humidity in the test condition were selected as 21 ± 2 ºC and 55 ± 2 % RH, respectively.

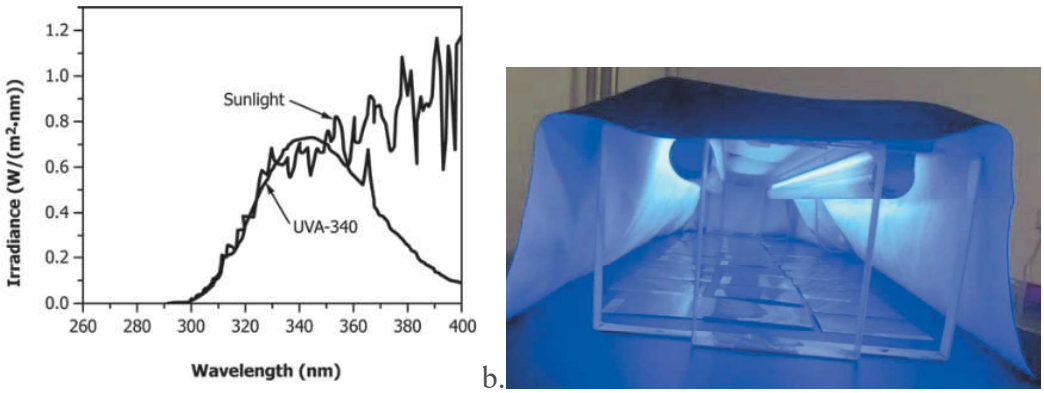


a. b.

**Figure 3.3.** a. Spectral power distribution of UVA-340 lamp and sunlight [5]; b. experimental procedure.

The effect of the ultraviolet radiation is significant because the epoxy resin degrades under it. [6] The mechanism of the degradation is described in Figure 3.4.a. The degradation starts with methyl-group, which reacts with oxygen to form the acetyloxyl radical ($CH_3COO\cdot$). The step Figure 3.4.b.(3) shows the attack of the hydroxyl-group by acetyloxyl radical. The acetic acid obtained on the previous reaction degrade under the light and react to form carbonyl (Figure 3.4.b.(5))

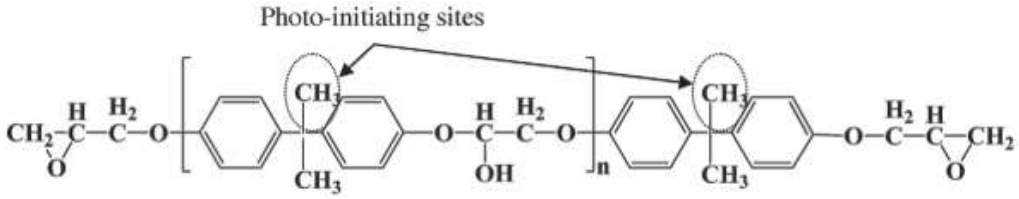


a.

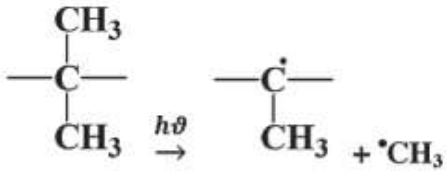

b. (1)



(2)

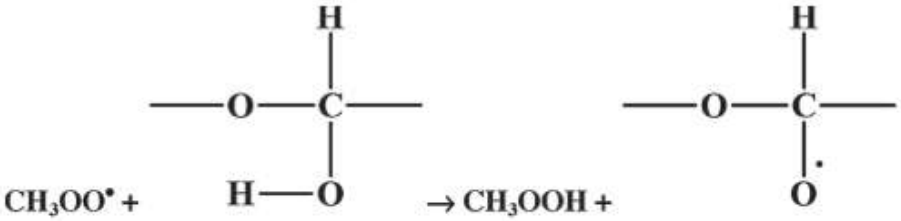

(3)

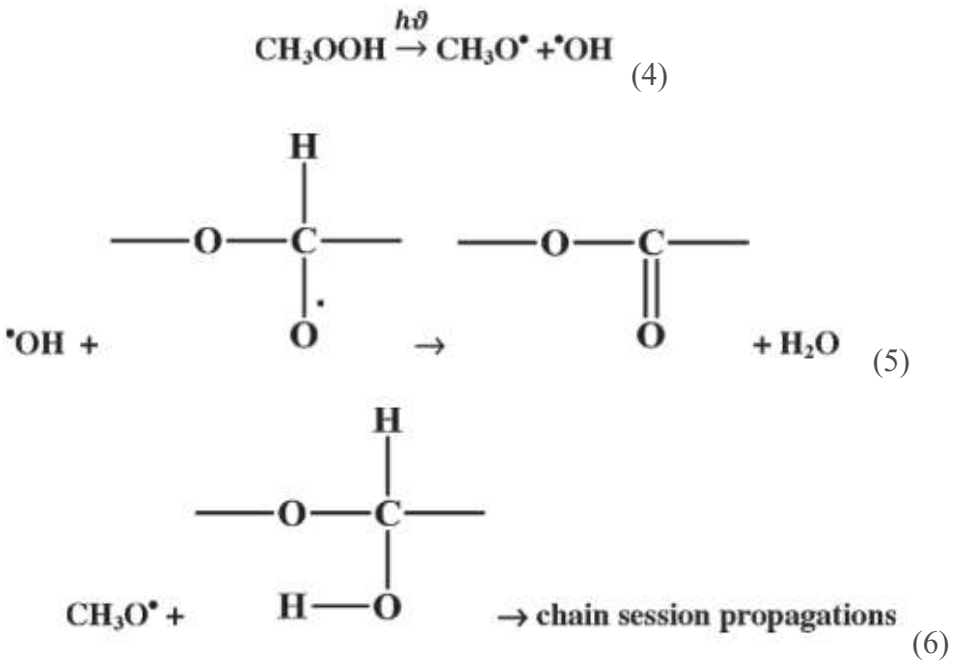


**Figure 3.4.** a. Initiating of the epoxy resin degradation; b. (1-6) Steps of epoxy degradation. [7]

To analyze the degree of coating degradation, the carbonyl index was calculated regarding the following equation: [8]

Carbonyl index = Absorbance $I_{1720}$/ Absorbance $I_{2925}$

Where $I_{1720}$ – absorbance intensity of carbonyl bond peak at 1720 $cm^{-1}$; $I_{2925}$ – absorbance intensity of methyl bond at 2925 $cm^{-1}$. The absorbance intensity was calculated from transmittance intensity:

Absorbance Intensity = -Log(Transmittance intensity).

### 3.3.2. Immersion Degradation

Immersion test of the coating film was performed to simulate the effect of salted water. The samples were placed in the 3.5 % NaCl solution at 23±2ºC for 1000 hours. The uncoated steel was protected from the degradation with 3M tape. The samples were weight before and after the test to calculate the water intake during the immersion using the following equation:

$$m_{intake} = m_{before} - m_{after}$$

### 3.3.3. Weathering Degradation

The weathering degradation was performed in the UV Test chamber (Atlas Material Testing Technology Ltd.) based on the standard BS EN ISO 11507. The test carries for 125 cycles, equal to 1000 hours. One cycle consists of two parts: irradiation (dry) phase at 60±3ºC for 4 hours and condensation phase at 50±3ºC for 4 hours. [9] The scheme of the equipment used is shown in Figure 3.5.

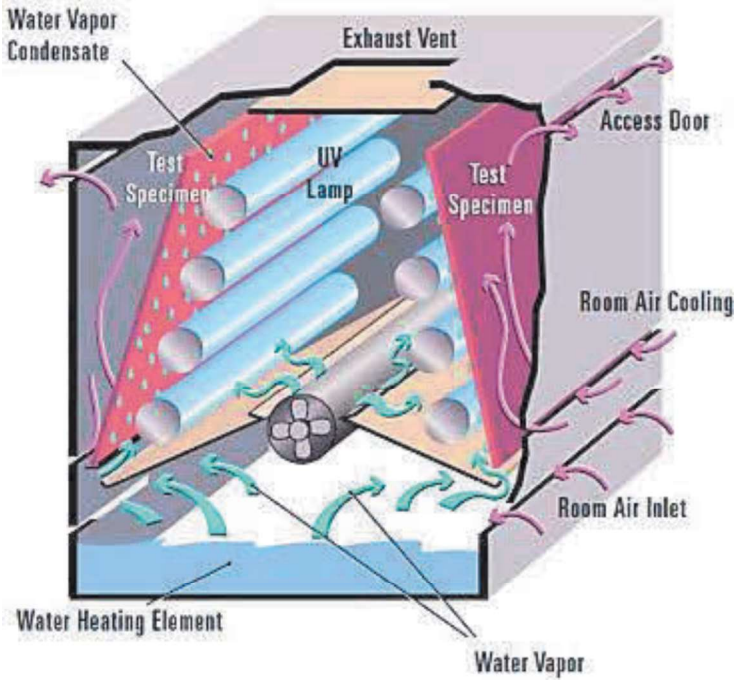


**Figure 3.5.** Schematic illustration of the ATLAS UV test chamber. [10]

## 3.4. Materials Characterization

Different analyses were carried out to characterize the carbon-based materials and coating film before and after degradation. The surface properties, chemical composition, and mechanical properties were investigated

### 3.4.1. Electrochemical Measurements

Electrochemical properties were tested using the coating cell (Bio-Logic Science Instruments) and 1470E multi-channel potentiostat (Solartron Analytical) with a three-electrode system in 3,5% NaCl solution. Coated metal electrode, Pt sheet and SCE in 0,1KCl (E(25ºC) = 0.334V) [11] acted as working electrode (WE),

auxiliary or counter electrode (CE), and reference electrode (RE), respectively. The area of the working electrode was 1cm$^2$. (Figure 3.6.)

These three electrodes, WE, CE and RE, formed two circuits in the electrolyte: one consists of WE and RE, which can be assumed as an open circuit, the RE with constant potential is used to determine the electrode potential of WE. The other one consists of WE and CE, the CE being used to realize the electrochemical reaction equilibrium in an electrolytic cell, as the redox reaction happens at two relative electrodes. RE is just a reference of potential for WE and the CE matches, WE used to obtain the electrochemical characteristics of WE materials. Pt sheet was chosen as CE for its good chemical stability and the SCE as RE for its negligible potential change during the test.

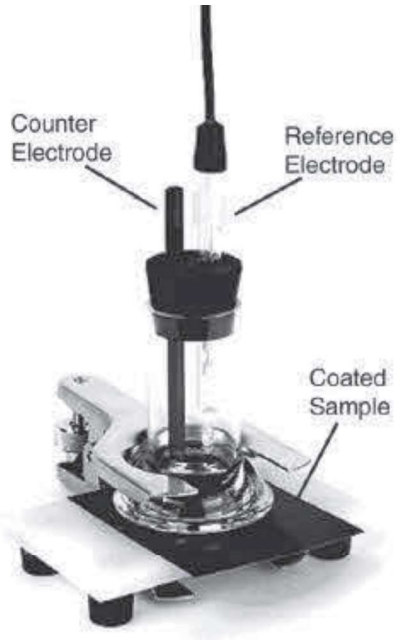


**Figure 3.6.** Cell for the electrochemical testing of the coating. [12]

Potentiodynamic polarization experiment is effective technique for the analysis of corrosion characteristics. (Chapter 2.1.3) The corrosion rate was calculated from the Tafel plot which was measured after stabilizing of open circuit potential (OCP) with the fluctuation less than 2mV in 1000s, the scanning rate of the testing was 0.1 mV/s and measurements were carried out from OCP to +1.2V (vs. OCP).

The electrochemical impedance spectroscopy (EIS) is a powerful technique to analyze coating degradation. The electrochemical measurements were carried out after stabilizing OCP with the fluctuation of less than 2mV for 1000s at OCP with potential amplitude 5mV and frequencies from $10^{-1}$ to $10^{6}$Hz.

Figure 3.7. shows the common equivalent circuit to analyze the coating degradations. There are four sectors in the model: electrolyte (the resistance of the electrolyte ($R_u$) between WE and RE), coating (coating capacitance ($C_{coating}$) which depends only on the total sample area and coating pore resistance ($R_{pore}$)), corrosion reaction (polarization resistance ($R_p$) and double layer electrode capacitance ($C_{dl}$) of the delaminated area), and metal (stainless steel working electrode). [13] The capacitor element could be changed to the constant phase element (CPE) [14] to fit the non-ideal capacitor. The constant phase element defined accordingly the equation below, and when n = 1 it is ideal capacitor, n = 0.5 it is Warburg element, n = 0 it is resistance, n = -1 it is inductance: [15]

$$Q_{CPE} = \frac{1}{Y_0(j\omega)^n}$$

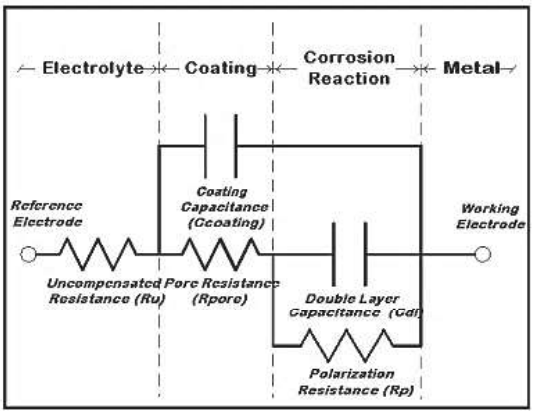


**Figure 3.7.** Equivalent circuit for impedance behavior of the polymer-coated metal. [16]

However, there are several steps of coating degradation and the equivalent circuit changes. If the coating is not damaged, it has excellent barrier properties, and coating resistance is very high. Therefore, the Nyquist plot does not have a lot of the information, and the Bode plot shows a straight line with high impedance at low frequency. At the second step, (Figure 3.8.b.) the water absorption takes place, and

the water intake could be calculated from changing the capacity value based on the equation: [17]

$$Volume(H20) = \frac{log\frac{C_t}{C_0}}{\log \varepsilon_w}$$

Where $C_t$ – coating capacitance at time t; $C_0$ – initial coating capacitance; $\varepsilon_w$ – dielectric constant of water – 80. The Nyquist and Bode plots haven't changed at this step.

Figure 3.8.c. shows the semicircle that corresponds to the penetration of the electrolyte to the metal surface, and the value of pore resistance is lower in comparison with the initial. The last two stages corresponded to the corrosion process on the metal surface, initiation, and coating damage step, respectively. Furthermore, the equivalent circuit changed to the two-time constants. (Figure 3.8.d and e.) The small semicircle corresponds to the coating capacitance, and semicircle at lower frequency is due to the double-layer capacitance.

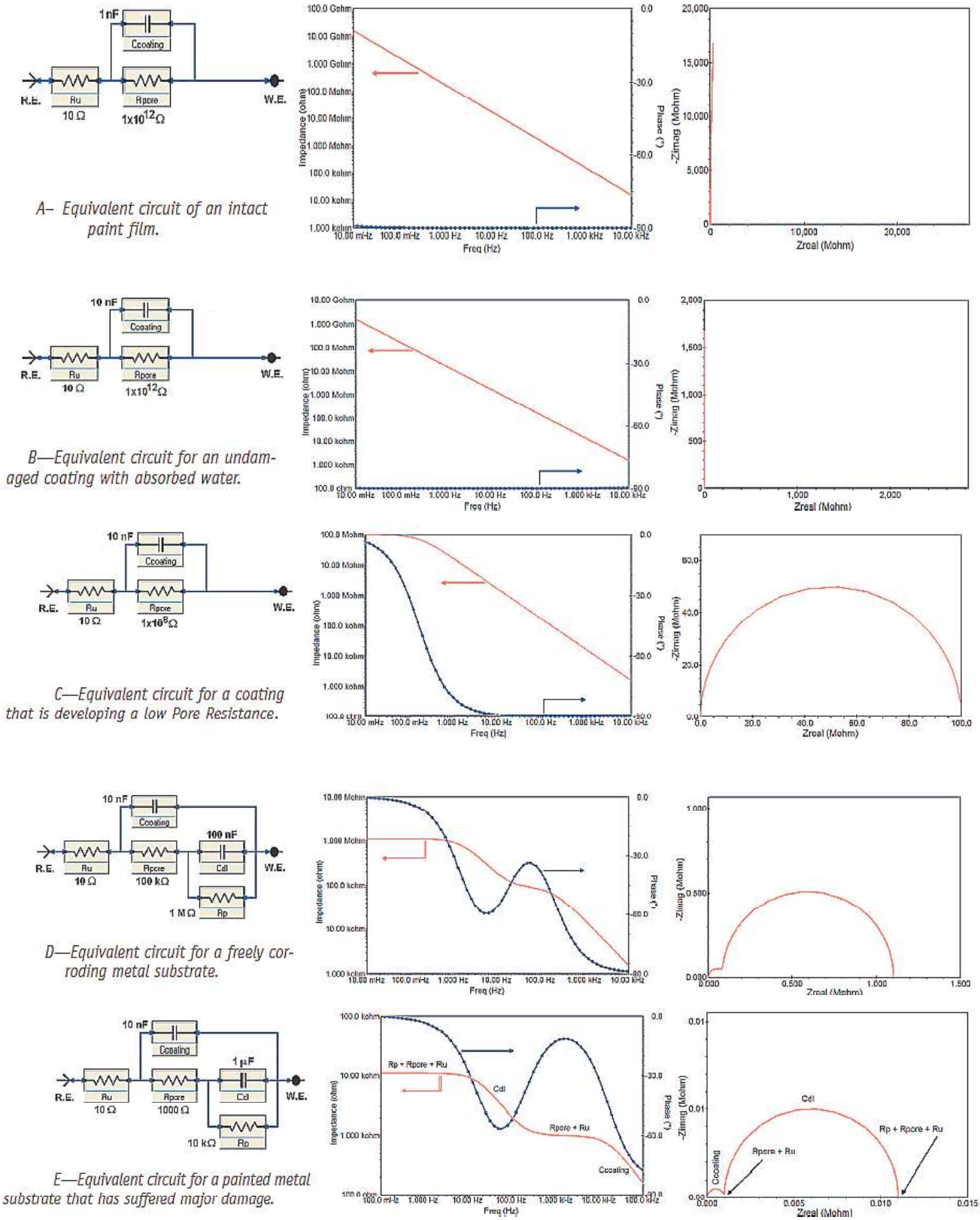


**Figure 3.8.** Equivalent circuit, Niquist and Bode plote for five stages of the coating degradation. [18]

### 3.4.2. Calculation of the Corrosion Characteristics

Corrosion normally occurs at the rate determined by an equilibrium between anodic and cathodic reactions. Figure 3.9. describes this process. The straight lines represent the theoretical current for the anodic and cathodic reactions. The $i_0$ and β–coefficient can be estimated using the Tafel equation:

$$E = bLog\, i + a\,,$$

Where $a = -\left(\frac{RT}{\alpha nF}\right) Ln\, i_0$, and $b = 2{,}3(\frac{RT}{\alpha nF})$

The pink line is the total current of the cathodic and anodic currents. The sharp point determined the corrosion current and where the reaction changes from cathodic to anodic.

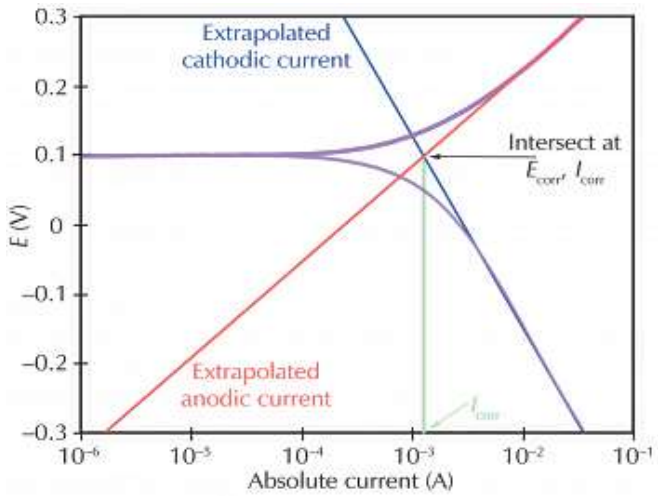


**Figure 3.9.** Tafel analysis. [19]

Once $I_{corr}$ and $E_{corr}$ are obtained we could calculate the corrosion rate of the metal. The corrosion rate in mm/yr can be calculated using formula [20]:

$$r = \frac{K \times i_{corr} \times EW}{\rho}$$

Where K – constant $3.27\times10^{-3}$, mm g/μA cm yr; ρ – density of the metal or alloy in g/cm$^3$, the density of the stainless steel 316L = 7.98 b/cm$^3$ [21]; $i_{corr}$ – corrosion current density in μA/cm$^2$; EW – equivalent weight.

The equivalent weight for the alloy could be calculated by the formula:

$$EW = \frac{1}{\sum \frac{n_i f_i}{W_i}}$$

Where $f_i$ is the mass fraction of the $i^{th}$ element in the alloy; $W_i$ – the atomic weight of the $i^{th}$ element in the alloy; $n_i$ – valence of the $i^{th}$ element. The equivalent weight for stainless steel 316L is 25.5. [20]

### 3.4.3. Carbon-based Materials Characterization

***Scanning Electron Microscope***

Materials morphology was studied by scanning electron microscope (SEM) (JEOL JSM-6390LA with an accelerating voltage of 20-25 kV). For analysis, a small amount of the sample (less than 1 mg) was applied to the conductive tape, located on the polished aluminum substrate was placed in the microscope camera. The camera was evacuated to a residual pressure of $10^{-4}$ Pa. The samples were exposed to the electron beam with the energy of the primary electrons of 10 kV. The focal distance of the electron beam was changed in a range from 5 to 15 mm.

***X-ray Photoelectron Spectroscopy***

XPS is widely used for the measurement of the chemical composition, valence state on the surface of the carbon nanomatreials, which is reflected in binding energy. As each element has its own unique binding energy peaks, it is easy to identify the elemental composition. XPS was performed on Axis Ultra DLD† spectrometer (Kratos Analytical Ltd). Monochromatic X-ray radiation of AlKα (1486.7 eV) was used. The spectra were obtained in constant transmission energy equal to 160 eV for the overview of the spectrum and 20eV for individual lines. The content of the elements was determined using the sensitivity factors of the manufacturer of the spectrometer. The decomposition into components was carried out using the programs CasaXPS and Unifit 2006.

***Elemental analysis***

Elemental analysis on C, H, N was carried out on a Vario MicroCube† instrument (Elementar Analysensysteme GmbH). 2-5 mg of the sample placed in a tin boat was burned in the analyzer at 1150°C in an $O_2$ / He atmosphere in C, H, N - mode. Separation of combustion products of $CO_2$, $H_2O$, and $N_2$ was carried out by the method of temperature-programmed desorption from the adsorption column with the subsequent analysis of the gases with a katharometer ($CO_2$, $H_2O$, and $N_2$). The sulfanilic acid was used as a standard.

***Thermal gravimetric analysis***

Thermal gravimetric analysis (TGA) was carried out for the carbon nanotubes sample to check the presence of the impurities such as catalyst using Jupiter STA 449 PC (Netzsch). The sample around 10 – 20 mg was placed into the alund crucible and heated in the mix of air and argon atmosphere with rate 10$^{o}$C/min, with flow rate 40ml/min and 20ml/min, respectively. The results were processed in "NETZSCH-analysis" program.

### 3.4.4. Coating Film Characterization

***Scanning Electron Spectroscopy***

Surfaces of the coatings were analyzed by field emission scanning electron microscope FESEM JSM-6340F (JEOL Ltd). Before the analysis, samples were coated with the gold using JFC-1600 auto fine coater (JEOL Ltd) at the current of 20mA for 15 seconds. Then samples were exposed by the electron beam with a primary electron energy of 5kV.

***Fourier Transform Infrared Spectroscopy***

Chemical degradation was assessed by Fourier transform infrared spectroscopy with attenuated total reflection (FTIR-ATR) using a ZnSe prism with Frontier MIR Spectrometer† (PerkinElmer Inc.). Samples were analyzed in the infrared region of 600 cm-1 – 4000 cm-1and all spectra were the average of 32 scans

and repeated for at least 3 times. The background for FTIR spectra was plain polished SS.

### *Adhesion*

The adhesion test was carried accordingly ASTM D3359-17 standard. The six horizontal and six vertical cuts with 1mm apart were made by sharp knife and length 20mm. The adhesion tape 3M Scotch 600 were applied for 90 ± 3 second and rapidly removed with angle closer to 180º. The rate of the adhesion was measured accordingly the scale illustrated in Figure 3.10.

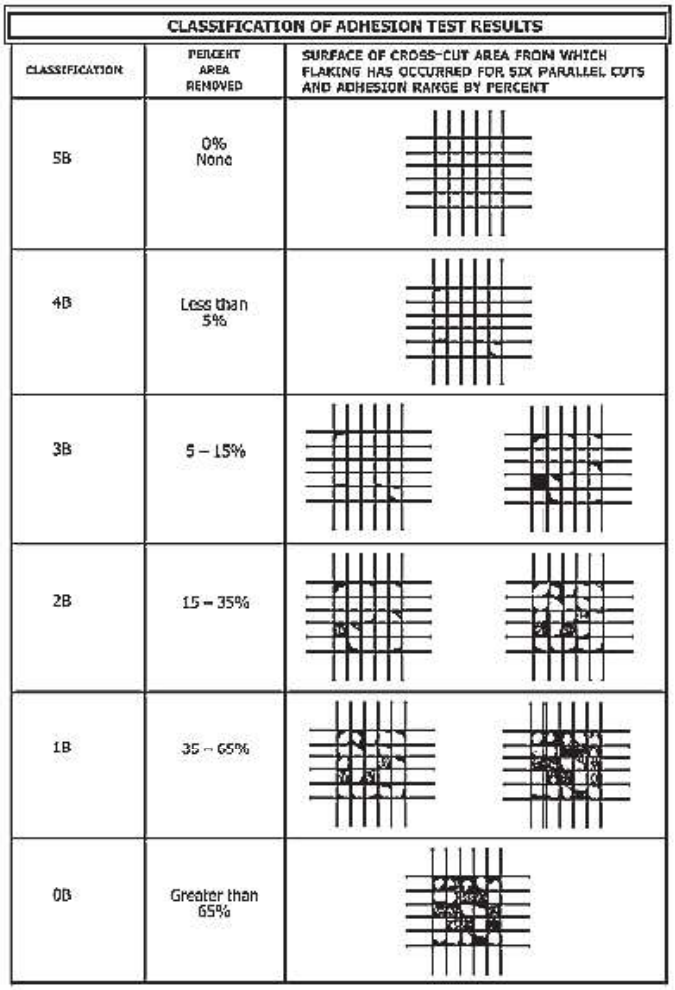


**Figure 3.10.** Classification of adhesion test results. [22]

***Hardness test***

Standard test to determine the hardness of the polymer coating film by pencil test, Derwent Academy (ACCO UK Ltd) pencils were used with hardness from 6B to 5H. The wood was removed for 5-6 mm and make the flat smooth cylinder free of chips or nicks by rubbing against the abrasive paper at the angle of 90º, as shown at Figure 3.11. The pencil held at 45º to the metal surface.

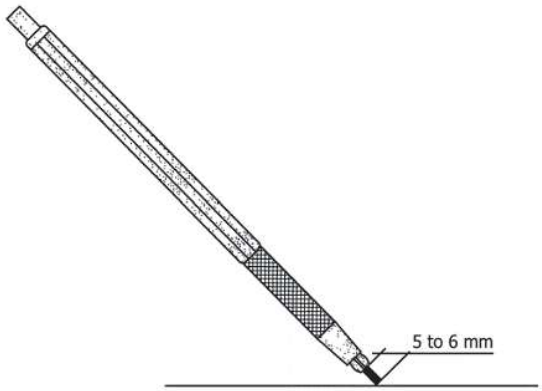


**Figure 3.11.** Procedure of hardness by pencil. [23]

The hardness scale of the pencil shown in Figure 3.12. To determine the gouge hardness, the pencil should be chosen, which will not cut through the film to the substrate for a distance of at least 3mm; the pencil which does not either cut through nor scratch the surface film, determine the scratch hardness.

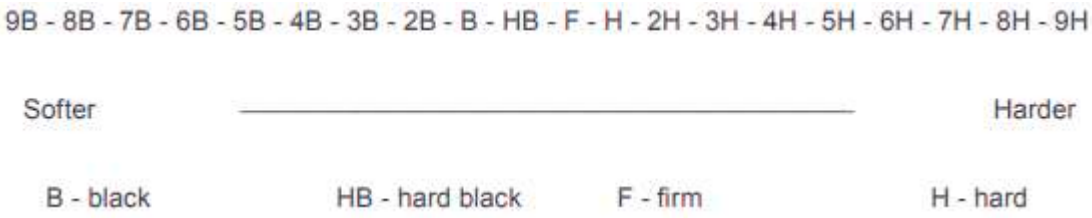


**Figure 3.12.** Hardness scale for wood pencil. [24]

**References**

[1] R. R. Bacsa, W. S. Bacsa, C. Laurent, A. Peigney, E. Flahaut, *J. Mater. Chem.* **2004**, *14*, 646.

[2] E. G. Rakov, *Russ. Chem. Rev.* **2000**, *69*, 35–52.

[3] S. J. R. H. R. E. O. William, *J. Am. Chem*. **1958**, *80*, 1339–1339.

[4] D. Du, P. Li, J. Ouyang, *ACS Appl. Mater. Interfaces*. **2015**, *7*, 26952–26958.

[5] A. International, *ASTM G154-16,*. **2016**, 1–11.

[6] A. Tcherbi-Narteh, M. Hosur, E. Triggs, S. Jeelani, *Polym. Degrad. Stab.* **2013**, *98*, 759–770.

[7] A. Ghasemi-Kahrizsangi, J. Neshati, H. Shariatpanahi, E. Akbarinezhad, *Prog. Org. Coatings*. **2015**, *85*, 199–207.

[8] B. K. Deka, T. K. Maji, *Compos. Part A*. **2011**, *42*, 2117–2125.

[9] International Organization for Standardization (ISO), *BS EN ISO 11507 2001*. **2007**, 1–17.

[10] "https://www.atlas-mts.com/products/standard-instruments/fluorescent-uv," **n.d.**

[11] R. BABOIAN, Ed. , *NACE CORROSION ENGINEER ' S REFERENCE Third Edition*, 3rd ed., NACE International **2002**.

[12] Bio-Logic Science Instruments, "https://www.bio-logic.net/accessories/corrosion-cell-kit/coating-cell/," **n.d.**

[13] F. Mansfeld, C. H. Tsail, *Corrosion*. **1991**, *47*, 958–963.

[14] A. Amirudin, D. Thieny, *Prog. Org. Coatings*. **1995**, *26*, 1–28.

[15] J. R. Macdonald, M. K. Brachman, *Rev. Mod. Phys.* **1956**, *28*, 393–422.

[16] C. H. Tsai, F. Mansfeld, *Corros. Sci.* **1993**, *49*, 726–737.

[17] D. M. Brasher, A. H. Kingsbury, *J. Appl. Chem.* **1954**, *4*, 62–72.

[18] D. Loveday, P. Peterson, B. Rodgers, *J. Coatings Technol.* **2004**, 88–93.

[19] *Appl. note GAMRY Idustry 'Getting Started with Electrochem. Corros. Meas.* **2017**, 1–8.

[20] A. International, *ASTM G102-89*. **2015**, 1–7.

[21] A. International, *ASTM G1 - 03*. **2017**, 1–9.

[22] A. International, *ASTM D3359-17*. **2017**, 1–9.

[23] A. International, *ASTM D3363 - 05*. **2011**, 1–3.

[24] International Organization for Standardization (ISO), *ISO 15184-12*. **2012**, 1–6.

# Chapter 4

# Carbon Nanomaterials Characterization

*Carbon-based materials, which include graphene oxide, nitrogen-doped graphene oxide, and cylindrical, conical, and nitrogen-doped carbon nanotubes were synthesized as an anticorrosion pigment. The main aim of this part of the work is the synthesis and physical characterization of the carbon-based nanomaterials, which were synthesized using chemical vapor deposition, ultrasonic spraying of the catalyst solution, and Hummer's methods. The synthesized materials were characterized using different methods, such as thermal analysis, scanning electron microscopy, X-ray photoelectron spectroscopy, and elemental analysis.*

## 4.1. Thermal Gravimetric Analysis

Thermal gravimetric analysis was carried out to analyze the amount of admixtures, such as amorphous carbon and metal catalysts. According to the thermal analysis, classical and nitrogen-doped carbon nanotubes have an admixture of amorphous carbon of 1 and 1.5 wt%, respectively, which was determined from the mass changes before 350 ºC (Figure 4.1.a, Figure A.1). Ash content of all carbon nanotubes samples varied from 2 to 4 wt%, which indicated that the samples are clean from catalyst precursor, so additional cleaning is not required (Figure A.2).

Graphene oxide and nitrogen-doped graphene oxide have mass changes at around 100 ºC due to water evaporation of 5 and 4 wt%, respectively (Figure 4.1.b, Figure A.3). Graphene oxide has one exotherm peak at 206 ºC and a mass change of 26 wt%; it has a second peak at 647 ºC with a mass change of 53 wt% due to decomposition.

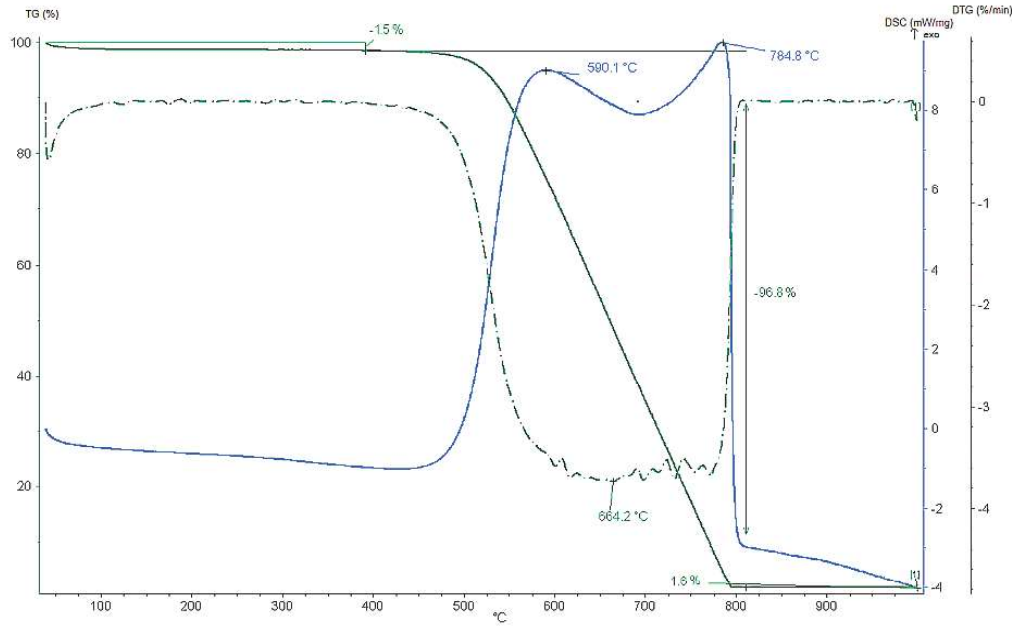


a.

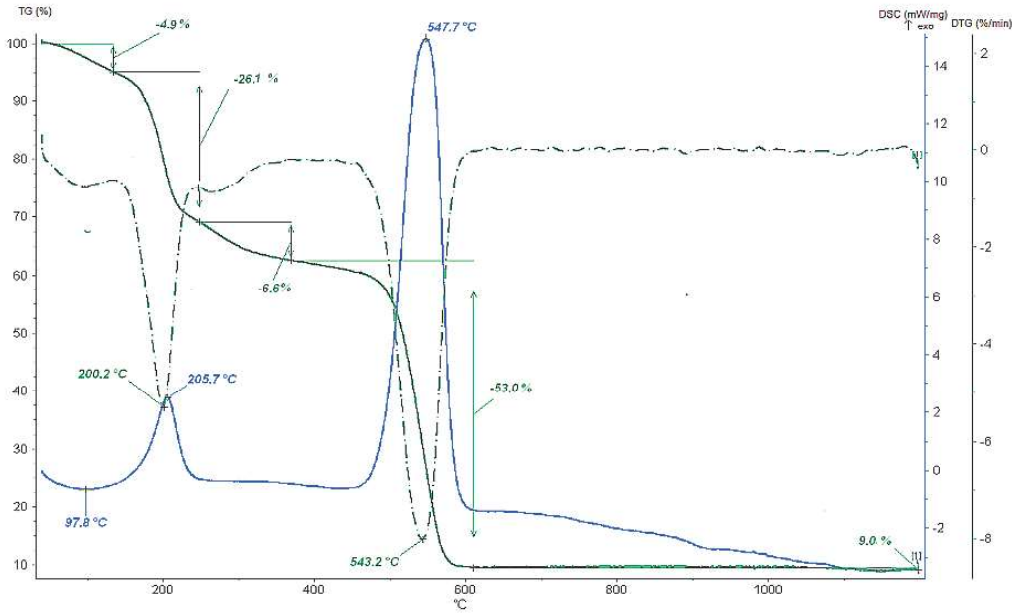


b.

**Figure 4.1.** Thermo gravimetric analysis of (a.) nitrogen-doped carbon nanotubes; (b.) graphene oxide.

## 4.2. Scanning Electron Microscopy

Scanning electron microscopy (SEM) was used to analyze the structure of carbon-based nanomaterials and the presence of defects in these materials.

Conical and cylindrical carbon nanotubes are types of multiwalled carbon nanotubes with different structures and properties. [1] The SEM image shows that conical CNT are more defective than cylindrical CNT and that their diameter is bigger, varying from 16 to 40 nm, which is related to structural features and the manner of synthesis (Figure 4.2. a and b). [2]

a. 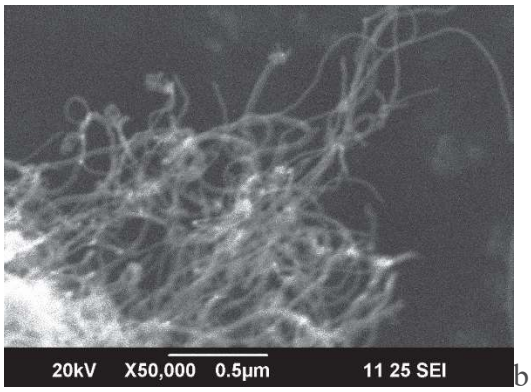

b. 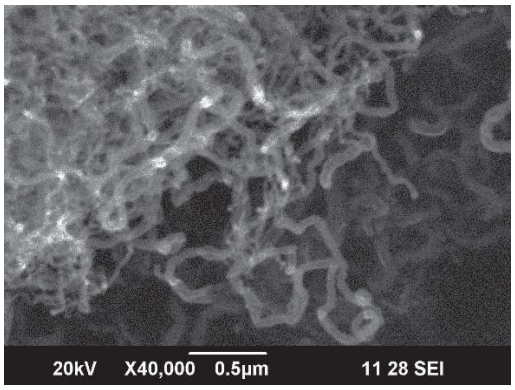

c. 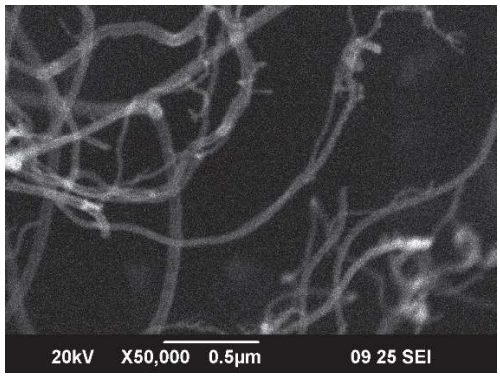


**Figure 4.2.** a. Scanning electron microscopy of cylindrical CNT; b. conical CNT; c. nitrogen-doped CNT.

Nitrogen-doped carbon nanotubes obtained using acetonitrile precursors have a diameter of 15–40 nm and have a structure that is closer to that of cylindrical CNT because they were synthesized using the CVD method (Figure 4.2.c).

a. 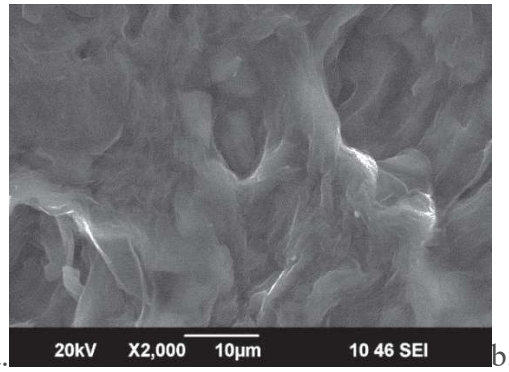

b. 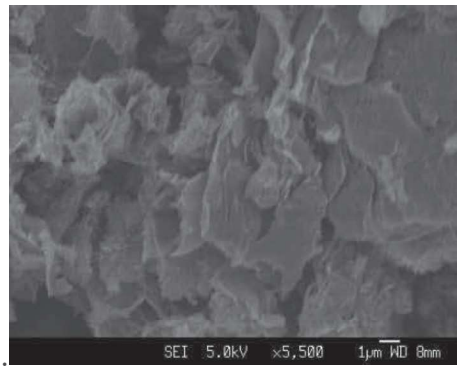


**Figure 4.3.** a. Scanning electron microscopy of graphene oxide; b. nitrogen-doped graphene oxide.

Figure 4.3 shows the microstructure of graphene oxide and nitrogen-doped graphene oxide. The structure of N-GO is similar to that of graphene oxide, which was synthesized from it using reduction and doping by melamine.

## 4.3. X-ray Photoelectron Spectroscopy and Elemental Analysis

For the nitrogen-doped materials and graphene oxide, X-ray photoelectron spectroscopy (XPS) analysis was conducted to determine the nitrogen content on the surface of the nanomaterials and the nature of the functional group. Elemental analysis (EA) was performed for N-CNT to get the total nitrogen percentage. The results are presented in Table 4.1.

**Table 4.1.** XPS and elemental analysis data

| Name | XPS | | | | | | EA |
|---|---|---|---|---|---|---|---|
| | Pyridine-like, % | $-NR_2$, % | N in graphene, % | $-C=N^+H-C-$, % | N - oxidized, % | $W_{surface}$, % | $W_{atom}$, % |
| N-CNT | 0.3 | 0.5 | 1.5 | 0.3 | 0.4 | 3 | 3.9 |
| N-GO | 2.2 | 2 | 0.8 | 0.2 | 0.2 | 5.4 | - |

According to the XPS, nitrogen-doped samples contain nitrogen on the surface in different states: nitrogen in pyridine molecules, nitrogen in amine molecules, nitrogen that replaces carbon in the graphene layer, protonated nitrogen, and oxidized nitrogen [3] Due to the very high carbon/nitrogen ratio and the vapor pressure of the acetonitrile precursor, the nitrogen percentage in the N-CNT achieved 3.0% and 3.9%, based on XPS and EA, respectively.

Melamine, which was used to synthesize nitrogen-doped graphene oxide, reduced the GO, and the oxygen percentage dropped from 44.9% (graphene oxide) to 24.3%. From the XPS spectra (Figure 4.4), the intensity decrease of the C-O bond can be determined.

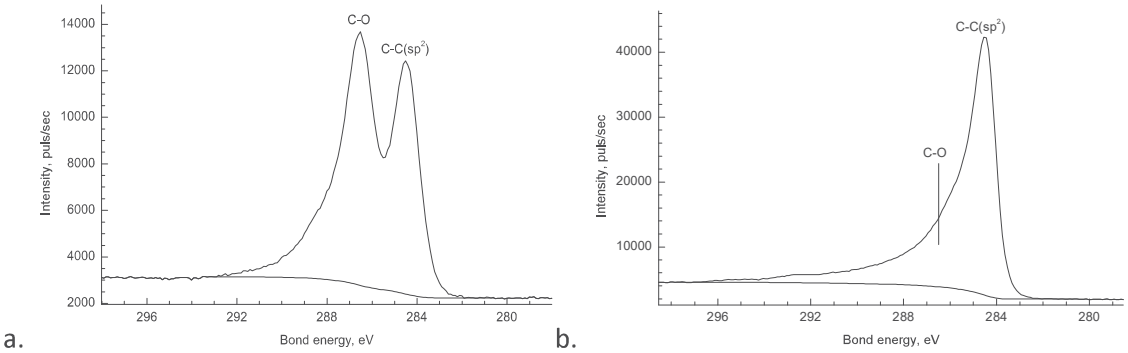


**Figure 4.4.** a. XPS spectra of graphene oxide; b. nitrogen-doped graphene oxide.

## 4.4. Summary

The synthesized materials are carbon-based materials with different structures, such as cylindrical and conical carbon nanotubes, graphene oxide, and nitrogen-doped analogs.

It is suggested that nitrogen doping of carbon nanotubes and graphene oxide can improve the cross-linking and ultraviolet stability. As was described before, the surface groups are very important because they enhance dispersion and improve the quality of the coating.

**References**

[1] A. V. Eletskii, *Uspekhi Fiz. Nauk*. **2008**, *174*, 1191.

[2] S. V. Savilov, A. S. Ivanov, A. V. Egorov, M. N. Kirikova, E. A. Arkhipova, V. V. Lunin, *Russ. J. Phys. Chem. A*. **2016**, *90*, 429–435.

[3] S. A. Chernyak, A. S. Ivanov, E. A. Arkhipova, A. V. Shumyantsev, N. E. Strokova, K. I. Maslakov, S. V. Savilov, V. V. Lunin, *Appl. Surf. Sci.* **2019**, *484*, 228–236.

# Chapter 5

# Carbon-based composite coating

*Corrosion protection of the composite coatings based on bisphenol A epoxy resin was investigated. The composite coating samples unexposed to the environment were used as a reference to investigate the degree of degradation under ultraviolet light, sodium chloride solution, and water condensation, which will be described in Chapters 6–8. The potentiodynamic polarization measurement was conducted to calculate the corrosion rate and the potential of the corrosion. The surface quality and degradation of the surface was controlled by field emission scanning electron microscopy (FESEM) analysis.*

## 5.1.Corrosion Behavior

For the bare metal, pure epoxy, and composite coatings with anticorrosion pigments, such as graphene oxide (GO), nitrogen-doped graphene oxide (N-GO), cylindrical (CNTcyl) and conical carbon nanotubes (CNTcon), and nitrogen-doped carbon nanotubes (N-CNT), the electrochemical corrosion test was performed. Several parallel experiments were done, and only repeatable data were used for analysis/conclusion to avoid accidental results due to uneven film coating.

The Tafel plot of pure stainless steel is shown in Figure 5.1. In the anodic slope, a rapid increase in the current density is observed, which indicates the occurrence of pitting corrosion. The potential of the pitting corrosion is 0.42 V, which is in agreement with the literature. [1] The calculation of the corrosion parameters was conducted, as described in Chapter 3.4.2. The corrosion current density is 4.8E-02 μA/cm$^2$, and the potential of corrosion is -0.22 V vs SCE (0.1 M KCl).

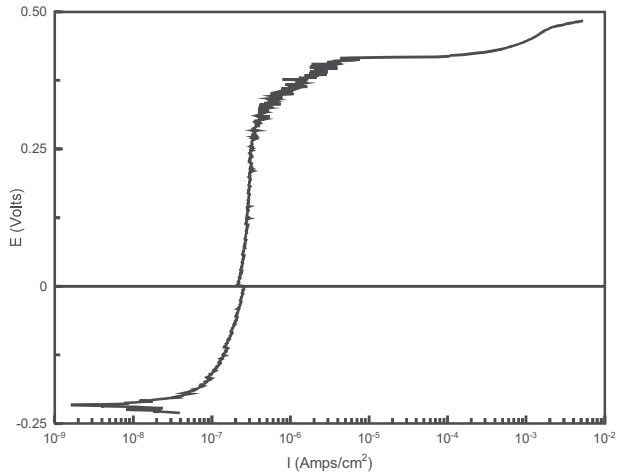


**Figure 5.1.** Polarization curve of stainless steel 316L.

When the metal was coated with epoxy resin, the character of the polarization curve changed, and the corrosion current can be detected from Figure 5.2.a. The limited current is inspected in the cathodic part of the graph (that is, the current remains almost constant with increasing scanning negative potential) and is caused by the limited diffusion of oxygen and water through the coating to the metal surface.

The protection of the metal by coating is evident, and the corrosion rate decreases from 5.0E-04 mm/yr (SS 316L) to 5.7E-05 mm/yr (pure epoxy coating).

Adding GO into the coating composition provides barrier protection, and the corrosion rate decreases more than four times (Table 5.1). The polarization curve of the GO composite coating performs differently from pure epoxy coating because pitting corrosion is occurring. The pitting potential and the repassivation potential [2] could be determined from the graph, which are 0.19 V and -0.42 V, respectively. The surface profile will be described in Chapter 5.3; however, the pits could be detected visually. It was proposed that the main reasons for the pitting corrosion to occur for the GO sample are excess water evaporation during the coating curing, which forms the epicenter of the pitting corrosion, and poor dispersion and cross-linking of the polymer–pigment composite.

Figure 5.2.a shows that the polarization curve of the nitrogen-doped graphene oxide composite coating is shifted to a higher potential, and no pitting corrosion is observed. The corrosion rate has almost the same value for the GO and N-GO coatings, but the potential of the corrosion is increased with nitrogen doping. This might happen due to the formation of chemical bonds between the pigment, epoxy resin, and curing precursor.

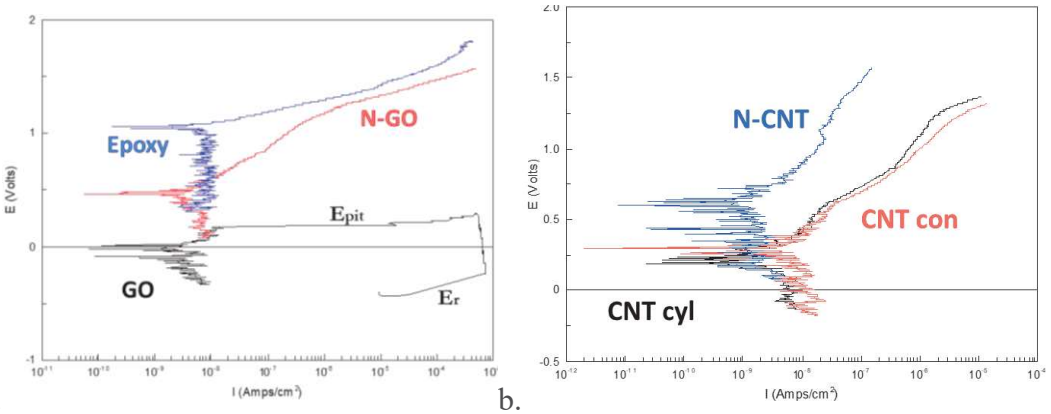


a. b.

**Figure 5.2.** a. Polatization curves for pure epoxy coating and composite coating with graphene oxide and nitrogen-doped graphene oxide pigments; b. Polarization curves for cylindrical, conical, and nitrogen-doped carbon nanotubes composite coatings.

Carbon nanotubes, as described in Chapter 2.4.3, provide corrosion protection in two ways: by the barrier and by adsorption. The corrosion current density of the conical CNT composite is higher than that of the cylindrical or nitrogen-doped CNT (Figure 5.2.b). The structure affects the agglomeration of the carbon nanotubes; therefore, the conical carbon nanotubes with a more defective structure perform worse. The CNT cyl and N-CNT were synthesized using the same method; as a result, they had a similar structure (Figure 4.2.a and c). The current density for these coatings has similar values, but for the N-CNT it is a bit lower (Table 5.1). However, the corrosion potential is higher for the nitrogen-doped coating, which indicates better protection and proves the hypothesis that nitrogen doping improves cross-linking.

**Table 5.1.** Electrochemical characteristics of the composite coating.

| Sample | $I_0$, μA/cm$^2$ | $E_0$, V | Corrosion rate, mm/yr | Thickness, μm |
|---|---|---|---|---|
| SS | 4.8E-02 | -0.22 | 5.0E-04 | - |
| Epoxy | 5.5E-03 | 1.05 | 5.7E-05 | 33±5 |
| GO | 1.3E-03 | -0.02<br>Epit = 0.19<br>Er = -0.42 | 1.4E-05 | 33±5 |
| N-GO | 1.4E-03 | 0.46 | 1.5E-05 | 32±5 |
| CNT con | 2.5E-03 | 0.27 | 2.6E-05 | 38±5 |
| CNT cyl | 1.7E-03 | 0.19 | 1.8E-05 | 37±5 |
| N-CNT | 1.3E-03 | 0.62 | 1.4E-05 | 38±5 |

## 5.2. Electrochemical Impedance Spectroscopy

Electrochemical impedance spectroscopy (EIS) is a powerful tool for investigating coating performance. The EIS measurements were performed for all samples. The dynamics of the changes in the EIS plots describe the information about coating efficiency. The Nyquist plots of the unexposed samples with GO-based and CNT-based pigments in the composition are shown in Figure 5.3. Based on the coatings' degradation steps [3], the performance of the coatings is outstanding and the coating resistance is high.

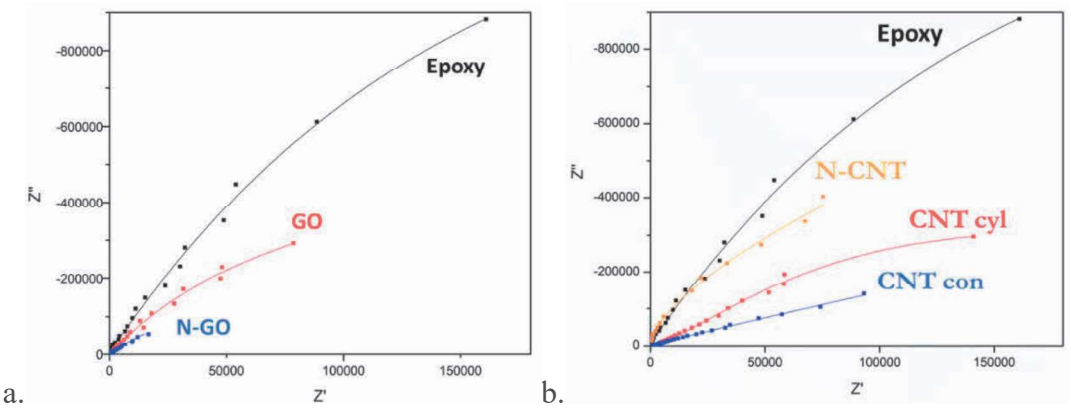


a. b.

**Figure 5.3.** The electrochemical impedance study in the Nyquist plot of the unexposed samples (a.) pure epoxy coating, and composite coating with graphene oxide and nitrogen-doped graphene oxide pigments; (b.) cylindrical, conical, and nitrogen-doped carbon nanotubes composite coatings.

Figure 5.4 shows the equivalent circuit that can be used to model the electrochemical impedance results. The equivalent circuit that contains the solution resistance ($R_s$) in series with the constant phase element of the coating ($CPE_{coating}$) and the pore resistance ($R_{pore}$) in parallel was used to fit the EIS data of the unexposed samples. The calculated capacity and pore resistance for pure epoxy and composite coatings with GO- and CNT-based pigments are shown in Table 4.3.

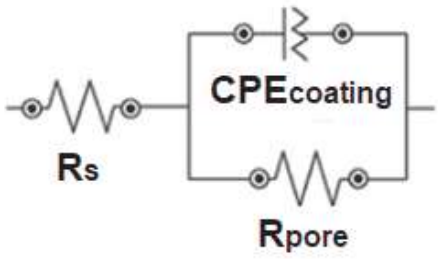


**Figure 5.4.** The equivalent circuit models for undamages coating film.

From the Nyquist plot, it can be determined that the pure epoxy coating has a higher pore resistance of 7.7 MΩ/cm$^2$, which is three and eight times higher than the pore resistances of the nitrogen-doped carbon nanotubes (2.4 MΩ/cm$^2$) and the nitrogen-doped graphene oxide (0.89 MΩ/cm$^2$) composite coating, respectively. These results do not agree with the corrosion rate, which was calculated from the polarization measurements. The main reason for this phenomenon is that the initial

coating resistance might be very high, but it will drop significantly during the exposure to the corrosive environment or UV radiation. The initial pore resistance of the graphene oxide composite coating is much higher than the resistance of the nitrogen-doped graphene oxide composite coating. Still, the graphene oxide allows pitting corrosion to occur, although the nitrogen doping improves the coating performance.

**Table 5.2.** Electrochemical parameters calculated from electrochemical impedance measurements.

| | $CPE_{coating}$, $nFs^{n-1}/cm^2$ | n | $R_{pore}$, $M\Omega/cm^2$ |
|---|---|---|---|
| Epoxy | 1.3 | 0.95 | 7.7 |
| GO | 7.5 | 0.89 | 7.2 |
| N-GO | 930 | 0.87 | 0.89 |
| CNTcyl | 94 | 0.80 | 2.5 |
| CNTcon | 780 | 0.65 | 3.6 |
| N-CNT | 0.77 | 0.96 | 2.4 |

The pore resistances of the cylindrical and nitrogen-doped CNT are similar, as well as the corrosion rates calculated from the Tafel region of the polarization curve. The conical CNT composite coating provides a higher initial resistance than the composite with cylindrical CNT. As reported earlier, the dynamics of the changes in the pore resistance under certain conditions are more informative.

The constant phase element [4] is the multifunctional element, which could describe the nonideal capacity element if n is close to 1, or the Warburg element, which characterizes the diffusion when n is equal to 0.5. From Table 5.2, it could be determined that n for the conical CNT composite coating is 0.65, which is closer to the diffusion prosses than the capacity. For all other samples, n is close to the capacity performance. Since the capacitance is directly proportional to the capacity area [5], the low values of the $CPE_{coating}$ indicate the lower exposure to the environment and micropore presence. The lowest capacity was demonstrated by the nitrogen-doped

carbon nanotubes composite coating (0.77 $nFs^{n-1}/cm^2$), followed by the epoxy coating (1.3 $nFs^{n-1}/cm^2$).

## 5.3. Surface Analysis

To investigate the surface changing under the corrosion process, field emission scanning electron microscopy (FESEM) was used. Figure 5.5 shows the microphotographs of the pure epoxy coating and of the composite coatings with graphene oxide and nitrogen-doped graphene oxide before and after potentiodynamic measurement. The unexposed epoxy coating surface had some initial defects with a circle form, such as bubbles, which are formed during the coating's curing process due to air and moisture diffusion. In this study, only the effect of carbon-based pigments was studied; therefore, no defoamer, dispersant, or leveling additives were added. These bubble structures do not much affect the corrosion process since the depth is less than 10 µm and the diameter is less than 15 µm. From Figure 5.5.a, it could be determined that the surface profile of the epoxy coating changed uniformly without damage but with increasing defectiveness.

a. 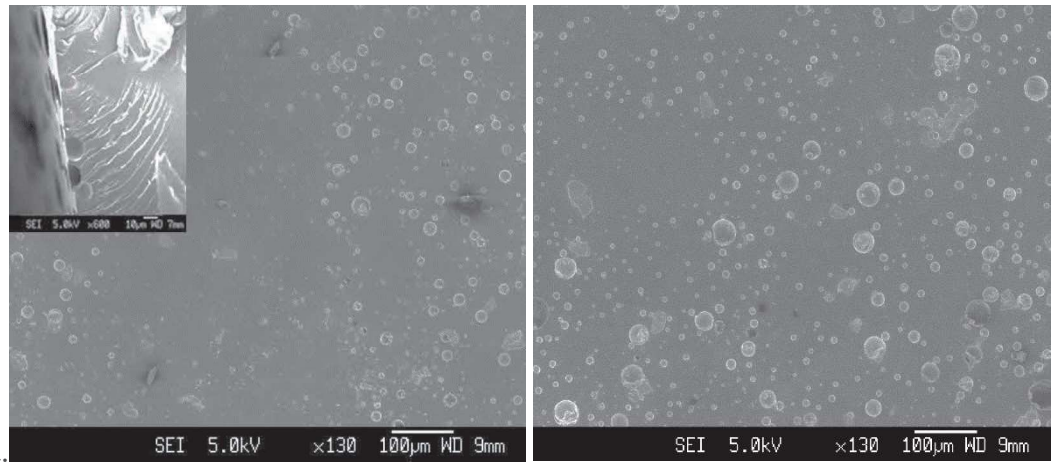

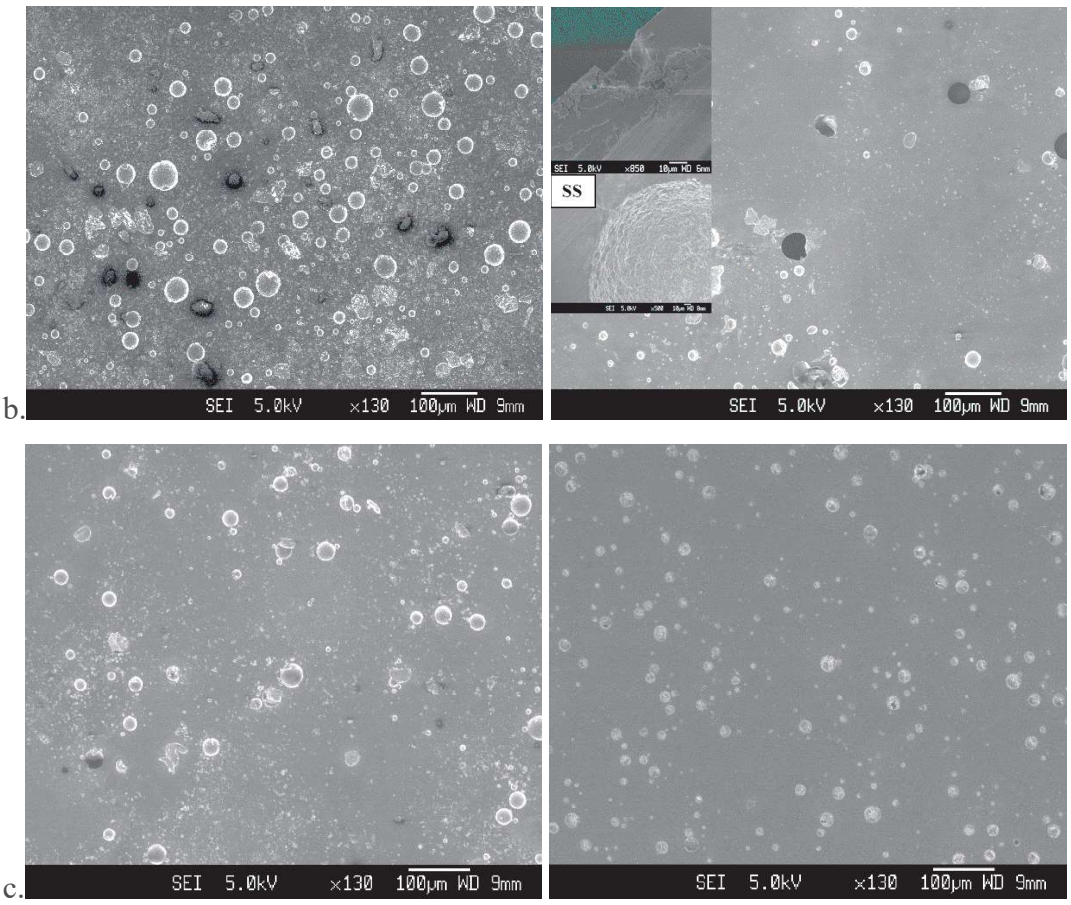


**Figure 5.5.** FESEM images of (a.) epoxy coating; (b.) graphene oxide composite coating; (c.) Nitrogen-doped graphene oxide, before and after potentiodynamic experiment.

Previously it was suggested that graphene oxide composite coating has worse performance and does not prevent pitting corrosion from occurring due to the presence of residual water. From the FESEM image of the GO composite coating before the potentiodynamic experiment (Figure 5.5.b, left), sizeable defects could be detected with a diameter of more than 45 µm, which initiates the hole formation during the corrosion process. The hole propagation launches the pitting corrosion together with the uniform corrosion. The composite coating with nitrogen-doped graphene oxide anticorrosion pigment exhibits a low corrosion rate and a high potential of corrosion. Figure 5.5.c shows not much difference between the coating surface before and after corrosion.

The surface changes for the cylindrical, conical, and nitrogen-doped carbon nanotubes composite coatings before and after corrosion are shown in Figure 5.6. Based on the calculated corrosion parameters, carbon nanotubes prevent the corrosion, and the corrosion rate is low. The surface of the composite coating based on cylindrical carbon nanotubes (Figure 5.6.a) degrades uniformly without any holes or cracks.

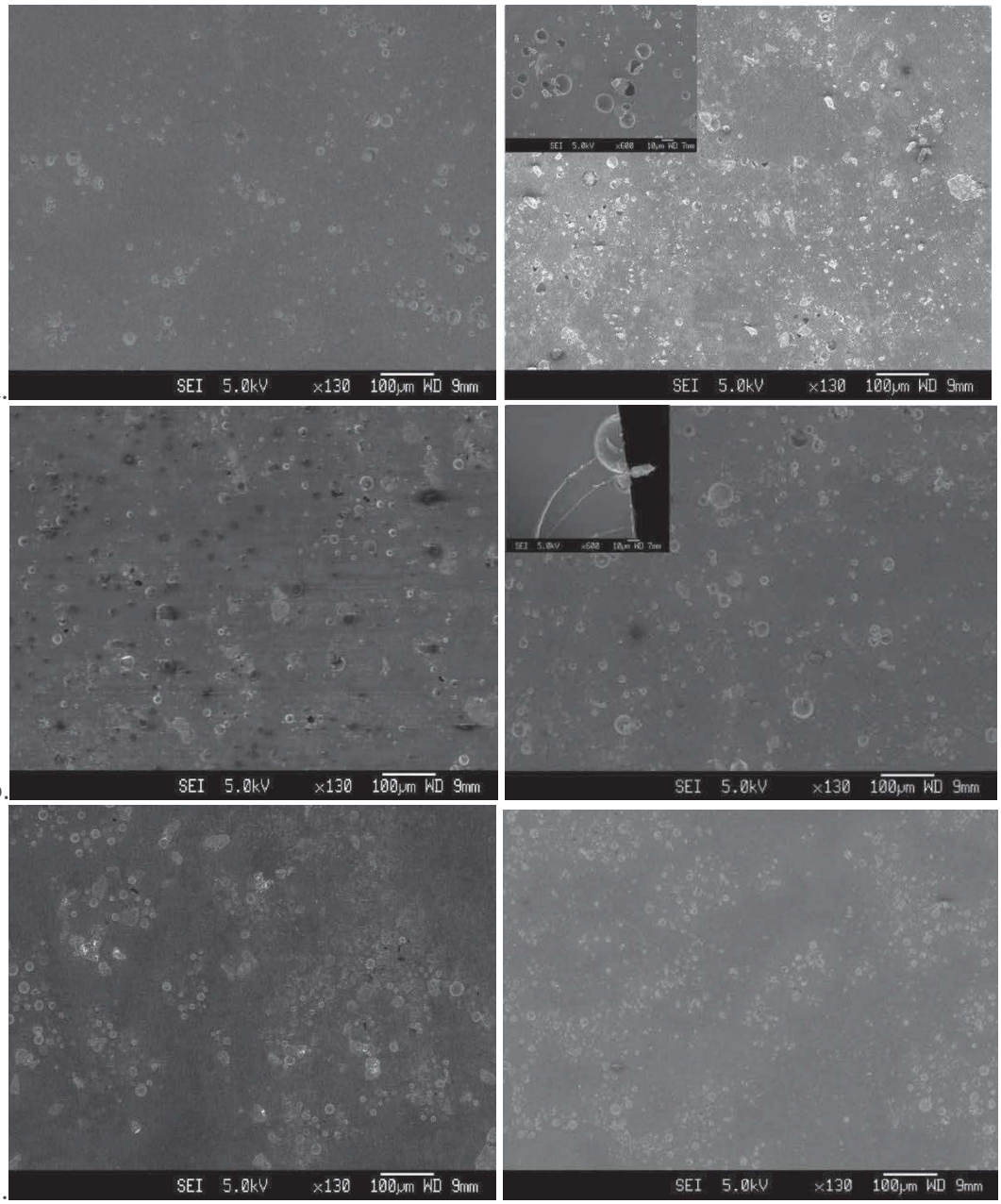


**Figure 5.6.** FESEM images of (a.) cylindrical CNT; (b.) conical CNT; (c.) nitrogen-doped CNT composite coating, before and after potentiodynamic experiment.

The corrosion rate of the conical carbon nanotubes is higher than that of the other CNT-based composite coatings. The formation of broad defects is observed in Figure 5.6.b, with a diameter of around 20 μm and a depth of 15 μm. Nitrogen-doped CNT improve the corrosion resistance, and the surface profile changes insignificantly.

## 5.4. Mechanical Properties

The mechanical properties were investigated according to the standard. Adhesion is a very important characteristic of a coating film, and it was tested based on the ASTM D3359-17 standard [6] by a tape test. In Chapter 3.4.4, the methodology and the analysis of the results were described. For all samples except the composite coating with conical CNT, the adhesion is excellent with 0% removed area (classification 5B). As shown in Table 5.3, the sample with conical CNT as a pigment shows less than 5% removed area.

**Table 5.3.** The mechanical properties of the coatings.

| | Adhesion | Hardness |
|---|---|---|
| Epoxy | 5B | 3H |
| GO | 5B | 3H |
| N-GO | 5B | 4H |
| CNTcyl | 5B | 3H |
| CNTcon | 4B | 4H |
| N-CNT | 5B | 4H |

Scratch hardness is a required characteristic of protective coatings. The measurements were carried out according to the ASTM D3363-05 standard. [7] The results are shown in Table 5.3. The hardness of the coating is quite high, over 3H pencil hardness. The nitrogen-doped GO and the conical and nitrogen-doped carbon nanotubes improve the hardness of the composite coating.

## 5.5. Summary

The corrosion and mechanical properties, as well as the surface of the coatings with different carbon-based pigments, were investigated.

The electrochemical measurements show that the addition of carbon-based pigments enhances the corrosion protection of the coating. The graphene oxide does not prevent pitting corrosion, and pits are observed on the stainless steel surface (Figure 5.5.b) due to the evaporation of residual water. Nitrogen doping improves the anticorrosion properties of the coating, and nitrogen-doped graphene oxide and nitrogen-doped carbon nanotubes provide the lowest corrosion rate and, based on surface analysis, prevent the propagation of uniform corrosion. Nitrogen doping also enhances the mechanical properties, such as hardness.

**References**

[1] C. T. Kwok, F. T. Cheng, H. C. Man, *Mater. Sci. Eng. A*. **2000**, *290*, 145–154.

[2] B. E. Wilde, E. Williams, *Electrochim. Acta*. **1971**, *16*, 1971–1985.

[3] D. Loveday, P. Peterson, B. Rodgers, *J. Coatings Technol.* **2004**, 88–93.

[4] J. R. Macdonald, M. K. Brachman, *Rev. Mod. Phys.* **1956**, *28*, 393–422.

[5] F. Mansfeld, *J. Appl. Electrochem.* **1995**, *25*, 187–202.

[6] A. International, *ASTM D3359-17*. **2017**, 1–9.

[7] A. International, *ASTM D3363 - 05*. **2011**, 1–3.

# Chapter 6

# Ultraviolet Degradation of the Composite Coating

*The Sun's radiation has a strong influence on the coating's stability and performance. The simulation experiments predict the coatings' efficiency. The degradation under ultraviolet lamps, which simulate the solar radiation, was carried out, followed by the electrochemical measurements of the affected coatings and the investigation of the coatings' degradation. The corrosion rate and the coatings' resistance were studied after exposure to UV radiation. The degree of the degradation was calculated, and changes in the mechanical properties are reported.*

## 6.1. Corrosion Behaivior

After the ultraviolet degradation, the polarization measurements were conducted. Figure 4.10 a and b show the polarization curves for the composite coatings with GO and N-GO (Figure 6.1.a) and for the coatings with cylindrical and conical CNT and N-CNT (Figure 6.1.b) that were exposed to UV radiation for 1000 h. The polarization curves for the coatings with GO and N-GO pigments had a significant difference before and after UV degradation (Figure 5.2.a and 6.1.a). Pitting and uniform corrosion occur at the same time for the pure epoxy coating and the GO and N-GO composite coatings, as shown in Figure 6.1.a. The corrosion current density and rate slightly increased for the samples after UV degradation. The corrosion rate for the composite coatings is more than five times lower (Table 6.1), which means that GO and N-GO protect the coating from uniform corrosion but not from pitting corrosion.

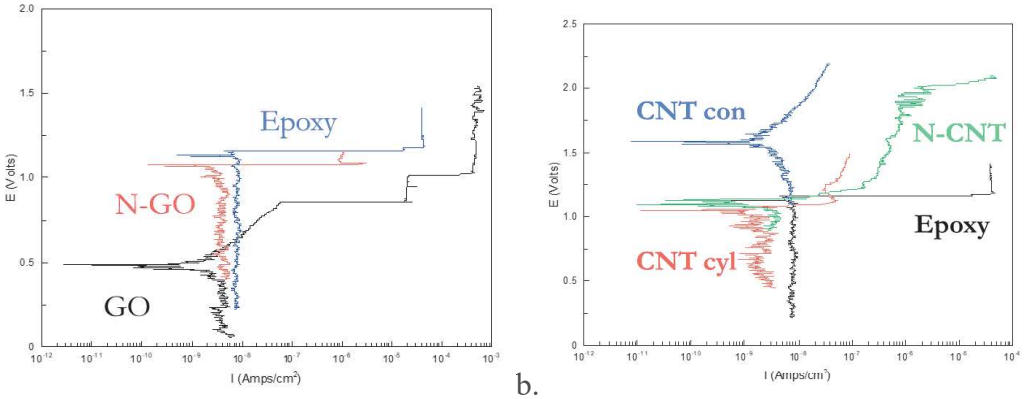


a. b.

**Figure 6.1.** Polatization curves for (a.) pure epoxy coating and composite coating with graphene oxide and nitrogen-doped graphene oxide pigments; (b.) cylindrical, conical, and nitrogen-doped carbon nanotubes composite coatings after degradation under ultraviolet radiation.

As seen in Table 5.1 and Table 6.1, for all the samples after exposure to UV radiation, the potential of corrosion significantly increased, which might have happened due to changes in the surface tension of the coatings under UV. Compared with GO and N-GO composite coatings, carbon nanotubes provide better protection

from UV and corrosion and prevent pitting corrosion from occurring (Figure 6.1.a and b).

Figure 6.1.b shows that carbon nanotubes improve the coatings' resistance. The corrosion rate decreases more than six times from 8.1E-05 mm/yr for the pure epoxy coating to 2.4E-05 mm/yr for the coating with conical carbon nanotubes pigment—1.4E-05 mm/yr for the cylindrical carbon nanotubes and 1.3E-05 mm/yr for the nitrogen-doped carbon nanotubes. The composite coating with N-CNT demonstrates the lowest corrosion rate and ensures UV protection.

**Table 6.1.** Electrochemical characteristics of the composite coating after degradation under ultraviolet radiation.

| Sample | $I_0$, μA/cm$^2$ | $E_0$, V | r (mm/yr) |
|---|---|---|---|
| Epoxy | 7.7E-03 | 1.13<br>Epit=1,16 | 8.1E-05 |
| GO | 1.5E-03 | 0.48<br>Epit=0,85 | 1.6E-05 |
| N-GO | 2.5E-03 | 1.06<br>Epit=1.08 | 2.6E-05 |
| CNTcon | 2.3E-03 | 1.59 | 2.4E-05 |
| CNTcyl | 1.3E-03 | 1.05 | 1.4E-05 |
| N-CNT | 1.2E-03 | 1.11 | 1.3E-05 |

From Table 5.1 and Table 6.1, the slight drop in the corrosion current density for the CNT-based composite coating after UV exposure in comparison with the unexposed samples can be determined. The reason for this phenomenon is the increased degree of cross-linking under UV radiation. Similar to the rate of the reference sample, the corrosion rates of the cylindrical and nitrogen-doped carbon nanotubes are lower than the rate of the conical CNT composite coating.

## 6.2. Electrochemical Impedance Spectroscopy

The impedance spectroscopy was conducted for the samples after exposure to UV when the OCP was stabilized. The Nyquist plots for the pure epoxy coating

and the composite coating with graphene-oxide-based and carbon-nanotubes-based pigments are shown in Figure 6.2. The Nyquist plots are quite different from those of the unexposed samples (Figure 5.3).

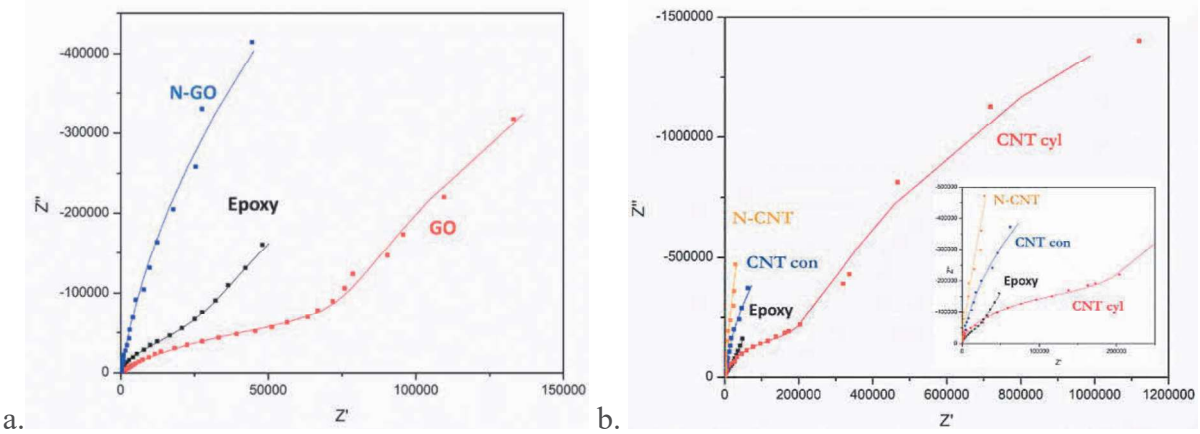


**Figure 6.2.** The electrochemical impedance study in the Nyquist plot of the samples after the exposure to the UV radiation (a.) pure epoxy coating, and composite coating with graphene oxide and nitrogen-doped graphene oxide pigments; (b.) cylindrical, conical, and nitrogen-doped carbon nanotubes composite coatings.

The equivalent circuit in Figure 6.3 was used to fit some of the samples, such as pure epoxy coating, composite coating with graphene oxide, and composite coating with cylindrical carbon nanotubes. The equivalent circuit consists of two capacitive time constants and the part that describes processes on the coating–metal interface. The corrosion process is started, and damage to the coating, such as delamination, might happen. The rest of the samples was fitted with a one-time-constant equivalent circuit, which is shown in Figure 5.4.

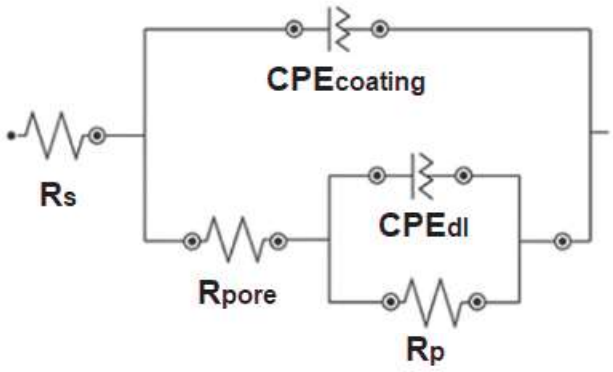


**Figure 6.3.** The equivalent circuit model for the corroded coated metal system. [1]

Figure 6.2.a presents the Nyquist plot of the epoxy coating and the GO and N-GO composite coatings. The electrochemical parameters were calculated based on the fitting model displayed in Table 6.2. The epoxy coating, which has the highest initial pore resistance, demonstrates a decrease of more than sixty times from 7.7 MΩ/cm$^2$ to 0.12 MΩ/cm$^2$. The corrosion resistance is also low in comparison with other samples and is equal to 2.1 MΩ/cm$^2$.

The graphene oxide composite coating has a high drop in pore resistance, and the impedance results were fitted with the two-time-constant model, which means that the corrosion process occurs on the metal surface. Positive dynamics of the changing of the EIS data for the nitrogen-doped GO composite coating are observed, and the pore resistance increased more than seven times and became 6.2 MΩ/cm$^2$. The capacitance also drops dramatically due to the better cross-linking of the polymer–pigment system, decreasing the presence of the micropores.

**Table 6.2.** Electrochemical parameters calculated from electrochemical impedance measurements after exposure to UV radiation.

| | CPEcoating, nFsn-1 /cm2 | n | Rpore, MΩ/cm2 | CPEdl, nFsn-1 /cm2 | n | Rcorr, MΩ/cm2 |
|---|---|---|---|---|---|---|
| Epoxy | 0.88 | 0.97 | 0.12 | 1.2 | 0.93 | 2.1 |
| GO | 18 | 0.77 | 0.17 | 6.8 | 0.99 | 3.8 |
| N-GO | 0.98 | 0.97 | 6.2 | - | - | - |
| CNTcyl | 1.1 | 0.96 | 0.28 | 9.4 | 0.86 | 4.5 |
| CNTcon | 1.1 | 0.96 | 3.2 | - | - | - |
| N-CNT | 0.69 | 0.97 | 23 | - | - | - |

The Nyquist plots for the carbon-nanotubes-based composite after UV degradation are shown in Figure 6.2.b, and the calculated results are presented in Table 6.2. The Nyquist plot of this composite is similar in behavior to the plots of the epoxy and graphene-oxide-based coatings. The coating and double-layer capacity can be determined. The pore resistance and corrosion resistance increase with adding

cylindrical carbon nanotubes in comparison with the graphene oxide and are equal to 0.28 MΩ/cm$^2$ and 4.5 MΩ/cm$^2$, respectively.

The composite coatings with conical and nitrogen-doped CNT demonstrate a high resistance and were fitted with a one-time-constant equivalent circuit. The n is changed for the conical CNT composite coating (Table 5.2 and Table 6.2) and becomes closer to 1, which means that the diffusion component changed to capacity behavior. The pore resistance remained constant for the coating with conical CNT pigment before and after UV exposure. The pore resistance of the nitrogen-doped CNT composite coating increases more than nine times from 2.4 MΩ/cm$^2$ to 23 MΩ/cm$^2$, which means proper protection due to additional cross-linking of the composite coating.

## 6.3. Surface Analysis

The surface analysis by scanning electron microscopy is critical to investigating the propagation of surface degradation. The FESEM images for the epoxy coating and the graphene-oxide-based and carbon-nanotubes-based composite coatings after exposure to ultraviolet radiation and after corrosion testing are shown in Figure 6.4 a-f.

a. 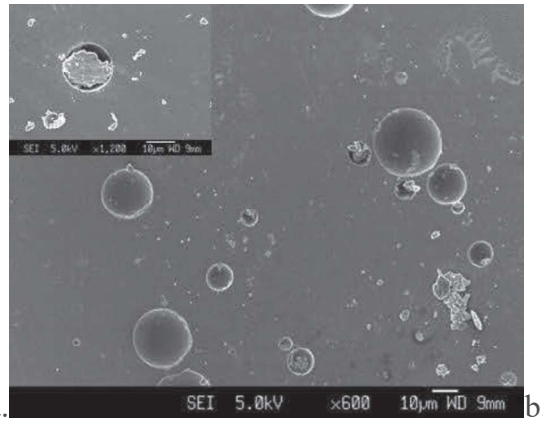

b. 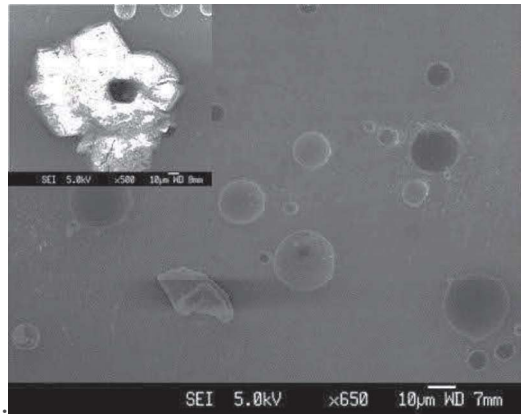

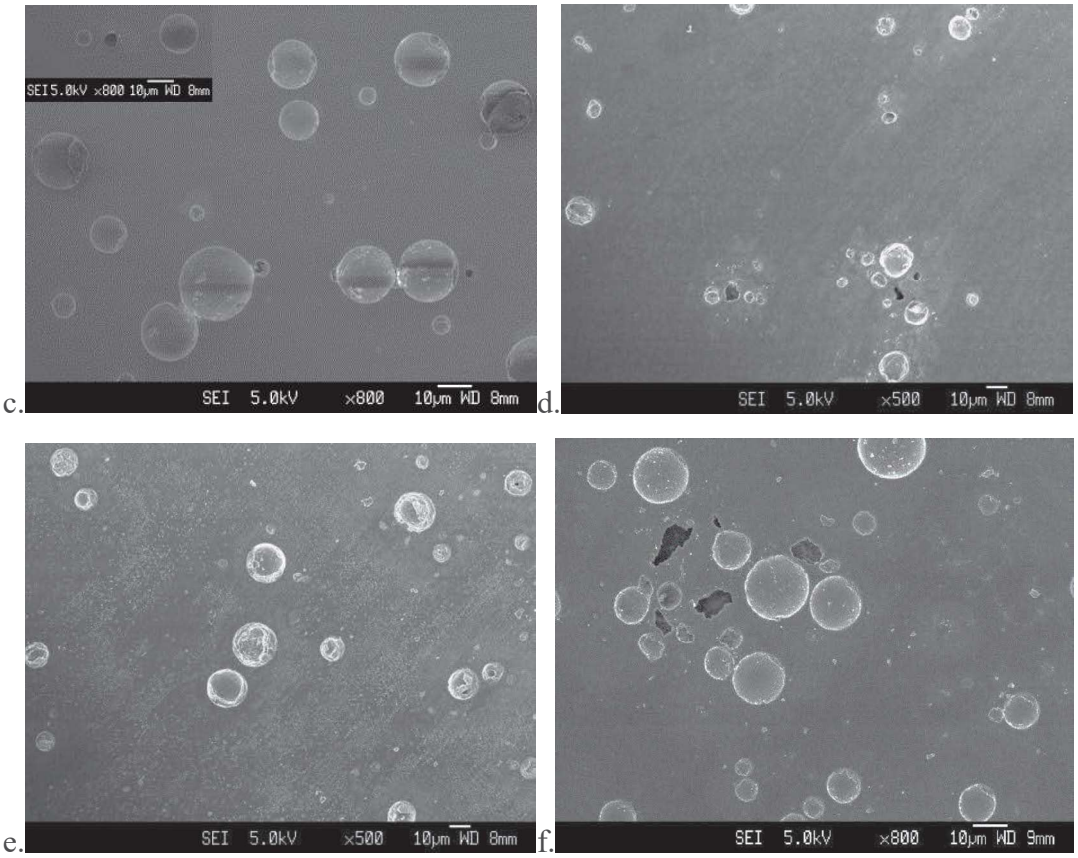


c. d. e. f.

**Figure 6.4.** Scanning electron images of (a.) epoxy coating; composite coating with (b.) graphene oxide; (c.) nitrogen-doped graphene oxide; (d.) cylindrical carbon nanotubes; (e.) conical carbon nanotubes; and (f.) nitrogen-doped carbon nanotubes after UV degradation and after corrosion test.

The surface profile does not change during ultraviolet degradation and is similar to the profiles in Figure 5.5 and Figure 5.6. The microimages of the surfaces after corrosion show the presence of the defects with a diameter from several micrometers to 20 µm.

Based on the electrochemical results, the epoxy coating and the composite coatings with graphene oxide and nitrogen-doped graphene oxide do not prevent pitting corrosion from occurring. The pits can be detected by FESEM and are shown in Figure 6.4. a-c. Figure 6.4.b presents a wide and deep pit with corrosion products that form a flower-like structure.

## 6.4. Degree of Degradation

To establish the influence of different carbon nanomaterials on the UV degradation of the exposed samples, ATR-FTIR studies were conducted on all the samples. The spectra for the samples before and after UV exposure are shown in Figure A.4, Figure A.5, Figure A.6, and Figure A.7. The broad peaks with a maximum wavelength of 3430 $cm^{-1}$ correspond to the stretching vibrations of the hydroxyl (-OH) band. The band appeared in the wavelength range of 2900–2800 $cm^{-1}$, which implies a methyl structure [2] The peaks at the wavelengths of 1660 and 1180 $cm^{-1}$ described stretching vibrations of the olefinic (C=C) and ether bands, respectively [3] The bands observed at wavelengths 1600, 1510, and 825 $cm^{-1}$ showed the characteristic bonding in the aromatic ring. [4] Symmetric and asymmetric stretching vibrations of the C-O bond were demonstrated with peaks at wavelengths of 1295, 1230, and 1110 $cm^{-1}$ [5]. [5]

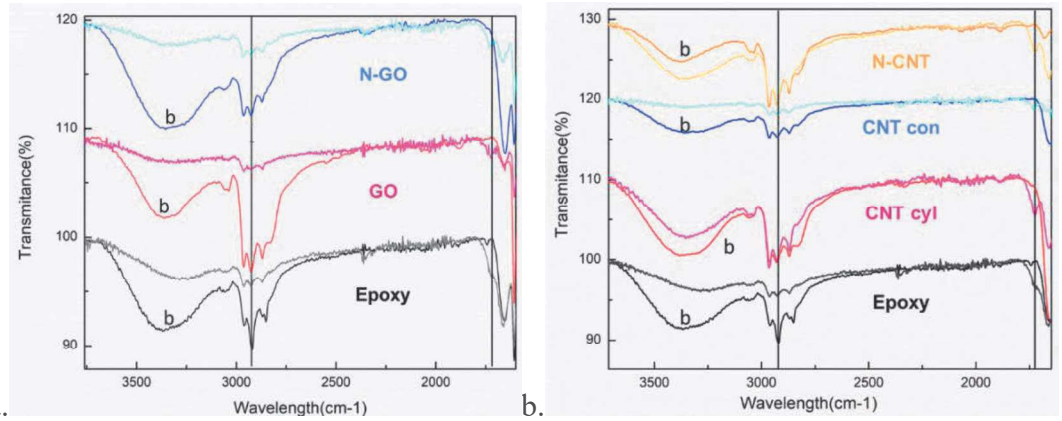


**Figure 6.5.** ATR-FTIR spectra of (a.) epoxy coating and graphene oxide-based composite coatings; (b.) carbon nanotubes-based composite coatings before and after ultraviolet exposure. (b-before UV degradation)

The epoxy resin can absorb UV radiation and degrade under UV. The degradation of the epoxy coating starts from the bonds of the methyl group to the main chain, and carbonyl groups with a peak wavelength of 1720 $cm^{-1}$ are produced. [6] Figure 6.5 shows the FTIR spectra from 3760 $cm^{-1}$ to 1600 $cm^{-1}$ for the reference coating and the samples exposed to UV radiation for 1000 hours. For the samples

after degradation under UV radiation, a significant decrease in the intensity of the peaks corresponding to the methyl band was observed.

Figure 6.5.a shows the FTIR spectra for the epoxy coating and the graphene-oxide-based composite coating. The intensity of the methyl band drops dramatically during the degradation under UV due to the initial step in the degradation process. The composite coatings with cylindrical and nitrogen-doped CNT as anticorrosion pigment had a slight decrease in intensity in comparison with other samples. (Figure 6.5.b). It means that these pigments prevent the epoxy resin from degradation under UV radiation. These results are in agreement with the corrosion parameters, which showed a high corrosion resistance. As seen in Figure 6.5.a and b, peaks with a wavelength of 1720 $cm^{-1}$, which corresponded to the formation of carbonyl groups due to degradation of the coating, were observed. To analyze the degree of degradation of the composite coating, the carbonyl index was calculated according to the equation described in Chapter 3.3.1.

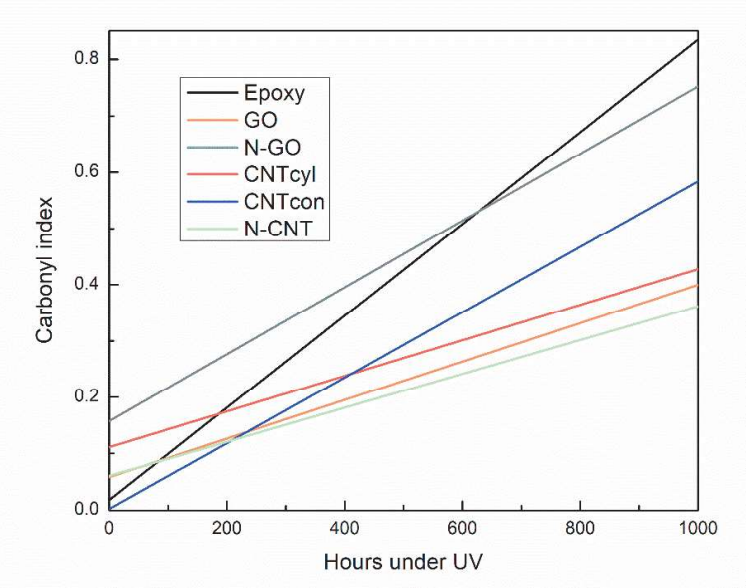


**Figure 6.6.** Carbonyl index for the composite coatings before and after degradation under UV radiation.

Figure 6.6 shows the carbonyl index values versus time of UV exposure for all the samples. The line gradient described the rate of coating degradation. From the

graph, it can be concluded that all the pigments slowed down the degradation under radiation because the line corresponding to the epoxy coating has the highest gradient. Carbon-nanotubes-based coatings demonstrated better protective properties than graphene-oxide-based coatings, which agrees with the corrosion test results, in which the GO and N-GO coatings exhibited two types of corrosion: uniform and pitting corrosion. The N-CNT composite coating has the lowest carbonyl index before and after exposure to UV radiation. N-CNT as a pigment improved the coating film and prevent the epoxy resin from degradation under UV radiation.

## 6.5. Mechanical Properties

The adhesion test and the test for hardness on the pencil scale were conducted for the samples after exposure to ultraviolet radiation for 1000 hours to analyze the changes in mechanical properties. Figure 6.7 shows the results of the mechanical test for the pure epoxy and composite coatings. The initial results were plotted with a square sign, and the results obtained after degradation under UV were plotted with a triangle sign.

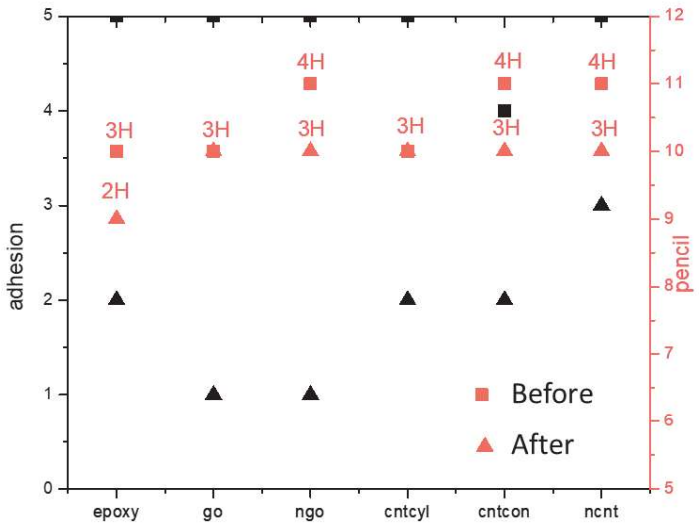


**Figure 6.7.** Adhesion and hardness of the coatings before and after degradation under UV radiation.

The adhesion of the coatings decreased from 5B (0% of removed coating) to more than 15% of coating removal. Such a drop in adhesion is caused by increased

surface tension and a higher degree of cross-linking. The adhesion of the graphene oxide and nitrogen-doped graphene oxide composite coatings ranges from 35% to 65% coating removal, which is equal to 1B according to the classification. This means that graphene-oxide-based pigments lose their mechanical properties under UV and cannot provide appropriate protection. The composite coatings with cylindrical and conical CNT pigments show the same adhesion as the pure epoxy coating. Nitrogen-doped carbon nanotubes improve the adhesion of the composite coating and prevent the degradation process.

**Table 6.3.** The mechanical properties of the coatings after the UV exposure.

| | Adhesion | Hardness |
|---|---|---|
| Epoxy | 2B | 2H |
| GO | 1B | 3H |
| N-GO | 1B | 3H |
| CNTcyl | 2B | 3H |
| CNTcon | 2B | 3H |
| N-CNT | 3B | 3H |

The results of the mechanical test after degradation under UV radiation based on the classification described in Chapter 3.4.4 are shown in Table 6.3. The hardness by the pencil test of the epoxy coating decreases from 3H to 2H during the degradation, but adding graphene oxide or carbon-nanotubes-based pigments improves it. The pencil hardness of all composites is 3H. For the composite coatings with graphene oxide and cylindrical CNT, the hardness is not affected by UV radiation. The hardness of the conical CNT, nitrogen-doped GO, and CNT decreases from 4H to 3H.

## 6.6. Summary

The influence of ultraviolet radiation on the coating's performance was investigated. The addition of carbon-based pigments prevent the coating from degradation and decreases the degree of degradation of the coating under UV radiation. Adding carbon nanotubes in the coating composition improves not only

the anticorrosion properties but also the mechanical properties and coating resistance.

**References**

[1] C. H. Tsai, F. Mansfeld, *Corros. Sci.* **1993**, *49*, 726–737.

[2] A. Ghasemi-Kahrizsangi, H. Shariatpanahi, J. Neshati, E. Akbarinezhad, *Appl. Surf. Sci.* **2015**, *353*, 530–539.

[3] A. M, M. GD, *Infrared Spectroscopy: Applications in Organic Chemistry*, Krieger Pub Co **1978**.

[4] D. Rosu, C. N. Cascaval, L. Rosu, *J. Photochem. Photobiol. A Chem.* **2006**, *177*, 218–224.

[5] A. Tcherbi-Narteh, M. Hosur, E. Triggs, S. Jeelani, *Polym. Degrad. Stab.* **2013**, *98*, 759–770.

[6] A. Ghasemi-Kahrizsangi, J. Neshati, H. Shariatpanahi, E. Akbarinezhad, *Prog. Org. Coatings*. **2015**, *85*, 199–207.

# Chapter 7

# Immersion Degradation of the Composite Coating

*Seawater has a strong effect on corrosion propagation. Immersion into seawater is one of the standard field coating tests. In this work, a laboratory simulation experiment was conducted. The samples were placed in a 3.5% sodium chloride solution for 1000 hours. The polarization testing and electrochemical impedance spectroscopy were performed to investigate the coatings' deformation and corrosion behavior. The mechanism of the degradation was studied using ATR-FTIR spectroscopy.*

## 7.1. Corrosion Behavior

Corrosion behavior was studied by a potentiodynamic experiment after stabilization of the OCP. The polarization curves for the composite coatings with GO-based and CNT-based pigments after immersion in sodium chloride solution are shown in Figure 7.1. From Figure 7.1.a, the corrosion potential and the corrosion rate can be determined for the graphene oxide and nitrogen-doped graphene oxide composite coatings. Two types of corrosion—uniform and pitting—occur in the pure epoxy coating after degradation. The potential of pitting corrosion is 1.16 V. The addition of GO in the composition does not prevent pitting corrosion, and the corrosion rate increased from 3.1E-05 mm/yr (epoxy coating) to 1.1E-04 mm/yr (with GO pigment).

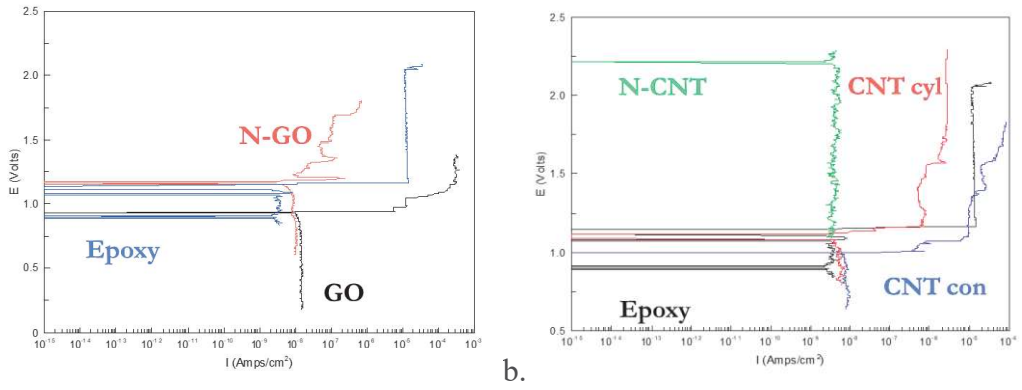


a. b.

**Figure 7.1.** Polatization curves for (a.) pure epoxy coating and composite coating with graphene oxide and nitrogen-doped graphene oxide pigments; (b.) cylindrical, conical, and nitrogen-doped carbon nanotubes composite coatings after immersion degradation.

The composite coating with nitrogen-doped GO pigment prevents the coating from pitting corrosion, and the passivation effect is shown. The passivation potential and critical current are equal to 1.2 V and 2.4E-07 A/cm$^2$, respectively. The passive current is equal to 8.9E-03 μA/cm$^2$, and the second passive region can be determined in Figure 4.18.a. Adding conical carbon nanotubes in the composition shows similar behavior of the passivation potential, critical current, and passive current, which are 1.0 V, 7.2E-07 A/cm$^2$, and 4.2E-07 A/cm$^2$, respectively.

The corrosion current and potential calculated from the Tafel region of the polarization curves are shown in Table 7.1.

**Table 7.1.** Electrochemical characteristics of the composite coating after immersion degradation.

| Sample | $I_0$, μA/cm$^2$ | $E_0$, V | r (mm/yr) |
|---|---|---|---|
| Epoxy | 2.9E-03 | 0.90<br>Epit=1,16 | 3.1E-05 |
| GO | 1.0E-02 | 0.94<br>Epit=0,94 | 1.1E-04 |
| N-GO | 5.1E-03 | 1.16 | 5.4E-05 |
| CNTcon | 7.2E-03 | 0.99 | 7.6E-05 |
| CNTcyl | 5.7E-03 | 1.09 | 6.0E-05 |
| N-CNT | 2.5E-03 | 2.21 | 2.6E-05 |

Carbon nanotubes perform better than graphene oxide pigments, which prevent the coating from pitting corrosion. Adding cylindrical CNT caused a slightly lower corrosion current than adding conical CNT. The corrosion potential is increased from conical to cylindrical CNT composite coating. Nitrogen doping decreases the corrosion rate and increases the potential of the corrosion, and a limited current density can be observed due to the diffusion process.

## 7.2. Electrochemical Impedance Spectroscopy

From the electrochemical analysis, the way in which the coating degrades can be determined. The Nyquist plot of the composite coating with graphene oxide, nitrogen-doped graphene oxide, and conical, cylindrical, and nitrogen-doped carbon nanotubes are shown in Figures 7.2.a and 7.2.b, respectively.

An equivalent circuit, illustrated in Figure 6.3, is used to analyze the data and calculate the electrochemical parameters. The first semicircle (Figure 7.2) describes the solvent–coating interface, and the constant phase element of the coating and pore resistance could be calculated.

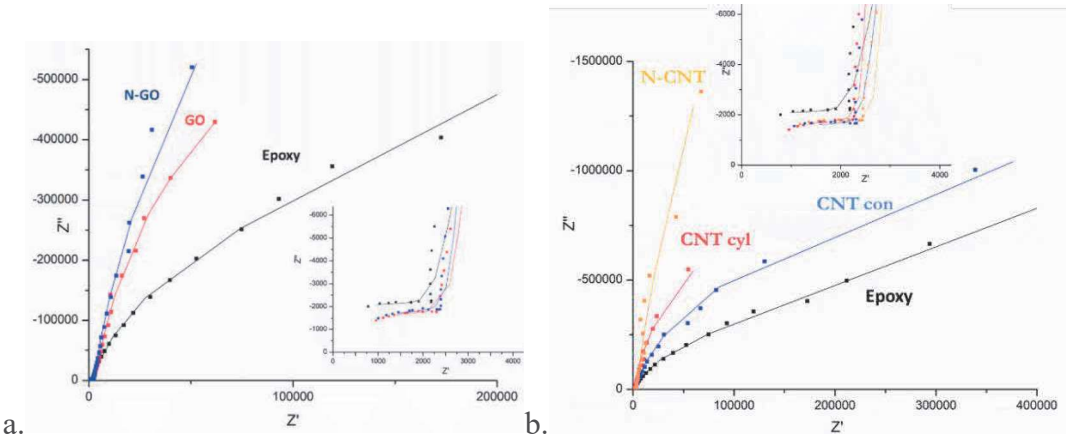


**Figure 7.2.** The electrochemical impedance study in the Nyquist plot of the samples after the exposure salted water (a.) pure epoxy coating, and composite coating with graphene oxide and nitrogen-doped graphene oxide pigments; (b.) cylindrical, conical, and nitrogen-doped carbon nanotubes composite coatings.

Table 7.2 displays the results calculated from the fitting curve using the two-time-constant equivalent circuit. The pore resistance decreased significantly in comparison with the initial resistance. The results are equivalent to the fourth step of the corrosion degradation process when the metal starts to corrode freely. The epoxy coating showed the lowest pore resistance and corrosion resistance. The carbon-based pigments improve the coating's resistance. However, the GO composite coating has a high corrosion rate and does not prevent pitting corrosion from occurring. As seen from the EIS data, the pore and corrosion resistance is much higher than in the pure epoxy coating. This phenomenon might be happening due to the lower water intake during immersion degradation, which will be described in Chapter 7.4. Nitrogen doping of the graphene oxide improves the coating's resistance. The water intake cannot be calculated from the EIS data because the corrosion process has started and the coating is not in the water intake stage.

**Table 7.2.** Electrochemical parameters calculated from electrochemical impedance measurements after immersion degradation.

| | $CPE_{coating}$, $nFs^{n-1}/cm^2$ | n | $R_{pore}$, $\Omega/cm^2$ | $CPE_{dl}$, $nFs^{n-1}/cm^2$ | n | $R_{corr}$,$M\Omega/cm^2$ |
|---|---|---|---|---|---|---|
| Epoxy | 0.034 | 0.99 | 3504 | 0.55 | 0.95 | 1.3 |
| GO | 0.037 | 0.98 | 3262 | 0.72 | 0.96 | 8.4 |
| N-GO | 0.058 | 0.99 | 3360 | 0.53 | 0.97 | 9.8 |
| CNTcyl | 0.64 | 0.99 | 3233 | 0.43 | 0.99 | 6.1 |
| CNTcon | 0.053 | 0.98 | 3095 | 0.63 | 0.97 | 3.8 |
| N-CNT | 0.049 | 0.99 | 3371 | 0.51 | 0.98 | 83 |

The double-layer capacity is low due to the initial step of the corrosion process. The Nyquist plots of the composite coatings with cylindrical, conical, and nitrogen-doped carbon nanotubes pigments are shown in Figure 7.2.b. The cylindrical and nitrogen-doped carbon nanotubes demonstrate higher resistance than the conical CNT composite coating, which agrees with the corrosion results. The composite coating with nitrogen-doped carbon nanotubes provided high pore and corrosion resistance.

## 7.3. Surface Analysis

The changes in the surface profile were investigated by field emission scanning electron microscopy. Figure 7.3 shows the electron microimages of the pure epoxy coating and the composite coatings with graphene oxide and nitrogen-doped graphene oxide after immersion in NaCl solution before and after the potentiodynamic experiment.

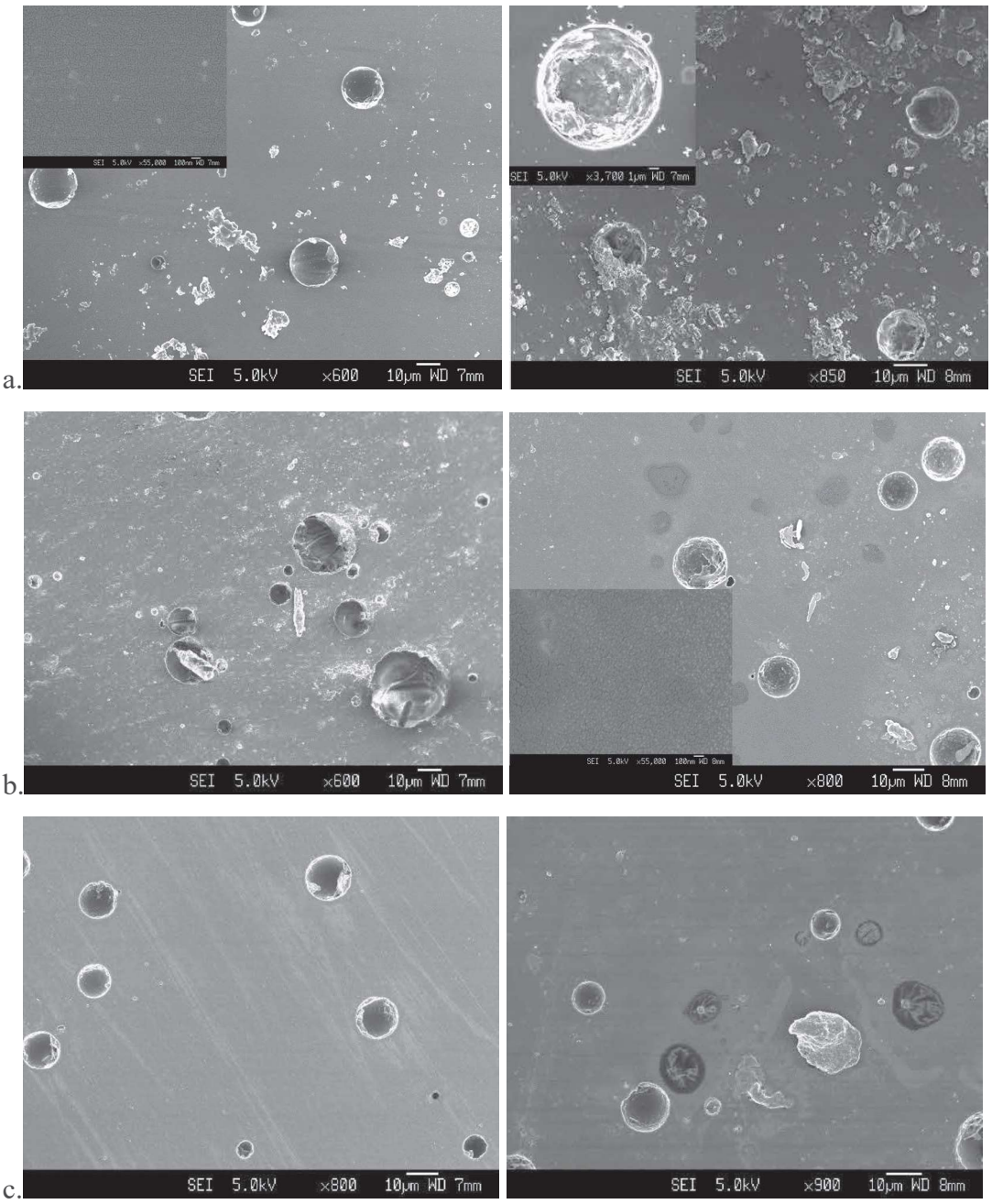


**Figure 7.3.** FESEM images of (a.) epoxy coating; (b.) graphene oxide composite coating; (c.) Nitrogen-doped graphene oxide, after immersion degradation before (left) and after (right) potentiodynamic experiment.

The surface profile of the epoxy coating described in Figure 7.3.a changes under immersion. The surface roughness increased, and nanocracks can be determined in high-resolution images. After corrosion testing, the propagation of spherical defects is observed. Figure 7.3.b and c. show the FESEM images of the GO

and N-GO composite coatings. The dark spots in Figure 7.3. b and c (right) correspond to the blisters that formed during the water adsorption and polarization experiment. The depth of the nanocracks increases under the corrosion process. Nitrogen doping improves the surface profile, which appears undamaged; the bubble defects observed are the same as before immersion. (Figure 5.5.c) The surface of the N-GO composite coating looks differently; however, no pits are observed. The formation of the dark defects corresponds to the propagation of uniform corrosion.

a.

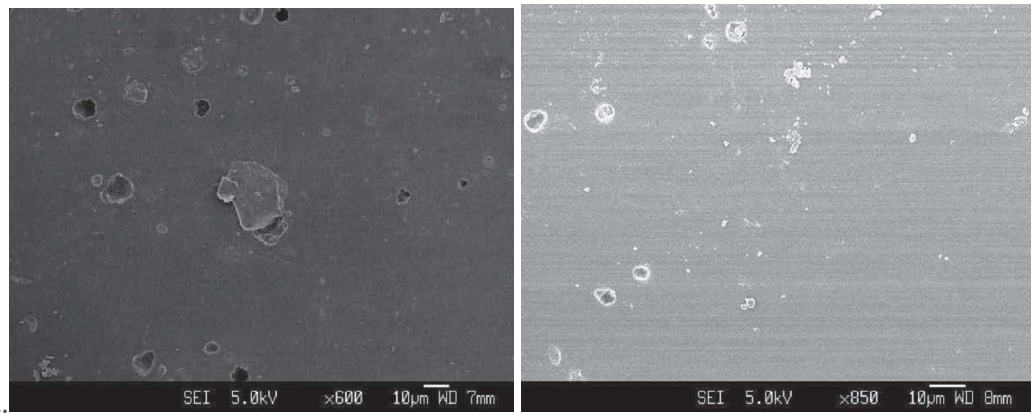


b.

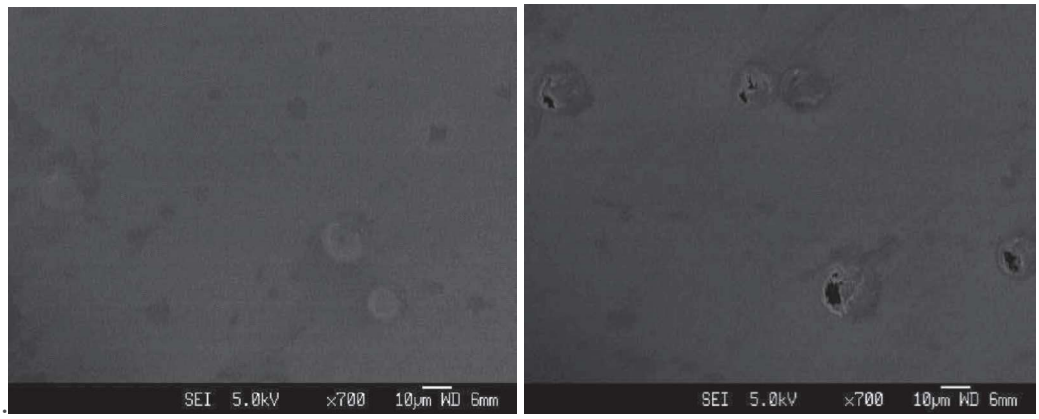

c. 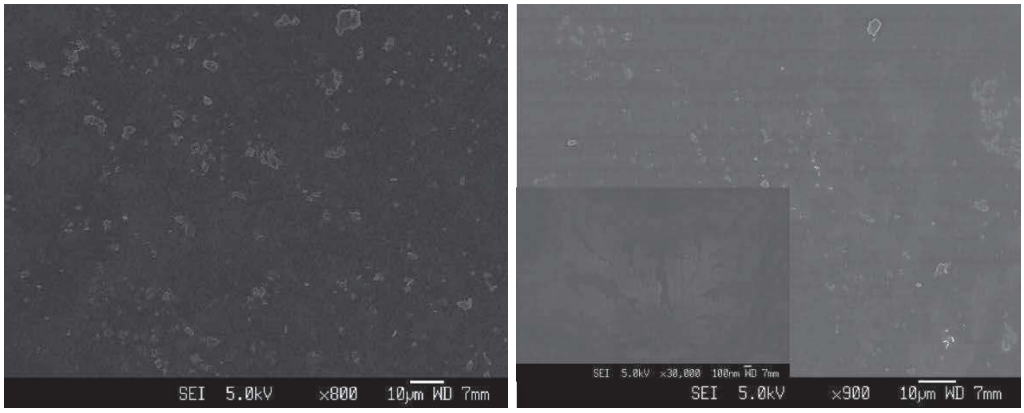


**Figure 7.4.** FESEM images of (a.) cylindrical CNT; (b.) conical CNT; (c.) nitrogen-doped CNT composite coating, after immersion degradation before (left) and after (right) potentiodynamic experiment.

Figure 7.4 demonstrates the microimages of the composite coatings with cylindrical, conical, and nitrogen-doped carbon nanotubes pigments after immersion. The composite coating with cylindrical CNT has some minor defects that do not affect the corrosion process. Based on the corrosion parameters that were calculated from the Tafel region of the polarization curve, the conical CNT composite coating has the highest corrosion rate in comparison with other carbon-nanotubes-based coatings. The blisters that are observed in Figure 7.4.b were formed during immersion and were broken under the corrosion process. The pore and corrosion resistance of the nitrogen-doped CNT composite coating is very high, also demonstrating a low corrosion rate; the FESEM images show an undamaged surface after the immersion experiment. The corrosion had a slight effect on the formation of uniform nanocracks.

## 7.4. Water Intake

The coating has a porous structure that absorbs moisture or water. Diffusion is critical in the corrosion process. The primary mechanism of corrosion protection is a barrier to the environment or the absorption of molecules or ions. The volume of the absorbed water has an effect on the performance of the coating.

The samples of the coated metal were weighed before and after the immersion experiment, and the volumes of the solution intake are shown in Figure 7.5. The

diagram shows that nitrogen-doped graphene oxide composite coating has the highest volume of adsorbed solution, but the protective properties of the composite coating are better than those of the epoxy coating or the GO composite coating. The main reason for this is the formation of hydrogen bonds between nitrogen-containing groups, such as pyridines, of the nitrogen-doped graphene oxide and water molecules. The FTIR analysis described in Chapter 7.5 will give information about the degradation process of the coating and the protection mechanism of the carbon-based pigments. The adding of graphene oxide in the composition decreases the absorption of the solution; however, it does not stop the degradation process, and the coating provides worse protection from pitting and uniform corrosion.

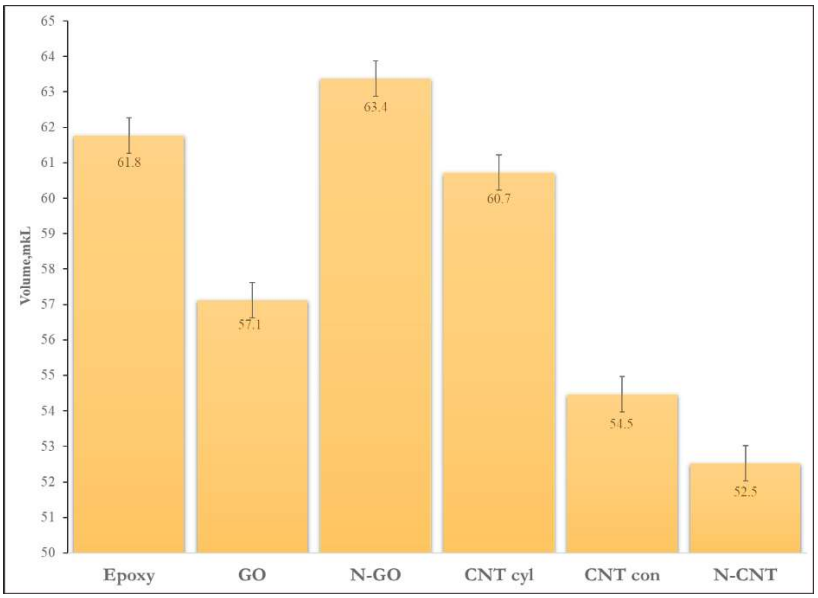


**Figure 7.5.** Water intake during the immersion experiment.

Carbon nanotubes prevent the diffusion of the solution and lower the adsorbed volume of the solution. Carbon nanotubes improve the hydrophobicity of the coating compared with graphene-oxide-based pigments. [1] The presence of defects in the conical CNT, which are more defective than the cylindrical CNT, prevents water diffusion. The hydrogen bonding between the nitrogen groups in the N-CNT prevents subsequent solution penetration. Carbon nanotubes, in contrast to graphene oxide, can absorb chlorine ions and oxygen, which improves corrosion protection. [2]

## 7.5. Degree of Degradation

FTIR spectroscopy is very informative in understanding the aging process under certain conditions. Figure 7.6 demonstrates the FTIR spectra in the wavelength range from 1650 $cm^{-1}$ to 3700 $cm^{-1}$ for the composite coating with different compositions before and after the immersion test. The full FTIR spectra are shown in Figure A.8 and Figure A.9. The character of the changes is different for composite coatings with different compositions. The different ways of coating degradation during the immersion test can be determined. The intensity of the broad peak around 3450 $cm^{-1}$, corresponding to the hydroxyl bond, dropped dramatically for some coatings, such as the pure epoxy coating and the composite coatings with nitrogen-doped graphene oxide and cylindrical carbon nanotubes (Figure 7.6.a and b). Significant changes in the intensity of the methyl band are observed, and a peak corresponding to the carbonyl bond with a maximum of 1720 $cm^{-1}$ appeared. These changes are happening due to the photo-oxidation of alkyd and phenyl groups (the same happens under exposure to UV radiation; see Chapter 6.4) and the hydrolysis of the aromatic ether linkage units [3]

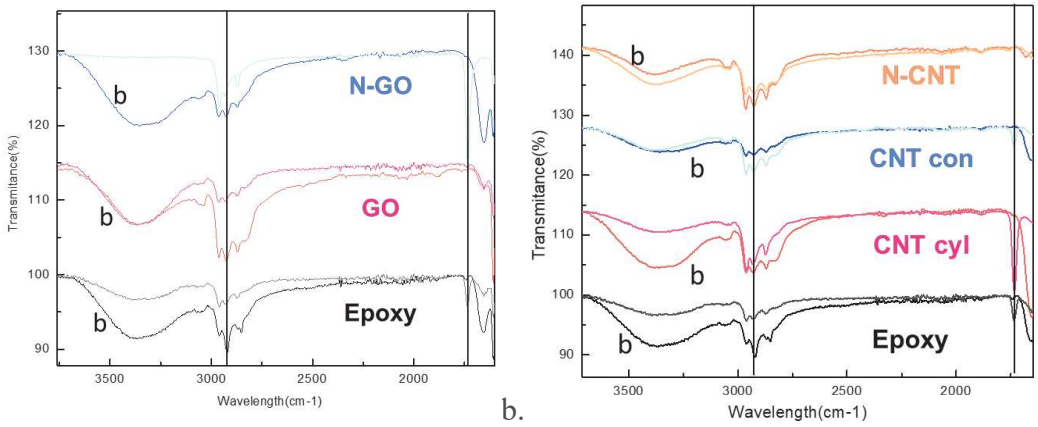


a. b.

**Figure 7.6.** ATR-FTIR spectra of (a.) epoxy coating and graphene oxide-based composite coatings; (b.) carbon nanotubes-based composite coatings before and after immersion exposure. (b-before immersion)

Figure 7.7.a shows the FTIR spectra of the epoxy resin in the wavelength range of 1700 $cm^{-1}$ to 600 $cm^{-1}$. A decrease in intensity of the bonds in the aromatic

ring at 1510 $cm^{-1}$ and 830 $cm^{-1}$ and vibrations of etheric bonds are observed due to degradation of the coating in the corrosive environment. The highly cross-linked areas of the coating become the initiator of the hydrolytic degradation in sodium chloride solution and under UV light, forming holes that propagate the corrosion. [4] The composite coating with conical CNT also degrades by the same mechanism; however, adding CNT pigments prevents the coating from degradation, and the intensity of the hydroxyl, methyl, and carbonyl bonds does not make a great difference. For the pure epoxy coating and the composite coatings with nitrogen-doped GO and cylindrical and conical CNT pigments, the carbonyl index was calculated and shown in Figure 7.8. The lowest degree of degradation is for the conical CNT composite coating, followed by the epoxy coating and the cylindrical CNT composite coating. The degree of degradation correlates with the volume of the adsorbed solution, which enhances the degradation process.

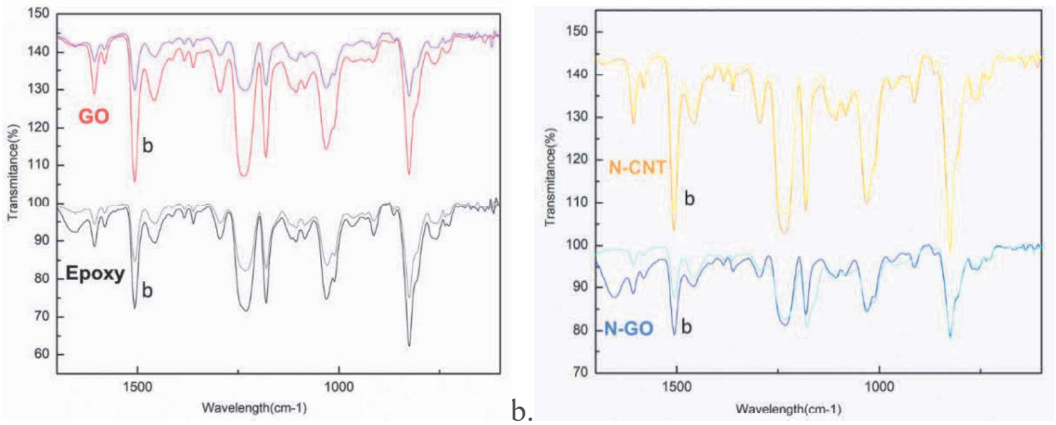


**Figure 7.7.** ATR-FTIR spectra of (a.) epoxy coating and graphene oxide composite coatings; (b.) nitrogen-doped graphene oxide and nitrogen-doped carbon nanotubes composite coatings before and after immersion exposure. (b-before immersion)

The change in the intensity of the hydroxyl bond and the appearance of the peak corresponding to the carbonyl bond are not observed for the composite coating with GO (Figure 7.6.a). However, from Figure 7.7.a, the significant drop in the intensity can be determined for almost all peaks, such as the stretching vibration of the -C-O- and aromatic ring, which means propagation in the degradation of the polymer chain.

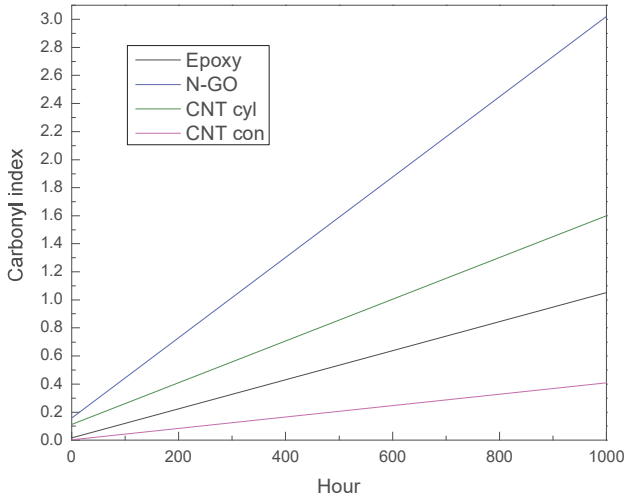


**Figure 7.8.** Carbonyl index for the composite coatings before and after immersion degradation.

From Figure 7.7.b, however, it can be determined that the nitrogen-doped graphene oxide composite coating has a high intensity of the carbonyl bond and that the intensity of the ether bond does not change, which means that the presence of nitrogen prevents the coating from hydrolytic degradation. The FTIR spectra of the composite coating with nitrogen-doped carbon nanotubes show no difference before and after immersion, which indicates an absence of significant degradation.

## 7.6. Mechanical Properties

The effect of water absorption on the mechanical properties will be described in this chapter. Figure 7.9 demonstrates the changes in the adhesion and pencil hardness for the composite coatings with graphene-oxide-based and carbon-nanotubes-based pigments.

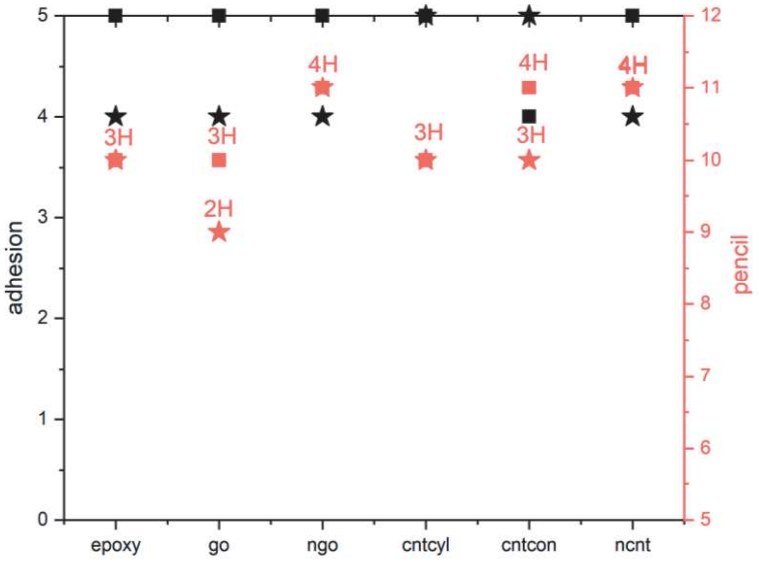


**Figure 7.9.** Adhesion and hardness of the coatings before and after immersion degradation.

The adhesion of the coating shows minor changes during the immersion experiment. For some of the samples, such as the epoxy coating and the composite coatings with graphene oxide, nitrogen-doped graphene oxide, and nitrogen-doped carbon nanotubes, the removed area is less than 5%.

**Table 7.3.** The mechanical properties of the coatings after immersion .

| | Adhesion | Hardness |
|---|---|---|
| Epoxy | 4B | 3H |
| GO | 4B | 2H |
| N-GO | 4B | 4H |
| CNTcyl | 5B | 3H |
| CNTcon | 5B | 3H |
| N-CNT | 4B | 4H |

The results of the mechanical tests are displayed in Table 7.3. The coating hardness on the pencil scale shows no changes for most of the samples. The graphene oxide composite coating demonstrates the lowest hardness due to the high degree of degradation, which was described in the previous chapter.

## 7.7. Summary

In this chapter, the effect of the sodium chloride solution on the coating's performance was investigated. The structural feature of the pigment has a strong effect not only on water absorption but also on the degradation process.

Nitrogen doping improves the properties of the pigment, and doped samples perform better than undoped samples. Using FTIR confirmed that the nitrogen-containing group prevents the coating from degradation, especially from hydrolytic degradation. The ability to absorb ions and molecules, a characteristic of carbon nanotubes, enhances the performance of carbon-nanotubes-based coatings.

## References

[1] H. Jeon, J. Park, M. Shon, *J. Ind. Eng. Chem.* **2013**, *19*, 849–853.

[2] E. V. Butyrskaya, L. S. Nechaeva, S. A. Zapryagaev, *Comput. Theor. Chem.* **2016**, *1090*, 1–5.

[3] S. Jana, W.-H. Zhong, *J. Appl. Polym. Sci.* **2007**, *106*, 3555–3563.

[4] B. Ramezanzadeh, M. M. Attar, *Mater. Chem. Phys.* **2011**, *130*, 1208–1219.

# Chapter 8

# Weathering Degradation of the Composite Coating

*In real-life situations, many different factors affect the coating, such as solar radiation, water splash, moisture, and dust. Ultraviolet radiation, together with moisture, has a strong effect on the coating's damage. The simulation experiments tested the coating's performance in real-life situations. The samples were exposed to UV radiation together with moisture based on the standard BS EN ISO 11507* [1] *for 1000 hours. After the simulation test, the corrosion properties, surface profile, and mechanical properties were investigated, and the degree of degradation was calculated for the composite coatings.*

## 8.1. Corrosion Behavior

The potentiodynamic experiment was conducted for the samples after weathering degradation. The polarization curves for the pure epoxy coating and the composite coatings with graphene-oxide-based and carbon-nanotubes-based pigments are shown in Figure 8.1. Ultraviolet radiation, together with moisture, had a substantial effect on the coatings' degradation, and the polarization curves changed significantly.

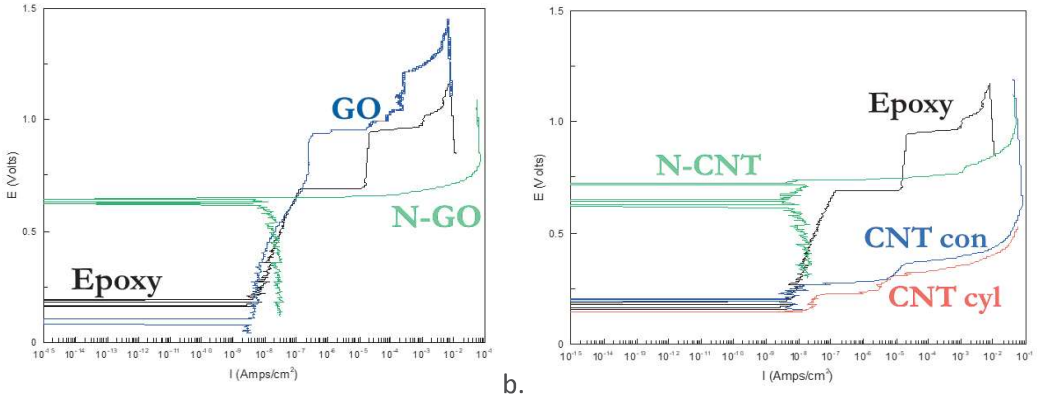


a. b.

**Figure 8.1.** Polarization curves for (a.) pure epoxy coating and composite coating with graphene oxide and nitrogen-doped graphene oxide pigments; (b.) cylindrical, conical, and nitrogen-doped carbon nanotubes composite coatings after weathering degradation.

Localized forms of corrosion, such as pitting or crack corrosion, can be determined from the polarization curves for all samples. The addition of only one pigment cannot provide full protection in such aggressive environments. From Figure 8.1.a, the positive influence of nitrogen doping is observed. Table 8.1 demonstrates the electrochemical parameters that were calculated from the polarization curves for the composite coatings. The composite coating with nitrogen-doped graphene oxide demonstrates a high potential of corrosion and a limited current, which is equal to 2.4E-08 A/cm$^2$. Adding N-GO in the coating's composition decreases the corrosion rate 1.5 times. Graphene oxide also decreases the corrosion rate; however, the potential of corrosion is lower than for pure epoxy resin.

**Table 8.1.** Electrochemical characteristics of the composite coating after weathering degradation.

| Sample | $I_0$, μA/cm$^2$ | $E_0$, V | r (mm/yr) |
|---|---|---|---|
| Epoxy | 6.0E-03 | 0.18/**Epit = 0.69/0.96** | 6.3E-05 |
| GO | 3.1E-03 | 0.10/**Epit=0,95** | 3.3E-05 |
| N-GO | 4.3E-03 | 0.64/**Epit=0.66** | 4.5E-05 |
| CNT con | 6.1E-03 | 0.19/**Epit = 0.28/0.39** | 6.4E-05 |
| CNT cyl | 1.5E-02 | 0.14/**Epit = 0.22/0.34** | 1.6E-04 |
| N-CNT | 3.9E-03 | 0.64/**Epit = 0.75** | 4.1E-05 |

Cylindrical and conical carbon nanotubes do not prevent the coating from weathering degradation, and the corrosion rate is higher than that for the pure epoxy coating. FTIR spectroscopy will give more information about the degradation process. Nitrogen-doped carbon nanotubes, as well as the nitrogen-doped graphene oxide coating, demonstrated a limited current due to the diffusion process. For the N-CNT coating, the potential of corrosion and the corrosion rate are 0.64 V and 3.9E-03 μA/cm$^2$, respectively.

## 8.2. Electrochemical Impedance Spectroscopy

Electrochemical impedance spectroscopy, which gives information about the coating's damage, was conducted after the weathering test. The Nyquist plots of the composite coatings with the different compositions are illustrated in Figure 8.2. Based on the classification described in Chapter 3.4.1, the coatings are very damaged, and their condition is equal to the last stage of coating degradation.

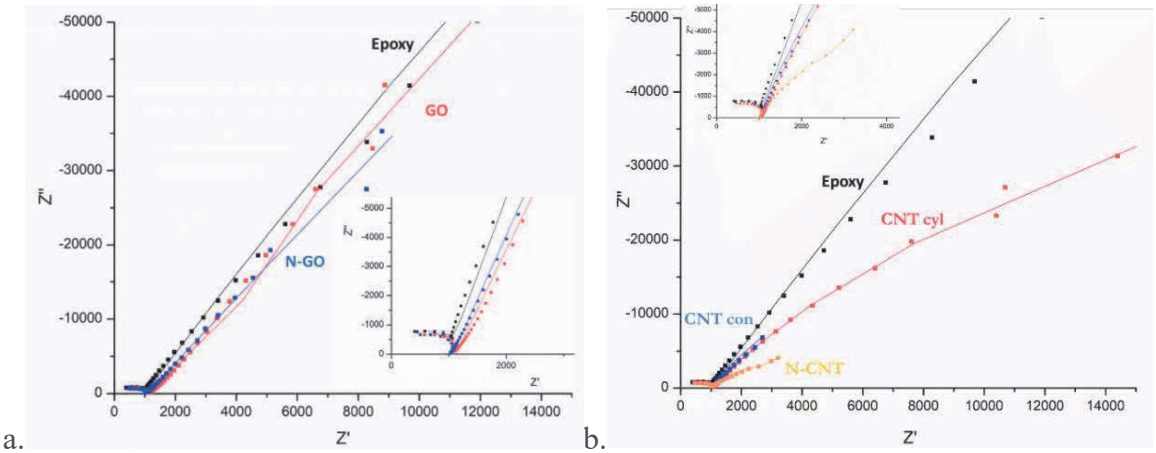


**Figure 8.2.** The electrochemical impedance study in the Nyquist plot of the samples after the exposure to the weathering (a.) pure epoxy coating, and composite coating with graphene oxide and nitrogen-doped graphene oxide pigments; (b.) cylindrical, conical, and nitrogen-doped carbon nanotubes composite coatings.

Figure 8.2.a illustrates the Nyquist plot of the epoxy coating and the composite coatings with graphene oxide and nitrogen-doped graphene oxide. Two semicircles are observed, and the data were fitted using a two-time-constant equivalent circuit, which is shown in Figure 6.3. The pore resistance for the epoxy coating drops from 7.7 MΩ/cm$^2$ to 1097 Ω/cm$^2$, and the corrosion resistance is 3.8 MΩ/cm$^2$. The polarization resistance increases with the addition of graphene oxide, which means a decrease in corrosion, in agreement with the results obtained from the potentiodynamic experiment. The pore resistance remains similar for all the coating samples, as demonstrated in Table 8.2.

**Table 8.2.** Electrochemical parameters calculated from electrochemical impedance measurements after weathering degradation.

| | $CPE_{coating}$, $nFs^{n-}/cm^2$ | n | $R_{pore}$, Ω/cm$^2$ | $C_{dl}$, $\mu Fs^{n-1}/cm^2$ | n | $R_{corr}$,MΩ/cm$^2$ |
|---|---|---|---|---|---|---|
| Epoxy | 0.065 | 0.98 | 1097 | 0.01 | 0.88 | 3.8 |
| GO | 0.12 | 0.99 | 1154 | 0,39 | 0.85 | 9.8 |
| N-GO | 0.13 | 0.99 | 1066 | 1.5 | 0.86 | 9.9 |
| CNTcyl | 0.12 | 0.98 | 1079 | 1.4 | 0.86 | 0.19 |

| | | | | | | |
|---|---|---|---|---|---|---|
| CNTcon | 0.13 | 0.98 | 1035 | 6.9 | 0.87 | 0.15 |
| N-CNT | 0.14 | 0.99 | 1085 | 40 | 0.84 | 0.02 |

From Figure 8.2.b, the electrochemical parameters for the composite coatings with cylindrical, conical, and nitrogen-doped carbon nanotubes can be calculated. The behavior of the composite coating with cylindrical and conical CNT is similar, and the polarization resistances are equal to 0.19 and 0.15 $M\Omega/cm^2$, respectively. The corrosion resistance of the nitrogen-doped carbon nanotubes is low (0.02 $M\Omega/cm^2$) and the double-layer capacity is high (40 $\mu Fs^{n-1}/cm^2$), which indicates that the delamination process has taken place.

## 8.3. Surface Analysis

The weathering degradation is severe for the coating, and the coating surface changed significantly. Figure 8.3 demonstrates FESEM images of the epoxy coating and the coatings with graphene oxide and nitrogen-doped graphene oxide. In comparison with the initial surface profile (Figure 5.5), after the ultraviolet radiation with moisture experiment, the surface looks damaged. From Figure 8.3.a and b (left), coating cracks and a wide deepening can be seen on the surfaces of the epoxy coating and the graphene oxide composite coating after weathering degradation. In the corrosion environment, the coating surface of the epoxy coating and that of the GO-based coating perform differently. The epoxy coating corrodes uniformly with a prolongation of the wide deepenings; however, the GO-based coating does not show the recesses but only a defective flat surface with a broad and deep crack, which causes the rapid increase in current density.

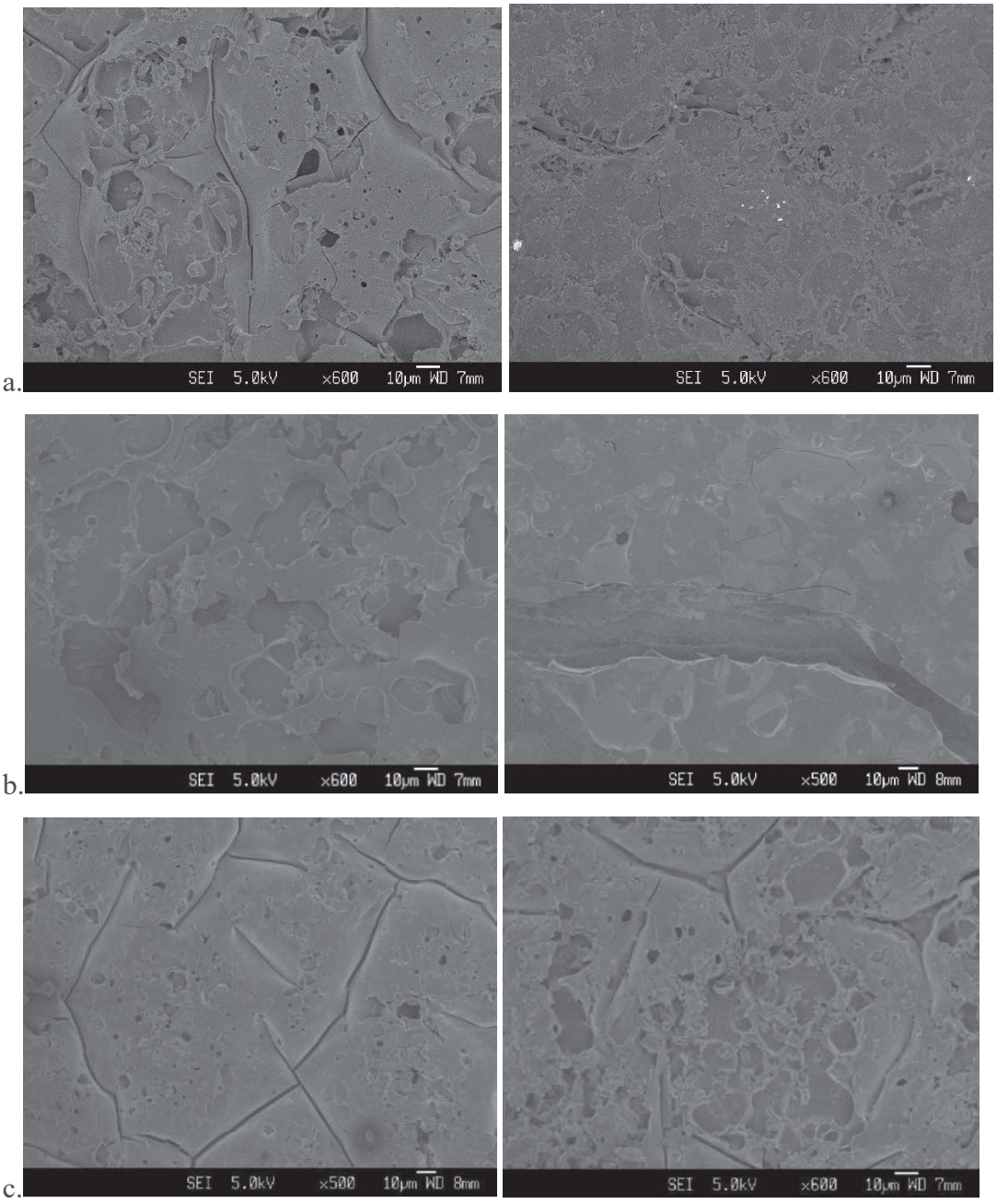


**Figure 8.3.** FESEM images of (a.) epoxy coating; (b.) graphene oxide composite coating; (c.) nitrogen-doped graphene oxide, after weathering degradation before (left) and after (right) potentiodynamic experiment.

Figure 8.3.c shows the nitrogen-doped graphene oxide composite coating before and after the polarization test, which was performed after weathering degradation. The surface of the N-GO composite coating degrades differently from the surfaces of the epoxy and GO coatings. Surface cracks and defects with a

diameter of less than 10 µm can be observed in Figure 8.3.c(left). During the potentiodynamic experiment, spreading of the defects is detected.

Low-magnification FESEM images were made to investigate the surface profile changes during the potentiodynamic test (Figure 8.4) for the composite coating with cylindrical carbon nanotubes. Figure 8.4.a demonstrates a rough surface with cracks, which formed during the coating degradation. After the corrosion process, the thickness of the coating drops heterogeneously, and crack propagation is observed.

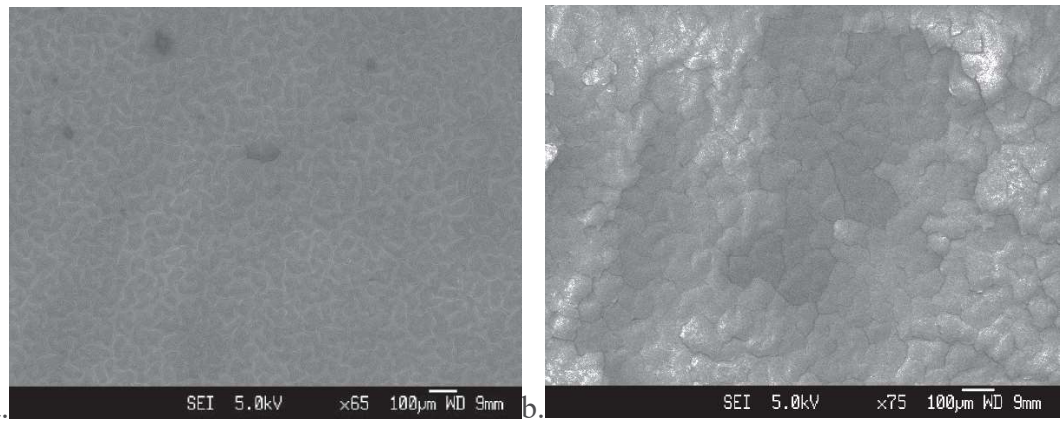


**Figure 8.4.** Low magnification FESEM images of cylindrical carbon nanotubes composite after weathering degradation (a.) before and (b.) after corrosion experiment.

Scanning electron images of the composite coatings with cylindrical, conical, and nitrogen-doped carbon nanotubes after weathering degradation are shown in Figure 8.5. The composite coatings with conical and cylindrical carbon nanotubes show similar surface profiles after weathering degradation based on SEM images (Figure 8.5.a and b, left). During the corrosion process, the surface deforms uniformly, but formation of cracks and holes is observed for cylindrical and conical CNT-based coatings, respectively, which cause localized corrosion to occur, and this will become a critical factor in the corrosion process.

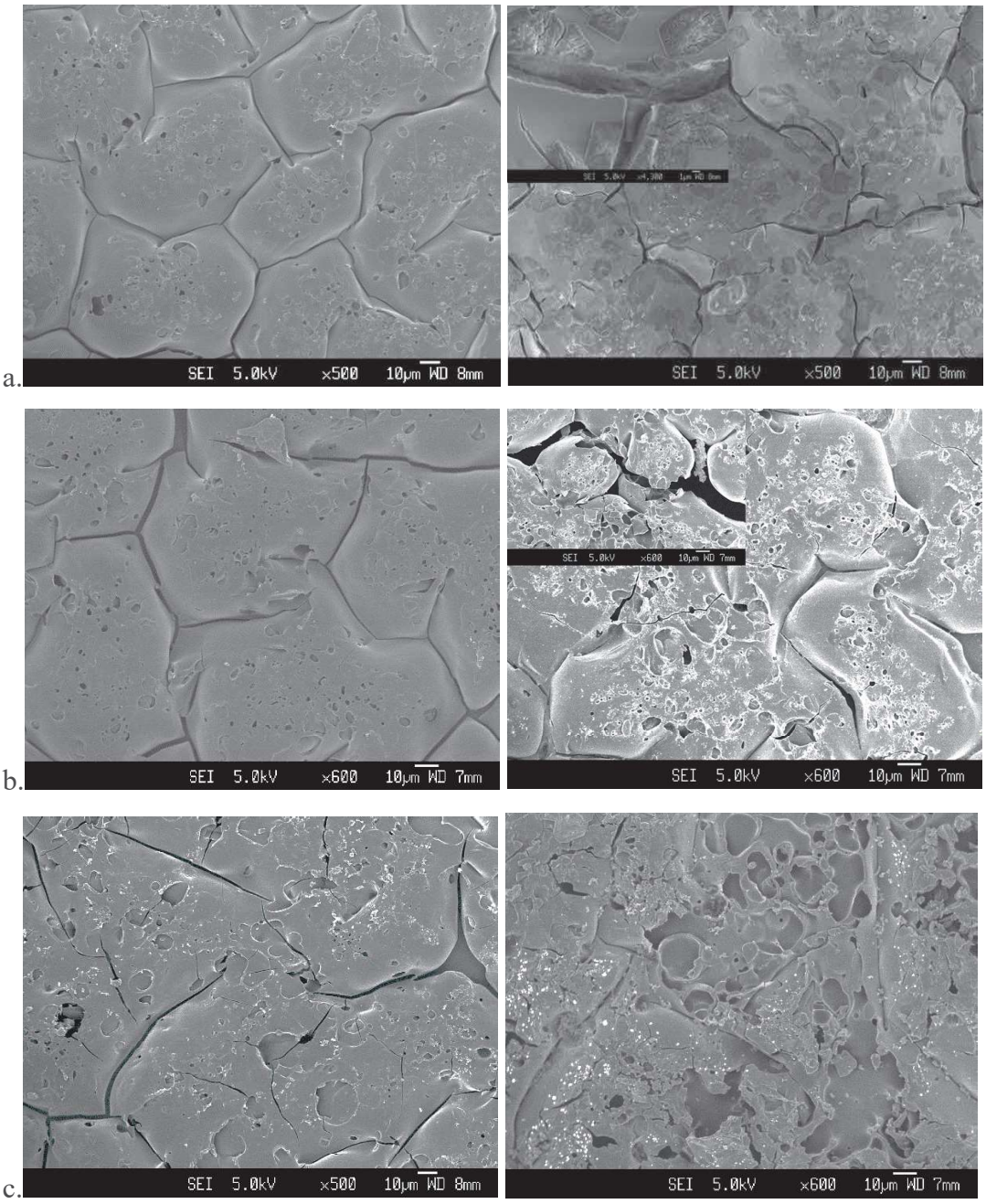


**Figure 8.5.** FESEM images of (a.) cylindrical CNT; (b.) conical CNT; (c.) nitrogen-doped CNT composite coating, after weathering degradation before (left) and after (right) potentiodynamic experiment.

The nitrogen-doped carbon nanotubes composite coating demonstrates a low corrosion rate and a high potential of corrosion. From the FESEM images shown in Figure 8.5.c, it can be determined that the surface before the corrosion is defective

with recesses with a diameter of less than 20 µm. During the corrosion, an increase in diameter of the recesses is observed.

## 8.4. Degree of Degradation

The influence of UV radiation and water condensation is powerful, as was mentioned before. The degradation process was studied by FTIR spectroscopy. The spectra of the composite coatings with GO and CNT-based pigments are shown in Figure 8.6 in the range of wavelengths from 3800 $cm^{-1}$ to 1650 $cm^{-1}$. In Figure A.10 and Figure A.11, ATR-FTIR spectra of the pure epoxy coating and the composite coatings with different compositions are displayed in the range of 600–4000 $cm^{-1}$.

From Figure 8.6.a, which illustrates the FTIR spectra of the pure epoxy coating and the GO-based composite coating, it can be determined that the intensity of stretching on the hydroxyl bond at 3350 $cm^{-1}$ and the intensity of the alkyd units at 2930 $cm^{-1}$ decreased and that the peak corresponding to the carbonyl bond has appeared due to degradation by the photo-oxidation mechanism.

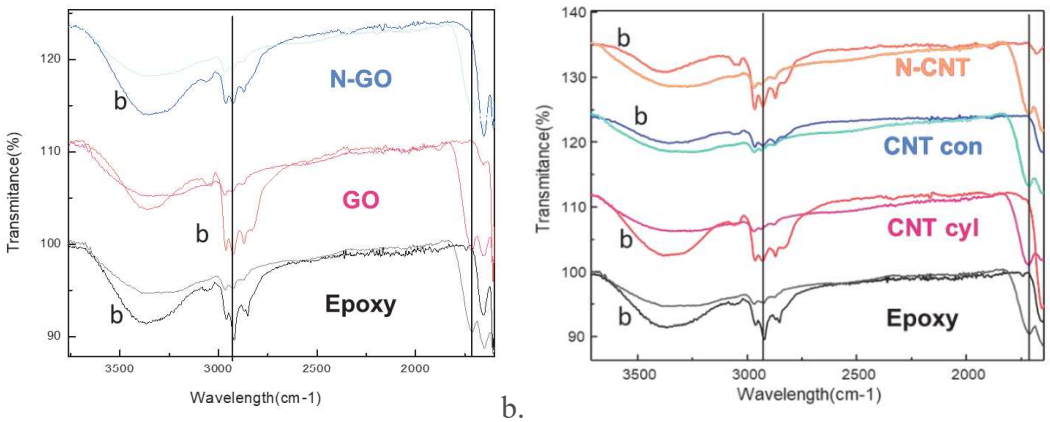


**Figure 8.6.** ATR-FTIR spectra of (a.) epoxy coating and graphene oxide-based composite coatings; (b.) carbon nanotubes-based composite coatings before and after weathering degradation. (b-before degradation)

The composite coating with cylindrical carbon nanotubes demonstrates a similar behavior; however, the intensity of the carboxyl bond for the conical and nitrogen-doped carbon nanotubes slightly increases. A peak at a wavelength of 1720

$cm^{-1}$ is observed in each spectrum. The peak intensity was used for the carbonyl index calculations to determine the degree of coating degradation.

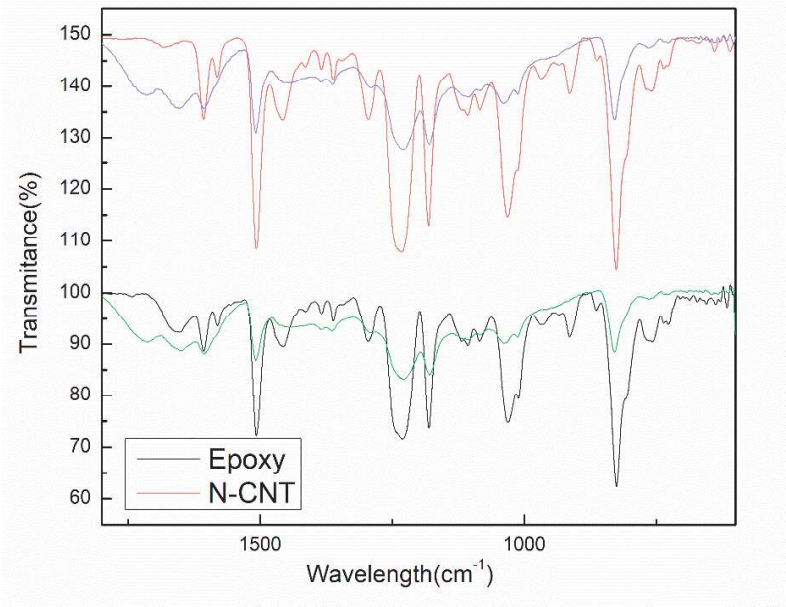


**Figure 8.7.** ATR-FTIR spectra of epoxy coating and nitrogen-doped carbon nanotubes composite coatings before and after weathering degradation (black, red curve - before degradation)

The FTIR spectra of the epoxy coating and the nitrogen-doped carbon nanotubes in the wavelength range of 600–1800 $cm^{-1}$ are illustrated in Figure 8.7. The intensities of most of the peaks drop dramatically for both coatings. The peaks corresponding to aromatic ring stretching at 1600 $cm^{-1}$, 1500 $cm^{-1}$, and 830 $cm^{-1}$, or stretching of the C-O bond at 1230 $cm^{-1}$ and 1030 $cm^{-1}$, change due to the coating's degradation process and breaks in the main polymer chain. The intensity of the peak at 1650 $cm^{-1}$, corresponding to O-H bending vibration, is the only one that increases during the degradation process.

The carbonyl index was calculated for all samples based on the formula described in Chapter 3.3.1. The results plotted versus the duration of the degradation test are shown in Figure 8.8.

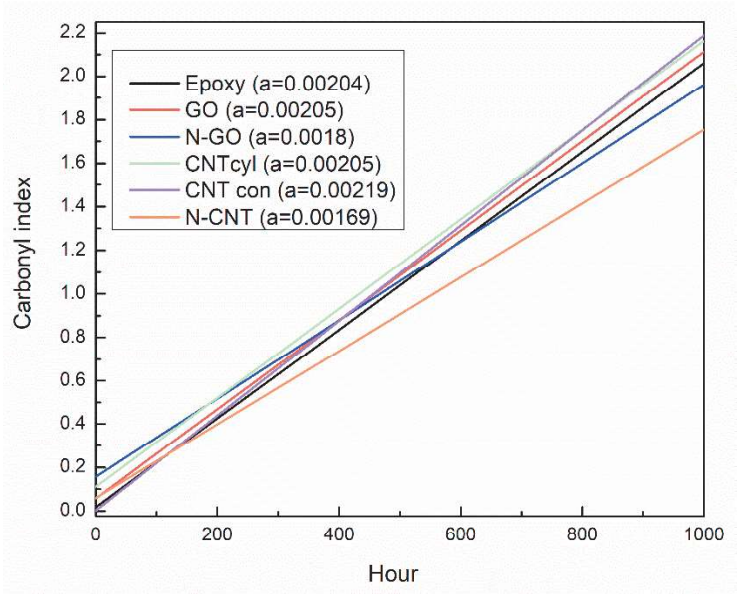


**Figure 8.8.** Carbonyl index for the composite coatings before and after weathering degradation.

The gradient of the line means the degree of coating degradation in a certain environment. The lowest value indicates the lowest degree of degradation. From Figure 8.8, the gradient (a) for each line was calculated. The nitrogen-doped carbon nanotubes composite coating demonstrates the lowest degree of degradation, followed by the composite coating with nitrogen-doped graphene oxide pigment, which indicates that nitrogen-containing groups form additional chemical bonds that prevent coating degradation.

The degree of degradation of the pure epoxy coating is similar to the degree of degradation of the composite coatings with graphene oxide and cylindrical carbon nanotubes, which means that adding only one pigment in the composition is not enough to provide the proper protection and that adding a higher percentage of carbon-based pigments might improve the coating's performance.

## 8.5. Mechanical Properties

Due to the high degradation degree of the coating film, the mechanical properties worsened under UV radiation and water condensation. Figure 8.9

illustrates the adhesion and the hardness on the pencil scale for the epoxy coating and for the graphene-oxide- and carbon-nanotubes-based composite coatings.

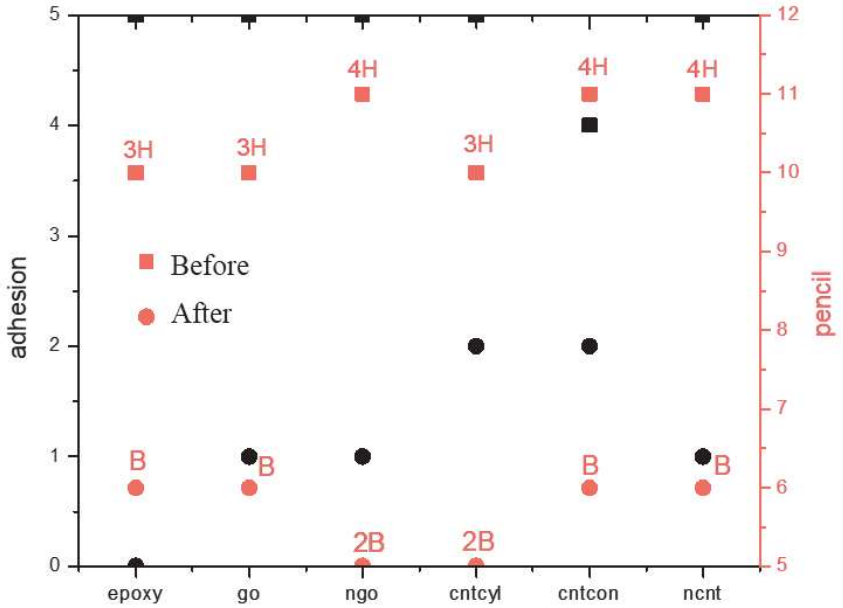


**Figure 8.9.** Adhesion and hardness of the coatings before and after weathering degradation.

The epoxy coating after weathering degradation demonstrates no adhesion, and more than 65% of the coating is removed after the tape pull test. The addition of carbon-based pigments, such as graphene oxide, nitrogen-doped graphene oxide, and nitrogen-doped carbon nanotubes, improves the adhesion, and 35%–65% of the coating is removed. The composite coatings with cylindrical and conical carbon nanotubes demonstrate a 2B grade of adhesion, which indicates the removal of 15% to 35% of the coating. During weathering degradation, the hydroxyl groups responsible for adhesion turned into carbonyl groups.

**Table 8.3.** The mechanical properties of the coatings after weathering degradation.

| | Adhesion | Hardness |
|---|---|---|
| Epoxy | 0B | B |
| GO | 1B | B |
| N-GO | 1B | 2B |
| CNTcyl | 2B | 2B |
| CNTcon | 2B | B |
| N-CNT | 1B | B |

The results of the mechanical tests for the coating after weathering degradation are shown in Table 8.3. The hardness of the epoxy coating drops from 3H to B based on the pencil scale. The hardness of the coating also becomes worse for the composite coating. This is the main reason for its weakening and the breakage of the chemical bonds in the main chain of the polymer matrix.

## 8.6. Summary

Ultraviolet radiation, together with water condensation, has a strong negative effect on the coating's protection properties. The addition of only one pigment is not enough to prevent the coating from degradation and corrosion. In industrial coatings, more than 30 different pigments and additives are used.

The addition of carbon-based pigments improves corrosion protection and the mechanical properties of the coatings except for cylindrical carbon nanotubes. From the surface analysis, it was determined that crack and hole formation is a critical factor in the corrosion process.

Nitrogen doping improves the anticorrosion properties by decreasing the corrosion rate more than 1.5 times. Nitrogen-doped pigments, such as graphene oxide and carbon nanotubes, prevent the coating from degradation in an aggressive environment.

**References**

[1] International Organization for Standardization (ISO), *BS EN ISO 115072001*. **2007**, 1–17.

# Chapter 9

# Conclusion and Future Recommendation

*This chapter is dedicated to the general conclusions, which were drawn from the fundamental research described in Chapters 5–8 based on solving the fundamental problem of creating innovative paints for corrosion prevention. The suggested mechanism of protection by nitrogen-doped carbon materials is described in this chapter. The research was done for conditions similar to industrial conditions to shorten the adaptation process for coatings in a real-factory setting. The investigation of the influence of the concentration of the pigment and nitrogen content is part of future work to make the research broader and deeper and to achieve better coating performance. The field experiment of an industrial coating with pigments synthesized in this work will show the real performance of the anticorrosion pigment in the coating.*

## 9.1. Suggested Mechanism of Protection

In the previous chapters, it was described that carbon-based pigments improve the stability of the coating under UV radiation, corrosive solutions, and weathering. However, it was noted that nitrogen-doped pigments, especially nitrogen-doped carbon nanotubes, provide better protection and show higher performance.

The nitrogen-doped carbon nanotubes composite coating demonstrates high resistance, a low corrosion rate, a low degree of degradation in different environments, a low absorption rate, and good mechanical properties. The main reason for this performance is an interaction between carbon nanotubes and bisphenol A epoxy resin, which is illustrated in Figure 9.1.

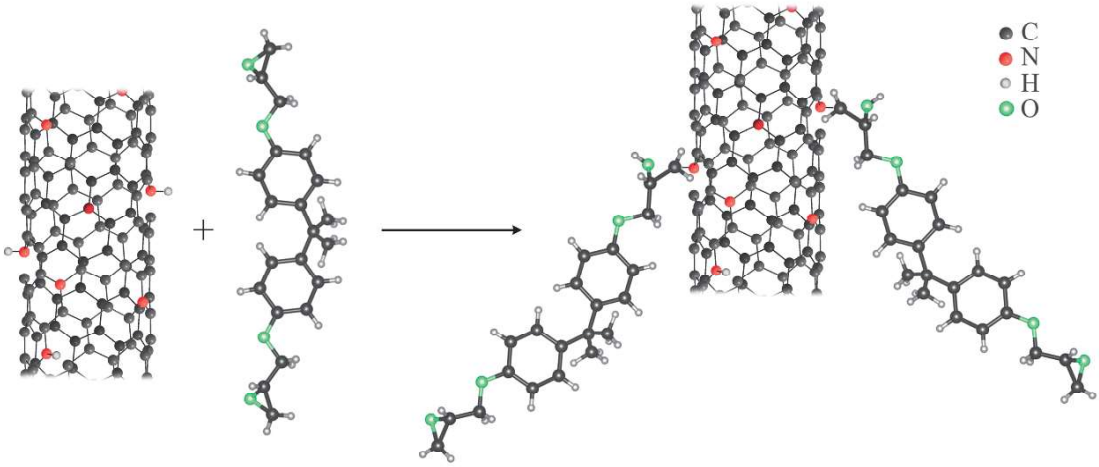


**Figure 9.1.** Mechanism of polymer – pigment interaction.

Based on the XPS results, amine groups are presented in the carbon nanotube structure; the percentage of it can be increased by further oxidation followed by reduction during the synthesis process. The amine groups can form the chemical bonds with the epoxy groups of bisphenol A epoxy resin, which provide better dispersion, a high degree of cross-linking, and resistance to degradation.

## 9.2. General Conclusions

- Carbon-based pigments, such as graphene oxide, nitrogen-doped graphene oxide, and cylindrical, conical, and nitrogen-doped carbon nanotubes, were synthesized for anticorrosion purposes. Graphene oxide was synthesized from graphite using Hammer's method and was used to obtain nitrogen-doped graphene oxide using melamine. By pyrolysis of organic precursors in the reactor, carbon nanotubes with different structures were synthesized. Physicochemical characterization was performed using SEM, TGA, XPS, and elemental analysis. Using acetonitrile precursors during carbon nanotubes synthesis, a nitrogen percentage of 3.9% nitrogen atoms was first achieved and melamine provided a nitrogen doping up to 5.4% on the surface of the nitrogen-doped graphene oxide.

- The composite coatings with five different carbon-based pigments were investigated. The electrochemical parameters of the coatings were obtained using a potentiodynamic experiment and electrochemical impedance spectroscopy. The coating was exposed to three different conditions: ultraviolet radiation, sodium chloride solution, and ultraviolet radiation together with deionized water condensation. The changes in the coating properties were determined by FESEM, ATR-FTIR, and mechanical tests.

- For the first time, a composite coating with nitrogen-doped pigments, such as nitrogen-doped graphene oxide and nitrogen-doped carbon nanotubes, was investigated as anticorrosion pigments. It was shown that nitrogen doping improves the corrosion protection and decreases the corrosion rate more than 3.5 times in comparison with pure epoxy resin.

- The effect of ultraviolet radiation on the coating's degradation process was investigated. The addition of carbon-based pigments prevents the photo-oxidation degradation of the epoxy resin by adsorbing UV light. Carbon nanotubes protect the coating from microcrack formation, which caused pitting corrosion to occur, in comparison with graphene oxide-based pigments.

- Cylindrical carbon nanotubes showed better performance than conical carbon nanotubes because the structure of the pigment plays a primary role in the pigment's contribution, and a more defective structure causes more defects in the coating. However, the defects of the conical carbon nanotubes prevent water absorption during the immersion simulation experiment and lower the resistance of the composite coating; also, the corrosion rate of the coating with conical nanotubes is higher than that of the coating with cylindrical carbon nanotubes.

- During the immersion test, two types of degradation were determined: photo-oxidation and hydrolytic degradation. ATR-FTIR analysis showed that nitrogen doping prevents the coatings from degradation of the main polymer chain, and nitrogen-doped carbon nanotubes also stop the formation of the carbonyl bond.

- Owing to their unique structure and properties, carbon-nanotubes-based pigments demonstrate better performance than graphene-oxide-based pigments. Moreover, they improve the mechanical properties under ultraviolet radiation (adhesion is 1B for graphene-oxide-based coatings and ranges from 2B to 3B for carbon-nanotubes-based coatings), prevent pitting corrosion (after ultraviolet radiation and in immersion degradation tests), and show lower water absorption and a lower degree of degradation in aggressive environments.

- Under weathering degradation, only nitrogen-doped pigments demonstrate a lower degree of degradation than pure epoxy resin, which means that polymer–pigment bonds prevent the coating from degradation under ultraviolet radiation and water condensation. Adding a higher percentage of carbon-based pigments might improve the coating's performance and resistance.

- The mechanism of coating protection by nitrogen-doped carbon nanotubes was determined. The pigment–polymer cross-linking improves the coating's performance, and the corrosion rate decreases in comparison with the pure

epoxy coating, from 5.7E-05 to 1.4E-05 mm/yr for the coating without any degradation, from 8.1E-05 to 1.3E-05 mm/yr for the coating after ultraviolet degradation, from 3.1E-05 to 2.6E-05 mm/yr for the coatings after immersion degradation, and from 6.3E-05 mm/yr to 4.1E-05 mm/yr for the coatings after weathering degradation

## 9.3. Future Recommendation

Corrosion is a fundamental problem, and it is impossible to stop the corrosion process; therefore, research in this area is critical. The development of highly efficient coatings for corrosion protection is crucial. In this chapter, useful future lines of investigation will be described.

### 9.3.1. Investigation of the Concentration Behavior

In the current work, a low concentration of pigment was chosen because of the high degree of agglomeration of the carbon-based pigment and because of the interest of the investigation in the influence of the type of materials on the properties. However, in industrial coating additives, such as dispersants, leveling and wetting agents are used, which control the dispersion of the pigment in the coating binder.

The concentration dependence of the carbon-based pigments, such as carbon nanotubes [1], graphene [2], graphene oxide [3], carbon black [4], was investigated by different authors; however, each system has its critical concentration above which the corrosion properties deteriorate. In Figure 9.2, the effect of the concentration of graphene (G) functionalized by poly(2-butylaniline) (P2BA) is illustrated. The corrosion rate increased, reaching 1% of graphene in coating composition due to the agglomeration of the sheets.

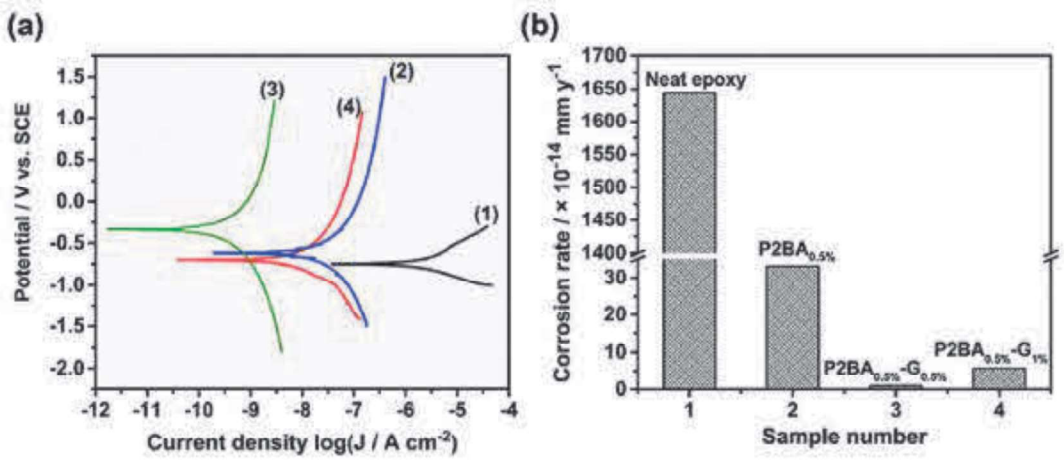


**Figure 9.2.** (a) Polarization curves of (1) neat epoxy, (2) P2BA 0.5%, (3) P2BA 0.5%-G 0.5% and (4) P2BA 0.5%-G 1% composite coatings; (b) corrosion rate of specimens after immersion in 3.5 wt % NaCl aqueous solution for 80 days. [2]

The main objectives of this research are to optimize the pigment percentage and to achieve the highest cost/efficiency ratio. It was suggested that the maximum pigment concentration that provides the highest corrosion protection would shift under exposure to different conditions, such as immersion or ultraviolet radiation.

### 9.3.2. Investigation of the Influence of Nitrogen Doping Content

In this work, novel research was performed based on using nitrogen-doped graphene oxide and nitrogen-doped carbon nanotubes for anticorrosion purposes. A maximum nitrogen percentage of up to 4 wt% in the carbon nanotube structures was achieved using acetonitrile as a precursor in the synthesis reaction. N,N,N',N'-tetramethylethylene-1,2-diamine, pyridine, and n-butylamine are allowed to reach 2.3%, 1.9%, and 2.4% of nitrogen, respectively. [5]

An increase in nitrogen content can be achieved by multistep carbon nanotube functionalization. Carboxylation can be performed by boiling in a 6 M $HNO_3$ solution for 3 h (Figure 9.3). The oxygen content might reach 15%. [6]

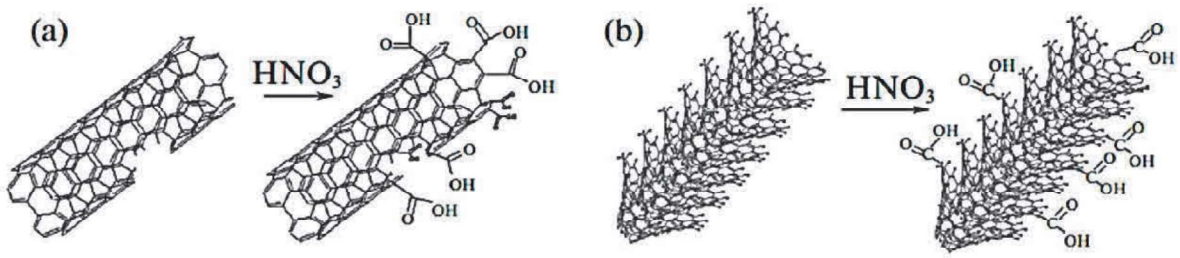


**Figure 9.3.** Scheme of carboxylation of (a) cylindrical and (b) conical carbon nanotubes after treatment with nitric acid. [6]

Dried carboxylated carbon nanotubes can be suspended in $SOCl_2$, followed by a reaction with ethylenediamine, as described in Figure 9.4. Amine functionalized carbon nanotubes allow the formation of a cross-linked polymer–pigment matrix to achieve better dispersion and anticorrosion properties.

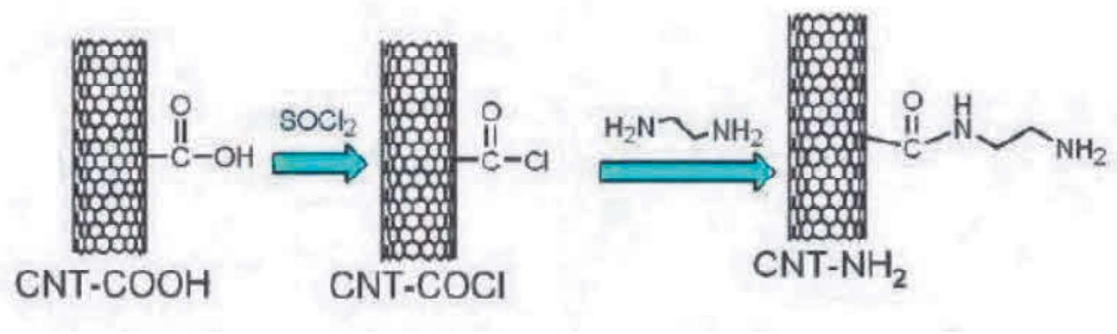


**Figure 9.4.** Scheme of the synthesis of the amine functionalized carbon nanotubes. [7]

It is suggested that there is a maximum above which the protective properties would decrease due to the high degree of cross-linking, which causes poor mechanical properties and high effectiveness of the corrosive environment. [8]

### 9.3.3. Investigation of the Influence of Modifying Epoxy Resin with the Siloxane Resin

The anticorrosion property of epoxy–nanocarbon composites has been shown to improve by adding certain types of modifiers. [9] [10] Fundamental research on the modified epoxy resin and the different carbon materials has not been reported yet. The interaction between modification binder and carbon materials and their corrosion behavior is a very promising area of study. The main objective of

modification is to improve adhesion, corrosion, antibiofouling, mechanical properties, thermal stability, hydrophobicity, weathering, and impact strength of epoxy resins using a second component such as polyurethane, silicones, siloxanes, or electroactive polymers, which are added as modifiers. The modifier with the best perspectives is siloxane, which provides good corrosion and chemical resistance. [11]

The modification of the epoxy resin can be maintained by hydroxyl-terminated poly(dimethyl)siloxane (HPDMS) and orthophosphoric acid as the catalyst, as shown in Figure 9.5.

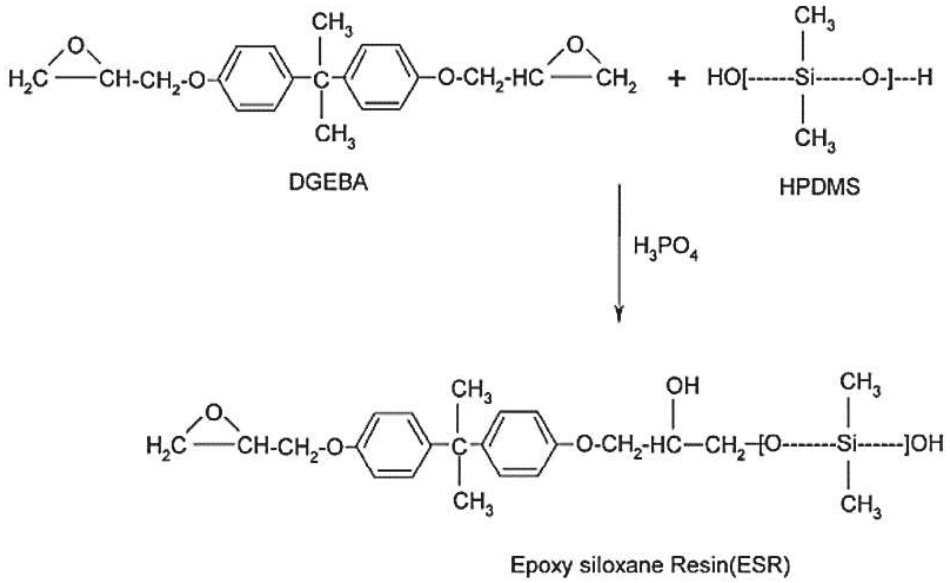


**Figure 9.5.** Scheme of synthesis of epoxy siloxane resin. [12]

Siloxane-modified epoxy–polyamide paints show no sign of leaching and phase separation; the paints also exhibit great physicomechanical and thermal resistance, high anticorrosive performance in acid, saline, and organic solvents environment [12] and corrosion protection. [13]

### 9.3.4. Investigation of the Anti-biofouling Properties of the Coating

In the marine industry, biofouling prevention is an important topic. According to the American Society for Testing and Materials (ASTM) standards, there are several methods for evaluating the degree of biofouling.

One of the test methods describes a procedure for biofouling testing in shallow marine environments, where the testing samples are exposed to seawater. For systems that are subjected to in situ partial immersion exposure, there is another procedure in which samples are fixed on the floating raft in such a way that they are partially out of the water. [15]

In addition, there is a method that determines the antifouling coating performance by erosion or ablation under specified conditions of hydrodynamic shear stress in seawater alternated with static exposure in seawater. This method consists of dynamic and static cycles of typically 30 days each. In the static mode, the experiment is the same as for the shallow environment. The dynamic exposure consists of subjecting the test panels to shear stress by rotating the drum underwater at some specified revolution rate, typically giving a peripheral speed of 15 knots (7.6 m/s). Film thickness is measured at certain intervals during exposure. [16]

The biofouling testing of the coatings should be conducted with an industrial collaborator such as Akzo Nobel (International Paint), one of the largest paint companies in the world, which had a biofouling testing center in Singapore.

**Reference**

[1] B. E. Gu, C. Y. Huang, T. H. Shen, Y. L. Lee, *Prog. Org. Coatings*. **2018**, *121*, 226–235.

[2] C. Chen, S. Qiu, M. Cui, S. Qin, G. Yan, H. Zhao, L. Wang, Q. Xue, *Carbon N. Y.* **2017**, *114*, 356–366.

[3] M. Rajabi, G. R. Rashed, D. Zaarei, *Corros. Eng. Sci. Technol.* **2014**, *50*, 509–516.

[4] A. Ghasemi-Kahrizsangi, H. Shariatpanahi, J. Neshati, E. Akbarinezhad, *Appl. Surf. Sci.* **2015**, *331*, 115–126.

[5] A. O. Artemova, *Lomonosov Moscow State Univ.* **2014**.

[6] S. V. Savilov, A. S. Ivanov, A. V. Egorov, M. N. Kirikova, E. A. Arkhipova, V. V. Lunin, *Russ. J. Phys. Chem. A*. **2016**, *90*, 429–435.

[7] B. Pan, D. Cui, C. S. Ozkan, M. Ozkan, P. Xu, T. Huang, F. Liu, H. Chen, Q. Li, R. He, et al., *J. Phys. Chem. C*. **2008**, *112*, 939–944.

[8] B. Ramezanzadeh, M. M. Attar, *Mater. Chem. Phys.* **2011**, *130*, 1208–1219.

[9] G. M. Spinks, A. J. Dominis, G. G. Wallace, D. E. Tallman, *J. Solid State Electrochem.* **2002**, *6*, 85–100.

[10] J. M. Yeh, H. Y. Huang, C. L. Chen, W. F. Su, Y. H. Yu, *Surf. Coatings Technol.* **2006**, *200*, 2753–2763.

[11] M. F. Montemor, *Surf. Coatings Technol.* **2014**, *258*, 17–37.

[12] S. Ahmad, A. P. Gupta, E. Sharmin, M. Alam, S. K. Pandey, *Prog. Org. Coatings*. **2005**, *54*, 248–255.

[13] J. M. Yeh, H. Y. Huang, C. L. Chen, W. F. Su, Y. H. Yu, *Surf. Coatings Technol.* **2006**, *200*, 2753–2763.

[14] A. International, *ASTM Stand. D3623-78a*. **2012**.

[15] A. International, *ASTM Stand. D 5479-94*. **2013**.

[16] ASTM International, *ASTM Stand. D4939-89*. **2013**.

# APPENDIX

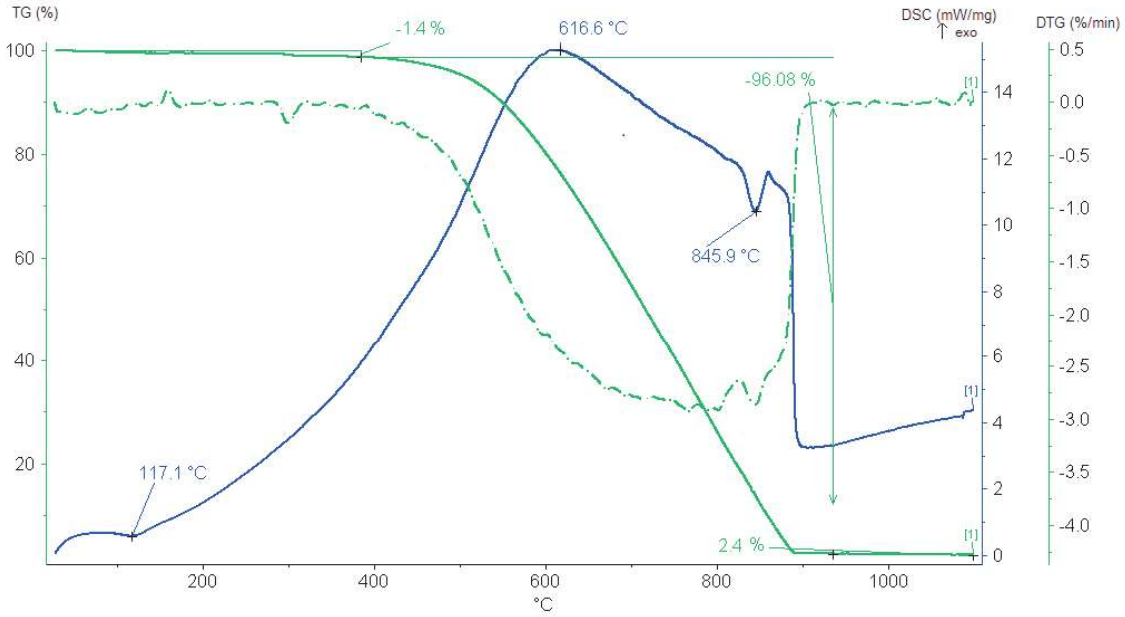


**Figure A.1.** Thermo gravimetric analysis of cylindrical carbon nanotubes.

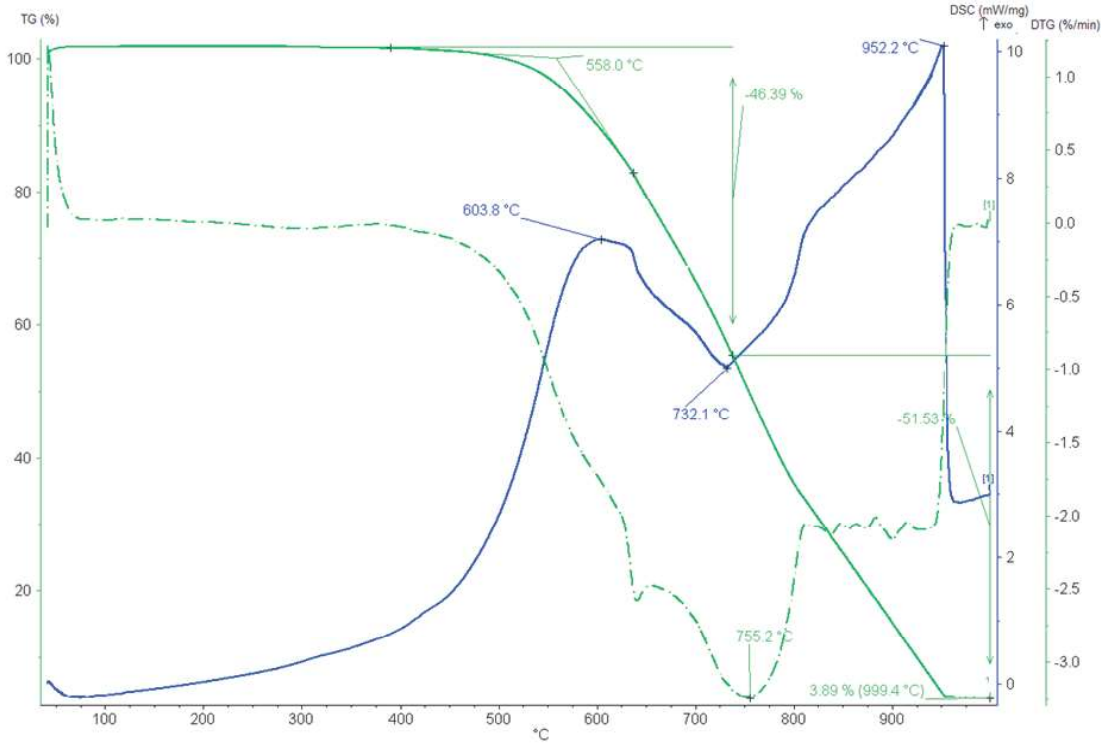


**Figure A.2.** Thermo gravimetric analysis of conical carbon nanotubes.

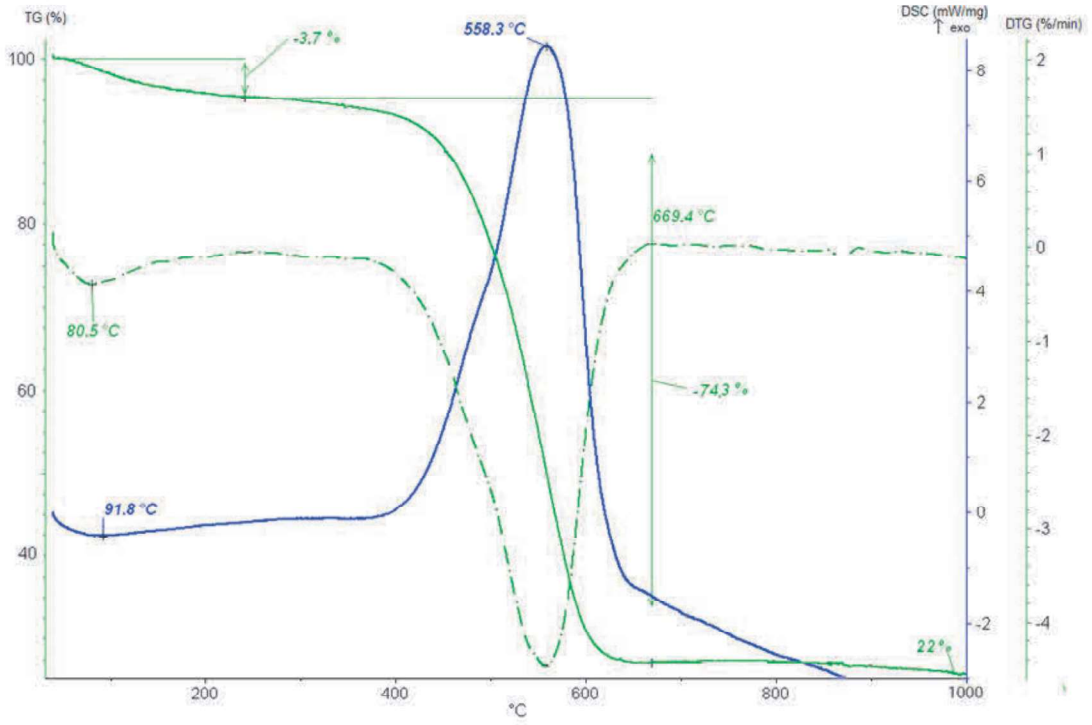


**Figure A.3.** Thermo gravimetric analysis of nitrogen-doped graphene oxide.

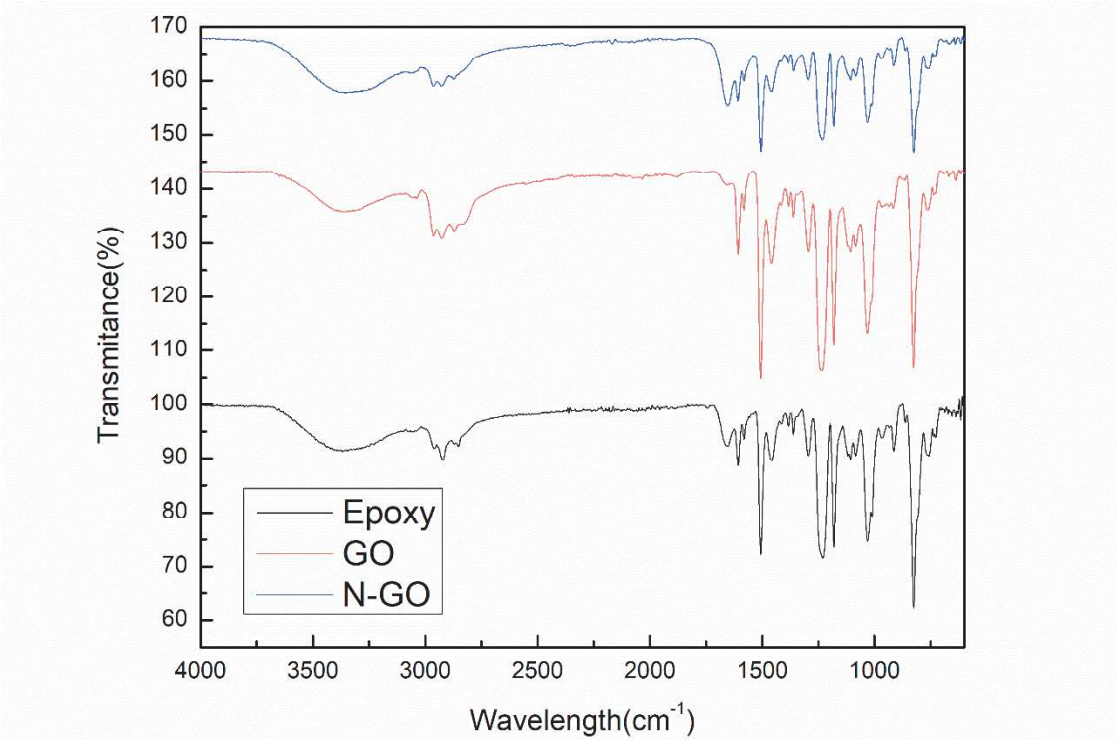


**Figure A.4.** ATR-FTIR spectra of epoxy coating and graphene oxide-based composite coatings.

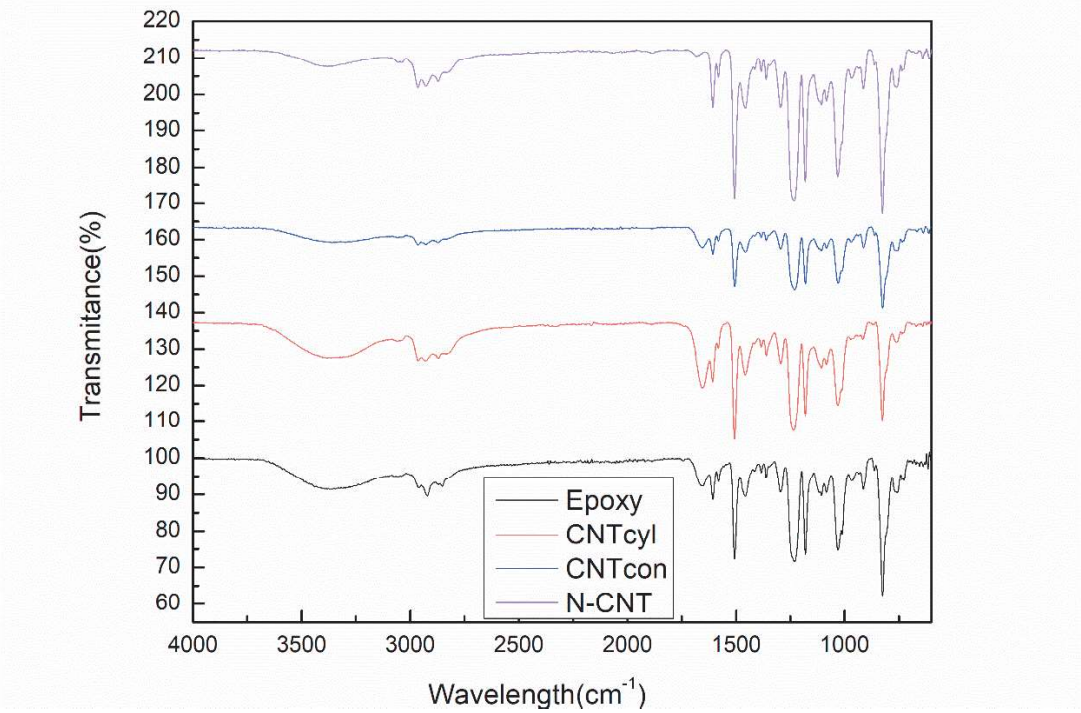


**Figure A.5.** ATR-FTIR spectra of epoxy coating and carbon nanotubes-based composite coatings.

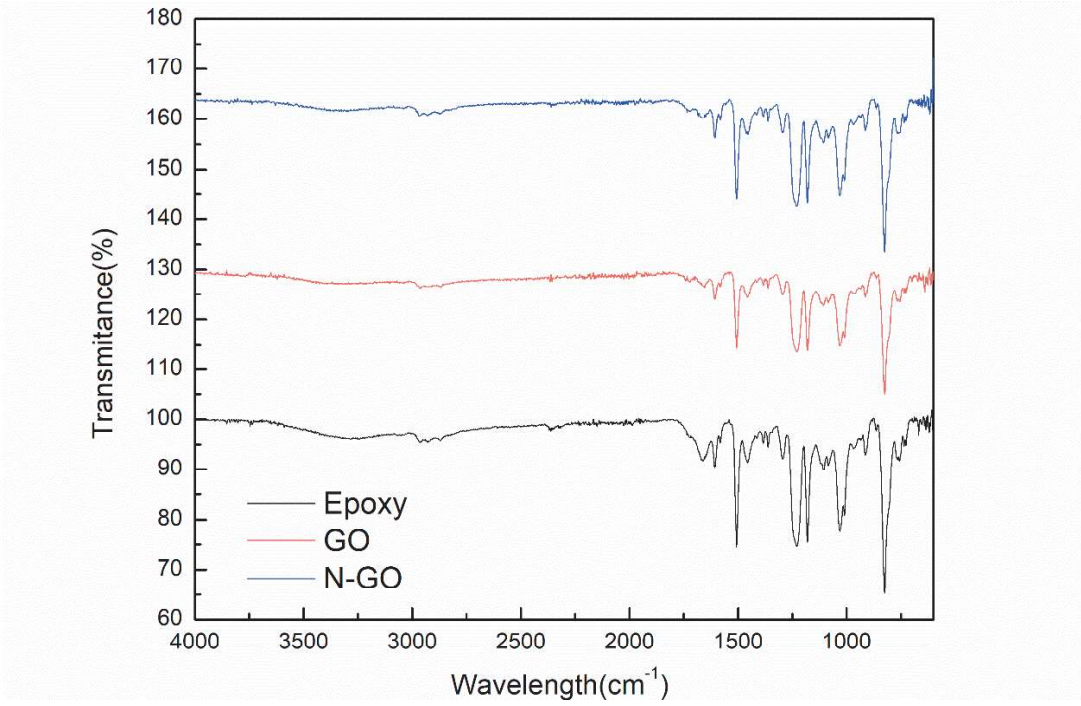


**Figure A.6.** ATR-FTIR spectra of epoxy coating and graphene oxide-based composite coatings after ultraviolet radiation.

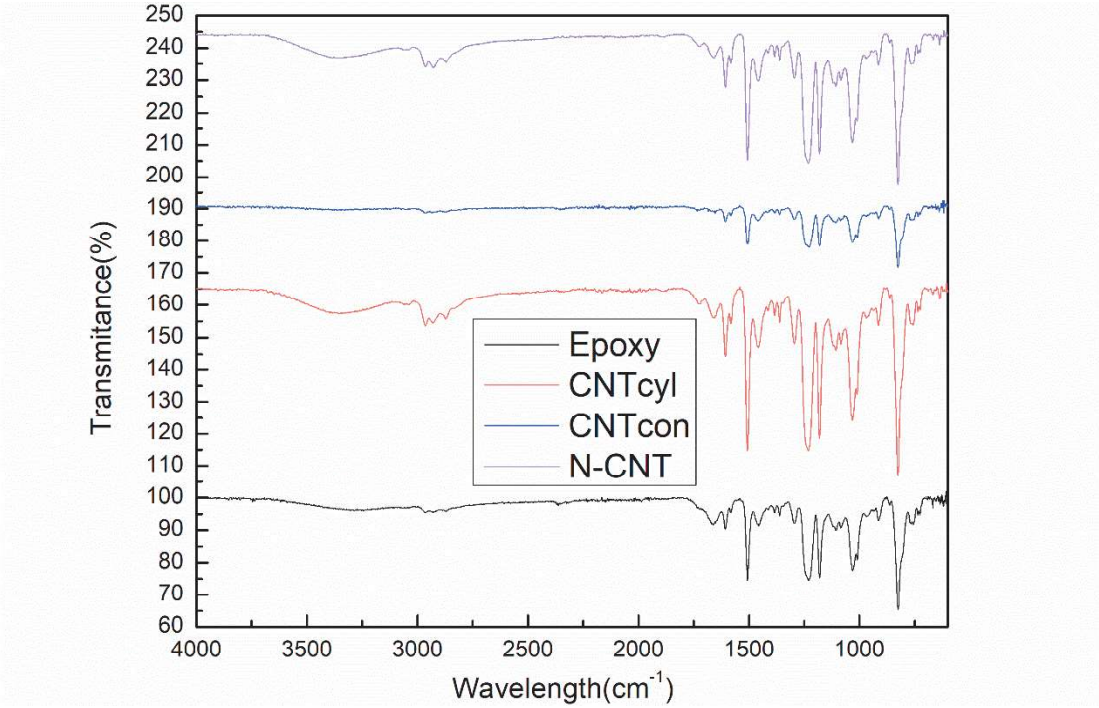


**Figure A.7.** ATR-FTIR spectra of epoxy coating and carbon nanotubes-based composite coatings after ultraviolet radiation.

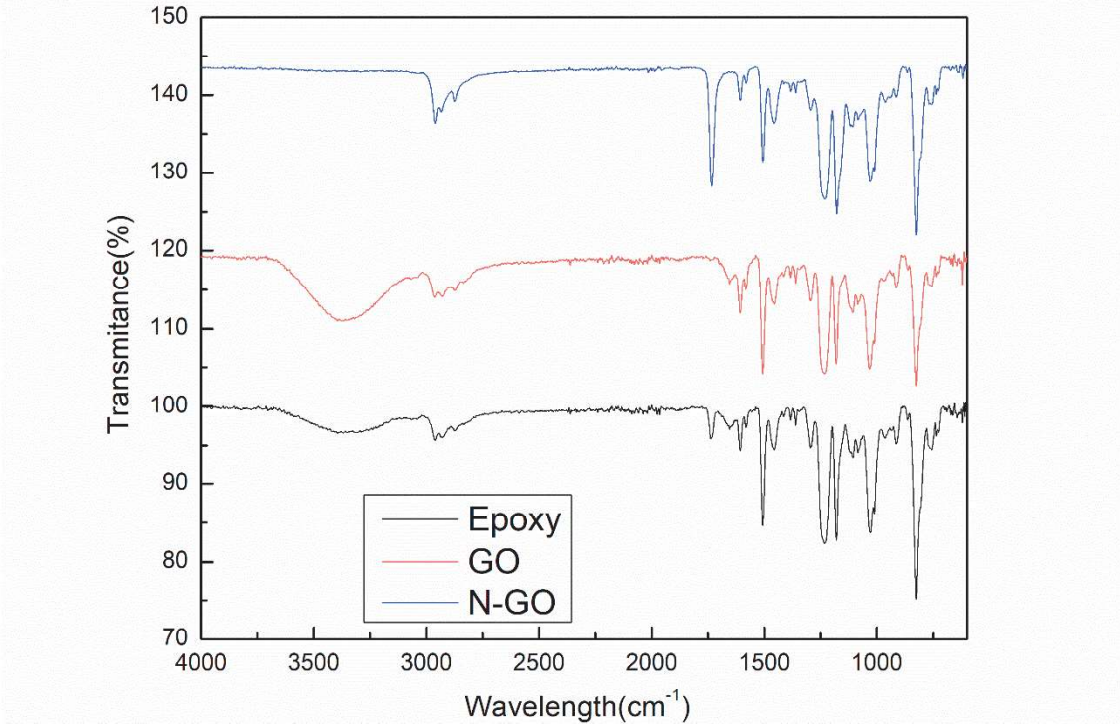


**Figure A.8.** ATR-FTIR spectra of epoxy coating and graphene oxide-based composite coatings after immersion degradation.

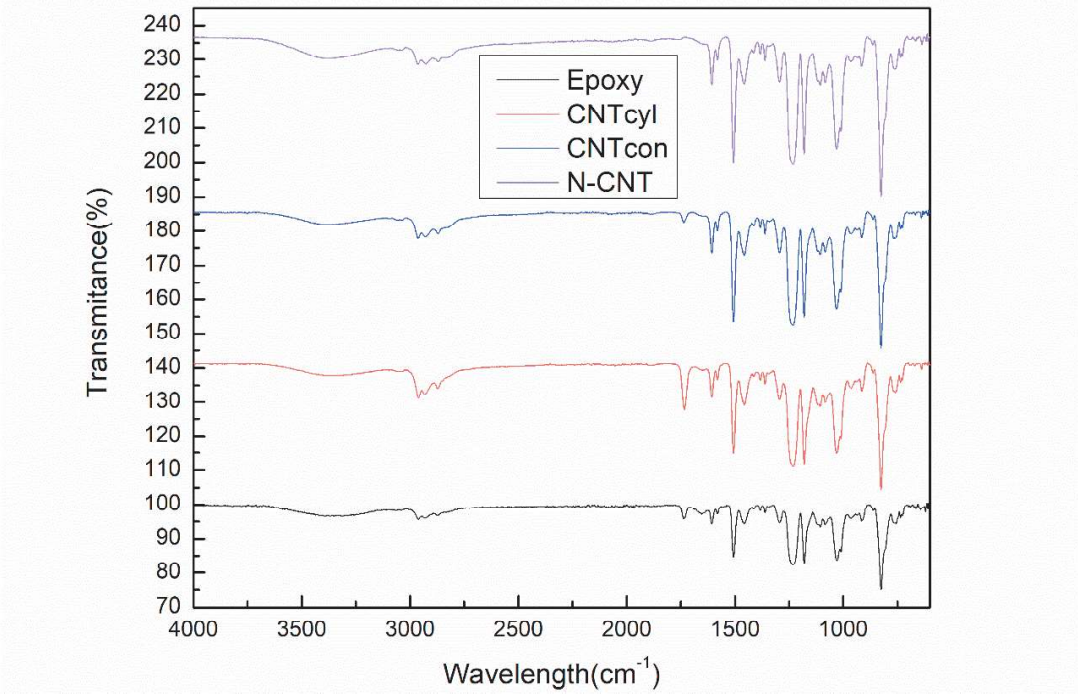


**Figure A.9.** ATR-FTIR spectra of epoxy coating and carbon nanotubes-based composite coatings after immersion degradation.

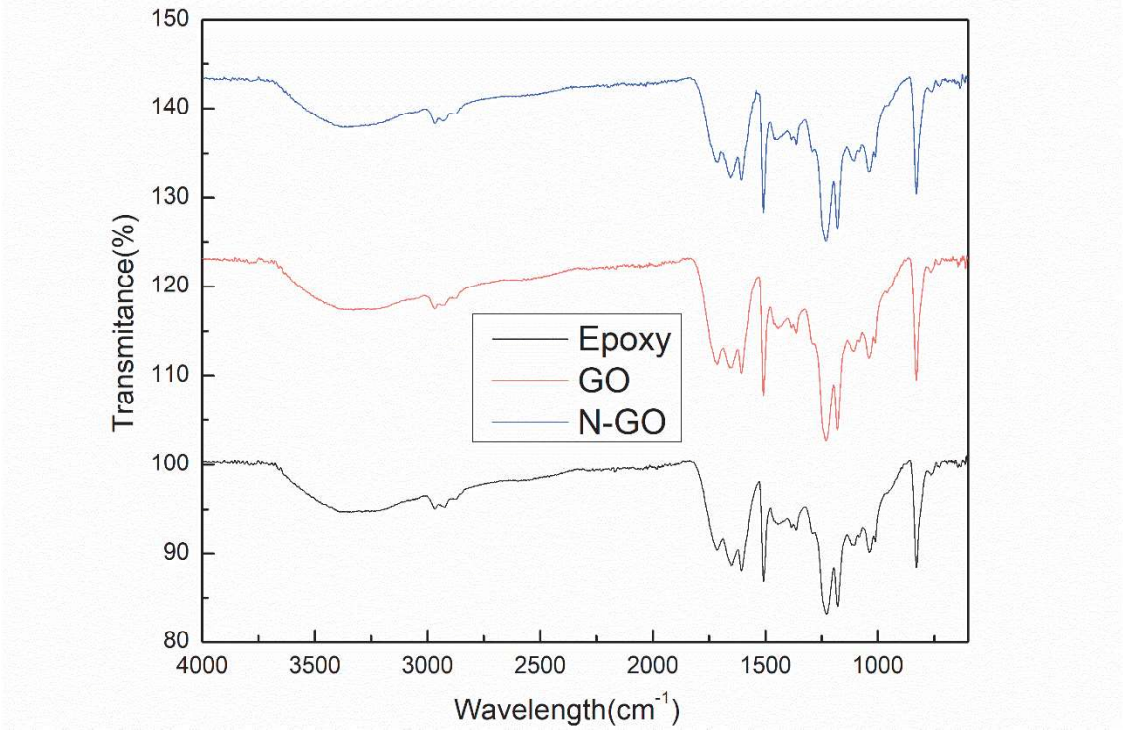


**Figure A.10.** ATR-FTIR spectra of epoxy coating and graphene oxide-based composite coatings after weathering degradation.

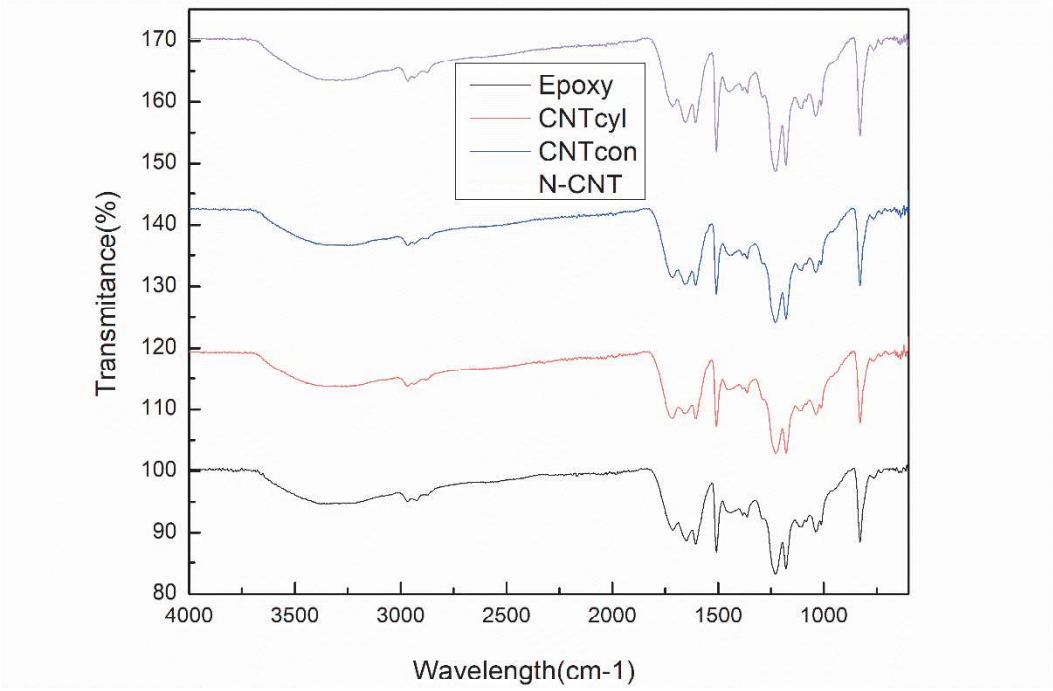


**Figure A.11.** ATR-FTIR spectra of epoxy coating and carbon nanotubes-based composite coatings after weathering degradation.